The First Supernovae

A DISSERTATION
SUBMITTED TO THE FACULTY OF THE GRADUATE SCHOOL
OF THE UNIVERSITY OF MINNESOTA
BY

Ke-Jung Chen

IN PARTIAL FULFILLMENT OF THE REQUIREMENTS
FOR THE DEGREE OF
Doctor of Philosophy

Prof. Alexander Heger

September, 2013

In memory of Professor Shiu-Chin Wu (1952 – 2008)

Abstract

Modern cosmological simulations predict that the first generation of stars formed with a mass scale around $100\,M_\odot$ some $300 - 400$ million years after the Big Bang. When the first stars reached the end of their lives, many of them might have died as energetic supernovae (SNe) that could have significantly impacted the early Universe via injecting large amounts of energy and metals into the primordial intergalactic medium (IGM). In this dissertation, I have studied the SNe from the first stars, using numerical simulations on powerful supercomputers. I use a new radiation hydrodynamics code, `CASTRO`, to model the physical processes behind the first SNe. I also simulate the cosmological impact of the first stars and their SNe by using cosmological simulations with `GADGET`. The goal of my dissertation is to provide a better understanding of the first SNe and their feedback to the early Universe, a study which will be facilitated by forthcoming telescopes.

The thesis is divided into three parts: the first SNe, their impact, and summary. In Part I, I present the results from my SN simulations. I provide relevant background knowledge of the thesis in Chapter 1. This chapter covers a brief overview of modern cosmology and the formation of the first stars and their evolution. Since the first stars are predicted to have been very massive, many of them could have died as SNe, comprising several different types. In this thesis, I first focus on the thermonuclear explosions of very massive stars. After setting the canvas, I introduce the computational approaches for simulating the first SNe. I use a new radiative hydrodynamic code, `CASTRO`, featuring massively parallel and adaptive mesh refinement (AMR). `CASTRO` is designed for modeling complicated astrophysical phenomena and for running on modern supercomputers. The architecture of `CASTRO` allows users to add new codes for solving their own problems. I present my novel numerical approaches associated with `CASTRO` in Chapter 2. I have developed several numerical algorithms, including a new mapping algorithm for multidimensional simulations, comprehensive nuclear reaction networks, and a post-Newtonian correction due to general relativity. The explosion setup for computing fully self-consistent 3D stellar evolution models from their formation to collapse is far beyond the realm of current computational power. One alternative is to first

evolve the main sequence star in a 1D stellar evolution code. Once the star reaches the pre-supernova phase, its 1D profiles can be mapped into multidimensional hydro codes, such as `CASTRO`, and continue to be evolved until the star explodes. I have developed a new mapping technique for initializing multidimensional simulations of stellar explosions with 1D stellar evolution models and imprinting them with velocity perturbations that reproduce the Kolmogorov energy spectrum expected for highly turbulent convective regions in stars. I have built a nuclear reaction code that allows me to follow the entire SN evolution by calculating the process of forging elements (nucleosynthesis) and the energetics during the explosion. Finally, I have developed physics codes for calculating the effect of the post-Newtonian correction due to general relativity.

Now I have geared up to start my simulations. In Chapter 3, I start with the SNe of the first stars with initial masses of $80-150\,\mathrm{M}_{\odot}$. Before these stars die, the violent instabilities in their stellar cores trigger the ejection of a few solar masses pulsationally. These ejected masses may lead to catastrophic collisions of ejecta and power extremely luminous optical transients called pulsational pair-instability supernovae (PPSNe), which may account for the superluminous SNe. I simulate a star of $110\,\mathrm{M}_{\odot}$ and find that the heavy elements ejected from stars are mainly ^{16}O and ^{12}C. There are no chemical elements heavier than ^{28}Si seen in the ejecta, so the radioactive isotope, ^{56}Ni, may not be seen in PPSNe. When the ejecta from different eruptions collide, it demonstrates a significant mixing caused by the fluid instabilities. The mixed region is very close to the photo-sphere of PPSNe and potentially alters their observational signatures such as light curves and spectra.

The first stars with initial masses of $150-260\,\mathrm{M}_{\odot}$ eventually develop a large oxygen core of high entropy in which large amounts of electron-positron pairs are created. Now the pressure-supporting photons convert into electrons and protons and lead to a dynamical instability of these stars. Pair-creation instabilities are so violent that they trigger a rapid contraction of the stellar core. Then the central temperature and density increase sufficiently to cause an explosive burning of oxygen and silicon. The energy released from the burning raises the pressure high enough to leave the instability regime and turn the contraction into an explosion called a pair-instability supernova (PSN). The explosion energy of PSN can reach $10^{53}\,\mathrm{erg}$, about 100 times more energetic than Type Ia SNe, and much ^{56}Ni can be produced up to tens of solar masses. In Chapter 4, I

present systematic 2D PSN simulations. My models follow the entire explosive nuclear burning and the explosion until the shock breaks out from the stellar surface. From my simulations, I find that fluid instabilities driven by oxygen and helium burning arise at the lower and upper boundaries of the oxygen shell at $\sim 20\,\mathrm{sec}$ to $100\,\mathrm{sec}$ after core bounce. When the shock propagates to the hydrogen envelope, a strong reverse shock forms, driving the development of Rayleigh–Taylor (RT) instabilities. These fluid instabilities can lead to a mixing of SN ejecta. The amount of mixing is closely related to the pre-supernova progenitors. The SNe from red supergiants demonstrate much more mixing than those from blue supergiants.

Recent study of Pop III stars suggests that the first stars can be born with a fast rotation, and rotation within stars can impact their evolution and their SN explosions. Hence, I also simulate rotating PSNe in Chapter 5. I perform a series of 2D calculations to investigate the impact of rotation at the early stage of PSNe. The results show that rotation generate an asymmetric explosion caused by a non-isotropic core collapse. The fluid instabilities develop in the inner region of the oxygen core, where explosive silicon burning occurs, affecting the production of ^{56}Ni. The explosive energy of PSNe is also altered by rotation. The impact of rotation depends on the rotation rates. Although the first stars are promising progenitors for PSNe, observational evidence suggests that a few present-day stars can die as PSNe too. With collaborators, I probe the possibility of PSNe for the local Universe in Chapter 6; the results suggest very little mixing for present-day PSNe. This is because metals within the stellar envelope can strip the hydrogen envelope of the stars. When the stars die as PSNe, there is no observable mixing due to the reverse shock. Simulations show only a mild mixing caused by burning at the onset of explosion. By considering the rotation and metallicity effect for the PSNe, we arrive at the question: If the first stars were extremely massive ($\gg 100\,\mathrm{M}_\odot$), what happened when they died? It is generally thought that stars of masses over $300\,\mathrm{M}_\odot$ simply die as black holes without SNe. In Chapter 7, I document finding an extraordinary SN of a $55,500\,\mathrm{M}_\odot$ star while we were investigating the properties of the first super massive stars and their compact remnants. Heger and I suspect that the key driver to the explosion of a super massive star is triggered by the general relativity, when the supporting pressure term starts to contribute a source of gravity. This catalyzes the explosive burning, leading to an explosion of energy up to $10^{55}\,\mathrm{erg}$, which is about

10,000 times more energetic than normal SNe. This implies a narrow mass window in which the super massive stars may die as SNe instead of collapsing into black holes. In Part I, I discuss the possible fate of the first stars as well as other massive stars. If the first stars were really massive and died as SNe, their energetics and synthesized metals must have returned to the early Universe. An important question arises: How does the stellar feedback of the first stars impact the early Universe?

In Part II, I study the impact of the stellar feedback. The stellar feedback from the first star may play an important role in forming the later stars and galaxies such as our Milky Way. In Chapter 8, I review the current understanding of the first galaxies' formation. The first galaxies comprised of the first systems of stars gravitationally bound in dark matter halos are naturally recognized as the building blocks of the early Universe. But how did the first galaxies form? A critical clue in answering this question is the feedback from the first stars and their SNe, as mentioned above. The first stars could be strong sources of UV radiation that created extensive H II regions that led to the cosmic re-ionization. At the same time, they forged the first metals dispersed to the IGM through SN explosions. Enrichment from the first metals might result in the formation of the second generation of stars. But what are the details of the feedback process that occurred in the early Universe? In order to study the impact of the first stars and SNe, I have performed cosmological simulations. In Chapter 9, I introduce the computational approaches for my cosmological simulations with a code that computes gravitational forces using a tree algorithm and models gas dynamics using smoothed particle hydrodynamics (SPH). I use a modified version of `GADGET`, including radiative transfer, cooling, chemistry and heating of primordial gas, and diffusion of chemical elements. I start by investigating the impact of a single first star on its host halo in Chapter 10. The stellar impact depends on the mass of the stars; the more massive the stars are, the more UV photons can be produced , which leads to a more extensive region of ionized hydrogen and helium. The mass of a star also determines its fate. Depending on how massive they are, stars can die as several different kinds of SNe and yield very different explosion energetics and amounts of metals. Chemical enrichment could alter the cooling of gas and affect the star formation inside the first galaxies. For an energetic SNe, I find that its metals can be dispersed to about 1 kpc within five million years after the SNe occurred. The latest studies of the first star formation

suggest these stars may fragment into binaries instead of forming single stars inside the minihalo. Thus, I investigate the impact of the first binaries in Chapter 11. I select a series of binaries, combining two stars of different masses. The results show that the feedback is weaker from the binaries than from single stars with the same amount of mass as the binary system in both radiative and chemical feedback because the UV radiation and metal production significantly increase as the mass of the star increases. A unique feedback from the binaries is x-ray emission, from so-called x-ray binaries that arise from the accretion of matter from a companion star onto the compact object. The x-ray can have an extensive impact on the IGM due to its penetration of the IGM.

In Part III, I summarize the findings of my thesis in Chapter 12. This is the first attempt to understand the evolution and explosions of massive stars and their cosmological consequences. Essentially, I try to fill a gap from the first stars to the consequent galactic environment. However, much effort is still required to refine the models before we can provide more robust predictions. Finally, I list my planned future work in Chapter 13. With fast-growing computational power, simulations will be able to resolve the spatial scale as well as relevant physical processes that occur. Future telescopes can probe the most distant Universe. With both the forthcoming data and the sophisticated models, the most enigmatic and radical mystery of these first luminous objects will be revealed in the foreseeable future.

Contents

List of Tables

List of Figures

Preface

One of the frontiers in modern cosmology is understanding the end of the cosmic dark age, when the first luminous objects (e.g., stars, supernovae (SNe), and galaxies) reshaped the primordial Universe into the present one of much complexity. In this dissertation, I use numerical simulations to study the evolution of the first supernovae and their cosmological consequences. To push the model frontiers of the first SNe, I apply new numerical approaches to advance models of the first SNe. The goal of my dissertation is to provide a better understanding of the first SNe that may be observed by the large telescopes of the future.

Modern space- and ground-based telescopes have detected galaxies and SNe to high redshift. However, current models of these objects are still crude and need intensive refinement before they can provide useful predictions for observation. Until recently, the limitations of computing power have kept us from producing numerical simulations that can resolve the relevant spatial scales and physical processes. The advancement of supercomputing power allows us to start investigating the formation of the first stars, and recent work focusing on first star formation suggests that these stars could have been very massive, having a typical mass scale of about $50 - 100$ solar masses ($M_{\odot}$). Some of them might have died as energetic thermonuclear supernovae, called pair-instability supernovae (PSNe). Such powerful explosions could dump considerable energy and spread the previously-forged elements to the inter-galactic medium (IGM) that significantly impacted later star formation. Most important of all, the forthcoming observatories will probe these first luminous objects; therefore, it is timely that we try to provide meaningful models for understanding the incoming observational data.

The first SNe models came mainly from 1D simulations. The SN explosion, however, is a multidimensional problem because only multi-D calculations can properly evolve

the mixing caused by the fluid instabilities during the explosion. The mixing of SN ejecta can alter the explosion, much like stirring a fire or blowing air into a hot grill. Hence, I use 2D and 3D hydrodynamics simulations and consider the relevant physics (e.g., nuclear burning) to model the first SNe and to gain a better understanding of the mixing of SN ejecta.

After the first stars died as SNe, their synthesized metals were dispersed into the early Universe. How did this early influx of metals affect the formation of later stars and galaxies? To answer this important question, I use cosmological simulations to study the impact of the first stars and their SNe. In contrast to previous works, my simulations include the most realistic feedback from the first stars and SNe. The results offer a better understanding about the physical properties of the early Universe (e.g., temperature, density, and chemical enrichment) that hold the keys to the assembly of the first galaxies.

Working on such ambitious projects in the limited time of my graduate study is almost like a "mission impossible". The supernova simulations and cosmological simulations require very different research approaches because of the different nature of the problems. Fortunately, I was extremely lucky to receive much support from a group of outstanding scientists, and resources from several organizations that have helped me complete this task. First of all, I would like to thank my thesis advisor, Prof. Alexander Heger, for his generous support in myriad forms. He has been a wonderful advisor since I started to work with him. With his support, I attended several conferences and meetings during my graduate study. This significantly benefited my academic career; I have met and interacted with many outstanding scientists. Although Prof. Heger left Minnesota in Summer 2012, we still keep in touch through email and Skype. Without his support, I could not have gone this far. Second, I would like to thank my great mentor, Prof. Stan Woosley, who led our research team for several years. He is a leading figure and academic example, and I wish to follow in his footsteps. He is always kind and helpful to me. He indeed has played an important role in my graduate study. Third, I would like to thank Prof. Tom Jones who taught me the skills of problem-solving and useful astrophysical knowledge. Fourth, I was very lucky to work with Prof. Volker Bromm and his group at the University of Texas, Austin. Prof. Bromm is not only an

outstanding scientist but also an excellent teacher. He has guided me to run cosmological simulations and taught me how to write up scientific results for publications. In addition to these great mentors, I would also thank Dr. Ann Almgren. She taught me scientific computation and offered considerable help to me in debugging codes and in writing new codes. She virtually serves as a co-advisor. I thank Prof. Lars Bildsten, who served as an outstanding advisor while I was a Graduate Fellow at the Kavli Institute of Theoretical Physics (KITP). It has been my pleasure to work with the nuclear physics group led by Prof. Joe Kapusta and Prof. Yong Qian at the University of Minnesota. Externally, I have received much technical support from Dr. John Bell and the fellow scientists at Center for Computational Sciences and Engineering (CCSE), the Lawrence Berkeley Lab, who offered me a strong backup whenever I encountered trouble running my simulations. I am grateful to Prof. Deb Thornton, Prof. Paul Haines, Dr. Laurens Keek, and Pam Vo for reviewing my thesis. Finally, I would like to thank my thesis committee members, Prof. Tom Jones, Prof. Yong Qian, and Prof. Clem Pryke.

In terms of resources, I very much appreciate the kind support of the organizations shown in Figure 1. Without their support, I would not have been able to survive my graduate study. Especially, I would like to thank the University of Minnesota, Twin Cities, for supporting and hosting my graduate study. Furthermore, I thank the Kavli Institute of Theoretical Physics at UC Santa Barbara, the University of Texas at Austin, and the Monash University at Melbourne for their hospitality during my visits. Some grants, such as AAS ITG, funded my trips to conferences, which allowed me to present my work. Major financial support for my graduate study came from the US DOE Program for Scientific Discovery through Advanced Computing (SciDAC; DE-FC02-09ER41618), from the US Department of Energy under grant DE-FG02-87ER40328, the Stanwood Johnston Fellowship from the University of Minnesota, and the KITP Graduate Fellowship, which was supported in part by the National Science Foundation under Grant No. NSF PHY11-25915. My numerical simulations were performed with allocations from the National Energy Research Scientific Computing Center and the Minnesota Supercomputing Institute.

Being a graduate student at Minnesota was very pleasant; even though the winter was sort of bitter, people were friendly and nice to each other. Among all of my friends, I would like to thank Laurens Keek, Andrea Mehner, Meng-Ru Wu, Chien-Te Wu, Cindy

Chen, Chia Wei, Pam Vo, and Chen Hou. We had numerous wonderful times having fun or discussing science. Last but not least, I would like to thank my family members for their endless support. My parents gave me the freedom to pursue my own interests and have always stood by my side. My godmother has treated me like her own son and cared about me. My brother and his wife are always great hosts whenever I visit them in Taiwan. There are too many people I should thank, and I apologize if I have missed anyone or any group. In the end, I thank God and Taiwan, which foster my life and bless me all the time.

Figure 1: Logos of supporting agencies. My research has been strongly supported by these organizations in the form of funding, resources, and service.

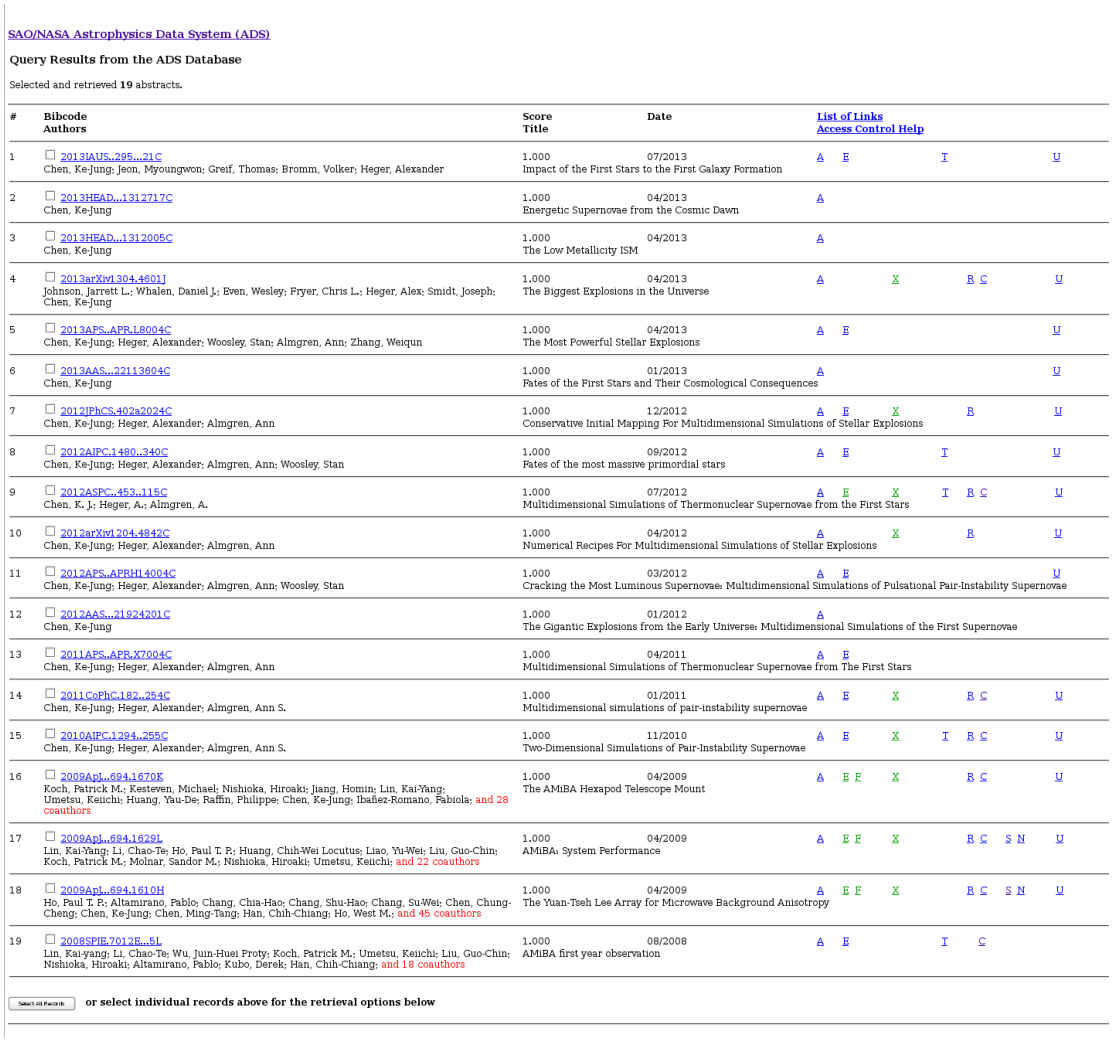

SAO/NASA Astrophysics Data System (ADS)

Query Results from the ADS Database

Selected and retrieved **19** abstracts.

#	Bibcode Authors	Score Title	Date	List of Links Access Control Help
1	2013IAUS..295...21C Chen, Ke-Jung; Jeon, Myoungwon; Greif, Thomas; Bromm, Volker; Heger, Alexander	1.000 Impact of the First Stars to the First Galaxy Formation	07/2013	A E T U
2	2013HEAD...1312717C Chen, Ke-Jung	1.000 Energetic Supernovae from the Cosmic Dawn	04/2013	A
3	2013HEAD...1312005C Chen, Ke-Jung	1.000 The Low Metallicity ISM	04/2013	A
4	2013arXiv1304.4601J Johnson, Jarrett L.; Whalen, Daniel J.; Even, Wesley; Fryer, Chris L.; Heger, Alex; Smidt, Joseph; Chen, Ke-Jung	1.000 The Biggest Explosions in the Universe	04/2013	A X R C U
5	2013APS..APR.L8004C Chen, Ke-Jung; Heger, Alexander; Woosley, Stan; Almgren, Ann; Zhang, Weiqun	1.000 The Most Powerful Stellar Explosions	04/2013	A E U
6	2013AAS...22113604C Chen, Ke-Jung	1.000 Fates of the First Stars and Their Cosmological Consequences	01/2013	A U
7	2012JPhCS.402a2024C Chen, Ke-Jung; Heger, Alexander; Almgren, Ann	1.000 Conservative Initial Mapping For Multidimensional Simulations of Stellar Explosions	12/2012	A E X R U
8	2012AIPC.1480..340C Chen, Ke-Jung; Heger, Alexander; Almgren, Ann; Woosley, Stan	1.000 Fates of the most massive primordial stars	09/2012	A E T U
9	2012ASPC..453..115C Chen, K. J.; Heger, A.; Almgren, A.	1.000 Multidimensional Simulations of Thermonuclear Supernovae from the First Stars	07/2012	A E X T R C U
10	2012arXiv1204.4842C Chen, Ke-Jung; Heger, Alexander; Almgren, Ann	1.000 Numerical Recipes For Multidimensional Simulations of Stellar Explosions	04/2012	A X R U
11	2012APS..APRH14004C Chen, Ke-Jung; Heger, Alexander; Almgren, Ann; Woosley, Stan	1.000 Cracking the Most Luminous Supernovae: Multidimensional Simulations of Pulsational Pair-Instability Supernovae	03/2012	A E U
12	2012AAS...21924201C Chen, Ke-Jung	1.000 The Gigantic Explosions from the Early Universe: Multidimensional Simulations of the First Supernovae	01/2012	A
13	2011APS..APR.X7004C Chen, Ke-Jung; Heger, Alexander; Almgren, Ann	1.000 Multidimensional Simulations of Thermonuclear Supernovae from The First Stars	04/2011	A E
14	2011CoPhC.182..254C Chen, Ke-Jung; Heger, Alexander; Almgren, Ann S.	1.000 Multidimensional simulations of pair-instability supernovae	01/2011	A E X R C U
15	2010AIPC.1294..255C Chen, Ke-Jung; Heger, Alexander; Almgren, Ann S.	1.000 Two-Dimensional Simulations of Pair-Instability Supernovae	11/2010	A E X T R C U
16	2009ApJ...694.1670K Koch, Patrick M.; Kesteven, Michael; Nishioka, Hiroaki; Jiang, Homin; Lin, Kai-Yang; Umetsu, Keiichi; Huang, Yau-De; Raffin, Philippe; Chen, Ke-Jung; Ibañez-Romano, Fabiola; and 28 coauthors	1.000 The AMiBA Hexapod Telescope Mount	04/2009	A E F X R C U
17	2009ApJ...694.1629L Lin, Kai-Yang; Li, Chao-Te; Ho, Paul T. P.; Huang, Chih-Wei Locutus; Liao, Yu-Wei; Liu, Guo-Chin; Koch, Patrick M.; Molnar, Sandor M.; Nishioka, Hiroaki; Umetsu, Keiichi; and 22 coauthors	1.000 AMiBA: System Performance	04/2009	A E F X R C S N U
18	2009ApJ...694.1610H Ho, Paul T. P.; Altamirano, Pablo; Chang, Chia-Hao; Chang, Shu-Hao; Chang, Su-Wei; Chen, Chung-Cheng; Chen, Ke-Jung; Chen, Ming-Tang; Han, Chih-Chiang; Ho, West M.; and 45 coauthors	1.000 The Yuan-Tseh Lee Array for Microwave Background Anisotropy	04/2009	A E F X R C S N U
19	2008SPIE.7012E...5L Lin, Kai-yang; Li, Chao-Te; Wu, Juin-Huei Proty; Koch, Patrick M.; Umetsu, Keiichi; Liu, Guo-Chin; Nishioka, Hiroaki; Altamirano, Pablo; Kubo, Derek; Han, Chih-Chiang; and 18 coauthors	1.000 AMiBA first year observation	08/2008	A E T C

Select All Records **or select individual records above for the retrieval options below**

Figure 2: ADS snapshot of published articles, proceedings, and abstracts during my Ph.D. work.

Part I

The First Cosmic Explosions

Chapter 1

The First Stars

The birth of the first stars declares the end of the cosmic dark age and marks the transition of the primordial Universe. In Part I of this thesis, we discuss the extraordinary fate of the first stars. It is necessary to understand how the first stars formed and how they evolved. This chapter serves as an introduction to the background knowledge needed for understanding this thesis. We start with an overview of the standard cosmology models that explain the formation of large scale structures in § 1.1. The dark matter halos inside the large scale structures function as gravitational wells that hatch the primordial gas to form stars. In § 1.2, we discuss the current understanding of first star formation. Once the first stars form, they start evolving and forging the first chemical elements above hydrogen and helium. We discuss the stellar evolution, focusing on the first stars, in § 1.3. The fate of the stars depends on their initial mass as well as their composition. The first stars are predicted to form at a mass scale of $50 - 100\,\mathrm{M}_{\odot}$. In § 1.4, we discuss the fate of the first massive stars, which is also the main theme of Part I.

1.1 The Early Universe

The creation and evolution of the Universe has been one of the most fascinating subjects in modern cosmology. It is proper to provide the background of the early Universe, which hatched the first stars, supernovae, and galaxies, which are the major topics of this thesis. This section aims to provide a brief overview of modern cosmology. There are

several reviews about the early Universe. We list only some of them for readers interested in having a more comprehensive understanding of modern cosmology. The recommended entry-level textbooks about the early Universe are Liddle (2003) for undergraduate students and Peacock (1999) for graduate students. For more specific studies, Kolb and Turner (1990) provide a comprehensive introduction to the Inflationary model and the Big Bang Nucleosynthesis. Dodelson (2003) discusses the quantum fluctuation from Inflation and how it was seeded as initial perturbations for the large scale structure formation. Those who are interested in the dynamics and evolution of the Universe can consult two classic books by Peebles (1980, 1993).

Our Universe is believed to have been born from the Big Bang at the time when the density and temperature of the Universe were infinite. At the beginning of the Big Bang, all fundamental physical forces—such as gravitational, electro-magnetic, strong, and weak forces—were united. Due to the rapid expansion of the Universe, the temperature dropped quickly, and the fundamental forces became separated. At about 10^{-36} sec after the Big Bang commenced, the Universe went through a very short and rapid expansion called Inflation (Guth, 1981; Linde, 1982). The rapid expansion seeded the quantum fluctuations into space-time. These fluctuations later became the initial perturbations of the Universe, which led to the formation of large scale structures. A few minutes later, the atomic nuclei could start to form. Then protons and neutrons began to combine into atomic nuclei: helium (24% in mass), hydrogen (76 % in mass), and a trace amount of lithium. The Big Bang Nucleosynthesis lasted only until the temperatures and densities of baryons became too low for further nucleosynthesis, which was about several minutes. The elements necessary for life, such as carbon and oxygen, had not been made at this moment.

About 300,000 years after the Big Bang, the Universe cooled below $10,000\,\mathrm{K}$. At that time, protons and electrons could recombine into neutral hydrogen. Without the opacity from free electrons, the photons decoupled from the matter and streamed freely. This radiation is called the cosmic microwave background radiation (CMB), and it was first detected by Penzias and Wilson (1965). It fits perfectly with a black-body of temperature about $2.73\,\mathrm{K}$. In 1992, the Cosmic Background Explorer (COBE) detected the anisotropy of the CMB, which shed the light of understanding on the structure formation of the early Universe. More recent results from the Wilkinson Microwave Anisotropy

Probe (WMAP) helped to confirm inflationary cosmology and determined the cosmological parameters with an unprecedented precision. The success of CMB observation confirmed that the Universe contains about 5 % of baryon, 25 % of cold dark matter (CDM), and 70% of dark energy (Λ). Except for baryon, the intrinsic properties of cold dark matter and dark energy are poorly understood. Significant experimental effort has been made for studying the dark sectors of the Universe; promising progress should be made in the near future. Nevertheless, the Big Bang Nucleosynthesis, inflationary models, and ΛCDM form the foundation of modern cosmology.

The initial perturbation seeded by inflation began evolving through gravity. In Figure 1.1, we show the formation of a large scale structure from our cosmological simulation with `GADGET`. This example consists of 128^3 dark matter particles, and 128^3 gas particles, following structure formation in a periodic box of size $50\,h^{-1}\,\mathrm{Mpc}^3$ in a ΛCDM Universe. The simulation begins at the redshift of $z \sim 10$ and ends at $z \sim 0$; the distribution of particles is homogeneous and isotopic with a very tiny gaussian fluctuation. The dark matter particles (black dots) evolved into highly clustered structures hierarchically through gravity.

There was no star at the time when the CMB was emitted because the density of primordial gas was too low and could not condense to form stars. The Universe then entered the cosmic dark ages when there was no light from stars. Some several hundred million years after the Big Bang, the dark matter collapsed into so-called minihalos with masses of $10^5 - 10^6\,\mathrm{M}_\odot$, which would become the birth sites for the first stars because such halos could provide gravitational wells that retained the gas to form stars. The light from the first stars ended the dark ages, which had lasted for several hundred million years. In addition, the first stars started to forge the first metals that became the building blocks of later stars and galaxies. Thus, the first stars play a crucial role in the evolution of the Universe, and their extraordinary fate is the main theme of Part I. Figure 1.2 shows the timeline of the Universe. The observable Universe spans about 13.7 billion years, starting with the Big Bang and quickly expanding during Inflation. After $380,000$ years, the CMB was emitted from the last scattering surface. Later, the Universe entered the dark ages until the first stars were born. Hereafter, the planets, stars, and galaxies started to form.

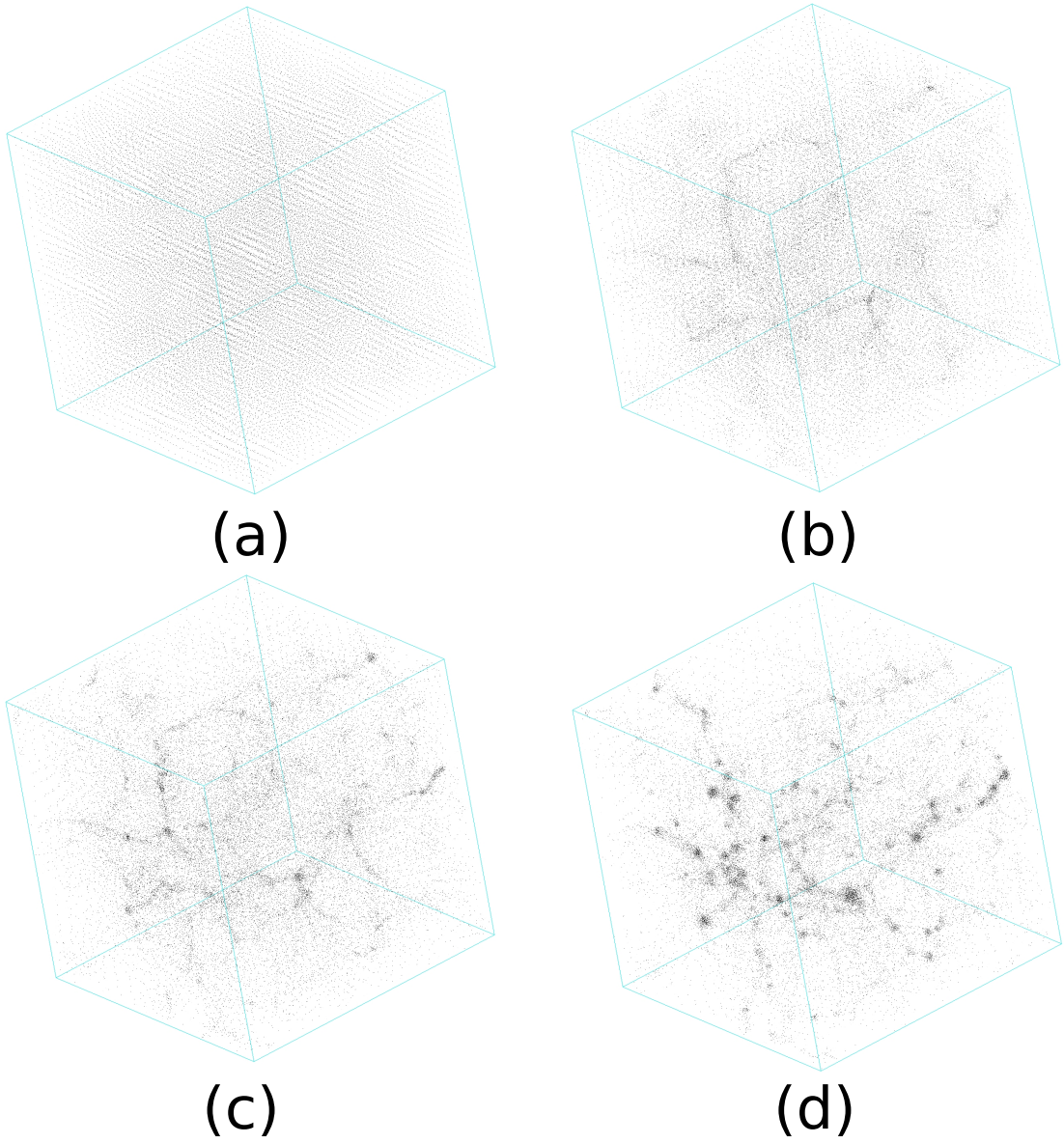

Figure 1.1: The formation of large scale structure. The black dots represent the dark matter particles. The evolution follows from panel (a) → (b) → (c) → (d).

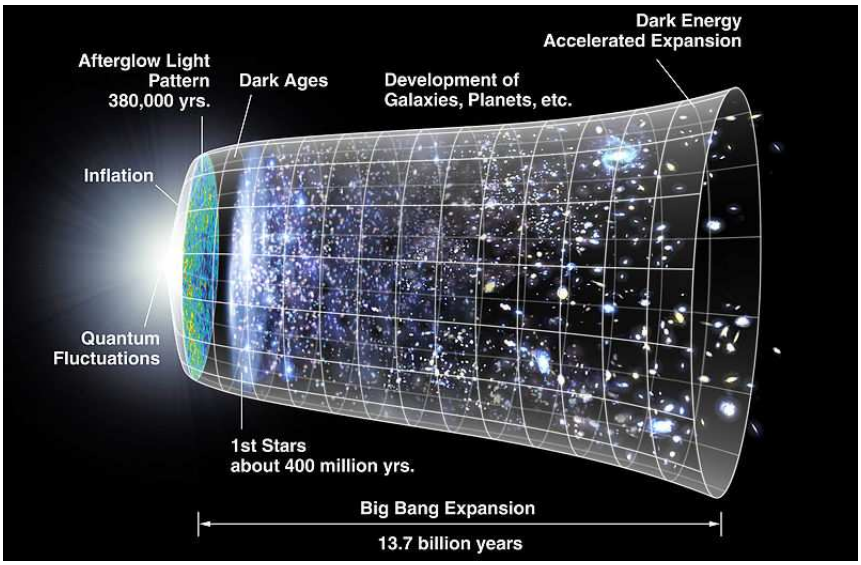

Figure 1.2: The illustration shows the evolution of cosmic structure from the Big Bang. The first stars appeared, terminating the cosmic dark age about 400 million years after the Big Bang. (Credit: NASA/WMAP Science Team)

1.2 Star Formation

Formation of the first stars transformed the simple early Universe into a highly complicated one. The first stars made from the hydrogen and helium left from the Big Bang are called the Population III (Pop III) stars, which are ancestors of the current stars like our Sun. The study of the first stars has recently received increasing attention because the tools for this study have become available, including the forthcoming high-z observatories, which will probe the cosmic dark ages, and the advancement of modern supercomputers, which allow us to carry out more sophisticated simulations. In this section, we review the recent advancement of our understanding of the first star formation.

The ΛCDM model offers a fundamental theory for the large scale formation, suggesting that the cosmic structure formed in a hierarchical manner. The first stars must form along with the structural evolution of the Universe. The conditions for the star

formation are that the cooling time scale of halos must be smaller than their dynamical time scale. According to Bromm and Larson (2004), the low-mass dark matter halos have a virial temperature of $\propto M^{2/3}(1+z)$, where M is the halo mass and z is the redshift. Metal cooling was absent in the early Universe, and the cooling of gas occurred primarily through molecular hydrogen, H_2. The dominating H_2 formation goes through $H + e^- \rightarrow H^- + \gamma$ and $H^- + H \rightarrow H_2 + e^-$. Sources of free electrons, e^-, come from the recombination or collision excitation of gas when dark matter halos merge. Pioneering work of Tegmark et al. (1997) suggests that the first star was born in the halos, which reach a H_2 fraction of 10^{-4}. Abel et al. (2002) suggest that the first stars form inside halos of $\sim 10^6\,M_\odot$ at $z \sim 30$. The size of Pop III star-forming clouds is comparable to the virial radius of the halos, about 100 pc. The detailed shape of the cloud is determined by its angular momentum, which depends on the resolution of the simulations.

So far there is no direct detection of Pop III stars. Nevertheless, the observation of present-day stars may provide us hints to study the first star formation. The present-day (Pop I) stars are born inside a giant molecular cloud of size about 100 pc. Because the cloud is supported by the pressure from turbulence flow or magnetic field, its structure appears to be very complex and inhomogeneous. $1,000 - 1,000,000$ stars usually form inside the cloud. Salpeter (1955) suggests the observed initial mass function (IMF) of Pop I stars to be

$$N(M_*) = N_0\, M_*^{-2.35}, \tag{1.1}$$

where N is the number of stars, M_* is the stellar mass, and N_0 is a constant. The characteristic mass scale of the Salpeter IMF is about $1\,M_\odot$, which means most of the Pop I stars form as massive as our Sun. It is very difficult to calculate the Pop I IMF from first principles because present-day star formation involves magneto-hydrodynamics, turbulent flow, and complex chemistry. However, the initial conditions of the primordial Universe, such as the cosmological parameters, are better understood. In addition, the metal-free and magnetic-free gas makes the simulation of Pop III star formation more accessible. For simulating the Pop III star formation, we need 3D cosmological simulations of dark matter and gas, including cooling and chemistry for primordial gas. The initial conditions of simulations use the cosmological parameters from the CMB measurement.

The key feature for cosmological simulation is handling a large dynamical range. Two popular setups for simulating the first star formation are mesh-based (Abel et al., 2000, 2002) and Lagrangian techniques (Bromm et al., 2002, 2009). The mesh-based technique usually employs the adaptive mesh refinement (AMR), which creates finer grids to resolve the structures of interests such as gas flow inside the dark matter halos. The other approach is called smoothed particle hydrodynamics (SPH), which uses particles to model the fluid elements. The mass distribution of particles is based on a kernel function. The results of AMR and SPH simulations both agree on the characteristics of the first star-forming cloud, $T_c \approx 200\,\mathrm{K}$ and $n_c \approx 10^4\,\mathrm{cm}^{-3}$. The T_c is determined by H_2 cooling, which is the dominating coolant at that time. The lowest energy levels of H_2 are collisional excitation and subsequent rotational transitions with an energy gap of $\Delta E/k_\mathrm{B} \simeq 512\,\mathrm{K}$. Atomic hydrogen can cool down to several hundred K through collisions with H_2; n_c is explained by the saturation of H_2 cooling: below n_c, the cooling rate is $\propto n^2$; above n_c, the cooling rate is $\propto n$. Once the gas reaches the characteristic status, the cooling then becomes inefficient and the gas cloud becomes a quasi-hydrostatic. The cloud eventually collapses when the its mass is larger than its Jeans mass (Bromm and Larson, 2004),

$$M_J = 700\left(\frac{T}{200\,\mathrm{K}}\right)^{3/2}\left(\frac{n}{10^4\,\mathrm{cm}^{-3}}\right)^{-1/2}\ \mathrm{M}_\odot. \tag{1.2}$$

The Jeans mass is determined by the balance between the gravity and pressure of gas. For the first star formation, the pressure here is mainly from the thermal pressure of the gas. However, it is unclear whether the cloud forms into a single star or fragments into multiple stars. To answer this question, evolving the cloud to a higher density and following the subsequent accretion are required. The cloud mass at least sets up a maximum mass for the final stellar mass. But the exact mass of the stars is determined by the accretion history when the star forms. Bromm and Loeb (2004) suggest that the first stars can be very massive, having a typical mass of $100\,\mathrm{M}_\odot$ with a broad spectrum of mass distribution.

1.3 Stellar Evolution

After the first star has formed, its core temperature increases due to Kelvin-Helmholtz contraction and eventually ignites hydrogen burning. In contrast to the present-day stars, there was no metal present inside the first stars. They first burn hydrogen into helium through p-p chains, then burn helium through the 3α reaction. A detailed description of hydrogen burning can be found in e.g. Prialnik (2000). After the first carbon and oxygen have been made, the first stars can burn the hydrogen in a more effective way through the CNO cycle. Once stable hydrogen burning at the core of the star occurs, the first stars enter their main sequence. The lifespan of a star on the main sequence mainly depends on its initial mass and composition. The energy released from nuclear burning is used to supply the radiation. Once the hydrogen is depleted, the star completes the main sequence and starts to burn helium as well as the resulting nuclei. In the following sections, we introduce the advanced burning stages of stars before the stars die.

1.3.1 Advanced Burning

The luminosity of stars is powered by the nuclear fusion that occurs inside the stars. Light elements are synthesized into heavy elements, and the accompanying energy is released. We review the advanced burning stages based on Kippenhahn and Weigert (1990); Arnett (1996); Prialnik (2000); Woosley et al. (2002). First, the helium burning consists of two steps,

$$^4\mathrm{He} + {}^4\mathrm{He} \rightarrow {}^8\mathrm{Be}, \quad {}^8\mathrm{Be} + {}^4\mathrm{He} \rightarrow {}^{12}\mathrm{C}. \tag{1.3}$$

The process is known as the $3\,\alpha$ reaction because three helium (α) are involved. It yields $5.8 \times 10^{17}\,\mathrm{erg\,g^{-1}}$. ^{8}Be determines the overall reaction rate, and its production is proportional to the square of the ^{4}He number density. So the energy generation rate is proportional to the density square. The formula of the energy generation rate of the $3\,\alpha$ reaction is (Prialnik, 2000)

$$q_{3\alpha} \propto \rho^2 T^{40}. \tag{1.4}$$

Some α capture reaction may occur, if sufficient ^{12}C are present. But at such a temperature, only

$$^{12}\mathrm{C} + {}^{4}\mathrm{He} \rightarrow {}^{16}\mathrm{O} \tag{1.5}$$

is significant; other capture reaction rates are too low. So the major products of helium burning are carbon and oxygen, and the ratio of ^{12}C/^{16}O depends on temperature. After the helium burning, the star starts to burn carbon and oxygen, which requires higher temperatures to ignite. Carbon starts to burn when the temperatures reach 5×10^8 K. There are several channels of reactions,

$$^{12}\mathrm{C} + {}^{12}\mathrm{C} \longrightarrow \begin{array}{l} {}^{23}\mathrm{Mg} + \gamma \\ {}^{24}\mathrm{Mg} + n \\ {}^{23}\mathrm{Na} + p \\ {}^{20}\mathrm{Ne} + \alpha \\ {}^{16}\mathrm{O} + 2\alpha. \end{array}$$

The overall energy generation is about $5.2 \times 10^{17}\,\mathrm{erg\,g^{-1}}$. The process of oxygen burning ignites at a temperature of 10^9 K. Similar to ^{12}C, there are several channels available:

$$^{16}\mathrm{O} + {}^{16}\mathrm{O} \longrightarrow \begin{array}{l} {}^{28}\mathrm{Si} + \gamma \\ {}^{32}\mathrm{S} + n \\ {}^{31}\mathrm{P} + p \\ {}^{28}\mathrm{Si} + \alpha \\ {}^{24}\mathrm{Mg} + 2\alpha. \end{array}$$

The average energy released is about $4.8 \times$, $10^{17}\,\mathrm{erg\,g^{-1}}$. There is little interaction between carbon and oxygen for the intermediate temperature that ignites carbon burning because the carbon can quickly burn out by self interaction. The light elements produced from carbon and oxygen burning are immediately captured by the existing heavy nuclei. The major isotope produced after oxygen burning is ^{28}Si.

Silicon burning follows the oxygen burning and is the final advanced burning stage that releases energy. The temperature of silicon burning is about 3×10^9 K. In such

high temperatures, energetic photons are able to disintegrate the heavy nuclei; this process is called photodisintegration. During the silicon burning, part of the silicon is first photodisintegrated; the light isotopes are then recaptured by the silicon, and the resulting isotopes are photodisintegrated recursively. Such reactions build up a comprehensive reaction network and tend to reach a status called nuclear statistical equilibrium (NSE). The forward and backward reaction rates in NSE are almost equal. However, a perfect NSE only occurs at temperatures $> 7 \times 10^9\,\mathrm{K}$. At the end, silicon burns into the iron group, including iron, cobalt, and nickel, and no more energy can be released from burning these isotopes. The major nuclear burning reactions inside a star are listed in Table 1.1. However, not every star goes through all of these burning processes; it depends on their initial masses.

Fuel	Reaction	$T_{\mathrm{min}}[10^6\,\mathrm{K}]$	yields
H	$p-p$	4	He
H	CNO	15	He
He	$3\,\alpha$	100	C,O
C	C+C	600	O, Ne, Na, Mg
O	O+O	1000	Mg, S, P, Si
Si	NSE to iron group	3000	Co, Fe, Ni

Table 1.1: T_{min}: the minimum temperature to ignite the burning. (Data comes from Prialnik (2000); Woosley et al. (2002))

Energetic photons may turn into electron-positron pairs when they interact with the nucleus. The threshold energy of a photon for pair-production is $h\nu \sim 2m_ec^2$, where m_e is the rest mass of the electron and c is the speed of light. This energy scale corresponds to a temperature of about $T \sim 2m_ec^2/k_{\mathrm{B}} \sim 10^{10}\,\mathrm{K}$. At temperatures higher than $10^9\,\mathrm{K}$, photons in the tail of the Planck distribution are energetic enough to create e^+e^- pairs. Pair production can lead to dynamical instabilities in the cores of stars because the pressure-supporting photons have become exhausted and turned into pairs. Pair-instabilities usually occur in very massive stars with masses over $80\,\mathrm{M}_\odot$. If

the temperature is sufficiently high, the stable iron group elements can also be photodisintegrated and break into α particles and neutrons. This process is called iron photodisintegration:

$$^{56}\mathrm{Fe} + \gamma \rightarrow 13\,^{4}\mathrm{He} + 4n. \tag{1.6}$$

This reaction requires a photon energy over 100 MeV. Helium becomes more abundant than iron when the temperature rises over $7 \times 10^9\,\mathrm{K}$. Helium can be disintegrated into neutrons and protons at even higher temperatures. In general, the heavy nuclei are created at temperatures within $\sim 10^6 - 5 \times 10^9\,\mathrm{K}$ through nuclear fusion and destroyed by energetic photons when the temperature is over $5 \times 10^9\,\mathrm{K}$. Figure 1.3 summarizes the phase diagram of the stellar interior and burning and presents the schematic evolution tracks of stars of different masses. In the left panel, we show the density and the temperature phase diagram. When the relative lower density is subjected to high temperature, the equation for the state of gas can be described as ideal gas or radiation. For lower temperatures with a relatively higher density, quantum effects need to be considered for describing the equation of state. The gas can be degenerate or relativistic degenerate. In the middle panel, we show the different burning phases that occurs in the phase diagram. The black lines or strips show the approximate temperatures and densities when the burning occurs. We plot the evolution tracks of central densities and temperatures of stars with different masses in the right panel. The $0.15\,\mathrm{M}_\odot$ star may never reach the helium-burning stage before its core becomes degenerate, and eventually it dies as a brown dwarf. The $1.5\,\mathrm{M}_\odot$ star, which is similar to our Sun, dies as a white dwarf after it finishes the central helium burning. Once the star becomes more massive than $10\,\mathrm{M}_\odot$, such as the $15\,\mathrm{M}_\odot$ star, it can go through all the burning stages we have mentioned, and it dies as a core−collapse supernovae. If the Pop III stars were more massive than $80\,\mathrm{M}_\odot$, they would encounter the pair-instabilities, which trigger a collapse of the stars, and they die as pair-instability supernovae (Heger and Woosley, 2002).

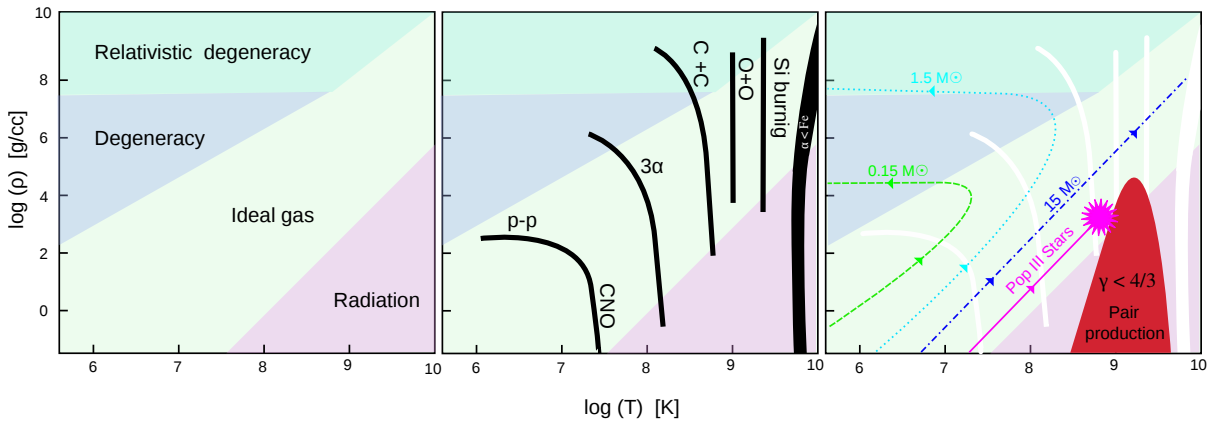

Figure 1.3: Temperature-Density phase diagram based on Prialnik (2000): The x-axis and y-axis indicate the temperature and density, respectively. Colored patches show the equation of state for matter (e.g., the radiation-dominated region (pink color) appears at a higher temperature with a lower density). In the middle panel, the black strips indicate the threshold for ignition of different burning phases in the phase diagram. In the right panel, the stellar evolution of stellar cores is shown in dashed lines. The red region shows the pair-instability region where the adiabatic index γ is below $\frac{4}{3}$.

1.3.2 Dynamical stability of stars

We have mentioned several different fates of stars in the previous section. One common occurrence is that before the stars die, they encounter an instability that goes violent, the stars cannot restore it, and this leads to the catastrophic collapse of stars. It is relevant to provide an example of dynamical instability. The hydro−equilibrium means that the motion of fluid is too slow to be observed. To verify whether the state is a true equilibrium or not, we need to apply a perturbation to the equilibrium and evaluate the resulting response. The force balance inside a star is between the gravitational force and pressure gradient. In a simplified model, we consider a gas sphere of mass M, which is in a hydrodynamic equilibrium,

$$\frac{dP}{dr} = -\rho\frac{Gm}{r^2}, \tag{1.7}$$

is equal to

$$\frac{dP}{dm} = -\frac{Gm}{4\pi\, r^4}, \tag{1.8}$$

in mass coordinate and its integration yields

$$P = -\int_m^M \frac{Gm}{4\pi\, r^4} dm. \tag{1.9}$$

Similar to (Prialnik, 2000), we now perturb the system by compressing it by:

$$\delta r = \alpha\, r, \tag{1.10}$$

$\alpha \ll 1$. Now the new density, $\tilde{\rho}$ and radius, $\tilde{r}$ become

$$\tilde{r} = r - \alpha\, r = r(1 - \alpha),$$
$$\tilde{\rho} = \frac{dm}{4\pi\, \tilde{r}^2 d\tilde{r}} \approx \rho(1 + 3\alpha).$$

New pressure from hydrodynamics can be calculated by using the equation

$$\tilde{P}_h = \int_m^M \frac{Gm}{4\pi\, \tilde{r}^4} dm = \int_m^M \frac{Gm}{4\pi\,(1-\alpha\,)^4 r^4} dm = (1 + 4\alpha)P. \tag{1.11}$$

Assuming the contraction is adiabatic, the gas pressure can be expressed as

$$\tilde{P}_{\rm gas} = K_{\rm a}\tilde{\rho}^{\,\gamma_{\rm a}} = K_{\rm a}[\rho(1 + 3\alpha)]^{\gamma_{\rm a}} = (1 + 3\gamma_{\rm a}\alpha)P, \tag{1.12}$$

where $K_{\rm a}$ is a constant. The contraction of the gas sphere can be restored when

$$\tilde{P}_{\rm gas} > \tilde{P}_h \quad \longrightarrow \quad (1 + 3\gamma_{\rm a}\alpha)P > (1 + 4\alpha)P. \tag{1.13}$$

Therefore, the condition for dynamical stability is

$$\gamma_{\rm a} > 4/3, \tag{1.14}$$

which can be further extended to a global stability (Prialnik, 2000),

$$\int (\gamma_{\rm a} - 4/3)\frac{P}{\rho}\, dm > 4/3, \tag{1.15}$$

which implies that the star can be stable if $\gamma_{\rm a} > 4/3$ occurs in the region where P/ρ is dominated, e.g., the core of the star; even the outer envelope may have $\gamma_{\rm a} < 4/3$.

1.4 Fate of Massive Pop III Stars

The fate of a massive star is determined by its initial mass, composition, and history of mass loss. The latter is still poorly understood, as is the direct affect of the final mass. The explosion mechanism and remnant properties are thought to be determined by the mass of the helium core when the star dies. Kudritzki (2002) suggests that the mass loss rate of a star follows $\dot{m} \propto Z^{0.5}$, where Z is the metallicity of the star relative to the solar metallicity, $Z_{\odot}$. Since the Pop III stars have zero metallicity, it would favor the notion that Pop III stars retain most of their masses before they die. The Pop III stars with initial masses of $10 - 80\,\mathrm{M}_{\odot}$ eventually forge an iron core with masses similar to those of our Sun (Kippenhahn and Weigert, 1990). Once the mass of the iron core is larger than its Chandrasekhar mass (Chandrasekhar, 1942), the degenerate pressure of electrons is not able to support its own gravity; finally the star dies as a core collapse supernovae (CCSNe) or it collapses directly into a black hole (BH). The fate of these stars is complicated by several hurdles, such as neutrino physics, multi-scale, and multi-dimension (Janka and Mueller, 1996). If Pop III stars are more massive than $80\,\mathrm{M}_{\odot}$, after the central carbon burning, their cores encounter the electron-positron pair production instabilities, where large amounts of pressure-supporting photons are turned into e^{-}/e^{+} pairs, leading to dynamical instability of the core. The central temperatures start to oscillate. If the stars are more massive than $100\,\mathrm{M}_{\odot}$, the oscillation of temperatures becomes very violent. Several strong shocks may be sent out from the core before the stars die as CCSNe (Woosley et al., 2007). Those shocks are inadequate to blow up the entire star, but they are strong enough to eject several solar masses from the stellar envelope, as is illustrated in Figure 1.4. The catastrophic collisions of ejecta may power extremely luminous optical transients, the so-called pulsational pair-instability supernovae (PPSNe). We will discuss the PPSNe in Chapter 3.

Once the stars are over $150\,\mathrm{M}_{\odot}$ but less than $260\,\mathrm{M}_{\odot}$, instabilities are so violent they trigger a runaway collapse and eventually ignite the explosive oxygen and silicon burning, resulting in an energetic explosion and completely disrupting the star, as shown in Figure 1.5. This thermonuclear explosion is called a pair-instability supernova (PSN; Barkat et al. 1967; Glatzel et al. 1985; Heger and Woosley 2002, 2010; Kasen et al.

2011; Chen et al. 2011). PSN can produce an explosion energy up to 10^{53} erg, about 100 times more than the Type Ia SNe. Because of explosive silicon burning, a large amount of radioactive ^{56}Ni is synthesized. Such an energetic explosion makes them very bright, and they can be visible at large distances, so they may function as good tools for probing the early Universe. For the yields of PSNe, isotopes heavier than the iron group are completely absent because of a lack of neutron capture processes (r- and s-process). Comprehensive simulations of PSNe will be discussed in Chapter 4, Chapter 5, and Chapter 6.

What happens to even more massive stars? Previous models suggest that non-rotating stars with initial masses over $260\,M_\odot$ eventually die as BH without SN explosions. It is generally believed that the explosive burning is insufficient to revert the implosion because the SN shock is dissipated by the photo-disintegration of the heavy nuclei; thus these stars eventually die as BHs without SN explosions. However, we report an unusual explosion of a super massive star with a mass about $55,000\,M_\odot$ in Chapter 7. This unexpected explosion may have caused the post-Newtonian correction in the gravity. We finally summarize the fate of massive Pop III stars in Table 1.2 based on Woosley et al. (2002); Heger and Woosley (2010).

The Death of Massive Stars						
$M_*[M_\odot]$			He core $[M_\odot]$			Supernova Mechanism
10	$\leftrightarrow$	85	2	$\leftrightarrow$	32	CCSNe
80	$\leftrightarrow$	150	35	$\leftrightarrow$	60	PPSNe
150	$\leftrightarrow$	260	60	$\leftrightarrow$	133	PSNe
	$\geq$	260		$\geq$	133	BHs (?)

Table 1.2: Fate of massive stars

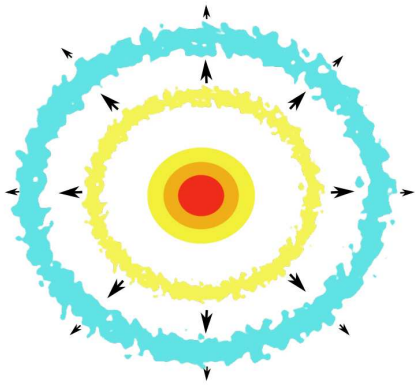

Figure 1.4: Illustration of PPSNe. The energy released from central burning is not sufficient to disperse the star but can easily eject masses from its envelope. A few outbursts of mass can occur before the star dies as a CCSN.

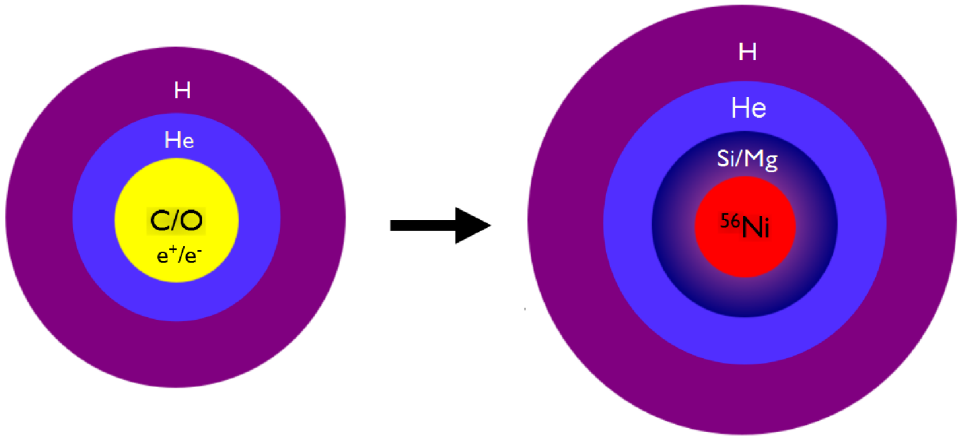

Figure 1.5: Physics of PSNe. After central helium burning, radiation energy is converted into electron and positron pairs; the core of the star becomes dynamically unstable, resulting in an implosion that ignites the oxygen and silicon explosively. The energy released from burning eventually blows up the star, and amounts of ^{56}Ni can be synthesized. (Image credit: Dan Kasen)

Chapter 2

Computational Approaches

We carry out our supernova simulations by using CASTRO (Almgren et al., 2010; Zhang et al., 2011), a massively parallel, multidimensional Eulerian, adaptive mesh refinement (AMR), hydrodynamics code for astrophysical applications. This code was originally developed at the Lawrence Berkeley Lab, and it is designed to run effectively on supercomputers of 10,000+ CPUs. CASTRO provides a powerful platform for simulating hydrodynamic and gravity for astrophysical gas dynamics. However, it still requires other physics to properly model supernova explosions. For this purpose, a great effort has been made to develop the relevant physics modules. We have developed a new mapping scheme to conservatively map the 1D initial conditions onto multidimensional zones. Instead of seeding the random initial perturbations for multidimensional simulations, we have developed new approaches to seed the initial perturbation based on the turbulent flow in the convection zones of stellar interiors. For the relevant physics modules, we have developed the nuclear reaction network to model the thermonuclear burning of SN explosions. The burning network calculates the energy generation rates and yields, which are coupled with the hydrodynamics of CASTRO self-consistently. A post-Newtonian correction for the super massive star is also included in CASTRO. In this chapter, we introduce basic features of CASTRO and discuss the new modules we have developed for our supernova simulations.

The structure of this chapter is as follows: we first describe features of CASTRO in § 2.1, then introduce the nuclear reaction network in § 2.2. The algorithms for the conservative mapping and seeding of initial perturbations are presented in § 2.3 and

§ 2.4, respectively. We discuss post-Newtonian gravity in § 2.5 and an approach for resolving the large dynamic scale of our simulations in § 2.6. At the end, we present the scaling performance of CASTRO in § 2.7 and introduce VISIT, the tool for visualization CASTRO output, in § 2.8.

2.1 CASTRO

CASTRO is a hydro code for solving compressible hydrodynamic equations of multicomponent including self-gravity and a general equation of state (EOS). The Eulerian grid of CASTRO uses adaptive mesh refinement (AMR), which constructs rectangular refinement grids hierarchically. Different coordinate systems are available in CASTRO, including spherical (1D), cylindrical (2D), and cartesian (3D). The flexible modules of CASTRO make it easy for users to implement new physics associated with their simulations.

In CASTRO, the hydrodynamics are evolved by solving the conservation equations of mass, momentum, and energy (Almgren et al., 2010) :

$$\frac{\partial \rho}{\partial t} = -\nabla \cdot (\rho \mathbf{u}), \tag{2.1}$$

$$\frac{\partial (\rho \mathbf{u})}{\partial t} = -\nabla \cdot (\rho \mathbf{u}\mathbf{u}) - \nabla p + \rho \mathbf{g}, \tag{2.2}$$

$$\frac{\partial (\rho E)}{\partial t} = -\nabla \cdot (\rho \mathbf{u} E + p\mathbf{u}) + \rho \dot{\epsilon}_{\rm nuc} + \rho \mathbf{u} \cdot \mathbf{g}., \tag{2.3}$$

where ρ, $\mathbf{u}$, e, and E are the mass density, velocity vector, internal energy per unit mass, and total energy per unit mass $E = e + \mathbf{u} \cdot \mathbf{u}/2$, respectively. The pressure, p, is calculated from the equation of state (EOS), $\mathbf{g}$ is the gravity, and $\dot{\epsilon}_{\rm nuc}$ is the energy generation rate per unit volume. CASTRO also evolves the reacting flow by considering the advection equations of the mass abundances of isotopes, X_i :

$$\frac{\partial (\rho X_i)}{\partial t} = -\nabla \cdot (\rho \mathbf{u} X_i) + \rho \dot{\omega}_i, \tag{2.4}$$

where $\dot{\omega}_i$ is the production rate for the i-th isotope having the form:

$$\dot{\omega}_i(\rho, X_i, T) = \frac{dX_i}{dt}, \tag{2.5}$$

is given from the nuclear reaction network that we shall describe later. Since masses are conservative quantities, the mass fractions are subject to the constraint that $\sum_i X_i = 1$.

CASTRO can support any general reaction network that takes as inputs the density, temperature, and mass fractions of isotopes, and it returns updated mass fractions and the energy generation rates. The input temperature is computed from the EOS before each call to the reaction network. At the end of the burning step, the results of burning provide the rates of energy generation/loss and abundance change to update Equation (2.3) and Equation (2.4). CASTRO also provides passively advected quantities; A_j, e.g., angular momentum, which will be used for our rotation models,

$$\frac{\partial(\rho A_j)}{\partial t} = -\nabla \cdot (\rho \mathbf{u} A_j). \tag{2.6}$$

In CASTRO, we use a sophisticated EOS (Timmes and Swesty, 2000) for stellar matter: the Helmholtz EOS, which considers the (non)degenerate and (non)relativistic electrons, electron-positron pair production, as well as ideal gas with radiation. The Helmholtz EOS is a tabular EOS that reads in ρ, T, and X_i of gas and yields its derived thermodynamics quantities. CASTRO offers different types of calculation for gravity, including Constant, Poisson, and Monopole. At the early stage of a supernova explosion, spherical symmetry is still a good approximation for the mass distribution of gas. Such an approximation creates a great advantage in calculating the gravity by saving a lot of computational time, so the monopole-type gravity is used in the simulations. For 2D or 3D CASTRO simulations, we first calculate a 1D radial average profile of density. We then compute the 1D profile of $\mathbf{g}$ and use it to calculate the gravity of the multidimensional grid cells.

The AMR in CASTRO refines the simulation domain in both space and time. Finer grids automatically replace coarse grids during the grid-refining process until the solution satisfies the AMR criteria, which are specified by users. These criteria can be the gradients of densities, velocities, or other physical quantities in the adjacent grids. The grid generation procedures automatically create or remove finer rectangular zones based on the refinement criteria. The AMR technique of CASTRO allows us to address our supernova simulation, which deals with a large dynamic scale. Simulating the mixing of supernova ejecta requires catching the features of fluid instabilities early on. These instabilities occur at much smaller scales compared with the overall simulation box. The uniform grid approach requires numerous zones and becomes very computationally expensive. Instead, AMR focuses on resolving the scale of interests and makes

our simulations run more efficiently. In Figure 2.1(a), we show the layout of two levels of a factor of two refinement. The refined grids are constructed hierarchically in the form of rectangles. The choice of refinement criteria allows us to resolve the structure we are most interested in. The most violent burning and physical process occurs at the center of the star, so we hierarchically apply finer zones at the center, as shown in Figure 2.1(b). These pre-refined zones are fixed and do not change with AMR criteria.

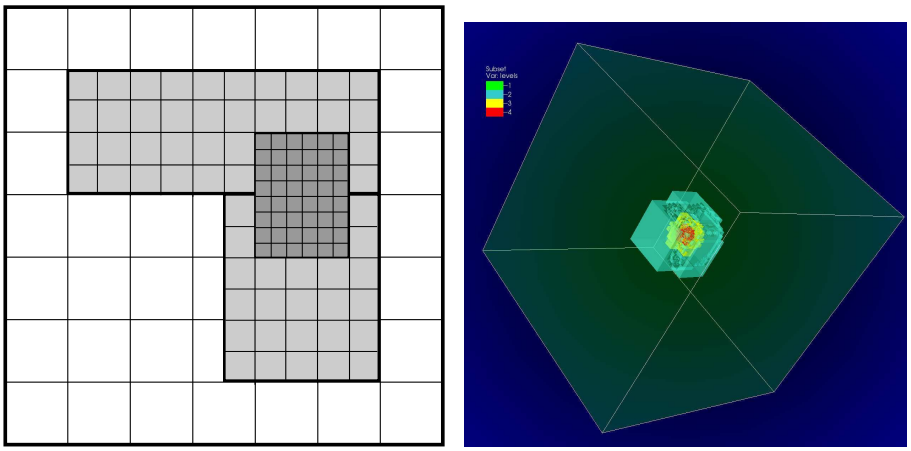

(a) AMR cartoon (b) 3D AMR

Figure 2.1: (a) Schematic diagram of AMR. When the AMR criteria are met, new finer grids are automatically generated to replace previous coarse grids. The two levels of refinement are shown in light-gray and dark-gray. (b) Nested AMR zones. The hierarchical grids are constructed from centers. Colors represent three different levels of refinement.

Figure 2.2 shows the power of AMR in the simulations. This is a snapshot taken from our 2D supernova simulation at the time when the fluid instabilities emerge. These fluid instabilities are caused by Rayleigh–Taylor (RT) instability and are the main drivers of the mixing of SN ejecta. The finest grids of AMR can resolve the detailed structure of fluid instabilities at minimal computational expense. In our simulations, AMR criteria are based on density gradient, velocity gradient, and pressure gradient.

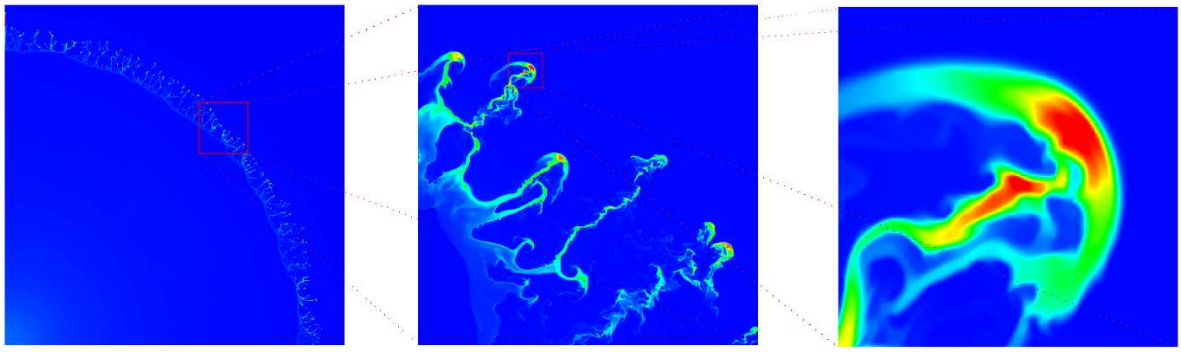

Figure 2.2: The power of AMR in our problem. Here is a snapshot of the density map from our 2D simulations at the time the reverse shock starts to accelerate the growth of the fluid instabilities. The images from left to right show close-ups of the instabilities. Here we show 3 levels of factor 4 refinement. It takes a factor of 64 times higher resolution to resolve to those instability structures.

2.2 Nuclear Reaction Networks

Modeling thermonuclear supernovae requires calculating the energy generation rate from nuclear burning, which occurs over a large range of temperatures, densities, and compositions. We have implemented the APPROX 7, 13, 19− isotope reaction networks (Weaver et al., 1978; Timmes, 1999) into `CASTRO`. Here, we introduce the 19 isotopes reaction network, which is the most comprehensive network afforded for multidimensional simulations. This network includes 19 isotopes: ^{1}H , ^{3}He, ^{4}He, ^{12}C, ^{14}N, ^{16}O, ^{20}Ne, ^{24}Mg, ^{28}Si, ^{32}S, ^{36}Ar, ^{40}Ca, ^{44}Ti, ^{48}Cr, ^{52}Fe, ^{54}Fe, ^{56}Ni, protons (from photo-disintegration), and neutrons. The 19−isotope network considers nuclear burning of alpha-chain reactions, heavy-ion reactions, hot CNO cycles, photo-disintegration of heavy elements, and neutrino energy loss, as shown in Figure 2.3. It is capable of efficiently calculating accurate energy generation rates for nuclear processes ranging from hydrogen to silicon burning.

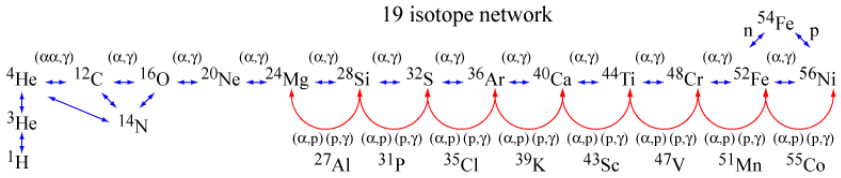

Figure 2.3: The cartoon shows the CNO cycles, α chain, and photo-disintegration of the 19−isotope network in `CASTRO` (Credit: Cococubed website of Frank Timmes).

The nuclear reaction networks are solved by means of integrating a system of ordinary differential equations. Because the reaction rates for most of the burning are extremely sensitive to temperatures to $\propto T^{15-40}$, it results in stiffness of the system of equations, which are usually solved by an implicit time integration scheme. We first consider the gas containing m isotopes with a density ρ and temperature T. The molar abundance of the i-th isotope is

$$Y_i = \frac{X_i}{A_i} = \frac{\rho_i}{\rho A_i} = \frac{n_i}{\rho N_A}, \tag{2.7}$$

where A_i is mass number, X_i is mass fraction, ρ_i is mass density, and N_A is the Avogadro's number. In Lagrangian coordinates, the continuity equation of the isotope has the form (Timmes, 1999)

$$\frac{dY_i}{dt} + \nabla \cdot (Y_i \mathbf{V}_i) = \dot{R}_i, \tag{2.8}$$

where

$$\dot{R}_i = \sum_{j,k} Y_l Y_k \lambda_{kj}(l) - Y_i Y_j \lambda_{jk}(i), \tag{2.9}$$

where $\dot{R}_i$ is the total reaction rate due to all binary reactions of the form $i(j,k)l$. λ_{jk} and λ_{kj} are the forward and reverse nuclear reaction rates, which usually have a strong temperature dependence. $\mathbf{V}_i$ are mass diffusion velocities due to pressure, temperature, and abundance gradients. The value of $\mathbf{V}_i$ is often small compared with other transport processes, so we can assume $\mathbf{V}_i = 0$, which allows us to decouple the reaction network from the hydrodynamics by using operator splitting. Equation (2.8) now becomes

$$\frac{dY_i}{dt} = \dot{R}_i. \tag{2.10}$$

This set of ordinary differential equations may be written in the more compact and standard form (Timmes, 1999)

$$\frac{d\mathbf{y}}{dt} = \mathbf{f}(\mathbf{y}); \tag{2.11}$$

its implicit differentiation gives

$$\mathbf{y}_{n+1} = \mathbf{y}_n + h\mathbf{f}(\mathbf{y}_{n+1}), \tag{2.12}$$

where h is a small time step. We linearize Equation (2.12) by using Newton's method,

$$\mathbf{y}_{n+1} = \mathbf{y}_n + h\left[\mathbf{f}(\mathbf{y}_n) + \left.\frac{\partial \mathbf{f}}{\partial \mathbf{y}}\right|_{\mathbf{y_n}} \cdot (\mathbf{y}_{n+1} - \mathbf{y}_n)\right]. \tag{2.13}$$

The rearranged Equation (2.13) yields

$$\mathbf{y}_{n+1} = \mathbf{y}_n + h\left[\mathbf{1} - h\frac{\partial \mathbf{f}}{\partial \mathbf{y}}\right]^{-1} \cdot \mathbf{f}(\mathbf{y}_n). \tag{2.14}$$

By defining $\Delta = \mathbf{y}_{n+1} - \mathbf{y}_n$, $\tilde{\mathbf{A}} = \frac{\mathbf{1}}{h} - \frac{\partial \mathbf{f}}{\partial \mathbf{y}}$, $\mathbf{b} = \mathbf{f}(\mathbf{y}_n)$, Equation (2.14) now is equivalent to a simple matrix equation

$$\tilde{\mathbf{A}} \cdot \Delta = \mathbf{b}. \tag{2.15}$$

If h is small enough, only one iteration of Newton's method may be accurate enough to solve Equation (2.11) using Equation (2.14). However, this method provides no estimate of how accurate the integration step is. We also do not know whether the time step is accurate enough. The Jacobian matrices $\tilde{\mathbf{J}} = \frac{\partial \mathbf{f}}{\partial \mathbf{y}}$ from nuclear reaction networks are neither positive-definite nor symmetric, and the magnitudes of the matrix elements are functions $X(t)$, $T(t)$, and $\rho(t)$. More importantly, the nuclear reaction rates are extremely sensitive to temperature, and X of different isotopes can differ by many orders of magnitude. The coefficients in Equation (2.10) can vary significantly and cause nuclear reaction network equations to become **stiff**.

The integration method for our network is based on a variable-order Bader–Deuflhard method (Press et al., 2007). Bader and Deuflhard (1983) found a semi-implicit discretization for stiff equation problems and obtained an implicit form of the midpoint rule,

$$\mathbf{y}_{n+1} - \mathbf{y}_{n-1} = 2h\mathbf{f}(\frac{\mathbf{y}_{n+1} + \mathbf{y}_{n-1}}{2}). \tag{2.16}$$

We linearize the right-hand side about $\mathbf{f}(\mathbf{y}_n)$ and obtain the semi-implicit midpoint rule

$$\left[\mathbf{1} - h\frac{\partial \mathbf{f}}{\partial \mathbf{y}}\right] \cdot \mathbf{y}_{n+1} = \left[\mathbf{1} + h\frac{\partial \mathbf{f}}{\partial \mathbf{y}}\right] \cdot \mathbf{y}_{n-1} + 2h\left[\mathbf{f}(\mathbf{y}_n) - \frac{\partial \mathbf{f}}{\partial \mathbf{y}} \cdot \mathbf{y_n}\right]. \tag{2.17}$$

Now the reaction network expressed in Equation (2.11) is advanced over a large time step, $H = mh$ for $\mathbf{y}_n$ to $\mathbf{y}_{n+1}$, where m is an integer. It is convenient to rewrite equations in terms of $\Delta_k \equiv \mathbf{y}_{k+1} - \mathbf{y}_k$. We use it with the first step from Equation (2.14) and start by calculating (Press et al., 2007)

$$\begin{aligned} \mathbf{y}_1 &= \mathbf{y}_0 + \Delta_0, \\ \Delta_0 &= \left[\mathbf{1} - h\frac{\partial \mathbf{f}}{\partial \mathbf{y}}\right]^{-1} \cdot h\mathbf{f}(\mathbf{y}_0). \end{aligned} \tag{2.18}$$

Then for $k = 1, ..., m-1$, set

$$\begin{aligned} \mathbf{y}_{k+1} &= \mathbf{y}_k + \Delta_k, \\ \Delta_k &= \Delta_{k-1} + 2\left[\mathbf{1} - h\frac{\partial \mathbf{f}}{\partial \mathbf{y}}\right]^{-1} \cdot [h\mathbf{f}(\mathbf{y}_k) - \Delta_{k-1}]. \end{aligned} \tag{2.19}$$

Finally, we calculate

$$\begin{aligned} \mathbf{y}_{n+1} &= \mathbf{y}_m + \Delta_m, \\ \Delta_m &= \left[\mathbf{1} - h\frac{\partial \mathbf{f}}{\partial \mathbf{y}}\right]^{-1} \cdot [h\mathbf{f}(\mathbf{y}_m) - \Delta_{m-1}]. \end{aligned} \tag{2.20}$$

This sequence (Timmes, 1999) may be executed a maximum of 7 times, which yields a 15th-order method. The exact number of times the staged sequence is executed depends on the accuracy requirements. The accuracy of an integration step is calculated by comparing the solutions derived from different orders. The linear algebra package `GIFT` (Müller, 1998) and the sparse storage package `MA28` (Duff et al., 1986) are used to execute the semi-implicit time integration methods described above. After solving the network equations, the average nuclear energy generated rate is calculated,

$$\dot{\epsilon}_{\rm nuc} = \sum_i \frac{\Delta Y_i}{\Delta t} B_i N_A - \dot{\epsilon}_\nu, \tag{2.21}$$

where B_i is the nuclear binding energy of the i-th isotope, and $\dot{\epsilon}_\nu$ is the energy loss rate due to neutrinos from Itoh et al. (1996).

In order to verify the burning network we just described, we compare the burning results from 1D CASTRO with the ones from KEPLER. We feed CASTRO and KEPLER with the identical initial conditions of a PSN progenitor and evolve both models until the explosive burning is finished. Figure 2.4 shows the results of verification tests. The results from CASTRO and KEPLER match very well. We also calculate the total energy produced from the two models. The deviation is less than one percent. It demonstrates that our network produces results consistent with the existing well-tested code.

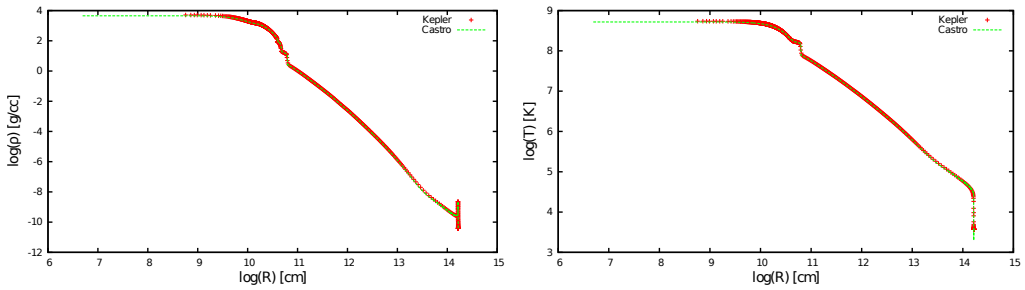

(a) Density (b) Temperature

Figure 2.4: Panels from left to right are profiles of density and temperature, respectively. The red crosses are from CASTRO, and the green line is from KEPLER.

2.3 Conservative Mapping

Multidimensional simulations shed light on modeling the mixing inside SNe (Herant and Woosley, 1994; Joggerst and Whalen, 2011). However, computing fully self-consistent 3D stellar evolution models, from their formation to collapse for the explosion setup is unavailable in terms of current supercomputer capability. One alternative approach is to first evolve the main sequence star in 1D stellar evolution codes such as KEPLER (Weaver et al., 1978) or MESA (Paxton et al., 2011). Once the star reaches the pre-supernova phase, its 1D profiles can then be mapped into multidimensional hydro codes such as CASTRO or FLASH (Fryxell et al., 2000) and continue to be evolved until the star explodes, as shown in Figure 2.5.

Differences between codes in dimensionality and coordinate mesh can lead to numerical issues such as violation of conservation of mass and energy when data are mapped from one code to another. A first, simple approach could be to initialize multidimensional grids by linear interpolation from corresponding mesh points on the 1D profiles. However, linear interpolation becomes invalid when the new grid fails to resolve critical features in the original profile, such as the inner core of a star. This is especially true when porting profiles from 1D Lagrangian codes, which can easily resolve very small spatial features in mass coordinate, to a fixed or adaptive Eulerian grid. In addition to conservation laws, some physical processes, such as nuclear burning, are very sensitive to temperature, so errors in mapping can lead to very different outcomes for the simulations, including altering the nucleosynthesis and energetics of SNe. Few studies have examined mapping 1D profiles to 2D or 3D meshes (Zingale et al., 2002), and none address the conservation of physical quantities by such procedures. We examine these issues and introduce a new scheme for mapping 1D data sets to multidimensional grids.

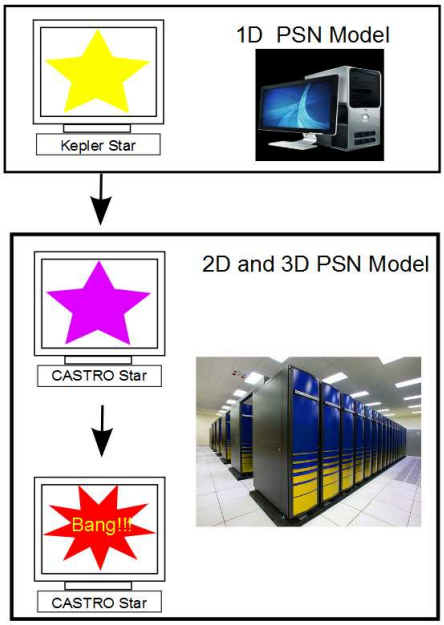

Figure 2.5: Illustration shows the procedure of simulations. The 1D stellar models are created by `KEPLER` using PCs. Then resulting 1D supernova-progenitor models are mapped onto multidimensional grids of `CASTRO` and follow the simulations using supercomputers such as Franklin until the stars blow up.

Since the star is very nearly in hydrostatic equilibrium and we want to conserve total energy, we must take care when mapping its profile from the uniform Lagrangian grid in mass coordinate to the new Eulerian spatial grid. Our method preserves the conservation of quantities such as mass and energy on the new mesh, assuring that they are analytically conserved in the evolution equations. Although this reconstruction does not guarantee that the star will be hydrostatic, it is a physically motivated constraint and sufficient for our simulations. The algorithm we describe is specific to our models but can be easily generalized to mappings of other 1D data to higher-dimensional grids.

2.3.1 Method

First, we construct a continuous (C^0) function that conserves the physical quantity upon mapping onto the new grid. An ideal choice for interpolation is the volume coordinate

V, the volume enclosed by a given radius from the center of the star. Then, integrating a density ρ_X (which can represent mass or internal energy density) with respect to the volume coordinate yields a conserved quantity X:

$$X = \int_{V_1}^{V_2} \rho_X \, \mathrm{d}V, \tag{2.22}$$

such as the total mass or total internal energy lying in the shell between V_1 and V_2. Next, we define a piecewise linear function in volume V that represents the conserved quantity ρ_X, preserves its monotonicity (no new artificial extrema), and is bounded by the extrema of the original data. The segments are constructed in two stages. First, we extend a line across the interface between adjacent zones that either ends or begins at the center of the smaller of the two zones, as shown in Figure 2.6 (note that uniform zones in mass coordinate do not result in uniform zones in V). The slope of the segment is chosen such that the area trimmed from one zone by the segment (a and b) is equal to the area added under the segment in the neighboring bin (a$'$=a and b$'$=b). If the two segments bounding a and a$'$, and b and b$'$ are joined together by a third in the center zone in Figure 2.6, two "kinks," or changes in slope, can arise in the interpolated quantity there; plus, the slope of the flat central segment is usually a poor approximation of the average gradient in that interval. We therefore construct two new segments that span the entire central zone and connect with the two original segments where they cross its interfaces, as shown in Figure 2.6. The new segments join each other at the position in the central bin where the areas c and c$'$ enclosed by the two segments are equal (note that they generally have different slopes). After repeating this procedure everywhere on the grid, each bin will be spanned by two linear segments that represent the interpolated quantity ρ_X at any V within the bin and have no more than one kink in ρ_X across the zone. Our scheme introduces some smearing (or smoothing) of the data, but it is limited at most to the width of one zone on the original grid. The result of our interpolation scheme is a piecewise linear reconstruction in V of the original profile in mass coordinate for which the quantity ρ_X can be determined at any V, not just the radii associated with the zone boundaries in the Lagrangian grid. We show this profile as a function of the radius associated with the volume coordinate V for a zero-metallicity 200 $\mathrm{M}_\odot$ star with $r \sim 2 \times 10^{13}$ cm from `KEPLER` (Heger and Woosley, 2002, 2010).

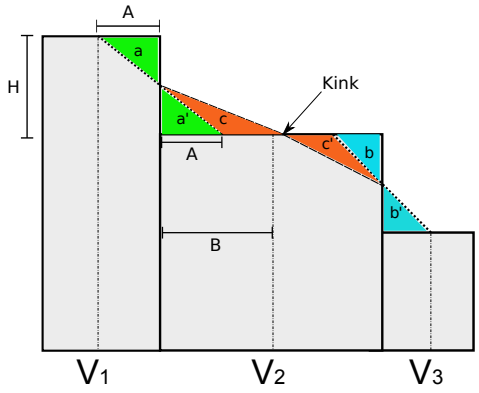

Figure 2.6: Constructing a piecewise-linear conservative profile: The rectangular bins represent the original 1D profile. The areas of different colors represent conserved quantities such as mass and internal energy. The conservative profile connects adjacent bins and makes a =a′ = $\frac{1}{4}H\times$ min(A,B), c = c′, and b = b′. Note that uniform zones in mass (Lagrangian coordinate) lead to non-uniform bins in the volume coordinate, as shown above.

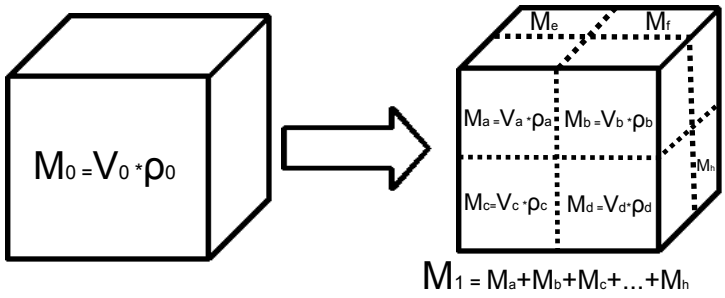

Figure 2.7: Volume subsampling: We first use the center of the volume element (V_0) to obtain its density (ρ_0) from the conservative profile and then calculate its mass (M_0 = $V_0 \times \rho_0$). We then partition the original volume element as shown and calculate the mass of each subvolume in the same manner as M_0. We obtain M_1 by summing over eight subvolumes M_a,M_b,M_c,...,M_h. We then compare M_1 and M_0; if their relative error is greater than some predetermined tolerance, the process is recursively repeated until $|(M_i\text{-}M_{i-1})/M_i|$ is less than 10^{-4}.

We populate the new multidimensional grid with conserved quantities from the reconstructed stellar profiles as follows. First, the distance of the selected mesh point from the center of the new grid is calculated. We then use this radius to obtain its V to reference the corresponding density in the piecewise linear profile of the star. The density assigned to the zone is then determined from adaptive iterative subsampling. This is done by first computing the total mass of the zone by multiplying its volume by the interpolated density. We then divide the zone into equal subvolumes whose sides are half the length of the original zone. New V are computed for the radii to the center of each of these subvolumes, and their densities are again read in from the reconstructed profile. The mass of each subvolume is then calculated by multiplying its interpolated density by its volume element (see Figure 2.7). These masses are then summed and compared to the mass previously calculated for the entire cell. If the relative error between the two masses is larger than the desired tolerance, each subvolume is again divided as before; masses are computed for all the constituents comprising the original zone, and they are then summed and compared to the zone mass from the previous iteration. This process continues recursively until the relative error in mass between the two most recent consecutive iterations falls within an acceptable value, typically 10^{-4}. The density we assign to the zone is just this converged mass divided by the volume of the entire cell. This method is used to map internal energy density and the partial densities of the chemical species to every zone on the new grid. The total density is then obtained from the sum of the partial densities; pressure and temperature in turn are determined from the equation of state. This method is easily applied to the hierarchy geometry of the target grid.

2.3.2 Results

We port a 1D stellar model from `KEPLER` into `CASTRO` to verify that our mapping is conservative. As an example, we use a 200 $M_\odot$ zero-metalicity pre-supernova star. As we show in Figure 2.10, our piecewise linear fits to the `KEPLER` data to reproduce the original stellar profile. Because our model fits smoothly, we interpolate the block histogram structure of the `KEPLER` bins (especially at larger radii); they reduce the number of unphysical sound waves that would have been introduced in `CASTRO` by the discontinuous

interfaces between these bins in the original data.[1] The density profile is key to the hydrodynamic and gravitational evolution of the explosion, and the temperature profile is crucial to the nuclear burning that powers the explosion. We first map the profile onto a 1D grid in CASTRO and plot the mass of the star as a function of grid resolution in Figure 2.8. The mass is independent of resolution for our conservative mapping because we subsample the quantity in each cell prior to initializing it, as described above. In contrast, the total mass from linear interpolation is very sensitive to the number of grid points but does eventually converge when the number of zones is sufficient to resolve the core of the star, in which most of its mass resides.

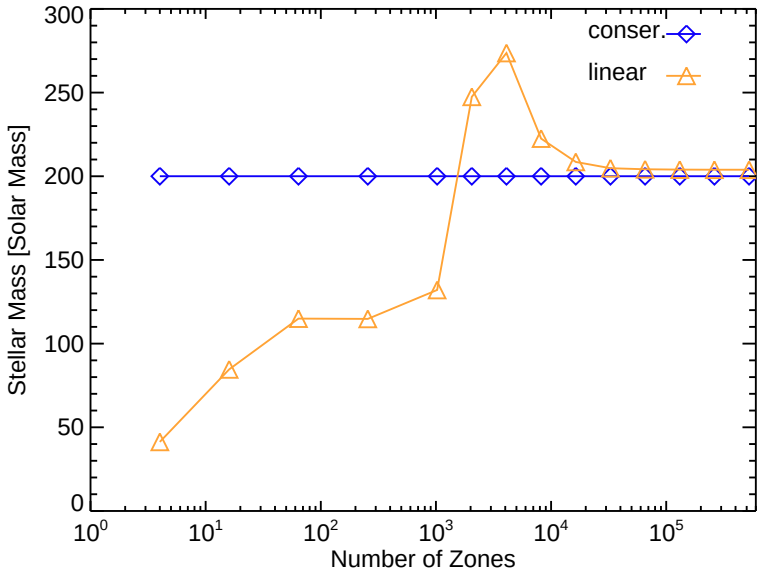

Figure 2.8: Total mass of the star on the 1D CASTRO grid as a function of number of zones: Conservative mapping (blue) preserves the mass of the star at all resolutions, while linear interpolation (orange) converges to 200 $M_\odot$ at a resolution of $\sim$ a few $\times 10^4$, when the grid begins to resolve the core of the star ($\sim 10^9$ cm). Even at very high resolutions, the results of linear interpolation are still off by a few percent from the targeted mass and start to be saturated at $\sim 10^5$ zones because the linear interpolation profile is not a conservative one.

[1] 1D data usually provides zone-averaged values; hence, a continuous and conservative profile needs to be reconstructed from zone-averaged values.

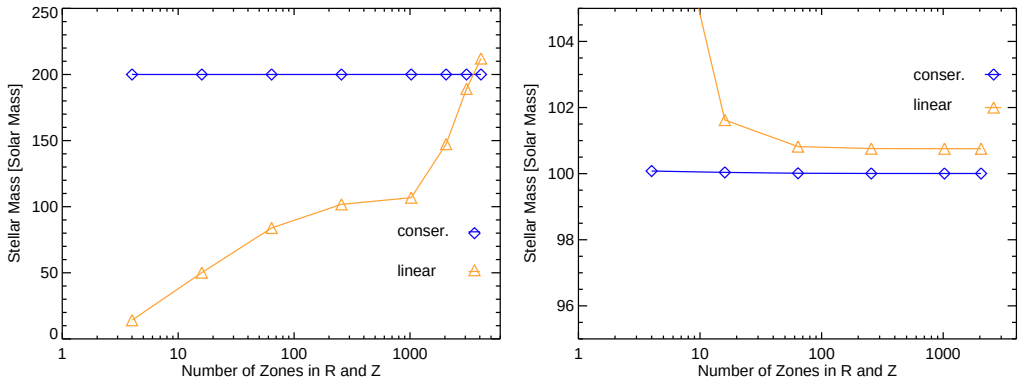

(a) 2D Mapped Mass of Entire Star (b) 2D Mapped Mass of Helium Core

Figure 2.9: (a) Total mass of the star on the new 2D `CASTRO` grid as a function of number of zones in both r and z direction: Conservative mapping (blue) recovers the mass of the star at all resolutions and linear interpolation (orange) approaches 200 $M_\odot$ at a resolution of $\sim 2048^2$. (b) Total mass of the He core on the 2D `CASTRO` grid as a function of number of zones in both r and z direction: Conservative mapping (blue) preserves its original mass at all resolutions, while linear interpolation (orange) begins to converge to 100 $M_\odot$ at a resolution of 64^2, but it is still off by $\sim 1\%$ even as the resolution approaches $\sim 2048^2$ because the linear interpolation profile is, by nature, not conservative.

We next map the `KEPLER` profile onto a 2D cylindrical grid (r, z) and a 3D cartesian grid (x, y, z) in `CASTRO`. The only difference between mapping to 1D, 2D, and 3D is the form of the volume elements used to subsample each cell, which are $4\pi r^2 \mathrm{d}r$, $2\pi r \mathrm{d}r\mathrm{d}z$, and $\mathrm{d}x\mathrm{d}y\mathrm{d}z$, respectively. We show the mass of the star as a function of resolution in Figure 2.9(a). Conservative mapping again preserves its mass at all grid resolutions. In 2D, more zones are required for linear interpolation to converge to the mass of the star. To further validate our conservative scheme, we map only the helium core of the star (~ 100 $M_\odot$ with $r \sim 10^{10}$ cm) onto the 2D grid. The helium core is crucial to modeling thermonuclear supernovae because it is where explosive burning begins. We show its mass as a function of resolution in Figure 2.9(b). We again recover all the mass of the core at all resolutions, whereas linear interpolation overestimates the mass by at least

$\sim 1\,\%$, even with large numbers of zones. Because of the property of reconstruction, conservative mapping is effective in 3D but requires much more computational time to subsample each cell to convergence. Furthermore, an impractical number of zones is needed for linear interpolation to reproduce the original mass of the star. 3D results are not presented here. We note that our method also works with AMR grids because both V and the interpolated quantities can be determined, and subsampling can be performed on every grid in the hierarchy. For the given domain, the results of conservative mapping are independent of the levels of AMR.

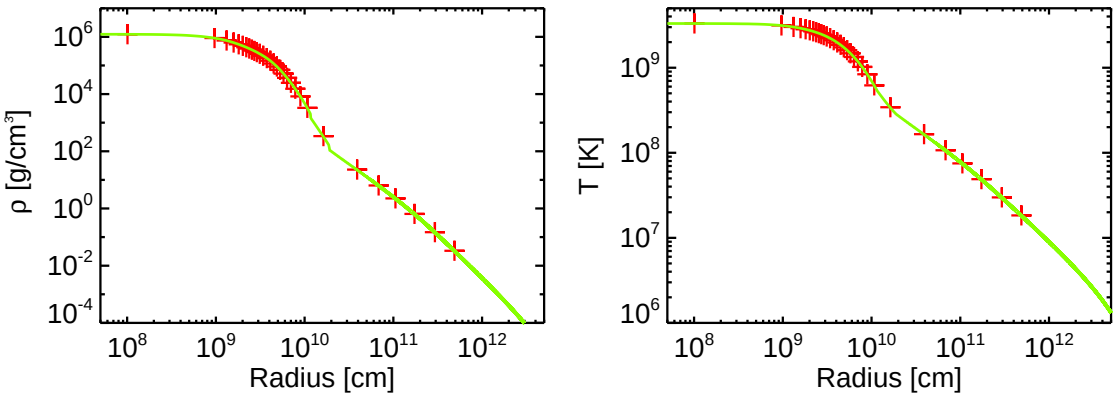

(a) Inner density profile

(b) Inner temperature profile

Figure 2.10: Inner density and temperature profiles of a 200 $M_\odot$ presupernova: Our piecewise linear profiles (green lines) fit their original `KEPLER` model (red crosses) very well. Since we map internal energy (a conserved quantity) rather than temperature, we calculate T from the equation of state using the density, elemental abundance, and internal energy.

2.4 Turbulent Perturbation

Seeding the pre-supernova profile of the star with realistic perturbations may be important to understanding how fluid instabilities later erupt and mix the star during the explosion. Massive stars usually develop convective zones prior to exploding as

SNe (Woosley et al., 2002; Heger and Woosley, 2002). Multidimensional stellar evolution models suggest that the fluid inside the convective regions can be highly turbulent (Porter and Woodward, 2000; Arnett and Meakin, 2011). However, in lieu of the 3D stellar evolution calculations necessary to produce such perturbations from first principles, multidimensional simulations are usually just seeded with random perturbations. In reality, if the star is convective and the fluid in those zones is turbulent (Davidson, 2004), a better approach is to imprint the multidimensional profiles with velocity perturbations with a Kolmogorov energy spectrum (Frisch, 1995).

Next we describe our scheme for seeding 2D and 3D stellar profiles with turbulent perturbations and present stellar evolution simulations with `CASTRO` with these profiles. In our setup, the perturbations have the following properties:

1. The perturbations are imprinted in the gas velocity, and their net momentum flux must be zero.

2. They are seeded in convectively unstable regions with a velocity spectrum $V(k) \sim k^{-5/6}$, where k is the wave number and the power index $-5/6$ is for a Kolmogorov spectrum with an assumption of constant density.

2.4.1 2D Perturbation

We first consider the mapping onto a polar coordinate grid in r and θ. To enforce zero net momentum and the boundary conditions in the simulation, we define a new variable $x = 1 + \cos\theta$ instead of using θ. The momentum flux of a density ρ and velocity v_r is then

$$\int_0^{\pi} 2\pi r^2 \rho v_r \sin\theta \, \mathrm{d}\theta = \int_0^{2} 2\pi r^2 \rho v_r \, \mathrm{d}x = 0 \tag{2.23}$$

if v_r has the form $\cos(2\pi n x)$, where n is an integer. When $\theta = 0$, π (the boundaries of a 2D grid), $x = 2$, 0 yields the maximum values for v_r that satisfy the boundary conditions in 2D cylindrical coordinates in `CASTRO`. There are two physical scales that constrain the wavelength of the perturbation in r. Based on the mixing length theory (Cox and Giuli, 1968), the eddy size of turbulence is $\alpha \times H_{\mathrm{p}}$; α is the mixing length parameter, and H_{p} is the pressure scale height. Here, we set $\alpha = 1.0$. Since the perturbation is only seeded in the convective zones, it is confined inside domain $D_c = r_{\mathrm{u}}$ - r_{b}, where r_{u} and

$r_{\rm b}$ are its upper and lower boundaries. The maximum wavelength of the perturbation must be smaller than $D_{\rm c}$ and $H_{\rm p}$. Inside a convective zone, we define a new variable, $y = \int_{r_{\rm b}}^{r} \frac{{\rm d}r}{H_{\rm p}(r)}$. We also define two oscillatory functions in x and y to generate the circular patterns that mimic the vortices of a turbulent fluid. Since the fluid inside the convective zone is turbulent, its energy spectrum is $E(k) \sim k^{-5/3}$. Assuming a constant density, the corresponding velocity spectrum is $V(k) \sim k^{-5/6}$. The perturbed velocity then has the form,

$$\begin{aligned} V_{\rm perb,r}(x,y) &= -\sum_a \sum_b V_{\rm p} \cdot \cos(2\pi a x) \cdot \cos(2\pi b y + \alpha_b), \\ V_{\rm perb,\theta}(x,y) &= \sum_a \sum_b V_{\rm p} \cdot \sin(2\pi a x) \cdot \cos(2\pi b y + \alpha_b), \\ V_{\rm p} &= V_{\rm d}(r) b^{-5/6}, \end{aligned} \tag{2.24}$$

where $V_{\rm perb,r}$ and $V_{{\rm perb},\theta}$ are the perturbed velocities in the r and θ directions, and a and b are angular and radial wavenumbers. 1D models provide only the information of convective velocities, $V_{\rm d}(r)$ along the radial direction, which can be treated as average velocities of angular directions, so we scale the amplitude of the perturbed velocity based on the radial wavenumber b. We also use a random phase, α_b, to smooth out numerical discontinuities caused by the perturbed modes while summing. Equations (2.24) by construction satisfy $V_{{\rm perb},\theta}(r,\theta) = 0$ when $\theta = 0$ and π, the boundary conditions in θ on the 2D grid. Also, we assume there is no overshooting between the upper and lower boundaries of convective zones and enforce $V_{\rm perb,r}$ to zero by setting $\alpha_b = \pi/2$ when "by" is an integer. The ultimate wavenumbers of a and b are also limited by D_c, H_p, and the resolution of simulation, $H_{\rm res}$.

2.4.2 3D Perturbation

In 3D, we use spherical coordinates, r, θ, and ϕ. Similar to 2D, we construct an oscillatory function for (θ, ϕ) by using spherical harmonics, $Y_{l,m}(\theta,\phi)$, where l and m are the wavenumbers in θ and ϕ. If the velocities are in the form of $Y_{l,m}(\theta,\phi)$, they automatically conserve momentum flux while summing all the modes l, m. In the radial direction, we use $\cos(cy)$, where c is the wavenumber in the radial direction and y is as

defined in 2D. The perturbation then has the following form:

$$
\begin{aligned}
&V_{\mathrm{perb,x}}(r,\theta,\phi) = V_{\mathrm{perb}}\sin(\theta)\cos(\phi),\\
&V_{\mathrm{perb,y}}(r,\theta,\phi) = V_{\mathrm{perb}}\sin(\theta)\sin(\phi),\\
&V_{\mathrm{perb,z}}(r,\theta,\phi) = V_{\mathrm{perb}}\cos(\theta),\\
&V_{\mathrm{perb}} = \sum_{c}\sum_{l}\sum_{m} V_{\mathrm{p}}\cdot Y_{l,m}(\theta+\omega_{lm},\phi+\omega_{lm})\cdot\cos(2\pi cy+\lambda_c), \quad V_{\mathrm{p}} = V_{\mathrm{d}}(r)c^{-5/6},
\end{aligned}
\tag{2.25}
$$

where $V_{\mathrm{perb,x}}$, $V_{\mathrm{perb,y}}$, $V_{\mathrm{perb,z}}$ are the perturbed velocities in the x, y, and z directions. We sum over the modes, applying random phases ω_{lm} and λ_c to smooth out numerical discontinuities caused by different perturbed modes. Similar to 2D, V_{p} is only scaled by radial wavenumber c. Because there are no reflective boundary conditions for 3D, we only take care of the boundary conditions in radial direction. We again assume there is no overshooting outside the boundaries of convective zones, so we enforce V_{perb} to zero by setting $\lambda_c = \pi/2$ when cy is an integer.

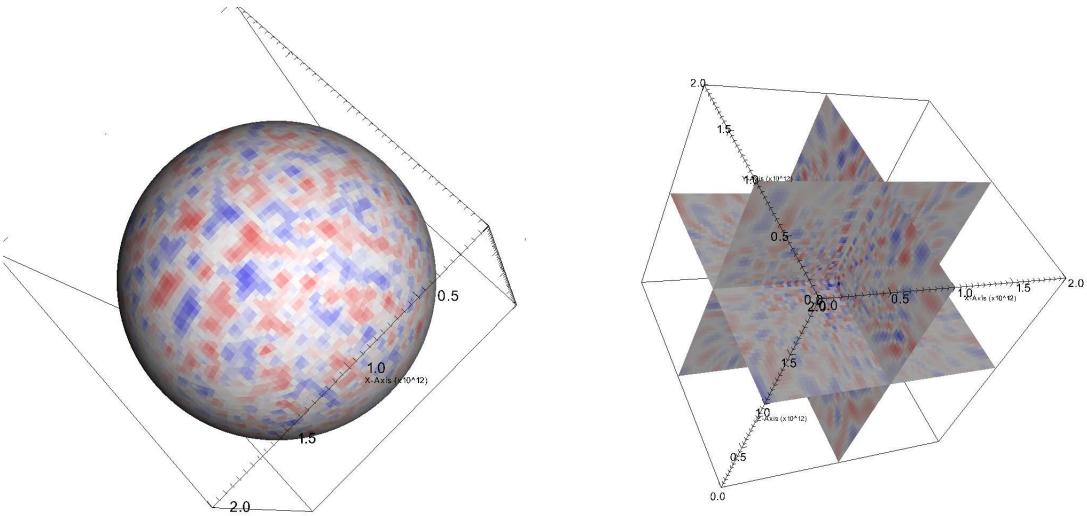

Figure 2.11: The left panel shows the perturbations constructed by using the Y_{lm} basis, and the right panel shows its inner slices.

2.4.3 Results

We first initialize perturbations on a 2D grid with a profile that is derived from a 1D KEPLER stellar evolution calculation. The perturbations are confined to regions that are convectively unstable (Heger et al., 2000). The magnitude $V_{\rm d}(r)$ of the perturbed velocity adopts the diffusion velocity, which is usually $\sim 1-10\%$ of the local sound speed. We again consider a zero-metalicity $200\,{\rm M}_\odot$ star in the pre-supernova phase. This star develops a large convection zone that extends out to the hydrogen envelope. We show the magnitude of the perturbed velocity generated by the two oscillatory functions discussed above on our 2D grid in Figure 2.12(a). The velocity field satisfies the reflecting boundary conditions on the 2D grid at $\theta = 0$ and π. In the right panel we show velocity vectors in the selected subregion on the left (blue rectangle). A clear vortex pattern that mimics a turbulent fluid is clearly visible. Figure 2.12(b) shows the energy spectrum of the fluid, which is basically a Kolmogorov spectrum $E(k) \sim k^{-5/3}$ except for fluctuations in part caused by the random phases in the sum over modes in r, and $V_{\rm d}(r)$ is not a constant across the convective region that produces an offset in the smaller k region. The energies would converge to the Kolmogorov spectrum in the limit of large k, but the maximum k of our simulation is limited to the resolution of the grid.

We next port our 1D KEPLER model to a 3D grid. In Figure 2.13(a), we show a slice of the magnitude of the perturbed velocity, which again exhibits the clear cell pattern reminiscent of the vortices of a turbulent fluid. The velocity pattern in 3D is more irregular than in 2D. We show the energy spectrum of the velocity field in Figure 2.13(b), which is similar to that of our 2D spectrum but with larger fluctuations that are again due to the random phases we assign to each spherical harmonic, and the $V_{\rm d}(r)$ is not a constant across the convective region that produces an offset in the smaller k region. Our 2D and 3D examples demonstrate that our scheme effectively generates turbulent fluid perturbations like those found in the convective regions of massive stars, with the desired initial velocity patterns and energy power spectra.

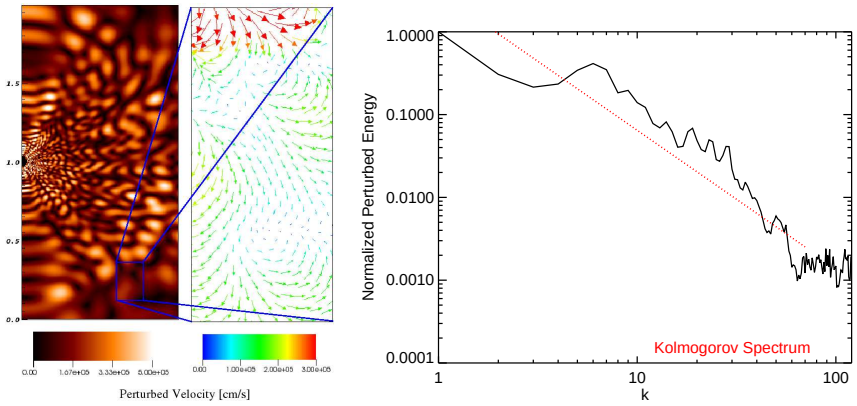

(a) 2D Perturbed Velocity (b) Energy power spectrum of 2D perturbed field

Figure 2.12: (a) 2D perturbed velocity in the interior of the star on physical scales $\sim 10^{12}$ cm: The closeup is the velocity vector field corresponding to the blue rectangle and exhibits a vortex pattern similar to that of a turbulent fluid. (b) Normalized kinetic energy power spectrum of a 2D perturbed field: The dotted red line is the Kolmogorov spectrum, $E(k) \sim k^{-5/3}$. The peak of the Kolmogorov spectrum is adjusted to fit the data. The scale of H_p is equaled to $k = 1$. The suppressed power at lower k is because of the inhomogenous of $V_p(r)$ at smaller k. The decay trend follows $k^{-5/3}$, and the fluctuations are caused by the radial oscillatory function with random phases.

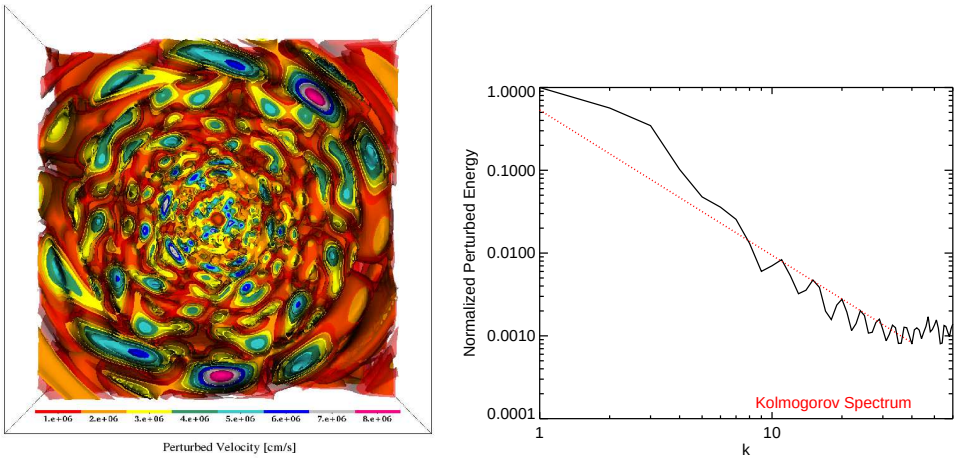

(a) 3D Perturbed Velocity

(b) Kinetic Energy Power Spectrum of 3D perturbed field

Figure 2.13: (a) 3D perturbed velocity field: The iso-surfaces show the magnitude of the perturbed velocity on physical scales of 10^{12} cm. (b) Corresponding energy power spectrum: The dotted red line shows the Kolmogorov spectrum, $E(k) \sim k^{-5/3}$. The peak of the Kolmogorov spectrum is adjusted to fit the data. The scale of H_p is equaled to $k = 1$. Similar to 2D, the decay trend follows $k^{-5/3}$, and the fluctuations are caused by the radial oscillatory function with random phases.

We do not claim the models here can fully reproduce the true turbulence found in simulations or laboratories. The scheme here is the first attempt to model the initial perturbations based on a more realistic setup. We seed initial perturbations to trigger the fluid instabilities on multidimensional simulations so we can study how they evolve with their surroundings. When the fluid instabilities start to evolve nonlinearly, the initial imprint of perturbation would be smeared out. The random perturbations and turbulent perturbations then give consistent results. Depending on the nature of problems, the random perturbations might take a longer time to evolve the fluid instabilities into turbulence because more relaxation time is required.

2.5 GR Correction

In the cases of very massive stars, the general relativity (GR) effect starts to play a role in the stellar evolution. First, we consider the hydrostatic equilibrium due to effects of GR, then derive GR-correction terms for Newtonian gravity. The correction term would be applied to the monopole-type of gravity calculation.

The formulae of GR-correction here are based on Kippenhahn and Weigert (1990). For detailed physics, please refer to Zeldovich and Novikov (1971). In a strong gravitational field, Einstein field equations are required to describe the gravity:

$$R_{ik} - \frac{1}{2} g_{ik} R = \frac{\kappa}{c^2} T_{ik}, \quad \kappa = \frac{8\pi G}{c^2}, \tag{2.26}$$

where R_{ik} is the Ricci tensor, g_{ik} is the metric tensor, R is the Riemann curvature, c is the speed of light, and G is the gravitational constant. For ideal gas, the energy momentum tensor T_{ik} has the non-vanishing components $T_{00} = \varrho c^2$, $T_{11} = T_{22} = T_{33} = P$ (ϱ contains rest mass and energy density; P is pressure). We are interested in a spherically symmetric mass distribution. The metric in a spherical coordinate (r, ϑ, φ) has the general form

$$ds^2 = e^{\nu} c^2 dt^2 - e^{\lambda} dr^2 - r^2 (d\vartheta^2 + \sin^2 \vartheta d\varphi), \tag{2.27}$$

with $\nu = \nu(r)$, $\lambda = \lambda(r)$. Now insert T_{ik} and ds into (2.26), then field equations can be reduced to three ordinary differential equations:

$$\frac{\kappa P}{c^2} = e^{-\lambda} (\frac{\nu'}{r} + \frac{1}{r^2}) - \frac{1}{r^2}, \tag{2.28}$$

$$\frac{\kappa P}{c^2} = \frac{1}{2} e^{-\lambda} (\nu'' + \frac{1}{2} \nu'^2 + \frac{\nu' - \lambda'}{r} - \frac{\nu' \lambda'}{2}), \tag{2.29}$$

$$\kappa \varrho = e^{-\lambda} (\frac{\lambda'}{r} - \frac{1}{r^2}) + \frac{1}{r^2}, \tag{2.30}$$

where primes means the derivatives with respect to r. After multiplying with $4\pi r^2$, (2.30) can be integrated and yields

$$\kappa m = 4\pi r (1 - e^{-\lambda}); \tag{2.31}$$

m is called the "gravitational mass" inside r defined as

$$m = \int_0^r 4\pi r^2 \varrho dr. \tag{2.32}$$

For $r = R$, m becomes the total mass M of the star. M here contains both the rest mass and energy divided by c^2. So the $\varrho = \varrho_0 + U/c^2$ contains the energy density U and rest mass density ϱ_0. Differentiation of Equation 2.28 with respect to r gives $P = P'(\lambda, \lambda', \nu, \nu', r)$, where $\lambda, \lambda', \nu, \nu'$ can be eliminated by Equations 2.28, 2.29, 2.30. Finally we obtain the Tolman–Oppenheinmer–Volkoff (TOV) equation for hydrostatic equilibrium in general relativity (Kippenhahn and Weigert, 1990):

$$\frac{dP}{dr} = -\frac{Gm}{r^2}\varrho(1 + \frac{P}{\varrho c^2})(1 + \frac{4\pi r^3 P}{mc^2})(1 - \frac{2Gm}{rc^2})^{-1}. \tag{2.33}$$

For the Newtonian case $c^2 \to \infty$, it reverts to the usual form,

$$\frac{dP}{dr} = -\frac{Gm}{r^2}\varrho. \tag{2.34}$$

Now we take effective monopole gravity as

$$\tilde{g} = -\frac{Gm}{r^2}(1 + \frac{P}{\varrho c^2})(1 + \frac{4\pi r^3 P}{mc^2})(1 - \frac{2Gm}{rc^2})^{-1}. \tag{2.35}$$

For general situations, we neglect the U/c^2 and potential energy in m because they are usually much smaller than ϱ_0. Only when T reaches 10^{13} K ($\mathrm{K}T \approx m_p c^2$, m_p is proton mass) does it start to make a difference. Equation 2.35 can be expressed as

$$\tilde{g} = -\frac{GM_{enc}}{r^2}(1 + \frac{P}{\varrho c^2})(1 + \frac{4\pi r^3 P}{M_{enc} c^2})(1 - \frac{2GM_{enc}}{rc^2})^{-1}, \tag{2.36}$$

where M_{enc} is the mass enclosure within r.

This part of the code is publicly available and documented in the `CASTRO` manual. Post-Newtonian correction of gravity is important for SNe from super massive stars, which will be discussed in Chapter 7.

2.6 Resolving the Early Stages of the Explosion

In addition to implementing realistic initial conditions and relevant physics for `CASTRO`, care must be taken to determine the resolution of multidimensional simulations required

to resolve the most important physical scales and yield consistent results, given the computational resources that are available. We provide a systematic approach for finding this resolution for multidimensional stellar explosions.

Simulations that include nuclear burning, which governs nucleosynthesis and the energetics of the explosion, are very different from purely hydrodynamical models because of the more stringent resolution required to resolve the scales of nuclear burning and the onset of fluid instabilities in the simulations. Because energy generation rates due to burning are very sensitive to temperature, errors in these rates as well as in nucleosynthesis can arise in zones that are not fully resolved. We determine the optimal resolution with a grid of 1D models in `CASTRO`. Beginning with a crude resolution, we evolve the pre-supernova star and its explosion until all burning is complete and then calculate the total energy of the supernova, which is the sum of the gravitational energy, internal energy, and kinetic energy. We then repeat the calculation with the same setup but with a finer resolution and again calculate the total energy of the explosion. We repeat this process until the total energy is converged. As shown in Figure 2.14, our example of a $200\,\mathrm{M}_\odot$ presupernova converges when the resolution of the grid approaches 10^8 cm.

The time scales of burning ($\mathrm{d}t_\mathrm{b}$) and hydrodynamics ($\mathrm{d}t_\mathrm{h}$) can be very disparate, so we adopt time steps of $min(\mathrm{d}t_\mathrm{h}, \mathrm{d}t_\mathrm{b})$ in our simulations, where $\mathrm{d}t_\mathrm{h} = \frac{\mathrm{d}x}{c_\mathrm{s}+|v|}$; $\mathrm{d}x$ is the grid resolution, c_s is the local sound speed, v is the fluid velocity, and the time scale for burning is $\mathrm{d}t_\mathrm{b}$, which is determined by both the energy generation rate and the rate of change of the abundances.

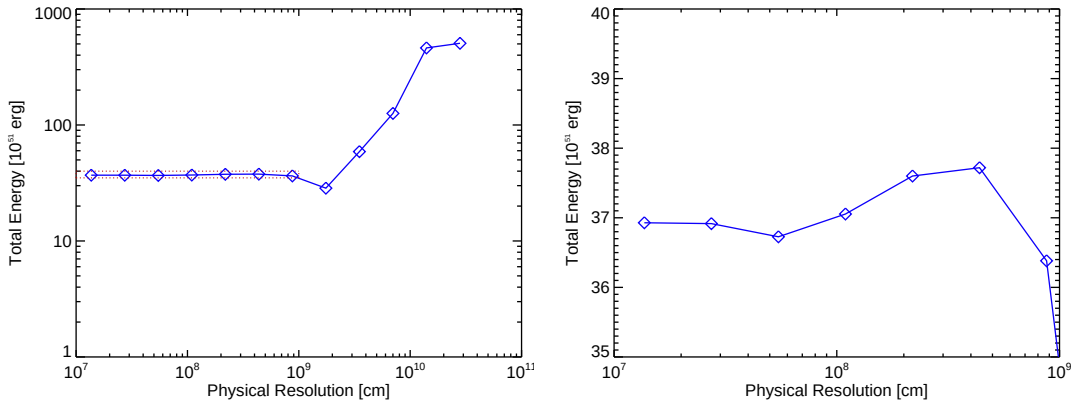

Figure 2.14: Total explosion energy as a function of resolution: The x-axis is the grid resolution, and the y-axis is the total energy, defined to be the sum of the gravitational energy, the internal energy, and the kinetic energy. The total energy is converged when the resolved scale is close to 10^8 cm. The right panel shows the zoom-in of the red box in the left panel.

2.6.1 Homographic Expansion

As we have shown, grid resolutions of 10^8 cm are needed to fully resolve nuclear burning in our model. However, the star can have a radius of up to several 10^{14} cm. This large dynamical range (10^6) makes it impractical to simulate the entire star at once while fully resolving all relevant physical processes. When the shock launches from the center of the star, the shock's traveling time scale is about a few days, which is much shorter than the Kelvin–Helmholtz time scale of the stars, about several million years. We can assume that when the shock propagates inside the star, the stellar evolution of the outer envelope is frozen. This allows us to trace the shock propagation without considering the overall stellar evolution. Hence, we instead begin our simulations with a coordinate mesh that encloses just the core of the star with zones that are fine enough to resolve explosive burning. We then halt the simulation as the SN shock approaches the grid boundaries, uniformly expand the simulation domain, and then restart the calculation. In each expansion we retain the same number of grids (see Figure 2.15). Although the resolution decreases after each expansion, it does not affect the results at later times

because burning is complete before the first expansion and emergent fluid instabilities are well resolved in later expansions. These uniform expansions are repeated until the fluid instabilities cease to evolve. There might be some possible sound waves generated from boundaries under such a setup. However, the normal SN shocks have a much higher mach number—above 10—while traveling inside the star. The sound waves could not contaminate the burning/fluid instabilities domains before the shock reaches the boundary of the simulation box.

Most stellar explosion problems need to deal with a large dynamic scale such as the case discussed here. It is computationally inefficient to simulate the entire star with a sufficient resolution. Because the time scale of the explosion is much shorter than the dynamic time of stars, we can follow the evolution of the shock by starting from the center of the star and tracing it until the shock breaks out of the stellar surface. The utility of homographic expansion is also available in `CASTRO`.

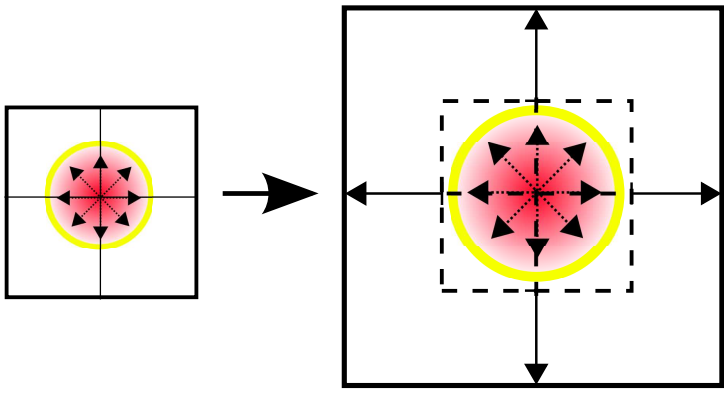

Figure 2.15: Homographic expansion: In both panels, the yellow circle is the SN shock, and the red region is the ejecta. The simulations begin with just the inner part of the star and a higher resolution (left panel) for capturing fluid instabilities and burning. After the explosion occurs, we follow the shock until it reaches the boundary of the simulation box. We then expand the simulation domain, mapping the final state of the previous calculation onto the new mesh with a new ambient medium that is taken from the initial profile.

2.7 Code Performance

To understand the parallel efficiency of CASTRO, a weak scaling study is performed, so that for each run there is exactly one 64^3 grid per processor. We run the Sod problem on 32($1024 \times 256 \times 256$), 256($2048 \times 512 \times 512$), 512($2048 \times 1024 \times 512$), 1024($2048 \times 1024 \times 1024$), and 8192($4096 \times 2048 \times 2048$) processors using only MPI-based parallelism on Itasca at the Minnesota Supercomputing Institute (MSI); the grid information is inside the parentheses. Collaborators also perform weak scaling tests on the Jaguar at the Oak Ridge Leadership Computing Facility, which runs white dwarf 3D problems on 8, 64, 512, 1024, 2048, 4096 and 8192 processors. Figure 2.16(b) shows the weak scaling of CASTRO on Itasca and Jaguar. For these scaling tests, we use only MPI-based parallelism with non-AMR grids. The results suggest CASTRO demonstrates a satisfying scaling performance within the number of CPU between $32 - 8192$ on both large supercomputers. The scaling behavior of CASTRO may depend on the calculations, especially while using AMR.

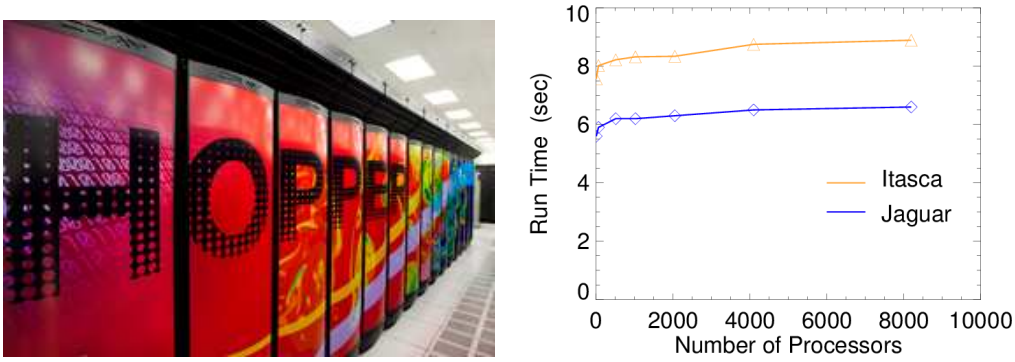

(a) **Hopper** Supercomputer

(b) CASTRO scaling

Figure 2.16: (a) CASTRO runs on some of the fastest supercomputers in the world, such as **Hopper** located at the Lawrence Berkeley Lab (Credit: NERSC website). (b) The weak scaling of CASTRO on Itasca and Jaguar. The Sod problem is used for the benchmark in the scaling of CASTRO, and the number of processors is scaled to the load of the job. The symbols are the data taken from our tests, for the case of perfect scaling, the curves should be flat. (Jaguar data provided by Ann Almgren and Andy Nonaka)

2.8 VISIT

We visualize and analyze the data generated from CASTRO by using custom software, VISIT (Childs et al., 2005), an interactive parallel visualization and graphical analysis tool. VISIT is developed by the DOE, Advanced Simulation and Computing Initiative (ASCI), and it is designed to visualize and analyze the results from large-scale simulations. VISIT contains a rich set of visualization features, and users can implement their tailored functions on VISIT. Users can also animate visualization through time, manipulate them, and save the images in several different formats. For our simulations, we usually use a pseudocolor plot for 2D visualization and a contour plot or volume plot for 3D visualization. The pseudocolor plot maps the physical quantities to colors on the same planar and generates 2D images. The contour maps 3D structures onto 2D iso-surfaces, and the volume plots fill 3D volume with colors based on their magnitude. Many examples are presented in the results of later chapters.

Chapter 3

Pulsational Pair-Instability Supernovae

Massive stars can die as different types of SNe, as we discussed in Chapter 1. We start with the supernovae of the first stars with initial masses of $80 - 150\,M_\odot$, which die as pulsational pair-instability supernovae (PPSNe). In this chapter, we present the results from 2D simulations of supernovae from a $110\,M_\odot$ star generated with `CASTRO`. Recent observations detect several superluminous supernovae that cannot be easily explained by the models of normal core-collapse supernovae. One of the possible explanations for these superluminous supernovae is the so-called pulsational pair-instability supernovae (PPSNe), theoretically predicted from the final moment before very massive stars die. The violent instabilities of the stellar core trigger the ejection of a few solar masses pulsationally. The catastrophic collisions of ejecta may power an extremely luminous optical transient that may explain the superluminous supernovae. We use 2D simulations to investigate the emergent eruptions of PPSNe and how they interact. We find that the heavy elements ejected from PPSNe are mainly ^{16}O and ^{12}C. There are no chemical elements heavier than ^{28}Si seen in the ejecta, so the radioactive isotope, ^{56}Ni, may not be seen in PPSNe. When the ejecta from different eruptions collide, it demonstrates a significant mixing caused by the fluid instabilities. The mixed region is very close to the photo-sphere of PPSNe and potentially alters their observational signatures, such as light curves and spectra.

3.1 Fate of Very Massive Stars I ($80\,M_\odot \leq M_* < 150\,M_\odot$)

Core-collapse supernovae (CCSNe), one of the most energetic explosions in the Universe, are thought to be the demise of massive stars (Bethe, 1990; Arnett, 1996; Woosley et al., 2002). In recent decades, theorists and observers have been fascinated by many different aspects of CCSNe, such as the explosion mechanisms, nucleosynthesis, compact remnant, etc. One of the most appealing features of CCSNe to astrophysicists is their light. Their powerful explosions, which are normally accompanied by magnificent electromagnetic displays, make the CCSNe unique tools for studying the Universe. The photons from CCSNe carry information about their progenitor stars as well as their host galaxies, which makes CCSNe a powerful tool for studying the Universe.

Stars with initial masses of $10 - 80\,M_\odot$ eventually forge an iron core with masses similar to our Sun through nuclear burning before they die (Kippenhahn and Weigert, 1990; Woosley and Janka, 2005). Once the mass of the iron core is larger than its Chandrasekhar mass (Chandrasekhar, 1942), the degenerate pressure of electrons can no longer support the gravity from the mass of the core itself; these conditions trigger the dramatic implosion of the core and compress the core to nucleon densities of about $10^{14}\,g\,cm^{-3}$. Most of the gravitational energy is released in the form of energetic neutrinos, which eventually power the CCSNe. The core of the star then collapses into a neutron star or a black hole, depending on the mass of the progenitor star (Woosley and Weaver, 1986; Woosley et al., 2002; Woosley and Janka, 2005). The neutrino-driven explosion mechanism for CCSNe is still poorly understood because it is complicated by issues of micro-physics, multi-scale, and multi-dimension (Burrows et al., 1995; Janka and Mueller, 1996; Mezzacappa et al., 1998; Murphy and Burrows, 2008; Nordhaus et al., 2010). It is predicted that only about 1% of the energy from neutrinos goes into the SN ejecta, which shines as brightly as the galaxy for a few weeks before fading away.

High luminosity with a moderate transit time (a few weeks) makes SNe a powerful tool to probe the distant Universe. Understanding SN explosions allows us to calculate the amount of the energy of the radiation streaming from the SN; then we may estimate the distance of the SN and its host galaxy based on the brightness we observe. Such technology has been applied to determine astronomical distances as well as the expansion rate of Universe, which are the important problems in modern cosmology.

Because of the advancement of modern CCDs, the detection rates of SNe have rapidly increased. Large SN surveys, such as the Nearby Supernova Factory (Aldering et al., 2002; Wood-Vasey et al., 2004) and the Palomar Transient Factory (Law et al., 2009; Rau et al., 2009), have rapidly increased the volume of SN data and sharpened our understanding about SNe and their host environments. More and more supernovae defying our previous classifications have been found in the last decade; they have challenged our understanding of the SN progenitors, their explosion mechanisms, and their surrounding environments. One new type of SNe found in recent observations is the superluminous SNe (SLSNe), such as SNe 2006gy and 2007bi (Smith and McCray, 2007; Gal-Yam et al., 2009; Pastorello et al., 2010; Quimby et al., 2007, 2011), which shine an order of magnitude brighter than general SNe that have been well studied in the literature (Filippenko, 1997; Smartt, 2009). These SLSNe are relatively scarce, comprising less than 5% of the total number of SNe that have been detected (Gal-Yam, 2012). They are usually found in galaxies with a lower brightness, e.g., dwarf galaxies. The engines of SLSNe challenge our understanding of CCSNe. First, the luminosity of SNe can be simply approximated in the form: $\propto 4\pi r^2 T^4$, where is r is the radius of the photo-sphere, and T is its effective surface temperature. If we assume the overall luminosity from the black body emission of hot ejecta, it requires either larger r or T to produce a more luminous SN. r is determined when the hot ejecta becomes optically thin, then the photons start to stream freely. T depends on the thermal energy of ejecta, which is directly related to the explosion energy. The duration of light curves is associated with the mass of ejecta determining the diffusion time scale and the size of the hot reservoir. In addition, radioactive isotopes such as ^{56}Ni and ^{56}Co can be made in SNe; their radioactive energy can also lift up the light curve.

There are two leading models for explaining the mechanisms of SLSNe. The first model is related to the radiation from a neutron star(Kasen and Bildsten, 2010; Woosley, 2010). After a massive star dies as a CCSN and leaves a neutron star behind, the strong magnetic field and fast rotation make the neutron star an effective source of dipole radiation, which might heat supernovae ejecta to produce a SLSN. Another promising model is related to the interaction between the SN shock and its stellar circumstance environment (CSM) (Chevalier and Blondin, 1995; Smith and McCray, 2007; Moriya et al., 2010; Chatzopoulos et al., 2011; Chevalier and Irwin, 2011; Moriya et al., 2013).

When the SN shock runs into the medium created during the star's evolution, the kinetic energy of the shock can effectively convert into radiation. Because the density of the CSM is usually very low, about $10^2 - 10^4\,\mathrm{cm}^{-3}$, that results in a small optical depth, τ, and the converted radiation can easily escape. In addition, the size of the photosphere of the SN becomes $10^{15}\,\mathrm{cm}$, about 10 times larger than its stellar radius; the peak luminosity of the SN can be boosted by an order of magnitude. But what causes the formation of the CSM? The CSM can come from the mass loss of massive stars as they evolve before they die as SNe, but, at present, the mass-loss rate driven by stellar wind is poorly understood. It is also not clear if CSM can be created when the stars eject a significant amount of mass in a short period of time before they die as SNe. We believe such outbursts of mass can be explained by robust instabilities rooted in the very massive stars of masses over $80\,\mathrm{M}_\odot$, which are called pulsational pair-instability supernova (PPSN) (Heger et al., 2003; Woosley et al., 2007).

Once the stars are more massive than $80\,\mathrm{M}_\odot$, after the central carbon burning, their cores encounter electron/positron production instability, in which the pressure-supporting photons are converted into electron and positron pairs, which softens the adiabatic index γ below 4/3. The temperature of the core starts to oscillate because of the dynamical instabilities. If the stars are close to $100\,\mathrm{M}_\odot$, the oscillation of their temperatures becomes very violent. Several strong shocks are sent out from the core before the stars die as CCSNe. Those shocks are inadequate to blow up the entire star, but they are strong enough to eject several solar masses from the stellar envelope. The energy of a pulse is about $10^{50}\,\mathrm{erg}$ (Woosley et al. (2007); Woosley, priv. comm.), while the typical binding energy for the hydrogen envelope of such massive stars is less than 10^{49} erg. Once the stars are over $150\,\mathrm{M}_\odot$, the pair instabilities trigger a runaway collapse in which the compression of the core raises the density and temperature, eventually igniting the explosive ^{16}O and ^{28}Si, turning the collapse into an energetic explosion, a pair-instability supernova (PSNe) (Barkat et al., 1967; Glatzel et al., 1985; Heger and Woosley, 2002; Kasen et al., 2011; Chen et al., 2011, 2012). PSN explosions might release explosion energy up to $10^{53}\,\mathrm{erg}$ and radioactive isotopes ^{56}Ni up to $50\,\mathrm{M}_\odot$. They ideally serve as candidates of SLSNe. However, PSNe could be much more rare in the local Universe, where high metallicity boosts the mass loss of stars and prevents them from turning into PSNe.

We turn our attention to the stars of masses falling between the gap of the CCSNe and PSNe regime. These stars eventually forge an iron core and die as CCSNe. But the appealing scenario is the outburst of mass before they die because of pair-instabilities. This provides a robust explanation for CSM models that may be a promising candidate for the SLSNe (Woosley et al., 2007). However, varieties of mixing driven by the fluid instabilities during the shock running into CSM might significantly alter the observational signatures of PPSNe. Only multidimensional hydrodynamics simulations can shed light on such phenomena. In this chapter, we perform the 2D hydro simulations, including nuclear burning, to model the PPSNe while the giant outburst and the catastrophic collisions of these ejecta occur; we investigate how mixing driven by fluid instabilities plays a role in PPSNe.

The structure of the chapter is as follows: we first describe our numerical approaches and initial pre-supernova models in § 3.2. Then we present the results in § 3.3 and discuss the emergent fluid instabilities during the pulsational outbursts in § 3.4. Finally, we conclude and summarize our findings in § 3.5.

3.2 Methodology

In this section, we discuss our numerical methods for carrying out the simulations. Since PPSNe occur for the progenitors of masses $80 - 150\,\mathrm{M}_\odot$, we select a $110\,\mathrm{M}_\odot$ star and evolve it using the 1D stellar evolution code, `KEPLER`. Until the pair-creation (e^+/e^-) instabilities occur, we map the resulting 1D profiles from `KEPLER` onto to the 2D axis-symmetric grids of `CASTRO` and follow the evolution of emergent eruptions caused by the burning triggered by pair-production instabilities. Because of the limitation of resolution, the 2D simulations cannot follow all the eruption episodes self-consistently. We alternatively switch between 1D and 2D to folllow the evolution of stellar interiors (1D), eruptions (1D, 2D), and shell collisions (2D) simultaneously.

3.2.1 Pre-supernova Progenitor

Our initial model uses a 110 $\mathrm{M}_\odot$ star, which is identical to Woosley et al. (2007), a promising candidate for explaining the superluminous SN 2006gy (Ofek et al., 2007; Smith et al., 2007). Hence, our work can be treated as an extension of Woosley et al.

(2007). New 2D simulations allow us to follow fluid instabilities from first principles, which cannot be studied by the previous 1D models.

The 1D spherical-symmetric model represents the star until its pre-supernova phase. We evolve a $110\,M_\odot$ star with the 1D Lagrangian hydro code, `KEPLER` (Weaver et al., 1978; Heger et al., 2001), which includes relevant physics processes for stellar evolution, such as nuclear burning and mixing due to convection. We evolve the star as it enters the pair-instability regime and its central temperatures start to pulse. At this time, the central carbon burning is ignited. These pulses in temperature act at a frequency close to the dynamical time scale of the core, about several hundred secs. When the core is approaching a density of $\rho_c \approx 4 \times 10^6\,\mathrm{g\,cm^{-3}}$ and a temperature of $T_c \approx 3 \times 10^9\,\mathrm{K}$, it triggers a collapse and ignites oxygen burning explosively. The energy released from the burning reverses the collapse and sends a shock into the envelope of the stars, ejecting the mass of the envelope. The core now reaches another equilibrium state. The compression of the core occurs three to four times pulsationally in a few days before the $110\,M_\odot$ star dies as a CCSNe. Each time, the emergent energetics differ, depending on the central temperatures, densities, and compositions. The later eruptions usually have a larger energy but eject less mass, which allows them to collide with previous ejecta. Pulsational eruptions become more violent for more massive stars until their masses approach the lower limit of pair-instability SNe, about $150\,M_\odot$. With 2D simulations, we want to study how the mixing of PPSNe ejecta is caused by fluid instabilites. There are two promising phases for fluid instabilities to develop: the onset of eruption and the colliding of ejecta.

3.2.2 Problem setup

We follow several critical phases of PPSNe that require 2D simulations, e.g., the occurrence of eruptions during the explosive burning, and, most important of all, within catastrophic collisions of ejecta that power superluminous transits. We perform 2D simulations by using `CASTRO`. The equations of state in `CASTRO` use the Helmholtz equation of state (Timmes and Swesty, 2000), which considers the situations of (non)degenerate and (non)relativistic electrons, electron-positron pair production, ion gas, and radiation. The derived thermodynamics are quantities (e.g., internal energy, pressure, etc.) calculated based on the inputs of the density, the temperature, and the abundance of

nuclear spices. To simulate the burning during the eruption, we use the 19-isotopes reaction network, which considers the heavy ion reactions, α chain, p-p chain, and the CNO cycle. The eruptions of shells inside PPSNe are mainly driven by the explosive carbon and oxygen burning that can be precisely modeled by the 19-isotopes network.

We map the 1D radial profile of `KEPLER` onto the 2D grids in `CASTRO` using the procedures based on Chen et al. (2011, 2012) that guarantee the conservative quantities; energy and mass are strictly preserved during the mapping. Our 2D simulations are constructed as 256×256 zones with three levels of a factor of 4 refinement, which provides a resolution sufficient to resolve the nuclear burning and the scales of fluid instabilities. The AMR refined criteria are set for the gradients of density, velocity, and pressure. Once the gradients between adjacent zones are larger than the criteria we set, finer grids are automatically generated to patch over previous coarse grids. Since we simulate only a hemisphere of the star, the lower boundaries of Z and R use reflect boundaries that prohibit the fluid from flowing across. The upper boundaries use outflow conditions that allow the fluid to move freely across the boundaries. Because the most violent burning occurs at the inner core of the star, nested grids are constructed from the center to ensure that the core constantly receives the highest spatial and time resolution. The self-gravity is included by computing the gravitational forces using monopole approximation, which, given the spherical symmetry of stars, is a valid approximation.

3.3 Fluid Instabilities during Eruption

During the collapse of stars, the central temperature rises quickly and ignites oxygen burning explosively. Such burning not only powers the explosion; if any fluid instability occurs during this time, it may easily result in significant mixing at the early phase of eruptions and affect the observational signature of the PPSN later. We first use `CASTRO` to study the fluid instabilities at the onset of eruption by considering the nuclear burning. Resolving the scale of nuclear burning requires high resolution, but instead of simulating the entire domain of the star, we initialize our simulations with a domain of $r = 4 \times 10^{11}\,\mathrm{cm}$, which includes the core of the star as well as part of the helium envelope. The initial conditions begin 70 sec before the second eruption. The burning layer is about to collapse when the simulation starts; the central temperature rises

to about 3×10^9 K. The explosive burning of oxygen is immediately ignited. Once the core pressure reaches the pressure of collapse, the shock is successfully launched. Figure 3.1(a) shows the evolution of radial velocity of our model. During explosive burning of oxygen, the burning layers remain intact, and no obvious mixing of layers appears during burning. There is no evidence of mixing hot ash and fuel. It suggests that the fluid instability during the explosive burning phase is minor. The synthesized products of oxygen burning mainly provide the energetics for the explosion, but they are not ejected by the fluid instabilities. We show the 2D radial velocity in Figure 3.1(b) at the time when the shock has travelled to $r \approx 3 \times 10^{11}$ cm. The falling and bouncing of ejecta are still occurring at the inner part. The fallback of un-ejected gas distorts some of the inner shells, which look minor at this time but may seed perturbations for subsequent eruptions.

We then follow the second eruption to study whether the post-eruption environment is significantly affected before the third eruption occurs. As shown in Figure 3.2, there is no further mixing driven by the reverse shock from the second pulse. Hence the pre-eruption environment of the third pulse is very similar to that of 1D models. This pre-collision study suggests that beginning with a 1D model is a viable means of directly simulating the shell collisions instead of following all eruptions.

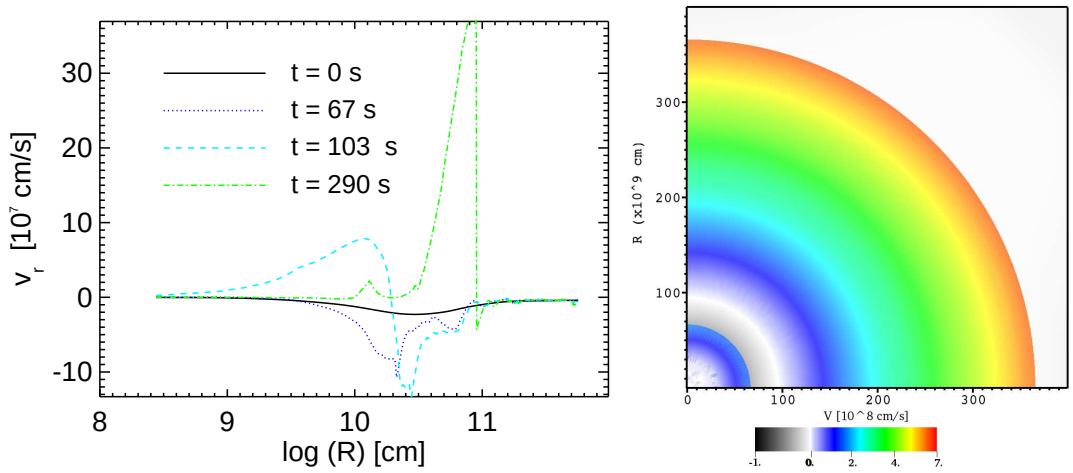

(a) Velocity evolution

(b) Velocity map

Figure 3.1: (a) Velocity evolution during the second eruption phase of PPSNe. (b) The hot color shows the positive radial velocities, and the grey color shows the negative radial velocities. The eruption sends out a shock with a max speed of about $700\,\mathrm{km\,s^{-1}}$ and ejects a few solar masses from the envelope. The unbound ejecta fall back to the inner core and bounce before the core reaches a new thermal equilibrium.

Our simulation is limited by resolution and by computational resources. When the third eruption occurs, the ejecta from the first eruption have propagated to a radius about $10^{16}\,\mathrm{cm}$. However, the resolution required to simulate the eruptions triggered by nuclear burning is $10^{8}\,\mathrm{cm}$ or even finer. It makes the following completed eruption episodes impractical. Because our pre-eruption simulations suggest only a slight distortion of the spherical-symmetry of the star, we should be able to simulate the post-eruption hydrodynamics using the initial conditions from 1D `KEPLER` models.

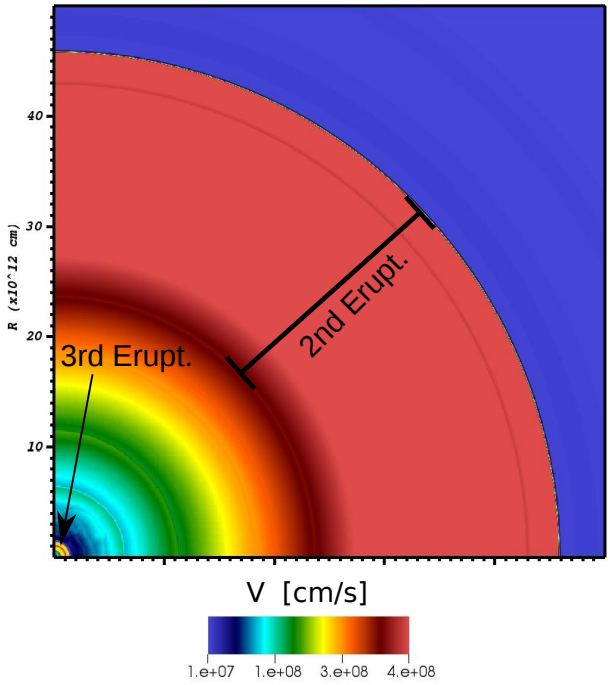

Figure 3.2: 2D velocity when the third eruption occurs. The distorted shell structure is created during the fallback of the second eruption. This shell structure is slightly affected, which creates a velocity perturbation of about 1% of the shock velocity.

3.4 The Colliding Shells

We start to generate 2D simulations with the initial condition at the time when the hydrogen envelope of the star has been expanded by the first eruption to a radius of 10^{16} cm, and the shock of the second eruption has approached to $r \sim 10^{15}$ cm. The shock of the third eruption is now at $r \sim 3 \times 10^{14}$cm. The third pulse has the most energetic eruption of the three, but it disperses the smallest mass. This leads to a highest shock velocity of the third pulse and allows it to catch up with previous eruptions. Figure 3.3 shows the evolution of the velocity profile inside the star. The two velocity peaks of eruption represent the shocks of the second and third eruptions, respectively. The strong shock of the third eruption hits the second eruption in two weeks. The collision

of the second and third eruptions might produce a burst of photons by converting parts of the kinetics of the collision into radiation. However, since the collision is still embedded inside the optically thin region, it could be hard to detect the transit because the emitted photons may be scattered/absorbed inside this optically thick region and smear the memory of the streaming photons. Within about 100 days, the two shocks of eruptions collide and merge into one and start to run into the extensive hydrogen envelope created by the first eruption. During the collision shock, the seed of fluid instability is created, and it will further develop later.

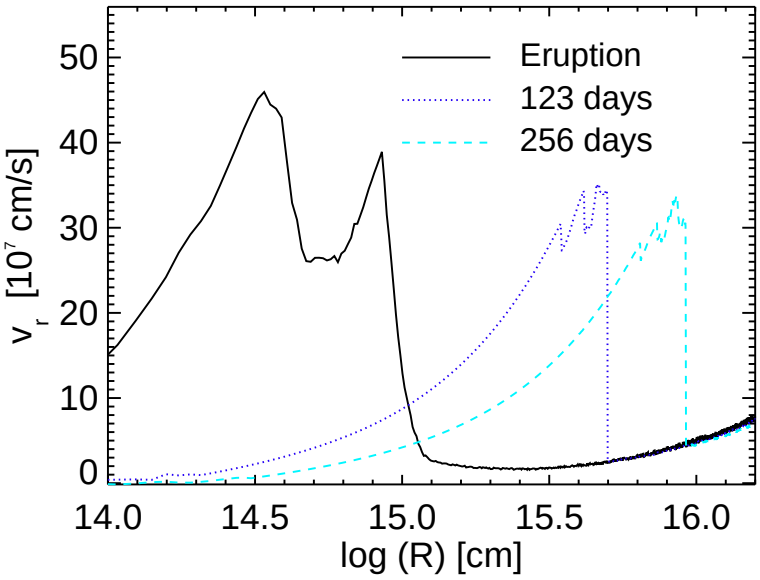

Figure 3.3: 1D velocity profile, showing the 1D radial velocity from our 2D simulation. The initial velocity (solid line) is at the time when the second eruption is entering the ejecta created by the first eruption. Later, the third eruption catches up to the second eruption, and together they run into the first ejecta (dotted line) and start to produce the luminous emission. The emission lasts until the shock travels to a radius about 10^{16} cm, shown in the dashed line.

Once the merging shock of the second and third pulses enters the extensive hydrogen-rich envelope that was expelled by the first eruption, the shock starts to decelerate because of the snowplow effect of the mass ahead of it. The slowdown forms a reverse shock,

producing a pressure gradient opposite to the density gradient; hence, Rayleigh–Taylor (RT) instability occurs. The seeds of perturbation now grow from the RT instabilities. At the same time, the kinetic energy of the ejecta turns into the thermal energy of the gas because of inelastic collision. Since the gas density outside the collision shells is very low, $\rho \lesssim 10^{-16}\,\mathrm{g\,cm^{-3}}$, it results in an optically thin environment for photons. The thermal radiation from the collided shells can easily escape once photons have been generated and without losing their energy through the free expansion of the ejecta. In addition, the photosphere of SN ejecta now has a large radius, $r \sim 10^{15}\,\mathrm{cm}$, which results in a very luminous optical transit that can be used to explain superluminous SNe.

Figure 3.4 shows the density and temperature of collision shells. The shock has approached a radius of $r \sim 10^{16}\,\mathrm{cm}$. From the density plot, the mixing appears behind the shock front. These mixing sites are close to the optically thin region where the photon streams start to decouple from the gas. The clumped structure caused by fluid instabilities may trap the thermal photons during the collision and affect the observational signatures of photons, and the mixture of the ejecta can also affect the observational signature.

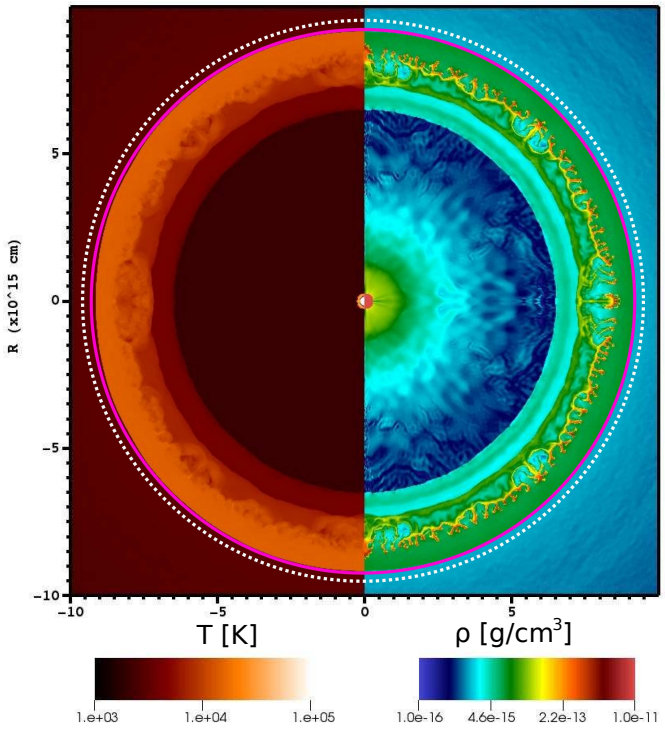

Figure 3.4: The collisions of ejecta: The pink dashed line shows the location of the shock front, and the white dashed line shows the photon sphere of $\tau \sim 0.2$. The radiation now starts to diffuse from the shock and structures from the mixing layers.

3.4.1 Mixing of Colliding Shells

There are two major mixing phases caused by the fluid instabilities. As shown in the previous results, the fluid instabilities occur early in the process, when the fallback of ejecta moderately produces minor fluid instabilities that can be treated as perturbations when the later eruptions occur. The more significant fluid instabilities occur most during the collisions of ejecta with previous ones. In Figure 3.5, we show the 1D isotope abundance of Figure 3.4. The mixing appears in a region the size about 10^{15} cm, where the intermediate elements, such as ^{12}C, ^{16}O, and ^{24}Mg, are dredged up. However, isotopes heavier than ^{28}Si are rarely seen in the ejecta.

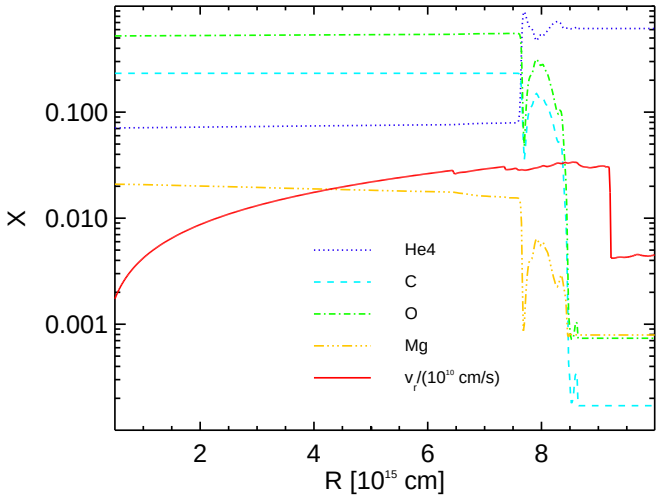

Figure 3.5: The mixing of colliding shells. We map 1D elemental abundance from Figure 3.4. The major mixing elements are ^{12}C and ^{16}O. Isotopes above ^{28}Si are barely ejected from the stars, so they are absent from the ejecta.

3.5 Conclusion

Some Pop III simulations suggest the fragmentation of the first stars, indicating that the masses of these first stars may fall between $50 - 150\,\mathrm{M}_{\odot}$. It suggests PPSNe can be possible outcomes of the fate of the Pop III stars, although their fate depends on how much mass they retain before they die. The mass-loss rate of massive stars is not well understood; the possible mechanisms are metallicity, stellar rotation, and interior instabilities. If the mass-loss rate is correlated to the metallicity as $\dot{M} \propto Z^{0.5}$, the Pop III stars may suffer less mass loss than the stars in our local Universe. This increases the probability of detecting the PPSNe at high redshift. In addition to the colliding shell, as we discuss above, they produce the superluminous event that makes the detection of these first supernovae more promising.

We have presented the 2D simulations of the pulsational pair-instability supernovae by using the new hydrodynamics code `CASTRO`. The fluid instabilities occur during the fallback of ejecta and the collisions of ejected shells. The collisions of ejecta produce the very significant mixture driven by fluid instabilities, which are located at the radiated

shells and can affect the light curves and spectra of the PPSNe. The radiation transport is required for calculating the light curves and spectra for these transients; we expect the mixing can intensify because the radiation cooling of clumps is amplified by the growth of fluid instabilities. We plan to apply our new radiation transport calculations to investigate more progenitor models and predict the observational signatures for them. The low-metallicity stars (Pop III/II stars) are the ideal progenitors of PPSNe. The future large space and ground observatories, such as the James Webb Space Telescope (JWST), will target the high redshift transits and will be able to directly detect the PPSNe from Pop III stars.

Chapter 4

Pair-Instability Supernovae

Numerical studies and theoretical estimates of Pop III star formation suggest that the first stars in the Universe could have been very massive. Non-rotating Pop III stars with masses of $150 - 260\,\mathrm{M}_{\odot}$ may have died as energetic thermonuclear supernovae, so-called pair-instability supernovae (PSNe). In this chapter, we present 2D simulations of PSNe using `CASTRO`. Our models follow the entire explosive nuclear burning and the explosion until the shock breaks out from the stellar surface. From our simulations, we find that fluid instabilities driven by oxygen and helium burning arise at the lower and upper boundaries of the oxygen shell at $\sim 20 - 100$ sec after core bounce. The instabilities driven by burning freeze out when the SN shock has passed the helium core. When the shock propagates through the hydrogen envelope, a strong reverse shock forms that drives the development of Rayleigh–Taylor (RT) instabilities. In red supergiant progenitors, the amplitudes of these instabilities are sufficient to mix the supernova ejecta and may alter the observational signature.

4.1 Fate of Very Massive Stars II ($150\,\mathrm{M}_{\odot} \leq \mathrm{M}_{*} \leq 260\,\mathrm{M}_{\odot}$)

Modern cosmological simulations suggest that the hierarchical assembly of dark matter (DM) halos provide the gravitational wells which allow the primordial gases to form stars and galaxies inside them. The first stars, called Population III (Pop III) stars (Bond et al., 1984; O'Shea et al., 2008), formed inside the mini DM halos ($\sim 10^{6}\,\mathrm{M}_{\odot}$) at $z \sim 30$. Massive Pop III stars are strong emitters of hydrogen-ionizing photons, building

up extended H II regions and contributing to cosmic re-ionization (Carr et al., 1984; Whalen et al., 2004; Kitayama et al., 2004; Alvarez and Abel, 2007; Abel et al., 2007). They also synthesized the first significant amounts of heavy chemical elements beyond lithium and dispersed them into the intergalactic medium through their supernova (SN) explosions. This chemical enrichment led to the formation of the second generation of stars (Pop II stars) that resided in the first galaxies (Wise and Abel, 2008; Greif et al., 2010b). *But how did these first stars die?*

Earlier results from the simulations of the first stars predicted that the Pop III stars formed with mass scales about $100\,\mathrm{M}_\odot$ (Abel et al., 2002; Bromm et al., 2009). Recent investigations (Turk et al., 2009; Stacy et al., 2010, 2012) have found that some fraction of Pop III stars forms in binaries or multiples, so the first stars could have been less massive than was originally thought. Even today, however, we do observe stars with initial masses larger than $150\,\mathrm{M}_\odot$ (Humphreys and Davidson, 1979; Davidson and Humphreys, 1997; Crowther et al., 2010). Pop III stars with initial masses of $150 - 260\,\mathrm{M}_\odot$ develop oxygen cores of $\gtrsim 50\,\mathrm{M}_\odot$ after central carbon burning (Barkat et al., 1967; Glatzel et al., 1985; Heger and Woosley, 2002, 2010). At this point, the core reaches sufficiently high temperatures ($\sim 10^9\,\mathrm{K}$) and at relatively low densities ($\sim 10^6\,\mathrm{g\,cm^{-3}}$) to favor the creation of electron-positron pairs (high-entropy hot plasma). The pressure-supporting photons turn into the rest masses for pairs and soften the adiabatic index γ_{ad} of the gas below a critical value of $4/3$, which causes a dynamical instability and triggers rapid contraction of the core. During contraction, core temperatures and densities swiftly rise, and oxygen and silicon ignite, burning rapidly. This reverses the preceding contraction (enough entropy is generated so the equation of state leaves the regime of pair instability), and a shock forms at the outer edge of the core. This thermonuclear explosion, known as a pair-instability supernova (PSN), completely disrupts the star with explosion energies of up to $10^{53}\,\mathrm{erg}$, leaving no compact remnant and producing up to $50\,\mathrm{M}_\odot$ of $^{56}\mathrm{Ni}$ (Heger and Woosley, 2002; Kasen et al., 2011).

Most current theoretical models of PSNe are based on one-dimensional calculations (Heger and Woosley, 2002). In the initial stages of a supernova, however, spherical symmetry is broken by fluid instabilities generated by burning that cannot be captured in 1D. Two-dimensional simulations of Pop III PSNe have recently been done by Joggerst and Whalen (2011), but their models started from 1D models that were mapped

into multi-D only after all explosive burning had completed; their models exclude instabilities driven during the burning stage. Their simulations find only mild dynamical instabilities. During burning, such instabilities may alter the energetics and nucleosynthesis of the SN by vigorously mixing its fuel, and they must be included in simulations to illuminate the true evolution of PSNe. In our previous work (Chen et al., 2011), we considered only the early stage of the explosion from collapse to bounce but did not follow the explosion until the shock broke out of the stellar surface. Here we present 2D PSN simulations that follow the entire evolution from the onset of explosive burning to the shock breakout at the stellar surface. We study the fluid instabilities that arise, and we discuss how mixing alters the nucleosynthesis and energetics of the explosion.

The structure of this chapter is as follows: we first describe our numerical approaches and initial presupernova models in § 4.2. Then we present the results in § 4.3 and discuss the fluid instabilities emerging during the explosion in § 4.4. Our conclusions are given in § 4.5.

4.2 Problem Setup

Our 2D simulation uses initial models that follow the hydrostatic evolution stages using `KEPLER` (Weaver et al., 1978; Heger et al., 2001), a one-dimensional spherically-symmetric Lagrangian code. In `KEPLER`, the evolution of the progenitor star is followed until the onset of explosive oxygen burning, just a few tens of seconds before the maximum compression (bounce) of the core. Then we map the resulting one-dimensional profiles onto multidimensional grids as the initial conditions for `CASTRO` (Almgren et al., 2010; Zhang et al., 2011). At this time, the most violent burning is about to occur, which suggests the most promising sites of emergent fluid instabilities. We then evolve the 2D `CASTRO` simulations until the shock breaks out from the stellar surface. Using such a setup allows us to capture the most important features of supernova explosion in 2D that available computational resources allow.

4.2.1 Presupernova Models

In primordial massive stars, hydrogen burning proceeds by the CNO cycle similar to their metal-rich counterparts; however, the carbon seeds have to be made directly in

the star by helium fusion (triple alpha process). Only a very small mass fraction of metals is sufficient to drive the cycle. Typical values are CNO mass fractions of 10^{-9} for central hydrogen burning and 10^{-7} for hydrogen shell burning. Thus the CNO cycle proceeds at a higher density and temperature, and overall lower entropy, than if there were metals present. Unlike metal-rich stars, the primordial stars have a very small entropy barrier between the hydrogen shell and the helium core during the core helium burning. For the massive stars, the pressure is dominated by radiation pressure, which facilitates convection. During helium core burning, the central convection zone, which is rich in carbon and oxygen, can get very close to the hydrogen-burning shell and even mix with it if there is sufficient convective penetration and overshooting or other convective boundary mixing (Meakin and Arnett, 2007; Arnett et al., 2009). When this mixing occurs, the carbon mass fraction of the hydrogen burning shell increases dramatically and leads to a rapid increase of the energy generation rate of the hydrogen shell; if temperature and density were fixed, the increase would be proportional to the enrichment in CNO. Depending on the extent of this mixing, this causes an expansion of the hydrogen envelope, and the star may become a red supergiant with a radius about one order of magnitude larger than the original size. If the overshooting is very weak, the stars keep their size and evolve into blue supergiants. The exact amount of the mixing that occurs, however, is still quite uncertain.

Based on the pre-SN models from Scannapieco et al. (2005), we select a suite of progenitor models containing weak and strong mixing for non-rotating stars with $150\,M_\odot$, $200\,M_\odot$, and $250\,M_\odot$ (Table 4.1). We name our models as `XYYY` where `X` indicates whether the star is a red (R) or blue (B) supergiant, and `YYY` is the initial mass of the star in solar masses (150, 200, or 250).

Name	M_*	$M_{\rm He}$	$\rho_{\rm c}$	$T_{\rm c}$	R	E	$M_{\rm Ni}$
	[$M_\odot$]	[$M_\odot$]	[10^6g cm^{-3}]	[10^9 K]	[10^{13} cm]	[10^{52} erg]	[$M_\odot$]
B150	150	67	1.40	3.25	16.54	1.29	0.07
B200	200	95	1.23	3.31	2.86	4.14	6.57
B250	250	109	1.11	3.34	23.06	7.23	28.05
R150	150	59	1.58	3.25	25.69	1.19	0.10
R200	200	86	1.27	3.31	27.68	3.43	4.66
R250	250	156	0.95	3.38	20.76	...	...

Table 4.1: M_*: initial stellar mass; $M_{\rm He}$: helium core mass at collapse; $\rho_{\rm c}$: central density at collapse; $T_{\rm c}$: central temperature at collapse; R: stellar radius; E: explosion energy; the last model did not explode; $M_{\rm Ni}$: ^{56}Ni production.

4.2.2 Mapping 1D Models into 2D

The 2D `CASTRO` simulations use the 1D `KEPLER` profiles as initial conditions. Because of differences between codes in dimensionality and coordinate mesh, mapping profiles from one code to the other can lead to numerical artifacts such as violation of conservation of mass, energy, and momentum. A simple approach could be to initialize multidimensional grids by linear interpolation from corresponding mesh points on the 1D profiles and then use the values of the interpolation function at the zone centers. Such a linear interpolation becomes invalid, however, when the new grid fails to resolve the structure of the original stellar model. This is especially true when porting profiles from 1D Lagrangian codes, which can easily resolve very small spatial features in mass coordinates on an Eulerian grid with finite resolution, even when using AMR and limiting the refinement levels to a reasonable extent. In addition to violating conservation laws, some physical processes, such as nuclear burning, are very sensitive to temperature, so slight errors in the mapping process may lead to different outcomes for the simulation. We use a new mapping procedure to conservatively map one-dimensional profiles onto multidimensional grids at any resolution (Chapter 2). We then seed the initial perturbation based on stellar convective velocities using the Kolmogorov spectrum as a guide instead

of implementing random perturbation, as discussed in Chapter 2.

4.3 Results

At the beginning of the CASTRO simulation, radiative pressure support of the core is taken away by e^- and e^+ production, and the cores of the stars start collapsing. During this time, the energy generation rate is dominated by the neutrino energy loss. Several seconds later, the collapsing core suddenly drives its temperature to reach the ignition of silicon burning, $T \approx 4 \times 10^9\,\mathrm{K}$. Such silicon burning is different from the silicon burning we discussed in Chapter 1 because the burning is now occurring at a non-hydro equilibrium state, and it only lasts about tens of secs. However, energy released from the burning is sufficient to reverse the collapse into an explosion. Figure 4.1 shows the velocity evolution during the onset of explosion. The in-falling velocities of collapsing shells are about $5 \times 10^8 - 10^9\,\mathrm{cm\,sec^{-1}}$. After the explosion occurs, a strong shock with velocity of about $10^9\,\mathrm{cm\,sec^{-1}}$ is launched and will propagate until it breaks out from the stellar surface.

For R250, it does not launch a strong shock; instead the in-falling velocity reaches $2 \times 10^9\,\mathrm{cm\,sec^{-1}}$, then the code crashes at 14 sec after the evolution because the explosion energy is insufficient to reverse the collapse into explosion. The explosion energy is completely sunk by the photon disintegration, so the shock fails to launch, and the star may eventually collapse into a black hole. Although our CASTRO models cannot follow the simulations of the entire black hole formation, evidence shows there is a runaway collapse in the velocity profile of R250. 1D KEPLER models suggest that R250 develops a large helium core of about $156\,\mathrm{M_\odot}$ and eventually dies as a black hole. In terms of thermal properties, we plot the temperature evolution during the collapse in Figure 4.2. The temperature first increases due to the contraction of the core and then quickly drops when the explosion occurs.

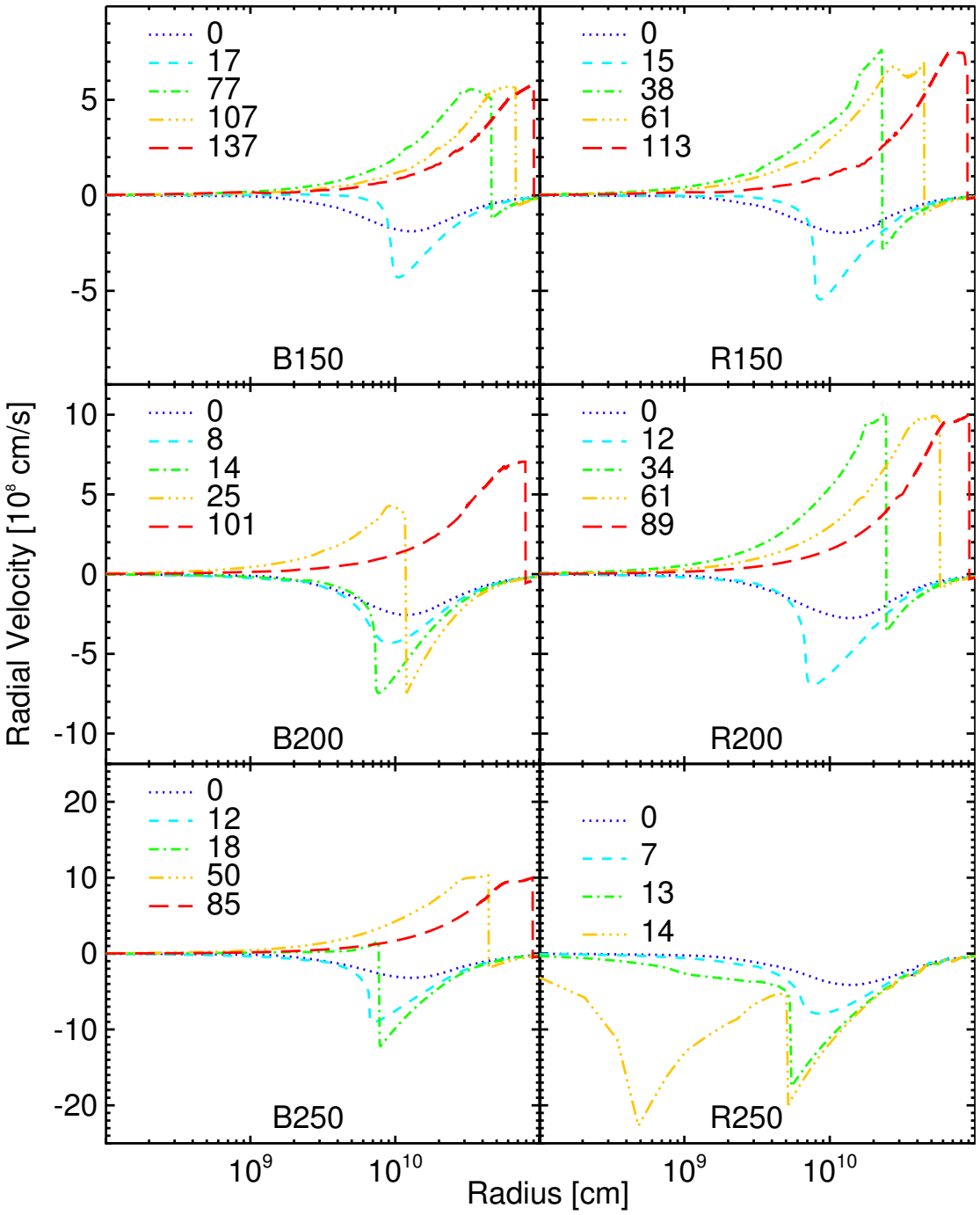

Figure 4.1: The evolution of radial velocity profiles during core bounce. The number for each curve is the time after the simulation started in the unit of sec. Except R250, all of the successful explosion models have a transition from infall velocity to outward shock.

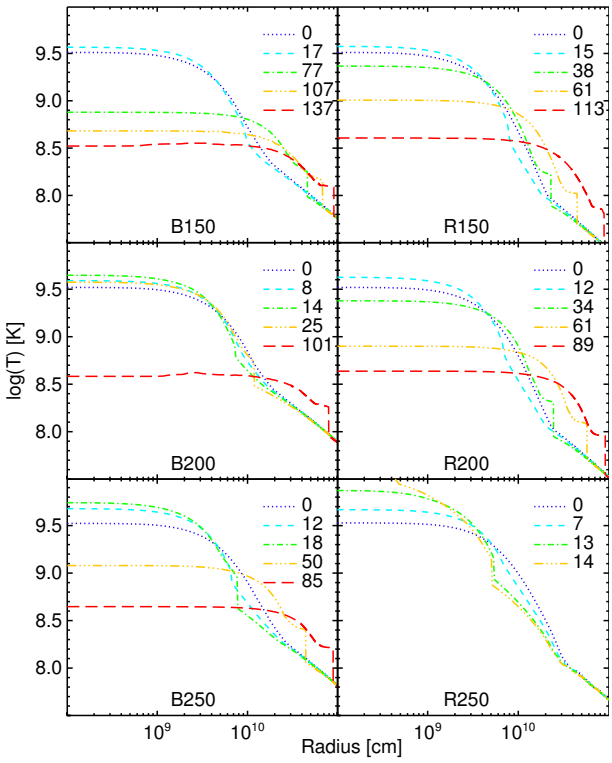

Figure 4.2: Evolution of inner temperature profiles during core bounce. When the shock approaches 10^{11} cm, the post-shock temperature has dropped close to 2×10^8 K or below. At this time, most of the explosive burning is finished. For R250, its inner temperature keeps increasing above 10^{10} K until the core may collapse into a black hole.

Due to silicon burning, ^{56}Ni is synthesized. Figure 4.3 shows the evolution of the central temperature, density, and ^{56}Ni production of `CASTRO` models in the first minute of simulations. The central density (ρ_c) and temperature (T_c) first increase because of the rapid contraction caused by collapse. At $15 - 20$ sec after the simulations start, ρ_c and T_c reach the maximum, then rapidly drop because the explosion starts to unbind the entire core. Higher T_c and ρ_c for more massive models flavor the production of ^{56}Ni. Table 4.1 summarizes the explosion energy released and ^{56}Ni production. The explosion mechanics of PSNe are insensitive to the dimensionality of simulations, so

these explosions are consistent with the 1D models of Heger and Woosley (2002).

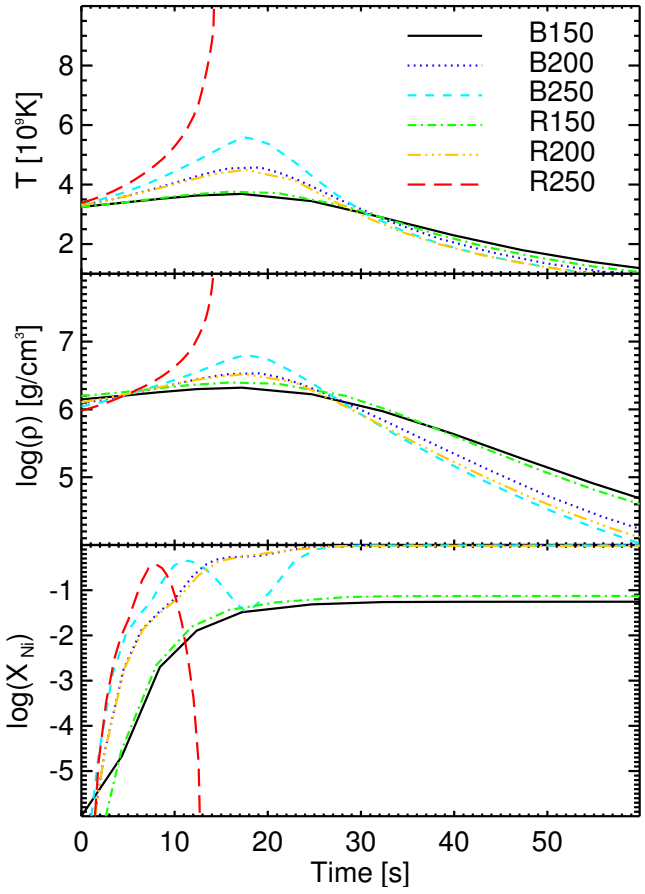

Figure 4.3: Evolution of ρ_c, T_c, and ^{56}Ni mass fraction in the first minute. Except in the case of R250, the density and temperature first increase due to the contraction of the core, then they decrease due to the explosion. The stronger explosion causes the faster decay of central density and temperature since the gas is ejected faster. The central ^{56}Ni mass builds rapidly in the first 20 sec because of the ignition of explosive ^{28}Si burning. The strong photo-disintegration causes the ^{56}Ni of B250 to vanish between $10 - 20$ sec.

4.3.1 Fluid Instabilities during Burning

In such a short and violent phase of explosion, do any fluid instabilities or mixing occur? Any fluid instabilities that occur can easily imprint on the density or elemental abundance pattern. Figure 4.4 shows both the density and the oxygen abundance of models when the explosive burning is finished. During the collapse, instabilities occur at the inner boundary of the oxygen-burning shell that are triggered by dynamic instability. Those instabilities do not develop sufficient amplitudes to dredge the newly synthesized ^{56}Ni to the upper boundary of the oxygen-burning shell. The explosive burning at the ^{28}Si core does not trigger any observable instabilities for all models. One possible reason is the stellar structure of these progenitor stars, which have a flat density and temperature profile at their inner core, 10^9 cm, where the ^{56}Ni is synthesized. Without a proper interface or discontinuity of physical quantities such as density, the development of fluid instabilities can be suppressed. We look at the upper-right contours of B150 and B200 in Figure 4.4. Some fluid instabilities have appeared, occurring at the interface between the oxygen core and helium envelope. The fluid instabilities freeze within 100 sec when the shock runs into the helium-rich envelope. The entropy generated by burning causes an entropy gradient across the contact discontinuity of different burning layers, leading to the development of fluid instabilities. The fluid instabilities appear at the outer boundary of the oxygen-burning shell, the close-up shown in Figure 4.6. By comparing the R and B models, we see more mixing is apparent in the B than R models because the B models have a more compact structure that provides more ^{4}He fuel for burning, and the steepened density structure of the ^{4}He core flavors the development of fluid instabilities. Figure 4.5 shows mixing of the isotope abundance for selected elements when the burning is over. At this time, because there is no other driving force to further evolving fluid instabilities, there is no evidence of ^{56}Ni (red dashed line) being dredged up to the oxygen-burning shell (green dot-dash line).

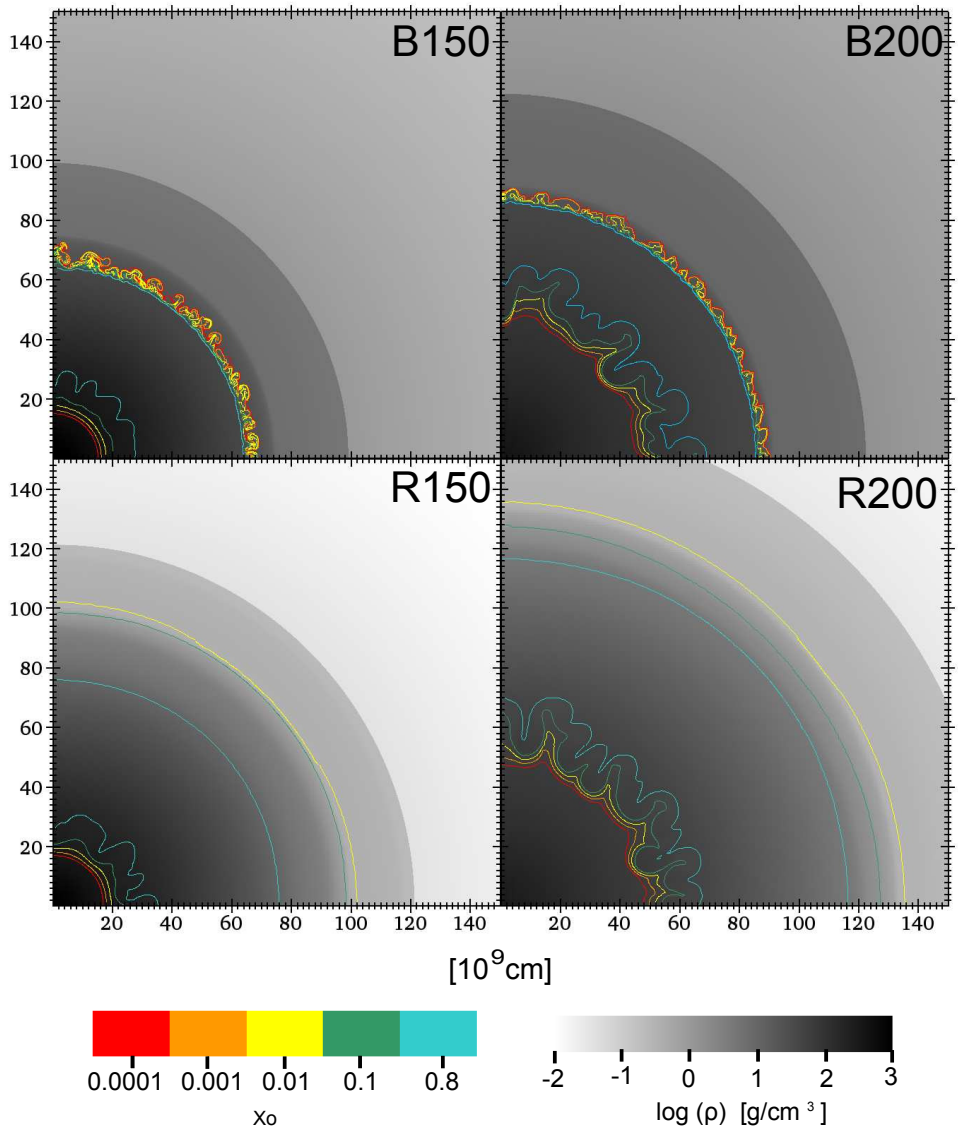

Figure 4.4: Density and oxygen-mass fraction. The snapshots are taken at 120 sec after the shock launches. At this time, no further burning is happening, and the newly synthesized ^{56}Ni then starts to decay and dumps energy into the ejecta. All the models show mild structure at the lower boundary of the oxygen-burning shell because of relic burning and dynamical instabilities. For B models, there are some fluid instabilities (colorful contours) appearing at the upper boundary of the oxygen-burning shell. The pattern of fluid instabilities is more obvious in the oxygen-mass fraction than in the density.

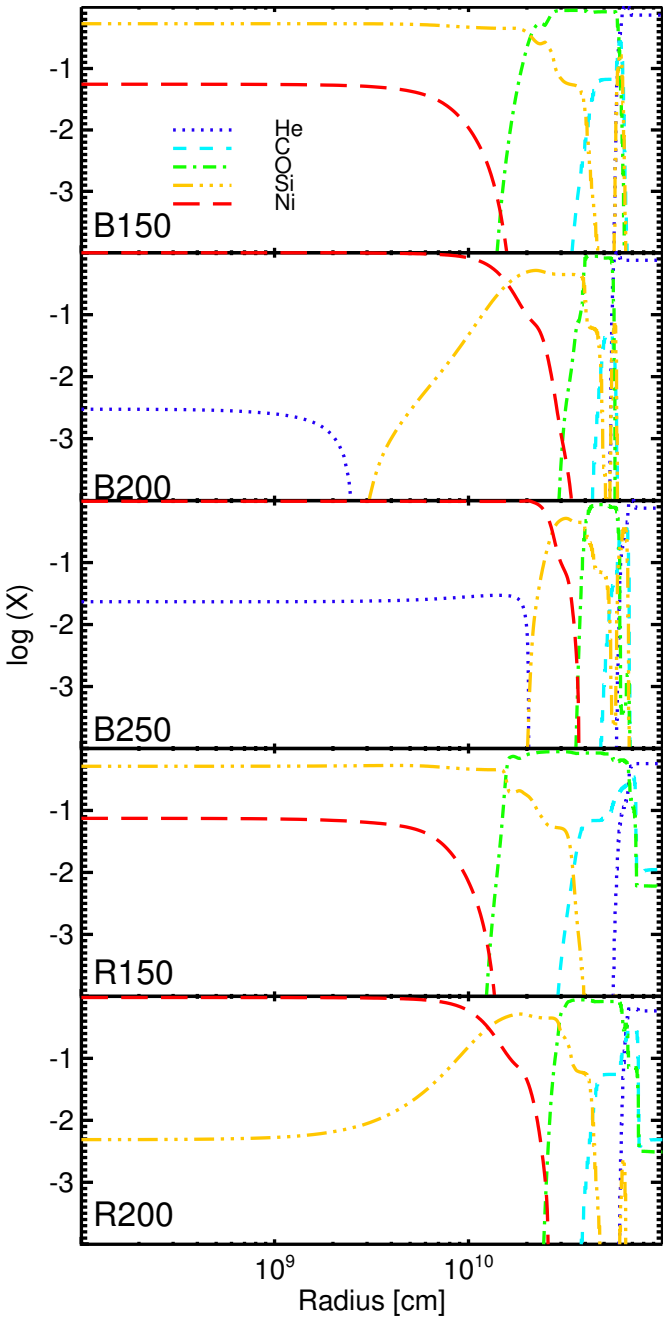

Figure 4.5: Elemental abundance patterns when the burning is already finished. The models of more massive stars produce more ^{56}Ni and have thinner oxygen-burning shells. For B200 and B250, there is some ^{4}He appearing at the inner part because of the photo-disintegration of ^{56}Ni during the explosive burning of ^{28}Si.

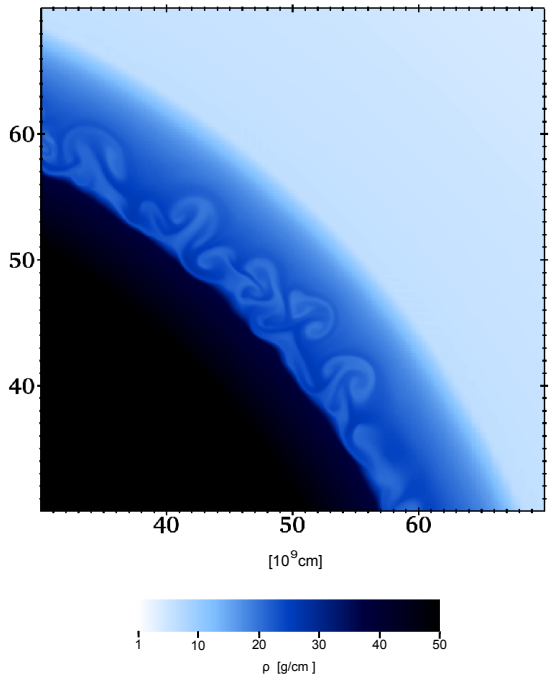

Figure 4.6: Closeup of fluid instabilities created by shock burning. The fluid instabilities at the upper boundary of the oxygen-burning shell of B150 in Figure 4.4. The fluid instabilities are driven by ^{4}He burning inside the post-shocked region, which have led to a mild mixing.

Once the shock runs into the hydrogen envelope, it is decelerated by the snowplowing mass ahead of it. We find emergent fluid instabilities, as shown in outer part (green contours) of Figure 4.7 and their close−up shown in Figure 4.8(a). Those instabilities are caused by the RT instabilities (Chandrasekhar, 1961). For the incompressible fluid, the RT instability happens when

$$\frac{\mathrm{d}P}{\mathrm{d}r}\frac{\mathrm{d}\rho}{\mathrm{d}r} < 0, \tag{4.1}$$

where P is the pressure and ρ is the density of the fluid. For a strong adiabatic shock traveling in the region where density follows a power law, the problem becomes self-similar, and any quantities in the problem can be expressed by a function, $f_w(A, E, t)$, defined by parameters of density, $\rho = Ar^w$; explosion energy, E; and time, t (Sedov,

1959; Herant and Woosley, 1994). Through dimensional analysis, the shock velocity has the form

$$V_s = A^{\frac{-1}{(5+w)}} E^{\frac{1}{(w+5)}} t^{\frac{-(w+3)}{5+w}}. \tag{4.2}$$

The evolution of shock velocity depends on w of the density profile. As $w = -3$, the shock velocity is independent of time. As $w < -3$, the shock is accelerated because the hot and high pressure material behind the shock dominates. As $w > -3$, the snowplow of material overtaken by the shock becomes dominating so that the shock slows down. The slow-down information is communicated to the fluid behind by the shock with sound speed, and it sets up a pressure gradient in the direction that the material was decelerated. The sound wave generated by the deceleration of the explosion shock can steepen this pressure gradient, then a reverse shock forms. A reverse shock actually travels outward in the spacial coordinate but inward in the mass coordinate. In Figure 4.8(b), we show the velocity profiles of models when the shock enters the hydrogen-rich envelope. R models demonstrate clear evidence of reverse shock formation. In contrast, the B models show no evidence of reverse shock. When the direction of the density gradient is opposite to that of the pressure gradient, the RT instability develops. The formation of reverse shock can be measured by ρr^3 based on Equation 4.2. In Figure 4.9, the R models have relatively more massive and extensive hydrogen envelopes than the B ones, which favors the formation of reverse shock and steepens the pressure gradient, leading to more mixing.

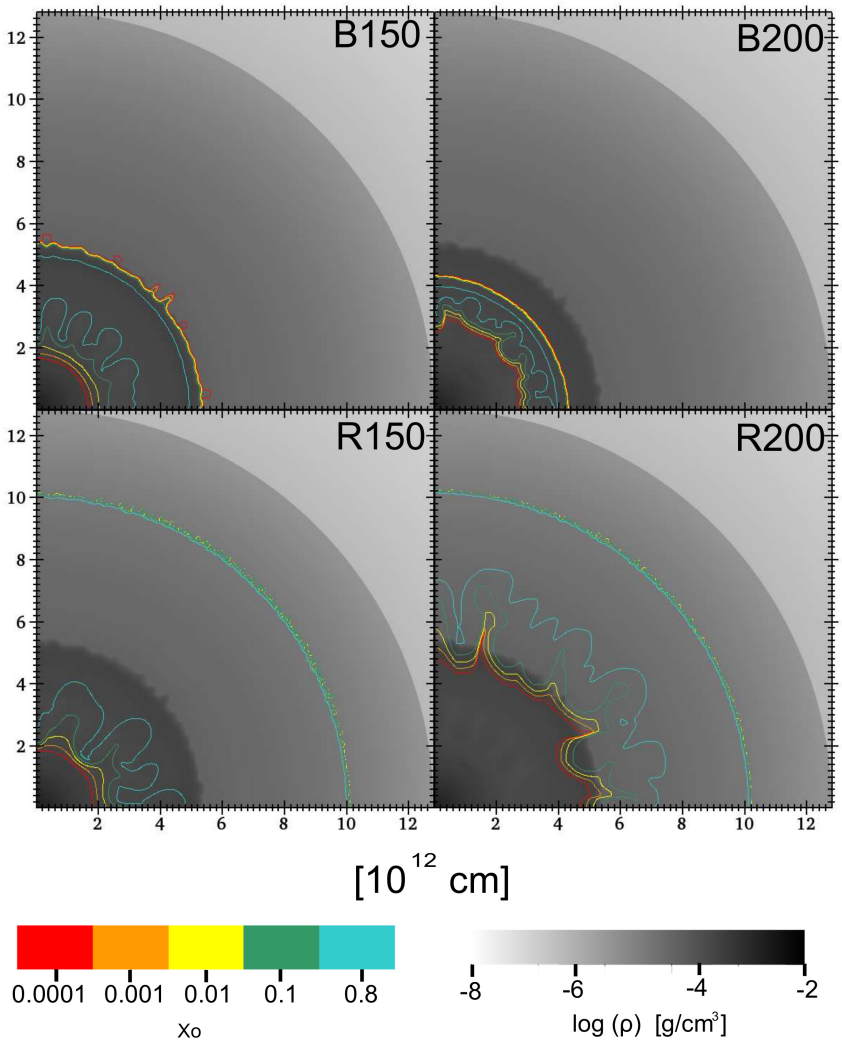

Figure 4.7: Density and ^{16}O mass fraction. The snapshots are taken at the time when the shock enters the hydrogen envelope. For R models, the strong reverse shock has formed to help develop the RT instability showing at the outer ring (green contour). The inner domains evolve as homological expansions but will later be affected by the growing fluid instabilities.

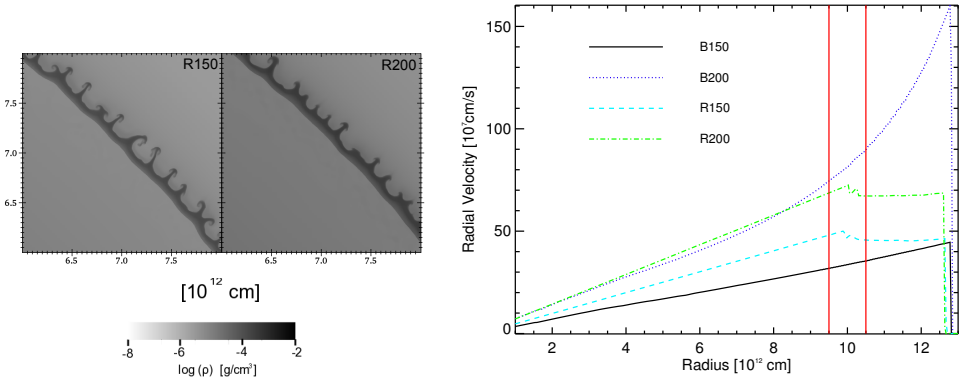

Figure 4.8: (a) Close-up of RT fingers. Fluid instabilities driven by RT first evolve linearly and form as fingertips. Soon they evolve into nonlinear models and become complicated structures. (b) Radial profiles of shocks. Once the forward shock runs into the hydrogen envelope, the region between the two red lines indicates the location of reverse shocks.

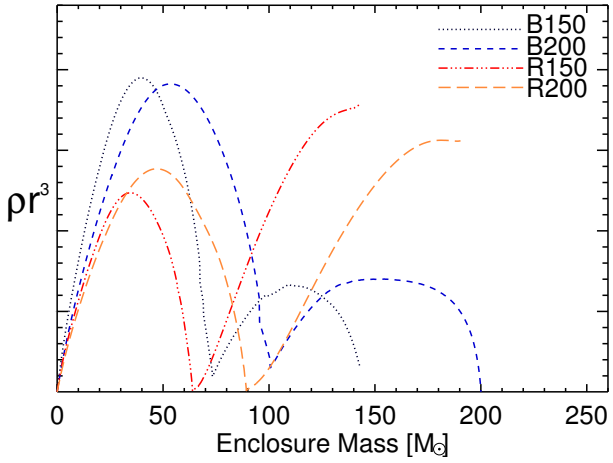

Figure 4.9: ρr^3 of initial models. The *y-axis* is in an arbitrary unit. For each model, there are two bump features. The first one presents the helium core; the other represents the hydrogen envelope. The R models have an extensive envelope, so they produce a bigger second bump than the B models do.

The fluid instabilities driven by the reverse shock formation can evolve until the shock breaks out from the stellar surface. As shown in Figure 4.10, the fluid instabilities of R models can become turbulent and lead to significant mixing of ejecta. The reverse shock soon dies out when the forward shock runs into the extremely low-density region of the interstellar medium (ISM). Figure 4.11 shows there is no reverse shock formation after the breakout, and the ejecta inside the stellar radius achieve the homological expansion stage. We use a lower-density surrounding to mimic the interstellar media. The reverse shock quickly dies out due to the forward shock traveling into a very low density ISM; we can evolve the shock until it propagates to a radius about 10 times the stellar radius to make sure there is no further mixing. The fluid instabilities are now frozen. R models show a significant mixing; however, only minor mixing happens beyond the boundary of the ^{56}Ni sphere. This implies that we might not see the γ ray emission coming from ^{56}Ni in the decay of PSNe; instead the significant amount of energy from ^{56}Ni decay turns into the thermal energy of the ejecta, making longer-lasting light curves than those of other SNe.

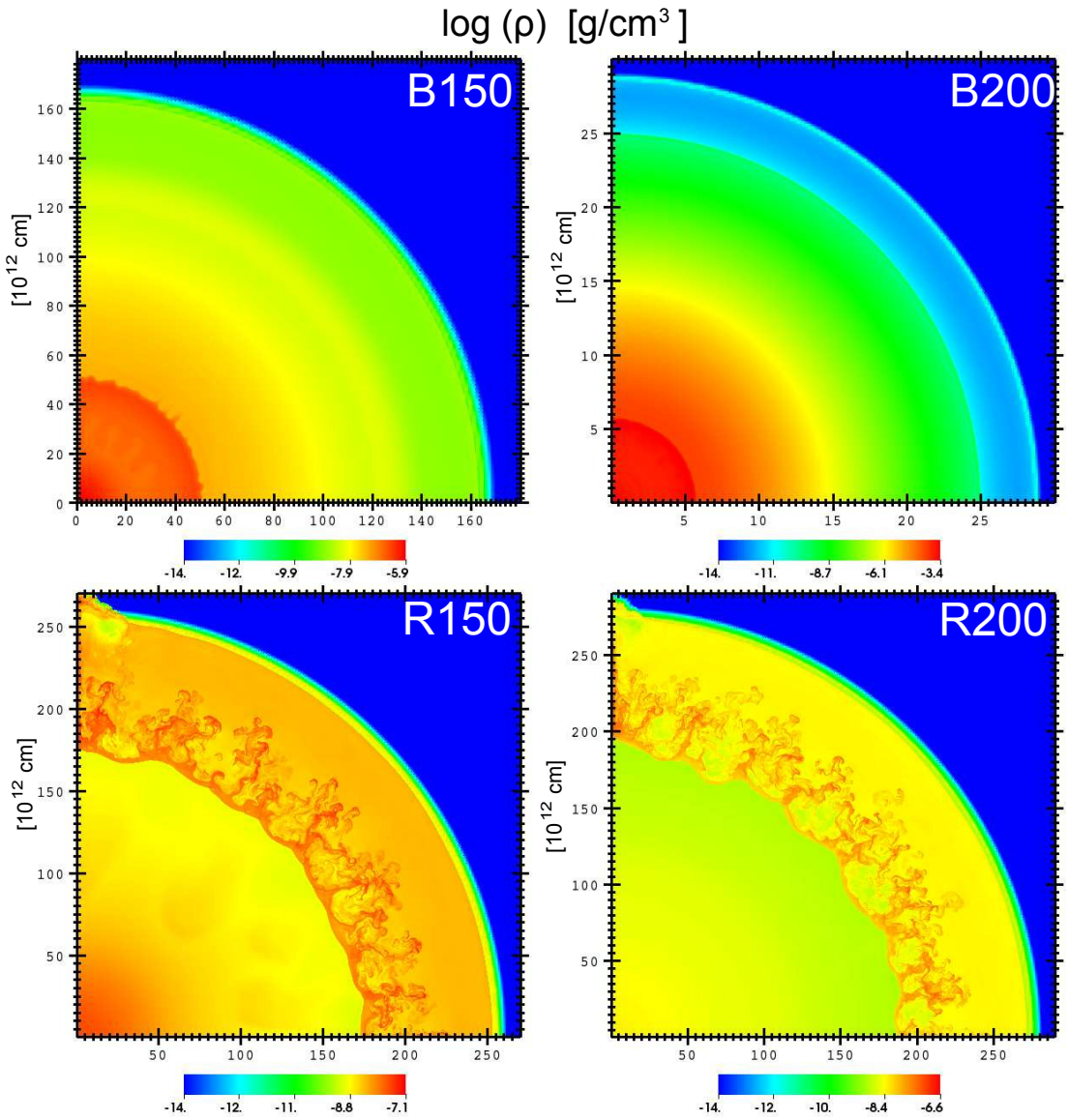

Figure 4.10: Density distribution before shock breakout. The fluid instabilities driven by the reverse-shock have evolved into large spatial scale and generated a significant mixing for R models. Once the shock breaks out from the stellar surface, the mixing stops abruptly.

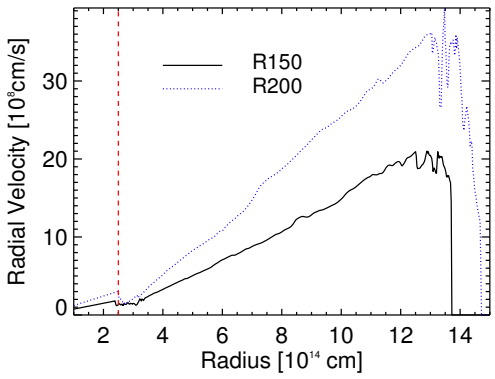

Figure 4.11: Radial velocity after the shock breakout. Now the shock has propagated to 1.5×10^{15} cm from the center of the original star. The density of the ISM is very low, about 10^{-4} times lower than the gas density of the stellar envelope, so the shock speed increases rapidly after breaking out from the stellar surface. Here we use a uniform density to mimic the ISM. The red-dashed line represents the original radius of the stars.

4.4 Discussion

During the core collapse, the pressure gradient points outward but the density gradient points inward, leading to the RT instability happening at the inner boundary of the oxygen-burning shells. Those instabilities occur for both B and R models and grow until the core bounce. The first instabilities are generated during the core collapse, which was mainly generated by dynamical instabilities and nuclear burning. Because the explosive ^{28}Si burning happens at the very center of the star, where the fluid instabilities cannot reach, there is no evidence of significant mixing of ^{56}Ni during the collapse. On the other hand, the burning time scale is short in comparison to the dynamical time scale. Fluid instabilities do not have time to grow big enough to generate mixing. The $200\,M_\odot$ models have more evolving instabilities than $150\,M_\odot$ ones because more massive stars have more compression of the core, favoring the growth of the fluid instabilities. We see less significant instability structures at the corresponding parts in the density than in elemental abundances such as ^{16}O because the gradient of isotopes is larger than the

density.

After the central oxygen/silicon burning finishes, a strong shock is launched, and this creates a discontinuous interface of temperature, density, and pressure when the shock just propagates into the helium envelope. The post-shock temperature is high enough to burn ^{4}He into ^{12}C, ^{16}O, and ^{56}Ni. The energy released from the helium burning creates a pressure gradient that is opposite to the density gradient as well as the elemental abundance gradient, which again leads to the RT instability, which is different from the normal fluid instabilities caused by the gradient of physical quantities and the pressure gradient, as mentioned above. The fluid instabilities here can mix the fuel into hot ashes then quickly burn the fuel, which enhances the pressure gradient and leads to more mixing. This positive feedback makes the fluid instabilities grow rapidly into turbulence in a very short time scale. About 100 sec after the core bounces, the post-shock temperature has dropped below 2×10^{8} K, and no more nuclear-burning-driven RT instability happens hereafter; the fluid instabilities then stop evolving until the reverse shock starts to form. ^{56}Ni has been synthesized through silicon burning, which is located at the innermost core of the stars. No fluid instabilities are able to mix ^{56}Ni at the earliest stage of explosion. Only mild mixing of ^{16}O, ^{12}C, and ^{4}He has been found in the oxygen-burning shells at this moment.

For red progenitors, when the shock propagates into the helium envelope, the reverse shock starts to grow the fluid instabilities, which generates a significant mixing. The mixing lasts until the shock propagates out of the stellar surface. In Figure 4.12, the wiggles of the abundance patterns are caused by the mixing, mostly contributed by the reverse-shock-driven instabilities. ^{16}O, ^{24}Mg, ^{28}Si, etc. in red progenitors have been transported from the inner to outer areas of the mass coordinate. There is only minor mixing of ^{12}C and ^{16}O caused by the burning stage of explosion in blue progenitors.

Our simulations show that the fluid instabilities of PSNe during the explosion stage can trigger the mixing of ejecta. The major mixing of PSNe seems to be driven by reverse shock similar to Type II supernovae (Chevalier, 1976; Fryxell et al., 1991; Herant and Woosley, 1994). The explosive burning during the collapse is less favored for developing the fluid instabilities due to the stellar structure. The mixing of PSNe is not as significant as the collapse of SNe from primordial stars with masses $15-40\,M_{\odot}$ (Joggerst et al., 2010). There might be more mixing if one starts the simulation right after the pair

instabilities happen or if one uses 2D presupernova models as initial conditions. However, without strong driving mechanics for the fluid instabilities, no additional mixing during the explosion can be expected.

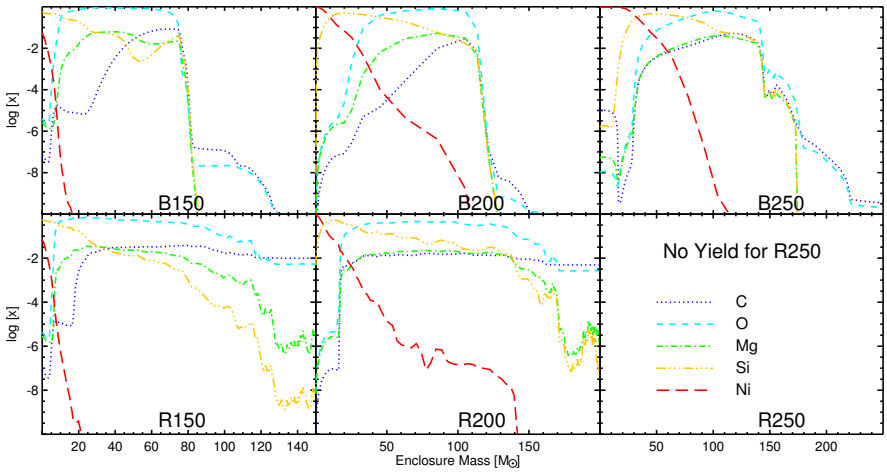

Figure 4.12: Elemental abundance patterns after the shock breakout. Now the shock has traveled to ten times the original stellar radius. No further mixing occurs at this time. For R models, the mixing driven by fluid instabilities has dragged inner heavier elements to the outer envelope of the stars.

4.5 Conclusions

We present the results from the 2D simulations of pair-instability supernovae, considering the nuclear burning, hydrodynamics, and new numerical approaches discussed in Chen et al. (2012). It is the first campaign to simulate PSNe starting with pre-supernova progenitors in two dimensions. Our simulations completely model the explosive burning and follow the explosion until the fluid instabilities cease evolving. A large amount of ^{56}Ni is made—up to 30 $M_\odot$. The amount of ^{56}Ni produced through ^{28}Si burning depends on the masses and types of the progenitors. During the contraction of the oxygen core, fluid instabilities are observed at the inner part of the oxygen-burning shell. However, those fluid instabilities are not deep enough to affect the ^{56}Ni production. No mixing of ^{56}Ni is found at this time. After the core bounces, the burning-driven fluid instabilities

occur at the outer boundary of the oxygen-burning shell due to the helium burning. The short growing time of fluid instabilities only allows slight mixing of intermediate elements within about 100 sec of the core bouncing.

For the red supergiant progenitors, when the shock propagates into the helium and hydrogen envelope, the fluid instabilities start to evolve because the formation of reverse shock leads the RT instability. The reverse shock dies out when the shock breaks out of the stellar surface. The fluid instabilities are significant enough to distort the spherical symmetry of the stars. The ejected oxygen-burning shell mixes with the surrounding metals, helium, and hydrogen. Although the outer edges of the ^{56}Ni-rich areas are slightly affected by the reverse-shock-driven fluid instabilities, the detection of γ ray emission is still unlikely for PSNe. Reverse-shock-driven fluid instabilities for blue supergiants are relatively weaker. Non-shelled ejecta of the blue supergiants are mostly from the fluid instabilities generated in the phase between onset of collapse and the onset of explosion.

Chapter 5

Impact of Rotation on Pair-Instability Supernovae

Recent study of Pop III stars suggests that the first stars could be born with a rapid rotation, and rotation within stars can impact their evolution and their SN explosion. In this chapter, we use `CASTRO` to investigate pair-instability supernovae (PSNe) considering the rotation. We perform a series of 2D calculations to investigate the impact of rotation at the explosion phase of PSNe. Simulations show that rotation results in an aspherical explosion caused by anisotropic collapse. In the case of a 50% critical rotation rate of the oxygen core, the ^{56}Ni production can be reduced by two orders of magnitude. An extreme case of a rate of 100% shows an interesting feature of overshooting along the equatorial direction caused by non-synchronized ignitions of explosion, so that shocks run into the infalling gas and generate Richtmyer−Meshkov instability.

5.1 Fate of Very Massive Rotating Stars ($150\,M_\odot \leq M_* \leq 260\,M_\odot$)

As we discussed in the previous chapter, the Pop III stars with masses of $150 - 260\,M_\odot$ could have died as energetic PSNe. However, these models do not include rotation in the simulations. In the real world, the processes of star formation usually endow a certain amount of angular momentum to the star and make it rotate. The rotational rates of massive stars are still poorly understood in both theoretical and observational aspects. Rotation can affect the stellar evolution as well as the supernova explosion.

The nucleosynthesis inside the stars changes due to the rotational mixing, so that the chemical composition of the star changes. If heavy elements are mixed out of the envelope of the stars, stellar wind can enhance the process by metal-driven lines. Strong wind would reduce the stellar mass dramatically, and then the helium core, eventually changing the fate of the stars. Studies of the stellar evolution of very massive stars that include rotation that have been published by Glatzel et al. (1985); Maeder and Meynet (2000); Heger et al. (2005); Hirschi (2007); Ekström et al. (2008). The recent results from Chatzopoulos and Wheeler (2012); Yoon et al. (2012) show that rotation can lower the mass criterion for PSN progenitors because mixing facilitates helium burning, resulting in a more massive oxygen core. The rotation rate for very massive stars or Pop III stars is poorly understood. Simulations by Stacy et al. (2011) suggest that the Pop III stars could rotate very fast, up to 50 % of keplerian rate at the surface. If such a high rotation does exist, it can affect the evolution of the stars and their supernovae. Multidimensional models of PSNe that include rotation are missing in the literature. We perform the first 2D models considering rotation to simulate PSNe and investigate how rotation impacts the explosive burning; we explore energetic SNe and nucleosynthesis during the explosion in the context of multidimensional simulations that simulate the fluid instabilities from first principles.

The structure of the chapter is as follows: we first describe our numerical approaches and setup in § 5.2. Then we present the results and discuss the how the fluid instabilities evolve during the explosion in § 5.3. Finally, we conclude and summarize our findings in § 5.4.

5.2 Methodology & Problem Setup

The self-consistent, multidimensional stellar evolution models from the main sequence to SN explosion are still unavailable because of the current limitations of computational power. Instead, we start simulating the stars using `KEPLER` (Weaver et al., 1978; Heger et al., 2001), a 1D spherically-symmetric Lagrangian code, and follow the evolution of stars up to $20-100$ seconds before the maximum compression of the core. Then we map the resulting 1D profiles from `KEPLER` onto 2D grids of `CASTRO` as the initial conditions. We then apply our differential rotation models and follow up the simulations until the

explosive burning ceases when the shock has been successfully launched. This setup is designed to catch the most important features of the supernova explosion in 2D with practical computational resources. In this section, we introduce our progenitor models, problem setup, and numerical methods.

5.2.1 Progenitor Models

We use progenitor stars of $150\,\mathrm{M}_\odot$, $200\,\mathrm{M}_\odot$, and $250\,\mathrm{M}_\odot$ with very little overshooting at the late-time evolution. These stars eventually become blue supergiants. Physical properties of these stars are listed in Table 5.1. We follow the 1D stellar models before most of the explosive burning is about to happen. Similar to the setup of previous chapters, the resulting 1D profiles are then mapped onto 2D cylindrical grids of `CASTRO` using a conserving mapping algorithm based on Chen et al. (2012). All progenitors are simulated by using three different rotation rates. In `CASTRO`, we use the 19 isotopes reaction network, which precisely models the explosive carbon, oxygen, and silicon burning of PSNe. For the EOS, we use the Helmholtz equation of state (Timmes and Swesty, 2000) and monopole approximation to compute the gravitational field.

Name	M_*	M_{He}	ρ_{c}	T_{c}	R
	$[\mathrm{M}_\odot]$	$[\mathrm{M}_\odot]$	$[10^6\mathrm{g\,cm^{-3}}]$	$[10^9\,\mathrm{K}]$	$[10^{13}\,\mathrm{cm}]$
B150	150	67	1.40	3.25	16.54
B200	200	95	1.23	3.31	2.86
B250	250	109	1.11	3.34	23.06

Table 5.1: M_*: initial stellar mass; M_{He}: helium core mass at collapse; ρ_{c}: central density at collapse; T_{c}: central temperature at collapse; and R: stellar radius.

In `CASTRO` simulations, care is taken to resolve the key elements of the explosion, catching the shock front and potential mixing of isotopes driven by fluid instabilities. The grid structure for 2D simulations uses 256×512 with three levels of a factor of 4 refinement to resolve a domain of $(4 \times 10^{11}) \times (8 \times 10^{11})\,\mathrm{cm}^2$. This setup can resolve burning and the structures of fluid instabilities of rotating PSNe. The AMR criteria are

set for gradients of density and velocity, and pressure over-gradient zones are automatically substituted by finer zones. 2D CASTRO uses a cylindrical coordinate R-Z. Z is set as the rotation axis. The lower boundary of R uses reflect conditions to prohibit fluid from entering; the remaining boundaries use outflow conditions that allow the fluid to freely cross over. We also lay out the nested zone structure to ensure that the inner core receives the highest spatial resolution at all times.

5.2.2 Rotation

We use a differential rotation mode by assuming non-uniform rates inside the stars. The inside of the oxygen core is dense and compact, and it behaves like a rigid body. Outside the oxygen core, the structure of the helium and hydrogen envelope is much diluted, so we assume a constant specific angular moment extending from the edge of the oxygen core to the stellar surface. This creates a smoothly decreasing rotation rate when the distance from the rotational axis increases, as shown in Figure 5.1. Because massive stars usually develop a convective core that distributes the angular momentum homogeneously, it leads to a constant ω inside the core. To identify the radius of oxygen and the suitable rotation rate, we plot the oxygen abundance for our models in Figure 5.2(a). The most abundant oxygen is located at the radius between $10^9 - 10^{10}$ cm, which tells us that the outer boundaries of the oxygen core is about 10^{10} cm. In Figure 5.2(b), we calculate the critical rotation rates as a function of radius for our models. Our assumption of oxygen rotating as a rigid body seems to be very suitable for the model. The critical rotation rates for the model are about 0.5 sec^{-1}, which we use for our simulations.

We therefore assume a constant rotation rate inside the oxygen core and apply the rotation rate as the critical rate at the boundary of the oxygen core. Here we use 50% of critical rates. Outside the oxygen core, the structure of the helium and hydrogen envelope is much diluted, so we assume a constant specific angular momentum extending from the edge of the oxygen core to the stellar surface. This creates a smoothly decreasing rotation rate when the distance from the rotational axis increases. The rotation is governed by the angular momentum. In CASTRO, the angular momentum, j, provides a force term in the Euler equation for fluids and itself is evolved by an advect

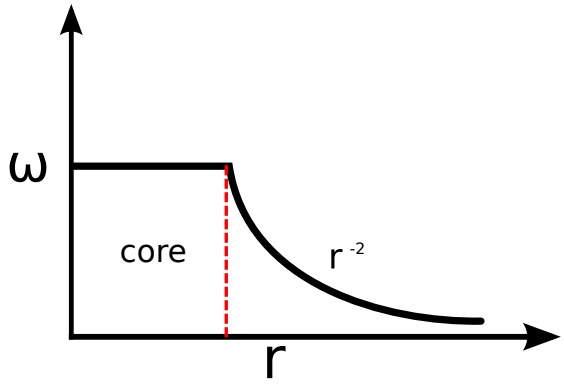

Figure 5.1: The illustration shows our differential rotation model. The ω inside the inner core ($r \leq r_c$) is assumed to be a constant. Once ($r > r_c$), ω decreases as r^{-2}, we assume a specific angular j constant.

equation:

$$\frac{\partial(\rho \mathbf{u})}{\partial t} = -\nabla \cdot (\rho \mathbf{u}\mathbf{u}) - \nabla p + \rho \mathbf{g} + \mathbf{F}_c, \tag{5.1}$$

$$\frac{\partial(\rho j)}{\partial t} = -\nabla \cdot (\rho \mathbf{u} j). \tag{5.2}$$

Here $\rho, \mathbf{u}, \mathbf{g}$ are the density, velocity vector, and gravitational vector, respectively. $\mathbf{F}_c$ is the centrifugal force generated by j, the angular momentum per unit mass. j is initialized at the beginning of the simulations then evolved with fluid elements in the advected equation as above.

5.3 Results

After the onset of the 2D `CASTRO` simulation, the rotating 200 $M_\odot$ star starts to collapse due to the dynamical instabilities of the core. In contrast to the non-rotating case, the collapse of the star becomes anisotropic. Rotation now provides a centrifugal force to resist the collapse. Because of centrifugal force, $\mathbf{F}_c \propto r_z \omega^2$, where r_z is the distance to the Z axis, the oxygen core receives a stronger $\mathbf{F}_c$ along the equator than it does along the pole, which leads to anisotropic compression of the core and the explosion. The maximum compression happens along the pole and yields strongest explosion and

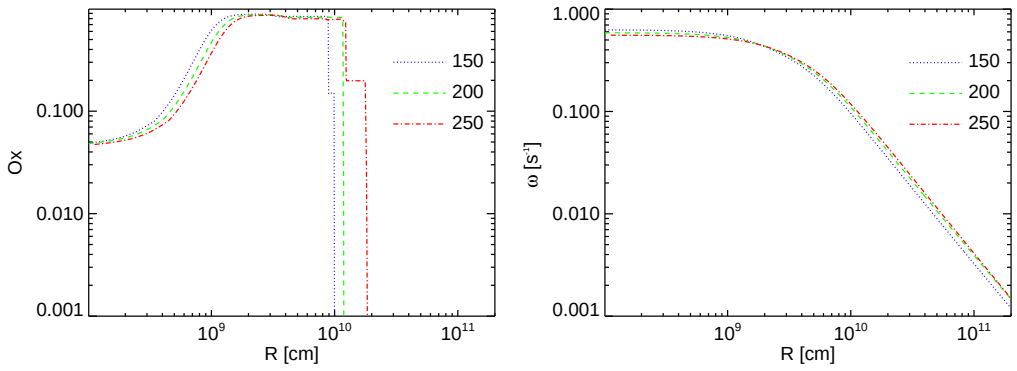

(a) Size of oxygen core for progenitor stars (b) Keplerian rotational rates

Figure 5.2: (a) The size of the oxygen cores of presupernovae can be identified by their oxygen abundance. (b) The critical ω as a function radius. The curve of ω behaves like a plateau inside the oxygen core, then decreases as r increases.

releases the shock wave. The core is ejected in an elliptical shape. Figure 5.4 shows the post-explosion of non-rotating (the left half) and rotating models (the right half). Both results are shown at the same evolving time in `CASTRO` simulations. The non-rotating model shows a stronger shock wave, and the oxygen shell demonstrates some mixing at the inner part; oxygen-burning shells are ejected. The rotating model, however, shows a relatively weaker shock caused by a weaker explosion; the inner oxygen-burning shells are distorted into ellipse shapes and show no mixing. Although the shock of the rotating model has been launched, the weaker explosion energy is ejected slowly. One key isotope is synthesized during the PSNe: ^{56}Ni emerges from the explosive ^{28}Si burning. The amount of ^{56}Ni produced can determine whether the PSNe is a brighter or a fainter SNe. In Figure 5.4, we show the corresponding ^{56}Ni abundance and gas density. ^{56}Ni has been synthesized in the non-rotating model (left half). Unexpectedly, there are no ^{56}Ni contours present in the rotating model. The detailed calculations of the model show only a trace of $10^{-3}\,M_\odot$ ^{56}Ni has been produced during the explosion. However, the non-rotating model has synthesized about $6.57\,M_\odot$ ^{56}Ni.

What happens if the core of the massive star rotates close to a 100% critical rotation rate? To answer this question, we simulate a $200\,M_\odot$ of a 100% keplerian rate at the

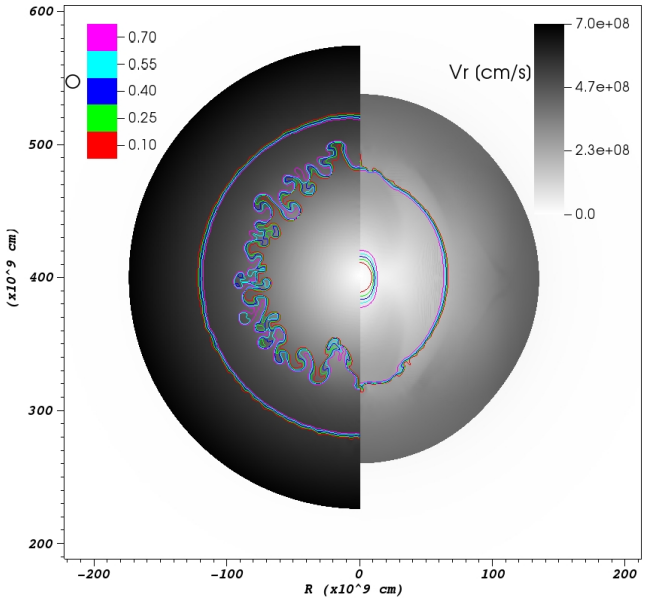

Figure 5.3: Comparison of rotating and non-rotating models from a 200 $M_\odot$ star. The left-side sphere is the non-rotating model, and the right side shows the rotating model of $\omega \sim 50\%$ critical rotational rate of the oxygen core. The color coding shows the radial velocities V_r, and the color contours are the ^{16}O mass fraction. Both snapshots are taken at the same time, about 200 sec after the onset of the explosion.

oxygen core. The anisotropic compression becomes ever stronger than the 50% case. The eclipse shape of the ejected core has an even larger eccentricity. One interesting fluid instability has been found in the carbon-burning shell, which is shown in Figure 5.5. The carbon shell breaks along the equator and overshoots some carbon into the oxygen core. This overshooting develops strong fluid instabilities. Since the explosion is anisotropic, the shocks are initialized at different times in different directions: the pole comes first, and the equator comes last. In this fast-rotating model, the shock from the pole has been sent out, but the gas along the equator is still collapsing. Once the shock runs into the collapsing gas, the Richtmyer−Meshkov (RM) instability (Brouillette, 2002) starts to develop. Mixing caused by RM instability drives carbon deep into the oxygen-rich envelope.

5.4 Conclusions

Stellar rotation plays a key role in both stellar evolution and the fate of the very massive stars, making them ideal candidates for Pop III stars. The nature of the rotation can be traced back to the formation of the stars, which endowed the star with angular momentum. The definite rotation rates for these massive stars are still unknown. Results of star formation suggest a high rotation rate is 50% of its break-up rate. We present the results of our study on the impact of rotation on PSNe using different rotational models. The 200 $M_\odot$ of a 50% critical rate demonstrates the onset of an anisotropic explosion in which ^{56}Ni production is strongly reduced. If this does, in fact, apply for PSN progenitors, massive ^{56}Ni production shown in previous PSN models may become incorrect. The luminosity of PSNe can be significantly attenuated. An extreme case of a 100% rate shows an interesting feature of overshooting along the equator caused by non-synchronized ignitions that send shocks into the infilling gas.

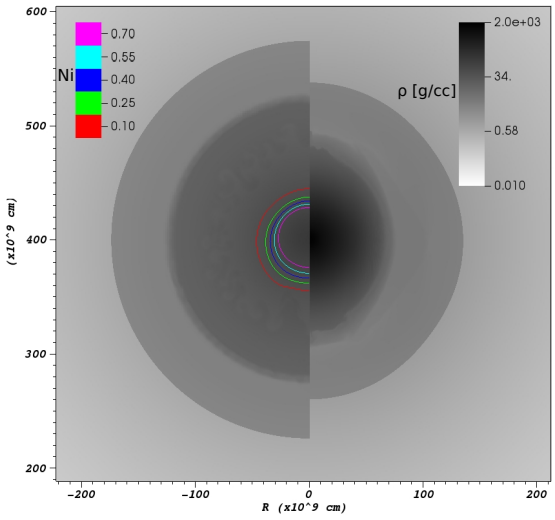

Figure 5.4: Comparison of rotating and non-rotating models from a 200 $M_\odot$ star. The left-side sphere is the non-rotating model, and the right side shows a rotating model of $\omega \sim 50\%$. The color coding shows the density, and the color contours are the ^{56}Ni mass fraction. Both snapshots are taken at the same time, about 200 sec after the onset of the explosion.

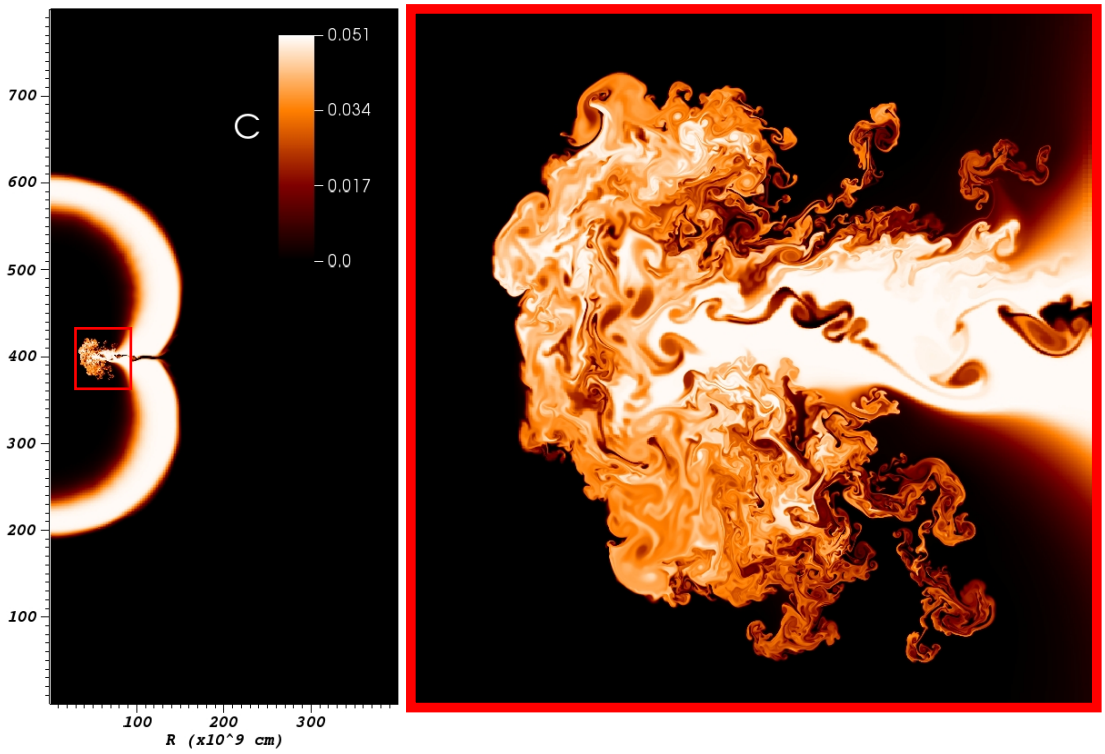

Figure 5.5: Hot-color shows the mass fraction of ^{12}C. Strong fluid instabilities occur during the explosion along the equator shown in the red box of the left panel; its close-up appears in the right panel.

Chapter 6

Pair-Instability Supernovae in the Local Universe

Although the first stars are promising progenitors for PSNe, observational evidence suggests that a few present-day stars can be massive enough to die as PSNe too. With collaborators, we study the PSNe from the local Universe. We perform 2D CASTRO simulations of a PSN from a progenitor star of $500\,\mathrm{M}_\odot$ with metallicity of $0.1\,Z_\odot$. The results suggest very little mixing for this PSN because metals inside the stellar envelope can create a strong stellar wind that strips the star's hydrogen envelope. When the stars die as PSNe, the reverse shock cannot form and develop the fluid instabilities. There is only a mild mixing caused by burning at the onset of the explosion.

6.1 Fate of Very Massive Stars of Non-Zero Metallicity

The detection of a pair-instability supernova candidate, SN 2007bi (Gal-Yam et al., 2009), has brought increasing attention about PSNe and posed a challenge to theories of galactic star formation. The formation of such a massive progenitor star with metallicity of $0.1\,Z_\odot$ is very unclear. In the case of $0.1\,Z_\odot$ stars, they could easily lose much of their mass over their lifetimes through strong stellar winds so that they need to form at even more massive volumes before they evolve into PSN progenitors. Understanding the observational signatures of PSNe at near-solar metallicities is key to identifying and properly interpreting these events as more are discovered. So far, PSN models have

focused on Pop III stars. Although their simulations are of zero-metallicity Pop III progenitors, it is interesting to investigate PSNe of metallicity in the local Universe.

The structure of this chapter is as follows: we first describe our numerical approaches and initial presupernova models in § 6.2. Then we present the results in § 6.3, and our conclusions are given in § 6.4.

6.2 Methodology & Problem Setup

Our initial model uses a $500\,M_\odot$ star of $0.1\,Z_\odot$ that is evolved using the `GENEVA` stellar evolution code (Hirschi et al., 2004). This model considers both mass loss and stellar rotation to calculate the resulting mass loss and mixing. The initial rotational velocity uses 40 % of critical rotation, corresponding to an equatorial velocity of 450 km/sec at the surface. The evolution of the progenitor star is followed until the onset of explosive oxygen burning, just a few tens of seconds before maximum compression (bounce) of the core. Then we map the resulting one-dimensional profiles onto 2D grids as the initial conditions for `CASTRO`. At this time, the explosive burning is about to occur, which is the promising phase of emergent fluid instabilities. Similar to our previous setup, we set up our 2D grids for `CASTRO` as 256×256 with three levels of a factor of 4 refinement to resolve the physical size of entities embedded in a domain about $10^{11} \times 10^{11}\,\mathrm{cm}^2$. Because the characteristic length for catching burning is about 10^8 cm, this setup is sufficient to resolve the burning scale. AMR criteria use the gradients of density, velocity, and pressure. Once the adjacent zones reach a gradient larger than the criteria we set, new finer grids are automatically created and patched over previous zones. Because we simulate only one hemisphere of the star, boundaries along the Z-axis and R-axis use reflect boundary conditions that prevent fluid from entering; the upper boundaries apply the outflow conditions that fluid can freely move across. The finer grid structure is nested hierarchically around the core of the star and assures that the core constantly has the highest resolution. Because spherical symmetry is still a good approximation for our problem, the gravitational field is calculated using a monopole approximation based on constructing a radial average of the density from 2D density on the grid. We evolve the 2D `CASTRO` simulations until the shock breaks out from the stellar surface.

6.3 Results

The 0.1 $Z_\odot$ 500 $M_\odot$ star has been evolved until tens of sec before its core reaches its maximum compression. At this time, the mass of the star now becomes about 92.5 $M_\odot$ due to the mass loss driven by stellar winds, and it becomes an oxygen-rich core. Figure 6.1 shows the isotope abundance of helium, carbon, oxygen, and silicon. Strong mass winds not only remove the hydrogen envelope but also strip the outer part of the helium core. The central temperature and density are 3.31×10^9 K and 1.24×10^6 g cm^{-3}, and the core experiences dynamical instability. The runaway collapse is about to happen. Similar to that of PSNe with zero-metallicity, the explosive oxygen burning drives the explosion and releases the energy of 3.33×10^{52} erg, and synthesizes 3.63 $M_\odot$ ^{56}Ni. Since the explosive burning can be a promising site for producing fluid instability, in Figure 6.3, we plot the oxygen-mass fraction and the size of the ^{56}Ni core about 20 sec after the explosion. The entire star is unbound and moderate burning instability appears at the inner boundary of the oxygen shell, mixing caused by these fluid instabilities is very limited. The distribution of ^{56}Ni is marked by the red contour of the ^{56}Ni mass fraction equal to 0.1. The newly synthesized ^{56}Ni maintains an almost spherical symmetry.

Since the size of the star is only about 4×10^{10}cm, it takes less than 30 sec from the onset of explosion to shock breakout. Figure 6.4 shows a snapshot of when the shock breakout is about to occur. The density map shows that the supernova still keeps a spherical symmetry. The out-going velocity vectors demonstrate that the entire star is unbound. To look into the ejecta, we plot the oxygen-mass fraction by using a contour plot. No mixing has been found by searching for distorted shells. Both explosion and shock propagation phases do not show prominent signs of mixing of SN ejecta by fluid instabilities. ρr^3 provides a good indicator of possible reverse shock. Figure 6.2 shows the ρr^3 in the mass coordinate of the model, showing a single bump in the plot; we also marked the position where the shock is initialized. The shock barely slows down while traveling into the bump, which is composed mainly of oxygen.

6.4 Conclusions

The formation of such a massive star of 500 $M_\odot$ with $Z = 0.1\, Z_\odot$ can challenge the theory of present-day star formation. One of the promising sites for such massive stars

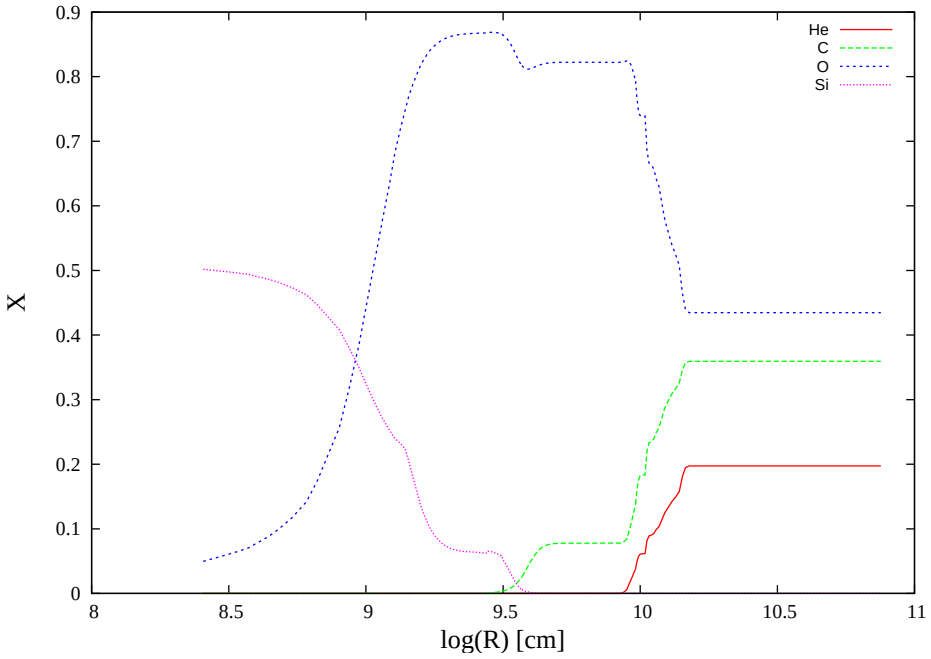

Figure 6.1: Elemental abundance of presupernova progenitor. The hydrogen envelope has been removed due to mass loss by winds and rotation.

formation is inside the dense star clusters, in which stars can merge through collision and result in very massive stars of mass around several hundred $M_{\odot}$. These non-zero metallicity PSNe may be look similar to blue progenitors, as we discussed in Chapter 4. For this model, it is similar to a $200\,M_{\odot}$ PSNe from the Pop III star.

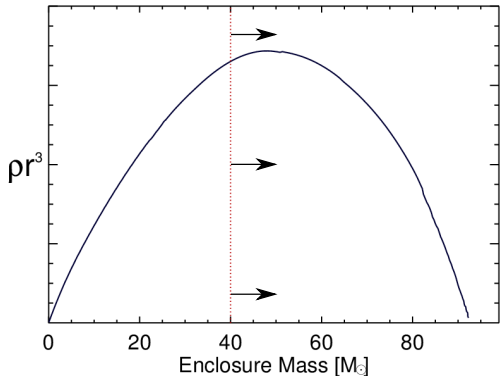

Figure 6.2: ρr^3 plot of model: The *y-axis* is in an arbitrary unit. There is only one bump feature, which is created by the oxygen-burning shell. The red dashed line indicates the approximate location where the shock begins. The shock only propagates through a short distance of uphill of the curve, so it is not likely to decelerate much and create a reverse shock, which would develop fluid instabilities.

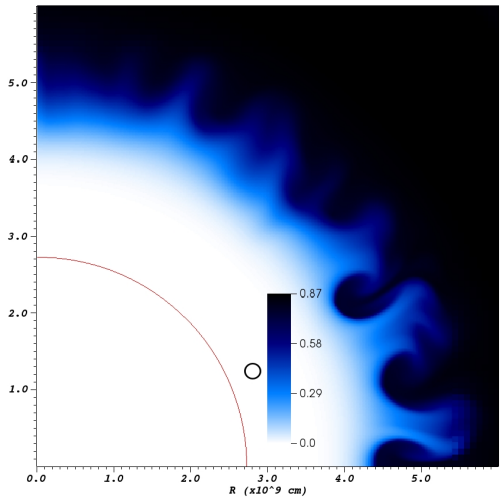

Figure 6.3: Burning instabilities of $0.1\,Z_{\odot}$ PSNe. Color coding presents the oxygen abundance and the red line indicates ^{56}Ni mass fraction equaled to 0.1. The inner part of the oxygen-burning shell shows a mild mixing during the explosion phase but it does not dredge up ^{56}Ni.

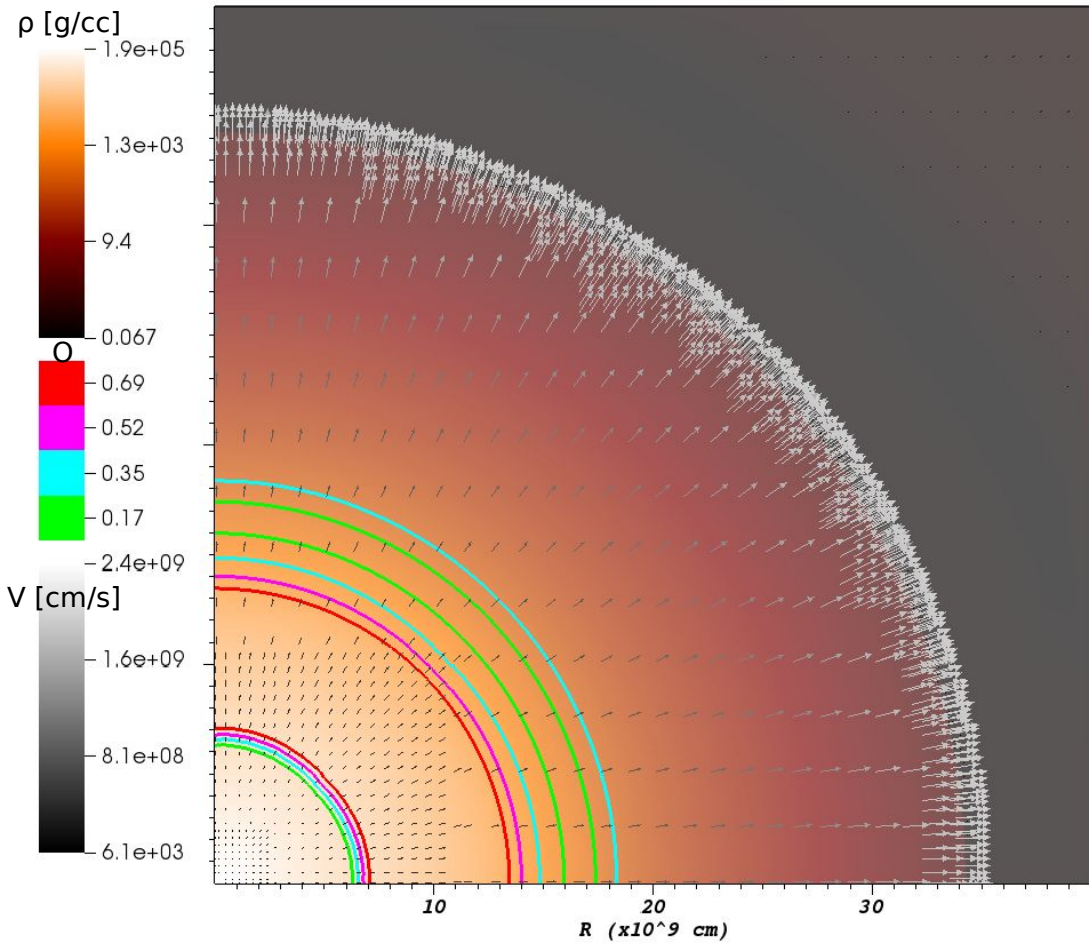

Figure 6.4: Snapshot before the shock breakout. The image contains three physical quantities: density (hot-color), oxygen abundance (contours), and velocity fields (gray vectors). The SN shows a fairly spherical symmetry, and no evidence of visible mixing is present.

Chapter 7

An Exploding Supermassive Star of $55,500\,M_\odot$

By considering the rotation and metallicity effects for PSNe, we arrive at the question: What happens when extremely massive stars ($\gg 100\,M_\odot$) die? We document finding an extraordinary supernova of a $55,500\,M_\odot$ while investigating the properties of the first super massive stars (SMS). In this chapter, we present the results from 2D simulations of an exploding supermassive star with a mass of $55,500\,M_\odot$. SMS may be the candidates for forming the seeds for the supermassive black holes inside galactic centers. However, the formation of SMS and their evolution are not well understood. Previous studies suggested that SMS of masses above $300\,M_\odot$ eventually die as black holes. We found an unusual explosion of a SMS of $55,500\,M_\odot$ that implies a narrow mass window for exploding SMS, called General-Relativity instability supernovae (GSNe). GSNe may be triggered by the general relativity instability that happens after central helium burning and leads to a runaway collapse of the core, eventually igniting the explosive oxygen burning and unbinding the star. The energy released from the burning is large enough to reverse the implosion into an explosion and unbind the SMS without leaving a compact remnant. Energy released from the GSN explosion is about 10^{55} erg, which is about $10,000$ times more energetic than is typical of supernovae. The main yields of SMS explosions are silicon and oxygen; only less than $1\,M_\odot$ ^{56}Ni is made. The ejecta mixes due to the fluid instabilities driven by burning during the very early phase of the

explosion. The large amount of energy and metals released from GSNe can significantly impact their host environment.

7.1 Fate of Extremely Massive Stars III ($M_* \gg 100\,M_\odot$)

Results from observational and theoretical studies (Kormendy and Richstone, 1995; Ferrarese and Merritt, 2000; Ferrarese and Ford, 2005; Gebhardt et al., 2000; Beifiori et al., 2012; McConnell and Ma, 2013) suggest that a supermassive black hole (SMBH) resides in each galaxy. These SMBHs play an important role in the evolution of the Universe through their feedback. Like giant monsters, they swallow nearby stars and gas, and spit out strong x-rays and powerful jets (Rees, 1984; Di Matteo et al., 2005) that impact scales from galactic star formation to host galaxy clusters. Quasars detected at the redshift of $z \geq 6$ (Fan et al., 2002, 2006) suggest that SMBHs had already formed when the Universe was only several hundred million years old. But how did SMBHs form in such a short time?

Models for the formation of SMBHs in the early Universe have been extensively discussed by many authors: Loeb and Rasio (1994); Madau and Rees (2001); Bromm and Loeb (2003); Begelman et al. (2006); Johnson and Bromm (2007b); Bromm and Yoshida (2011). Rees (1984) first pointed out the pathways of forming SMBHs. One of the possibilities is through the channel of SMS with masses $\geq 10,000\ M_\odot$. They might form in the center of the first galaxies through atomic hydrogen cooling (Johnson et al., 2012). If SMS could form in the early Universe, they could facilitate SMBH formation by providing promising seeds. Although the mechanism of SMS formation is not clear, the evolution of SMS has been studied by theorists (Fowler, 1966; Wheeler, 1977; Bond et al., 1984; Carr et al., 1984; Fuller et al., 1986; Fryer et al., 2001; Ohkubo et al., 2006) for three decades. The cores of stars with masses over $100\ M_\odot$would first encounter the pair-creation instabilities after central helium burning, when the core reaches sufficiently high temperatures ($\sim 10^9$ K) at relatively low densities ($\sim 10^6\,\mathrm{g\,cm^{-3}}$), favoring the creation of electron-positron pairs (high-entropy hot plasma). The pressure-supporting photons turn into the rest masses for $e^-/\,e^+$ pairs and soften the adiabatic index γ of the gas below a critical value of $4/3$, which leads to a dynamical instability and triggers a rapid contraction of the core. During contraction, core temperatures and densities swiftly rise,

and oxygen and silicon burn explosively. As discussed in Chapter 4, the burning energy of massive stars of $150 - 260\,M_\odot$ turns the implosion into thermonuclear-explosion pair-instability supernovae (Barkat et al., 1967; Glatzel et al., 1985; Heger and Woosley, 2002; Kasen et al., 2011; Chen et al., 2011, 2012). Previous results (Fryer et al., 2001; Ohkubo et al., 2006) suggest that non-rotating stars with initial masses over $300\,M_\odot$ eventually die as black holes without supernova explosions. It is generally believed that the explosive burning is insufficient to revert the implosion because the SN shock is dissipated by the photo-disintegration of the heavy nuclei; thus, these stars eventually die as BHs without SN explosions. Previous calculations of SMS have been done using very crude resolution, and some of them ignore post-Newtonian correction of gravity , the first-order correction of the general relativity effect Zeldovich and Novikov (1971), that might play an important role in the evolution of stars of $1,000 - 100,000\,M_\odot$, especially during their pre-explosion phase. We perform a systematic study of Pop III SMS and their remnants with high resolution 1D simulations considering updated nuclear reaction rates (Heger et al., 2001; Heger and Woosley, 2002) and the post-Newtonian correction. An explosion of a $55,500\,M_\odot$ star is found; we report our results of this explosion by presenting its 1D stellar model and the 2D simulation of the explosion. Our finding implies a possible mass range at the high-mass end of stars that might die as SNe instead of collapsing into BHs, as previously thought.

The structure of the chapter is arranged as follows: we first describe our simulation setup and numerical approaches for evolving a $55,500\,M_\odot$ in § 7.2. Then we present the results of our 1D stellar evolution model and its 2D explosion in § 7.3. We discuss the physical properties of an exploding $55,500\,M_\odot$ and its potential impact on its surroundings in § 7.4. We finally conclude and summarize our findings in § 7.5.

7.2 Methodology & Problem Setup

Computing 3D stellar evolution models from the main sequence to SN explosion is far beyond the capability of modern computational power. Instead, 1D models are usually used to evolve the stars from the main sequence to pre-supernova stage, when the spherical symmetry of the stars is a good approximation. However, violent fluid instabilities occur when stars die as supernovae; multidimensional models are required

to simulate the fluid instabilities and their resultant mixing. In our simulations, we first evolve a $55,500\,M_\odot$ star using KEPLER, a 1D stellar-evolution code that solves the hydrodynamics, nuclear burning, and convective mixing, etc. The 1D stellar evolution is followed until the core of the star encounters the dynamical instabilities, where the adiabatic γ is below $4/3$. Then we map the resulting 1D profiles onto the 2D axis-symmetrical grids of CASTRO. Because the violent fluid motion is about to occur, we would like to model the collapse to explosion with CASTRO. Our 2D simulation stops when the SN shock breaks out of the stellar surface. The strategy of combing 1D and 2D simulations allows us to simulate the different phases of SMS with a practical computational budget. In this section, we briefly introduce our computational codes and the setup of our simulations.

7.2.1 Computational Approaches

A $55,500\,M_\odot$ star is evolved by KEPLER using about 1,000 zones until about several thousand secs before onset of explosion. The resulting 1D KEPLER profile is then mapped onto 2D CASTRO grids by using a new mapping procedure based on Chen et al. (2012). The 2D grids for CASTRO are 256×512 with two levels of a factor of 4 refinement to resolve the physical radius of a star, 1.63×10^{13} cm. Because the characteristic length for catching burning is about 10^9 cm, this setup is sufficient to resolve the burning scale. AMR criteria accounts for the gradients of the density, velocity, and pressure. When adjacent zones have a gradient larger than the AMR criteria we set, new finer grids are adaptively generated and replace previous zones. The boundaries along the Z-axis set reflect boundary conditions that prevent fluid from entering; the other boundaries apply the outflow conditions that fluid can freely move across. The nested-zone structure is constructed at the inner core to assure the highest resolution. The gravitational field is calculated using a monopole approximation based on constructing a radial average of the density from the 2D density on the grid because the density distribution has a roughly spherical symmetry.

In the case of the very massive stars $\geq 1,000\,M_\odot$, it is necessary to calculate gravity by considering the first-order effect of general relativity (GR) in stellar evolution models.

We discuss post-Newtonian correction in our SMS model. The derivation of the first-order GR correction can be found in Chapter 2. We directly use Equation 2.33, Tolman–Oppenheinmer–Volkoff equation for hydrostatic equilibrium in general relativity:

$$\frac{dP}{dr} = -\frac{Gm}{r^2}\varrho(1+\frac{P}{\varrho c^2})(1+\frac{4\pi r^3 P}{mc^2})(1-\frac{2Gm}{rc^2})^{-1}, \tag{7.1}$$

where P is pressure, ϱ is density, r is the radius of star, c is the speed of light, G is the gravitational constant, and m is the enclosed mass at r.

7.3 Explosions

Our simulations start at the time a few thousands of secs before the core reaches its maximum compression. Before the explosion ignites, the temperature and density of the core are about $T_c \sim 1.2 \times 10^9\,\mathrm{K}$ and $\rho_c \sim 200\,\mathrm{g\,cm^{-3}}$. At this temperature and density, the neutrino heating is not important, but the ratio between P and ϱc^2 is about 3×10^{-3}, so the GR-correction term of Newtonian gravity should be included. An unexpected explosion occurs and releases about 1.08×10^{55}erg, and this energy is strong enough to reverse the collapse into the explosion, eventually unbinding the star. About four hours later the explosion, the shock breaks out from the stellar surface. Figure 12.2(a) and Figure 12.2(b) show the radial velocity and density evolution. It takes about one hour from the runaway collapse to explosion. The decreasing central density suggests that the entire star has been unbound.

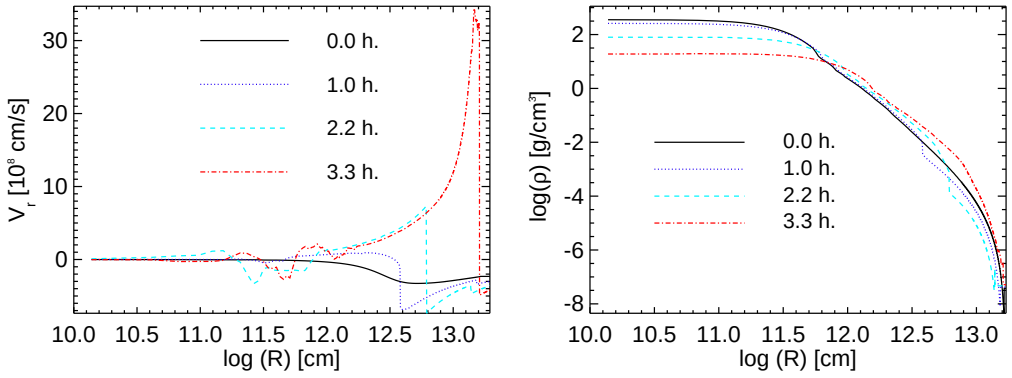

(a) Velocity evolution

(b) Density evolution

Figure 7.1: Velocity and density evolution of a GSN of $55,500\,M_\odot$ at the onset of explosion.

The density of the inner core drops with time, and it shows no evidence of forming any compact remnant such as a black hole. Element production before and after explosive burning is listed in Table 7.1. There is a trace amount of ^{56}Ni production at the edge of the oxygen-burning shell because of the α capture processes. The amount of ^{56}Ni is less than $1\,M_\odot$, which is too little to be detected. In contrast, the PSNe can synthesize the explosive ^{28}Si burning and yield a large amount of ^{56}Ni; hence, the light curves of GSNe are mainly powered by the thermal ejecta of the hot ejecta. There should be no ^{56}Ni decay trend in the light curves. Significant amounts of intermediate elements with atomic mass between ^{12}C and ^{40}Ca are synthesized during the explosion, and all of the yields are dispersed to its surroundings.

Table 7.1 shows the nuclear product before and after explosion. About $1,000\,M_\odot$ ^{16}O and $300\,M_\odot$ ^{20}Ne were burned into heavier elements such ^{24}Mg and ^{28}Si. Unlike the case of PSNe, there is no significant silicon burning right after oxygen burning. Less $1\,M_\odot$ is eventually synthesized inside the GSN.

Burning instabilities have already caused significant fluid instabilities and mixing at the core. When the shock propagates into the stellar envelope, there is no significant mass for snowplowing to occur. The reverse shock is weak and cannot lead to the Rayleigh–Taylor instabilities since the helium and hydrogen envelopes of SMS are not

Name	Before $M_\odot$	After $M_\odot$
^{16}O	7972	6920
^{20}Ne	5110	4808
^{24}Mg	7748	8906
^{28}Si	515	1433

Table 7.1: Nucleosynthesis products before and after explosion.

as extensive as the progenitors of the red supergiants. Figure 7.3 shows mixing of ^{16}O, ^{24}Mg, ^{28}Si, & ^{32}S when the shock has broken out of the surface. Most of the mixing process has ceased. The major drivers for mixing are fluid instabilities emergent during the burning; they mix the fuel and hot ash, which rapidly facilitate the process. If violent mixing occurs in the explosive stage, heavy elements can be possibly dredged out at a very early time and appear in the SNe spectra. In Figure 7.2, we show the 1D abundance patterns of ^{16}O, ^{20}Ne, and ^{24}Mg, as well as profiles of density and radial velocity. The oxygen burning causes a significant fluctuation in its end product, ^{28}Si.

7.4 Cosmological Impacts

GSNe may have had a very significant impact the early Universe by ejecting energetics and metals into their surroundings. One single GSN can provide about 100 time yields and energetics more than a PSN. Unlike PSNe, which can synthesize more iron group elements, the GSNe would mainly enrich the primordial gas with ^{12}C and ^{16}O. Traces of GSNe might be found in the early-type galaxies those are ^{56}Fe deficient but with ^{12}C and ^{16}O enhanced.

7.5 Conclusions

The formation of super massive stars is still unclear, they offer promising seeds for the resident super massive black hole inside the galaxies. Our stellar evolution models show that the super massive stars can explode, when we consider the general relativity correction during the stellar evolution. During the collapse of such super massive stars,

the pressure contributes the gravitational sources that affect the collapse and ignite the ^{12}C and ^{16}O burning, eventually leading to the unbinding of the stars. Due to significant amounts of mass ejected in the explosion, GSNe posit significant impacts their surroundings. If the super massive stars formed in the early Universe, we might have opportunities to find the fingerprints of their explosions.

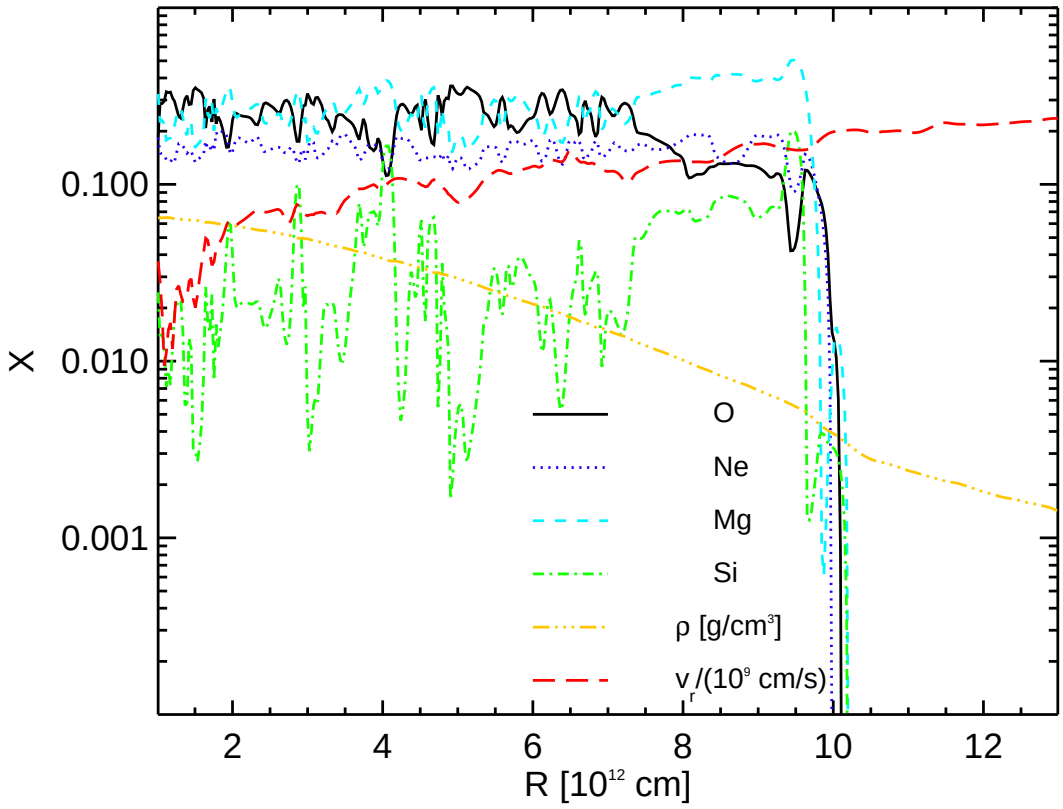

Figure 7.2: 1D physics profile after expolsion. The noisy elemental abundance pattern are caused by fluid instabilities during the explosion phase.

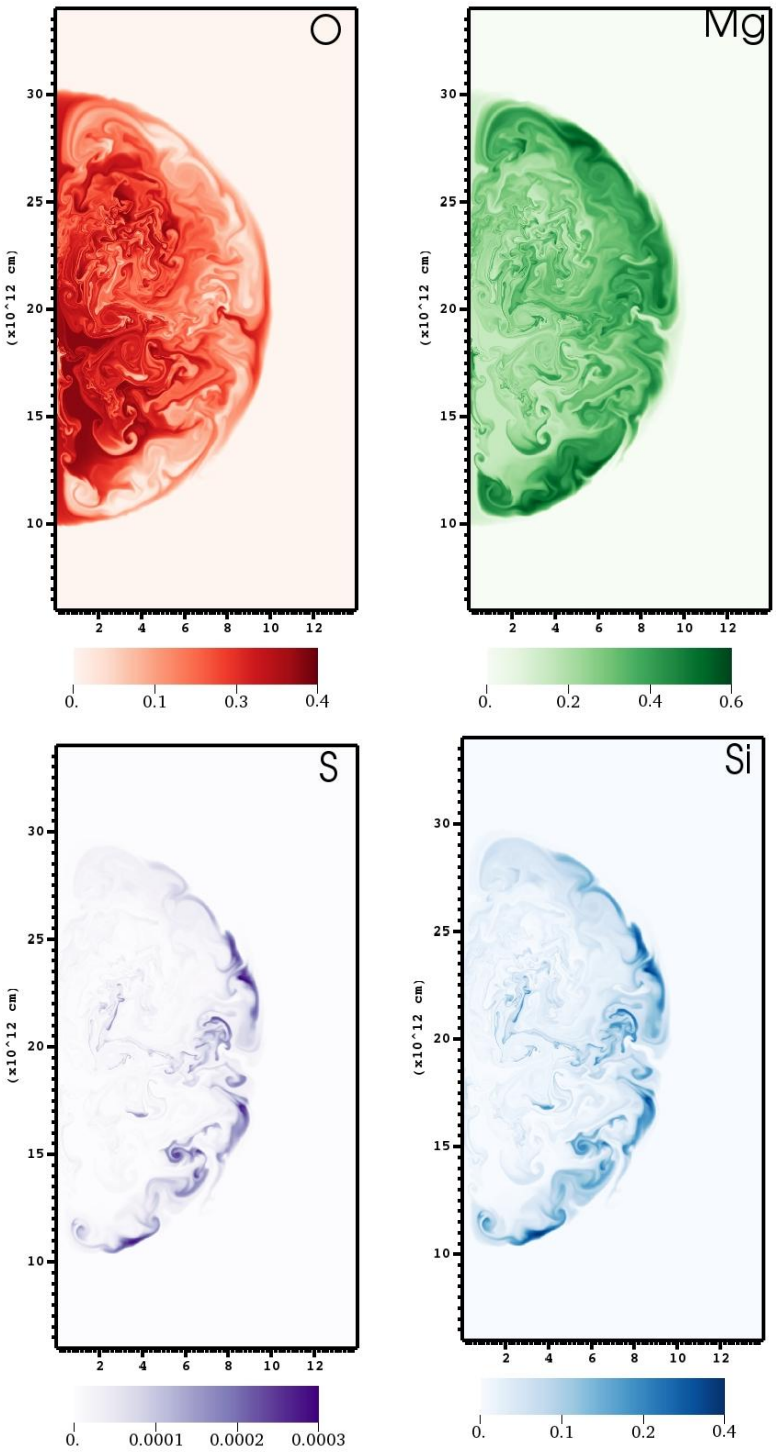

Figure 7.3: The mixing of ^{16}O, ^{24}Mg, ^{28}Si, and ^{32}S inside an GSN of $55,500\,\mathrm{M}_{\odot}$.

Part II

Impact of the First Stars and Supernovae

Chapter 8

From the First Stars to the First Galaxies

Galaxies are the building blocks of large-scale structures in the Universe. The detection of galaxies at $z \approx 10$ by the Hubble Space Telescope suggests that these galaxies formed within a few hundred million years (Myr) after the Big Bang. In Chapter 1, we discuss the Pop III stars that are predicted to form inside the dark matter halos of mass about $10^5\,\mathrm{M}_\odot$, known as minihalos. The gravitational wells of minihalos are very shallow, so they could not maintain a self-regulated star formation because the stellar feedback from the Pop III stars inside the minihalos could easily strip out the gas and prevent formation of the next subsequent stars. Thus the minihalos cannot be treated as the first galaxies. Instead, the first galaxies must be hosted by more massive halos generated from the merging of minihalos. The high redshift galaxies should come from the merger of the first galaxies. But *how did the first galaxies form*? and *what are the connections among the first stars, the first supernovae, and the first galaxies?*

A key to answering these questions is held by the Pop III stars formed inside the minihalos. As we discussed in Chapter 1, studies of the Pop III star formation suggest that these stars formed at mass scale around $100\,\mathrm{M}_\odot$, and many of them might have died as supernovae (Pop III SNe). The Pop III stars with initial masses of $10 - 150\,\mathrm{M}_\odot$ die as core collapse supernovae (CCSNe); those with initial masses of $150 - 260\,\mathrm{M}_\odot$ die as pair-instability supernovae (PSNe), and those with mass $> 260\,\mathrm{M}_\odot$ just collapse to

black holes. We temporarily neglect the feedback of exploding super massive stars here because of their scarcity. Massive Pop III stars could emit copious amounts of hydrogen-ionizing photons, which contribute to cosmic reionization. Their SNe dispersed the first metals to the intergalactic medium (IGM). This chemical enrichment could trigger the formation of the second generation of stars (Pop II stars). Finally, the minihalos and IGM, together with relic H II regions and metals from Pop III stars, jointly formed into the first galaxies, as shown in Figure 8.1.

The formation of the first galaxies not only depends on the evolution of dark matter but also on baryon, which provided the material for forming stars. The chemical, mechanical, and radiative feedback from the first stars makes the assembly process of the first galaxies much more complex. The model of first galaxy formation is still at its infant phase and is not sophisticated enough to offer reliable predictions. One of the obstacles for models is in resolving the relevant spatial scales and physical processes. Beneficial to the advancement of computational technology, new supercomputers allow us to perform more realistic cosmological simulations and start to investigate the first galaxy formation.

In Part II, we investigate the stellar feedback of Pop III stars using cosmological simulations. In a refinement of previous studies, our simulations consider a more realistic treatment of stellar feedback of Pop III stars. This chapter serves as an introduction to Part II. In this chapter, we first review the current understanding of the first galaxies in § 8.1. Then we discuss the role of the first stars in the first galaxy formation in § 8.2. The stellar feedback includes radiation during its stellar evolution and chemical enrichment when the star dies as a SN. We discuss the radiation feedback of the first stars in § 8.3 and the chemical enrichment of their SNe in § 8.4.

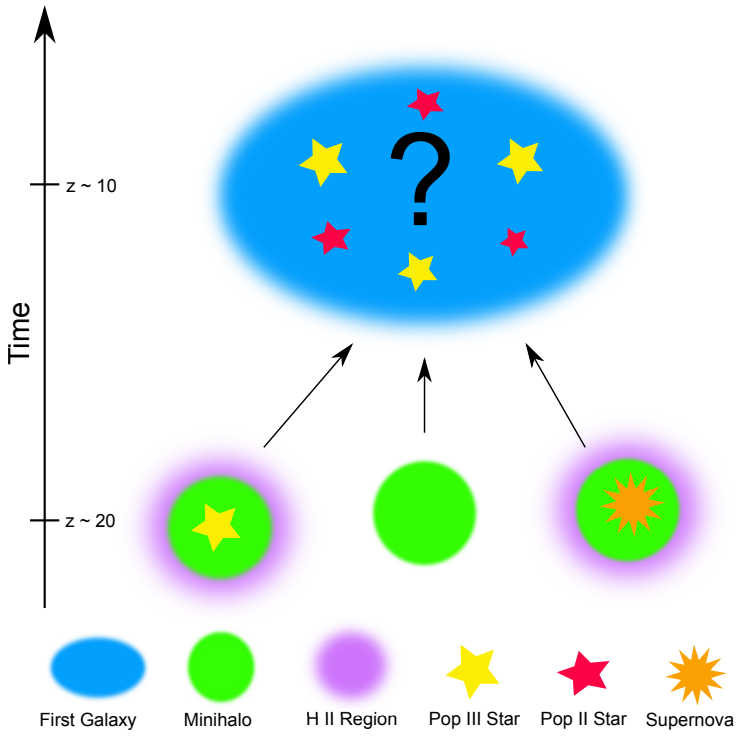

Figure 8.1: Assembly of the first galaxies. Based on the model of Bromm and Yoshida (2011), the first galaxies form with a mass of about 10^8 $M_\odot$ at $z \sim 10$. The feedback of previous Pop III stars can affect the star formation inside the first galaxy. The gravitational wells of minihalos are shallow, so they cannot be treated as galaxies in this scenario.

8.1 Assembly of the First Galaxies

There are several definitions of the first galaxy. In general, a galaxy should have multiple stars hosted in a bound halo; its potential well is deep enough to retain the gas heated by the UV radiation from stars or inside it (Barkana and Loeb, 2001; Bromm and Yoshida, 2011; Goodstein, 2011). In addition, SN explosions in the first galaxies can only trigger a minimum mass loss. In brief, a galaxy must have a stable and self-regulated star formation. The potential well of the halo is the most important factor determining whether it can be a galaxy or not. For a given halo mass at $z \gg 1$, the gravitational

binding energy of the halo can be estimated as (Bromm and Yoshida, 2011),

$$E_b = \frac{GM^2}{r_{\rm vir}} \simeq 5 \times 10^{53} \left(\frac{M}{10^8\,{\rm M}_\odot} \right)^{5/3} \left(\frac{\delta_c}{18\,\pi^2} \right)^{1/3} \left(\frac{1+z}{10} \right) {\rm erg}, \tag{8.1}$$

where $r_{\rm vir}$ is the virial radius of the halo and δ_c is the density contrast when the halo formed. The results of Wise and Abel (2008); Greif et al. (2010b) have suggested that dark matter halos of a mass of $10^8\,{\rm M}_\odot$ forming at $z \approx 10$ can satisfy the criteria. These halos have a virial temperature of about $10^4\,{\rm K}$, which is related to the characteristic temperature due to atomic hydrogen cooling. These halos are also called atomic cooling halos. Unlike minihalos, the dominating cooling process of gas is by H instead of H_2. Such halos also keep most of their gas that previously received stellar feedback, such as through radiation and the SN blast wave. For observers, there are two primordial types of galaxies that can be the first galaxies. The first galaxies can be defined as the highest redshift galaxies detected. However, such a definition may change once there is a new telescope. On the other hand, the galaxies containing zero metallicity may be defined as the first galaxies. However, chemical enrichment might already occur in the first galaxies. In this thesis, we use definitions based on Bromm and Yoshida (2011) for the first galaxies that are constructed by a dark matter halo and host the Pop III or Pop II stars.

8.2 Cosmological Consequences of the First Stars

The process of the first galaxy formation is highly complex because the initial conditions and relevant physics are not well understood. In the ΛCDM model, the first stars are predicted to have been born before the first galaxies formed. Thus the first stars together with primordial gas would offer a rockbed for the first galaxies. Feedback from the first stars would play an important role in determining the initial conditions for forming the first galaxies. The stellar feedback usually includes radiative (Schaerer, 2002) and supernova feedback (Ciardi and Ferrara, 2005). The massive Pop III stars produce UV radiation to ionize the primordial gas (Barkana and Loeb, 2007). The WMAP measured an increasing optical depth at $z \sim 15$, implying cosmic reionization by the massive Pop III stars. The SN feedback has both a mechanical and a chemical impact; the blast wave of the explosion injects heat and momentum to the surrounding IGM

and concurrently disperses metals into the primordial gas (Ferrarese and Merritt, 2000; Bromm and Larson, 2004). As discussed before, some Pop III stars may die as PSNe, and such explosion modes could quickly pollute the IGM with large amounts of metals. Such chemical enrichment can alter the subsequent star formation because additional metal cooling starts to function. Both radiative and SN feedback of the first stars transforms the simple Universe into a much more complex state by setting the initial conditions for the first galaxy formation.

8.3 Radiative Feedback

The radiation emitted from Pop III stars would affect the subsequent thermal properties of the primordial IGM, which changed the properties of star-forming clouds and affected the later star formation inside the first galaxies. The radiative feedback may have several different forms, e.g., UV photons and x-rays, depending on the stars and their compact remnants. Since H_2 is the most important coolant for the first star formation, it is relevant to learn how the radiation influences H_2. The hydrogen bond of H_2 is weak and can be easily broken by Lyman–Werner (LW) photons with energy in $11.2-13.6$ eV,

$$H_2 + \gamma \rightarrow H_2^* \rightarrow 2H. \tag{8.2}$$

H_2^* is an excited state, which is unstable and soon decays into two H. Massive Pop III stars could emit large amounts of UV photons, easily ionizing the primordial hydrogen and helium, thus suppressing the corresponding H_2 cooling. Without effective H_2 cooling, massive Pop III stars may not be able to form hereafter. On the other hand, in the ionized region, the abundance of free electrons may increase and facilitate the formation of H_2. It is still unclear whether the radiation from the Pop III stars is helpful (facilitating later star formation) or harmful (hampering later star formation). The overall impact of the radiative feedback on the H_2 is pretty uncertain. Besides ionizing primordial gas, energetic UV photons can photoheat the surrounding gas and allow it to escape the host halo and form an outflow. This disperses the gas inside the minihalos and may shut the later star formation off. More cosmological simulations of comprehensive radiative effects of the Pop III stars are necessary for clarifying this issue.

8.4 Supernova Feedback

Massive Pop III stars might die as energetic SNe and dump metal-rich ejecta to the IGM. The are two kinds of feedback from SNe: thermodynamical and chemical. The SN explosions produce strong shocks that blow up the stars (see Part I). When the SN shock breaks out of the stellar surface and propagates into the low-density ISM surrounding, it is suddenly accelerated a velocity above 10^4 km/s, about a few percent of the speed of light. The shock front can quickly reheat the relic H II regions created by the progenitor stars and maintain the ionized status of the H II region for an additional $1 \sim 2\,\mathrm{Myr}$. For chemical feedback, the SN ejecta are metal-rich and can pollute the pristine IGM to a metallicity of about 10^{-3}-$10^{-5}\,Z_\odot$ (Wise and Abel, 2008) inside a region of 1 kpc. The first metals are very important to the later star formation because the metal cooling affects the mass of scale during the star formation. Once the metallicity of the gas cloud reaches the critical metallicity, $10^{-3}\,Z_\odot$ (Schneider et al., 2012), Pop II stars that have a mass scale similar to present-day stars may start to form.

The SN feedback strongly depends on its progenitor stars, which determine the amount of explosion energy and metals produced. The massive Pop III stars with initial masses below $150\,\mathrm{M}_\odot$ are predicted to die as CCSNe. These CCSNe are thought to be driven by neutrinos and usually leave compact remnants such as neutron stars or black holes behind. Some of the synthesized metals may fall back into the compact remnants; some of the metals are ejected. Stars in the mass window between $150\,\mathrm{M}_\odot$ and $260\,\mathrm{M}_\odot$ PSNe are particularly interesting because they are located in the mass scale predicted by the simulations of the first stars. Based on the discussion in Chapter 4, PSNe are giant thermonuclear explosions, completely disrupting the progenitor stars and ejecting all the metals. Those more massive than $260\,\mathrm{M}_\odot$ may simply die as black holes, and most of the freshly synthesized metals are locked up in the black hole. Chemical enrichment of the IGM by Pop III SNe is important for understanding the transition in the star-formation mode from high-mass dominated to low-mass dominated (Bromm and Larson, 2004). If metals are very uniformly dispersed by the SNe, the transition may occur rather sharply. In contrast, if the enrichment is not very uniform, gas clumps of high-metallicity may appear and surround the primordial gas. In this case, the transition of star formation mode may occur more smoothly. Bromm and Loeb (2003) first present

numerical simulations of the first SN explosions at high redshifts ($z \approx 20$); they assume that one single PSN occurs inside the center of the minihalo and simulate the explosion. Their simulations explore two explosion energies of PSNe, 10^{51} erg and 10^{53} erg. Their results show that the explosion of 10^{53} erg can create giant metal bubbles the size of several kpc. The lower explosion energy instead shows relatively smaller regions of metal enrichment. More recent results from Greif et al. (2010b) show that the metals are dispersed uniformly due to the diffusion mixing. The resolutions of these simulations are still very crude. We are just starting to understand the complex processes of the first chemical enrichment by the first SNe. More sophisticated numerical simulations are presented in this thesis for advancing previous study.

Chapter 9

Cosmological Simulations with GADGET

GADGET (Springel, 2005) (**GA**laxies with **D**ark matter and **G**as int**E**rac**T**) is the main tool for our cosmological simulations. It is a well-tested, massively-parallel cosmological code that computes gravitational forces by using a tree algorithm and models gas dynamics by using smoothed particle hydrodynamics (SPH). We modified GADGET to include the relevant physics of the early Universe, such as star formation, radiative transfer, cooling, and chemistry. Cosmological simulations need to resolve the small-scale resolution under a huge domain. The SPH approach uses the Lagrangian coordinate instead of a spatial coordinate and is suitable for cosmological simulations. In addition to hydro and gravity, our simulations consider several feedback elements from the first stars, e.g., radiation, supernova explosion, metal diffusion, et al. Prof. Volker Bromm and his group at the University of Texas, Austin, provide major code development. We have contributed a new ray-tracing scheme of ionizing photons that allows us to consider the more realistic models.

In this chapter, we describe our computational approaches by introducing the features of GADGET and additional physics modules that we use for our simulations. We first introduce the hydrodynamics and gravity of SPH of GADGET in § 9.1. The cooling and chemical network of the primordial gas is discussed in § 9.2. Since the star formation in the context of cosmological simulations cannot be modeled from first principles, we

explain the sink particle approach for star formation in § 9.3. Once the first stars form in the simulation, they start to emit UV photons. In § 9.4, we discuss the algorithm of radiation transfer. The x-ray feedback is discussed in § 9.5. After several million years, the stars might die as supernovae. We discuss the treatment of the supernova explosion and metal transport in § 9.6. Finally, we present a scaling performance of `GADGET` running on large supercomputers in § 9.7.

9.1 Smoothed Particle Hydrodynamics

Smoothed particle hydrodynamics (Monaghan, 1992) uses a mesh-free Lagrangian method by dividing the fluid into discrete elements called particles. Each particle has its own position (r_i), velocity (v_i), mass (m_i), and thermal dynamical properties, such as internal energy per unit mass (u_i). Additionally, each particle is given a physical size called smoothing length (h). The distribution of physical quantities inside a particle is determined by a kernel function (W). The most popular choices of kernel functions are Gaussian and cubic spline functions. When each particle evolves with the local conditions, the smoothing length changes, so the spatial resolution of the fluid element becomes adaptive, which allows SPH to handle a large dynamic scale and be suitable for cosmological simulations. h of particles in higher-density regions becomes smaller because more particles accumulate. SPH automatically increases the spatial resolution of simulations. The major disadvantages of SPH are in catching shock fronts and resolving the fluid instabilities because of its artificial viscosity formulation, which injects the necessary entropy in shocks. The shock front becomes broadened over the smoothing scale, and true contact discontinuities cannot be resolved. However, SPH are very suitable for simulating the growing structures due to gravity, and SPH adaptively resolve higher-density regions of halos, which are usually the domain of interest.

We start by describing the basic set of equations for cosmological simulations of `GADGET`. There are two types of particles in `GADGET`: collisionless particles (e.g., cold dark matter) and gas particles; both components are coupled through gravity in an evolving background cosmology.

The equation of motions of these particles is determined by their Hamiltonian

(Springel, 2005)

$$H = \sum_i \frac{\boldsymbol{p}_i^2}{2\, m_i\, a(t)^2} + \frac{1}{2} \sum_{ij} \frac{m_i m_j\, \varphi(\boldsymbol{x}_i - \boldsymbol{x}_j)}{a(t)}, \tag{9.1}$$

where $H = H(\boldsymbol{p}_1, \ldots, \boldsymbol{p}_N, \boldsymbol{x}_1, \ldots, \boldsymbol{x}_N, t)$. The $\boldsymbol{x}_i$ are comoving vectors, $\boldsymbol{p}_i = a^2 m_i \dot{\boldsymbol{x}}_i$ is the canonical momenta, and $\varphi(\boldsymbol{x}_i - \boldsymbol{x}_j)$ is the interaction potential. The scale factor, $a(t)$, is determined by the background cosmology. The density distribution function of a single particle, $\tilde{\delta}(\boldsymbol{x})$, uses the form of the Dirac δ-function multiplied a normalized softening kernel function. The spline kernel of the particle used in `GADGET` is $\tilde{\delta}(\boldsymbol{x}) = W(|\boldsymbol{x}|, 2.8\epsilon)$, (Springel, 2005)

$$W(r,h) = \frac{8}{\pi h^3} \begin{cases} 1 - 6\left(\frac{r}{h}\right)^2 + 6\left(\frac{r}{h}\right)^3, & 0 \le \frac{r}{h} \le \frac{1}{2}, \\ 2\left(1 - \frac{r}{h}\right)^3, & \frac{1}{2} < \frac{r}{h} \le 1, \\ 0, & \frac{r}{h} > 1. \end{cases} \tag{9.2}$$

The density estimate `GADGET` has the form

$$\rho_i = \sum_{j=1}^{N} m_j W(|\boldsymbol{r}_{ij}|, h_i), \tag{9.3}$$

where $\boldsymbol{r}_{ij} \equiv \boldsymbol{r}_i - \boldsymbol{r}_j$, and $W(r,h)$ is the SPH smoothing kernel defined in Equation (9.2). Each SPH particle in `GADGET` has an adaptive smoothing length, h_i, which is defined in a way that its kernel volumes maintain a constant mass for the estimated density. So the relation between the smoothing length and the estimated density is

$$\frac{4\pi}{3} h_i^3 \rho_i = N_{\mathrm{sph}} \overline{m}, \tag{9.4}$$

where N_{sph} is the typical number of smoothing neighbors, and $\overline{m}$ is an average particle mass. By starting from a discretized version of the fluid Lagrangian, the equations of motion for the SPH particles are given by (Springel, 2005)

$$\frac{\mathrm{d}\boldsymbol{v}_i}{\mathrm{d}t} = -\sum_{j=1}^{N} m_j \left[f_i \frac{P_i}{\rho_i^2} \nabla_i W_{ij}(h_i) + f_j \frac{P_j}{\rho_j^2} \nabla_i W_{ij}(h_j) \right], \tag{9.5}$$

where the coefficients f_i are defined by

$$f_i = \left[1 + \frac{h_i}{3\rho_i} \frac{\partial \rho_i}{\partial h_i} \right]^{-1}, \tag{9.6}$$

where $W_{ij}(h) = W(|\boldsymbol{r}_i - \boldsymbol{r}_j|, h)$ h. The particle pressures are given by $P_i = A_i \rho_i^\gamma$, which means the system is adiabatic; the equations above already fully define reversible fluid dynamics in SPH. Because $A = A(s)$ is only a function of s for an ideal gas, we will often refer to A as "entropy." A_i of each particle remains constant in such a flow. In the real world, the flow of ideal gas can develop discontinuities, where entropy is generated through microphysics such as friction or turbulence. Therefore, modeling shock waves in SPH requires us to use an artificial viscosity to inject in the shock front. For this purpose, `GADGET` uses a viscous force,

$$\left.\frac{\mathrm{d}\boldsymbol{v}_i}{\mathrm{d}t}\right|_{\mathrm{visc}} = -\sum_{j=1}^{N} m_j \Pi_{ij} \nabla_i \overline{W}_{ij}\,, \tag{9.7}$$

where $\Pi_{ij} \geq 0$ is non-zero only when particles approach each other in physical space. Entropy generation rate by this viscosity is

$$\frac{\mathrm{d}A_i}{\mathrm{d}t} = \frac{1}{2}\frac{\gamma-1}{\rho_i^{\gamma-1}} \sum_{j=1}^{N} m_j \Pi_{ij} \boldsymbol{v}_{ij} \cdot \nabla_i \overline{W}_{ij}\,, \tag{9.8}$$

which transforms kinetic energy of gas irreversibly into heat. The symbol $\overline{W}_{ij}$ here is the arithmetic average of the two kernels $W_{ij}(h_i)$ and $W_{ij}(h_j)$. `GADGET` uses the artificial viscosity form from Monaghan (1992),

$$\Pi_{ij} = \begin{cases} \left[-\alpha c_{ij}\mu_{ij} + \beta\mu_{ij}^2\right]/\rho_{ij} & \text{if } \boldsymbol{v}_{ij}\cdot\boldsymbol{r}_{ij} < 0 \\ 0 & \text{otherwise,} \end{cases} \tag{9.9}$$

with

$$\mu_{ij} = \frac{h_{ij}\,\boldsymbol{v}_{ij}\cdot\boldsymbol{r}_{ij}}{|\boldsymbol{r}_{ij}|^2}. \tag{9.10}$$

where h_{ij}, ρ_{ij}, and c_{ij} are the average of the smoothing length, density, and sound speed for the two particles i and j. The value of the viscosity is determined by the parameters $\alpha \simeq 0.5 - 1.$ and $\beta = 2\,\alpha$. In the equation of motion, the viscosity behaves similar to a pressure term $P_{\mathrm{visc}} \simeq \frac{1}{2}\rho_{ij}^2 \Pi_{ij}$ assigned to the particles. The viscosity can be written as (Springel, 2005)

$$P_{\mathrm{visc}} \simeq \frac{\alpha}{2}\gamma \left[\frac{w_{ij}}{c_{ij}} + \frac{3}{2}\left(\frac{w_{ij}}{c_{ij}}\right)^2\right] P_{\mathrm{therm}}, \tag{9.11}$$

where $w_{ij} = \boldsymbol{v}_{ij}\cdot\boldsymbol{r}_{ij}/|\boldsymbol{r}_{ij}|$, if we assume roughly two particles have equal speeds and densities. This viscous pressure depends only on w/c, similar to a mach-number, and

not explicitly on the particle separation or smoothing length. Finally, the SPH time step is similar to a Courant time step:

$$\Delta t_i^{(\mathrm{hyd})} = \frac{C_{\mathrm{courant}}\, h_i}{\max_j (c_i + c_j - 3w_{ij})}. \tag{9.12}$$

The maximum here is determined with respect to all neighbors j of particle i. The above hydrodynamics equations are solved in physical coordinates because we usually use co-moving coordinates $\boldsymbol{x}$, co-moving momenta $\boldsymbol{p}$, and co-moving densities as computational variables in cosmological simulations. These variables are converted to physical variables for calculating hydrodynamics equations.

9.1.1 Gravity

The cold dark matter is collisionless particles, and they interact with each other only through gravity. Hence gravity is the dominating force that drives the large-scale structure formation in the Universe, and its computation is the workhorse of any cosmological simulation. The long-range nature of gravity within a high dynamic range of structure formation problems makes the computation of gravitational forces very challenging. In `GADGET`, the algorithm of computing gravitational forces employs the hierarchical multipole expansion called a tree algorithm. The method groups distant particles into larger cells, allowing their gravity to be accounted for by means of a single multipole force. In contrast to a direct-summation approach that needs N -1 partial forces per particle, the gravitational force using the tree method only requires about log N particle forces per particle. This greatly saves the computation cost. The most important characteristic of a gravitational tree code is the type of grouping employed. As a grouping algorithm, `GADGET` uses the geometrical oct-tree (Barnes and Hut, 1986) because of advantages in terms of memory consumption. The volume of the simulation is divided up into cubic cells in an oct-tree. Only neighboring particles are treated individually, but distant particles are grouped into a single cell. The oct-tree method significantly reduces the computation of pair interactions more than the method of direct N-body.

9.2 Cooling & Chemistry Networks of Primordial Gas

Cooling of the gas plays an important role in the star formation. The dark matter collapses into halos and provides gravitational wells for the primordial star formation. The mass of the gas cloud must be larger than its Jeans mass so the star formation can proceed. Cooling is an effective way to decrease the Jeans mass and trigger the star formation. The chemical cooling of the first star formation is relatively simple because no metals are available coolants at the time.

According to Bromm and Larson (2004), the dominant coolant in the first star formation is molecular hydrogen For the local Universe, the formation of H_2 occurs mainly at the surface of dust grains, where one hydrogen atom can be attached to the dust surface and combine with another hydrogen atom to form H_2. There is no dust when Pop III stars form; the channel of H_2 through dust grain is unavailable. H_2 formation of primordial gas can only go through gas phase reactions. The simplest reaction is

$$H + H \longrightarrow H_2 + \gamma, \tag{9.13}$$

which occurs when one of the hydrogen atoms is in an electronic state. When the densities of hydrogen become high enough, $n_H \geq 10^8\,cm^{-3}$, three-body formation of H_2 becomes possible:

$$H + H + H \longrightarrow H_2 + H, \tag{9.14}$$

$$H_2 + H + H \longrightarrow H_2 + H_2. \tag{9.15}$$

For the first star formation, the cloud collapses at the densities $n_H \sim 10^4\,cm^{-3}$. H_2 is dominated by two sets of reactions:

$$H + e^- \longrightarrow H^- + \gamma, \tag{9.16}$$

$$H^- + H \longrightarrow H_2 + e^-. \tag{9.17}$$

This reaction involves the H^- ion as an intermediate state,

$$H + H^+ \longrightarrow {H_2}^+ + \gamma, \tag{9.18}$$

$$H_2{}^+ + H \longrightarrow H_2 + H^+. \tag{9.19}$$

The second one involves the H^+ ion as an intermediate state. These two processes are denoted as the H^- pathway and the $H_2{}^+$ pathway, respectively. The difference between the two pathways is that the H^- path forms H_2 much faster than the $H_2{}^+$ does, so the H^- pathway dominates the production of H_2 in the gas phase. During the epoch of the first star formation, Bromm and Larson (2004) pointed out that molecular hydrogen fraction is $f_{H_2} = 10^{-3} \sim 10^{-4}$ at minihalos and $f_{H_2} \approx 10^{-6}$ at the IGM. For given H_2 abundances, density, and temperature, we are able to calculate the H_2 cooling. The values of H_2 cooling rates are not well-defined because of the uncertainties in the calculation of collisional de-excitation rates.

The cooling and chemistry network in our modified `GADGET` is based on Greif et al. (2010a) and include all relevant cooling mechanisms of primordial gas, such as H and He collisional ionization, excitation and recombination cooling, *bremsstrahlung*, and inverse Compton cooling; in addition, the collisional excitation cooling via H_2 and HD is also taken into account. For H_2 cooling, collisions with protons and electrons are explicitly included. The chemical network includes $H, H^+, H^-, H_2, H_2^+, He, He^+, He^{++}$, and e^-, D, D^+, and HD.

9.3 Sink Particles

Modern cosmological simulations can potentially use billions of particles to model the formation of the Universe. However, it is still challenging to resolve mass scales from galaxy clusters ($10^{13}\,M_\odot$) to a stellar scale ($1\,M_\odot$). For example, the resolution length in our simulation is about 1 pc, hence modeling the process of star formation on cosmological scales from first principles is impractical for the current setup. Alternatively, in the treatment of star formation and its feedback, sub-grid models are employed, meaning that a single particle behaves as a star, which comes from the results of stellar models. Also, when the gas density inside the simulations becomes increasingly high, the SPH smoothing length decreases according to the Courant condition and forces it to shrink the time steps very rapidly. When the resulting runaway collapse occurs, the simulation easily fails. Creating sink particles is required to bypass this numerical constraint and

to continue following the evolution of the overall system for longer. For the treatment of star formation, we apply the sink particle algorithm of Johnson and Bromm (2007a). We have to ensure that only gravitationally bound particles can be merged to form a sink particle and utilize the nature of the Jeans instability. We also consider how the density evolves with time inside the collapsing region of the first star formation when gas densities are close to $n_c \sim 10^4\,\mathrm{cm}^{-3}$ and subsequently increase rapidly by several orders of magnitude. So the most important criterion for a particle to be eligible for merging is $n > n_c$ because in the collapse around the sink particles, the velocity field surrounded by the sink must be converged fluid, which yields $\nabla \cdot \boldsymbol{v} < 0$. The neighboring particles around the sink particle should be bounded and follow with (Johnson and Bromm, 2007a);

$$E = E_g + E_k + E_t < 0, \tag{9.20}$$

where E, E_g, E_k and E_t are the overall binding, gravitational, kinetic, and thermal energies, respectively. Sink particles are usually assumed to be collisionless, so that they only interact with other particles through gravity. Once the sink particles are formed, the radiative feedback from the star particles would halt further accretion of in-falling gas. So collisionless properties of sink particles are reasonable for our study. The sink particles provide markers for the position of a Pop III star and its remnants, such as a black hole or supernovae, to which the detailed physics can be supplied.

Figure 9.1(a) shows a density snapshot of our cosmological simulations at the time when the first star is about to form inside one of the minihalos. The density of the gas cloud is approaching $10^4\,\mathrm{cm}^{-3}$, and its H_2 mass fraction rises to 10^{-3}, as shown in Figure 9.1(b). A runaway collapse of the cloud will occur, and a sink particle will be created for simulating the star formation.

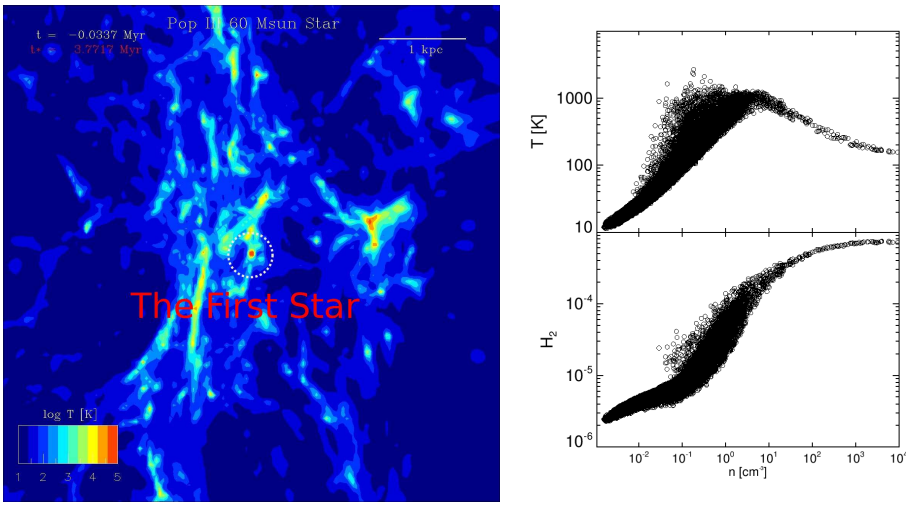

(a) (b)

Figure 9.1: (a) A sink particle (the first star) is about to form within the dark matter halo (white circle) of mass of $10^5\,M_\odot$ at $z \approx 28$. At this time, the gas density of H is approaching $10^4\,\mathrm{cm}^{-3}$. (b) Temperature and H_2 phase diagram. The center gas density of H is approaching $10^4\,\mathrm{cm}^{-3}$, and the H_2 fraction increases to about 10^{-3} to cool the gas cloud to about 200 K. There will be a runaway collapse, and a sink will form to mimic the star formation.

9.4 Radiative Transfer

When a Pop III star has formed inside the minihalo, the sink particle immediately turns into a point source of ionizing photons to mimic the birth of a star. The rate of ionizing photons emitted depends on the physical size of the star and its surface temperature based on the subgrid models of stars. Instead of simply assuming constant rates of emission, we use the results of one-dimensional stellar evolution from Heger and Woosley (2010) to construct the luminosity history of the Pop III stars that served as our sub-grid models for star particles. The luminosity of the star is actually evolving with time and demonstrates a considerable change. The streaming photons from the star then form an ionization front and build up H II regions. For tracing the propagation

of photons and the ionization front, we use the ray-tracing algorithm from Greif et al. (2009b), which solves the ionization front equation in a spherical grid by tracking 10^5 rays with 500 logarithmically spaced radial bins around the ray source. The propagation of the ray is coupled to the hydrodynamics of the gas through its chemical and thermal evolution. The transfer of the H_2-dissociating photons of Lyman–Werner (LW) band ($11.2 - 13.6\,\mathrm{eV}$) from Pop III stars is also included.

In the ray-tracing calculation, the particles' positions are transformed from Cartesian to spherical coordinates, radius (r), zenith angle (θ), and azimuth angle (ϕ). The volume of each particle is $\sim h^3$, when h is the smoothing length. The corresponding sizes in spherical coordinates are $\Delta r = h$, $\Delta\theta = h/r$, and $\Delta\phi = h/r\sin(\theta)$. Using spherical coordinates is for convenience in calculating the Strömgren sphere around the star,

$$n_n r_\mathrm{I}^2 \frac{dr_\mathrm{I}}{dt} = \frac{\dot{N}_\mathrm{ion}}{4\pi} - \alpha_\mathrm{B} \int_0^{r_\mathrm{I}} n_e n_+ r^2 dr, \tag{9.21}$$

where r_I is the position of the ionization front, $\dot{N}_\mathrm{ion}$ represents the number of ionizing photons emitted from the star per second, α_B is the case B recombination coefficient, and n_n, n_e, and n_+ are the number densities of neutral particles, electrons, and positively charged ions, respectively. The recombination coefficient is assumed to be constant at temperatures around $2 \times 10^4\,\mathrm{K}$. The ionizing photons for H I and He II emitted are

$$\dot{N}_\mathrm{ion} = \frac{\pi L_*}{\sigma T_\mathrm{eff}} \int_{\nu_\mathrm{min}}^{\infty} \frac{B_\nu}{h_\mathrm{P}\nu} \mathrm{d}\nu, \tag{9.22}$$

where h_P is the Planck's constant, σ is the Boltzmann's constant, σ_ν is the photo-ionization cross sections, and ν_min is the minimum frequency for the ionization photons of H I, He I, and He II. By assuming the blackbody spectrum of a star B_ν of an effective temperature, T_eff, its flux can be written

$$F_\nu = \frac{L_*}{4\sigma T_\mathrm{eff} r^2} B_\nu. \tag{9.23}$$

The size of the H II region is determined by solving Equation 9.21. The particles within the H II regions now save information about their distance from the star, which is used to calculate the ionization and heating rates,

$$k_\mathrm{ion} = \int_{\nu_\mathrm{min}}^{\infty} \frac{F_\nu \sigma_\nu}{h_\mathrm{P}\nu} \mathrm{d}\nu, \qquad \Gamma = n_n \int_{\nu_\mathrm{min}}^{\infty} F_\nu \sigma_\nu \Big(1 - \frac{\nu_\mathrm{min}}{\nu}\Big) \mathrm{d}\nu. \tag{9.24}$$

For a Pop III star of $100\,M_\odot$, the resulting ionization heating rates are about (Greif et al., 2009b)

$$k_{\rm ion,H\ I} = \frac{1.32\times10^{-6}}{r_{\rm pc}^2}\quad {\rm sec}^{-1}, \tag{9.25}$$

$$k_{\rm ion,He\ I} = \frac{1.43\times10^{-6}}{r_{\rm pc}^2}\quad {\rm sec}^{-1}, \tag{9.26}$$

$$k_{\rm ion,He\ II} = \frac{3.72\times10^{-8}}{r_{\rm pc}^2}\quad {\rm sec}^{-1}, \tag{9.27}$$

$$\Gamma_{\rm H\ I} = 1.28\times10^{-17}\left[\frac{n_{\rm HI}}{r_{\rm pc}^2}\right]\quad {\rm erg\,sec^{-1}\,cm^{-3}}, \tag{9.28}$$

$$\Gamma_{\rm He\ I} = 1.57\times10^{-17}\left[\frac{n_{\rm HeI}}{r_{\rm pc}^2}\right]\quad {\rm erg\,sec^{-1}\,cm^{-3}}, \tag{9.29}$$

$$\Gamma_{\rm He\ II} = 4.46\times10^{-19}\left[\frac{n_{\rm HeII}}{r_{\rm pc}^2}\right]\quad {\rm erg\,sec^{-1}\,cm^{-3}}, \tag{9.30}$$

where $r_{\rm pc}$ is the distance from the star in the unit of pc. H_2 is the most important coolant for cooling the primordial gas, which leads to formation of the first stars. However, its hydrogen bond is weak and can be easily broken by photons in the LW bands between 11.2 and 13.6 eV. The small H_2 fraction in the IGM creates only a little optical depth for LW photons, allowing them to propagate a much larger distance than ionizing photons. In our algorithm, self-shielding of H_2 is not included because it is only important when H_2 column densities are high. Here we treat the photodissociation of H_2 in the optically thin limit and the dissociation rate in a volume constrained by causality within a radius, $r = ct$. The dissociation rate is given by $k_{\rm H_2} = 1.1\times10^8 F_{\rm LW}\,{\rm sec}^{-1}$, where $F_{\rm LW}$ is the flux within LW bands. For a Pop III star with $100\,M_\odot$, the dissociation rate of H_2 is (Greif et al., 2009b)

$$k_{\rm H_2} = \frac{3.38\times10^{-7}}{r_{\rm pc}^2}\quad {\rm sec}^{-1}. \tag{9.31}$$

Figure 9.2 shows a He II region created by a $100\,M_\odot$ Pop III star. When the first star evolves to the main sequence and stable hydrogen burning at the core occurs, its surface temperature quickly rises to $T\sim2\times10^5$ K and begins to emit a large amount of ionizing photons for neutral hydrogen and helium. The gas inside the host halo is

strongly photoheated to temperatures of $T \sim 2 \times 10^4\,\mathrm{K}$, which allows the gas to escape the gravitational well of the host halo, forming an outflow.

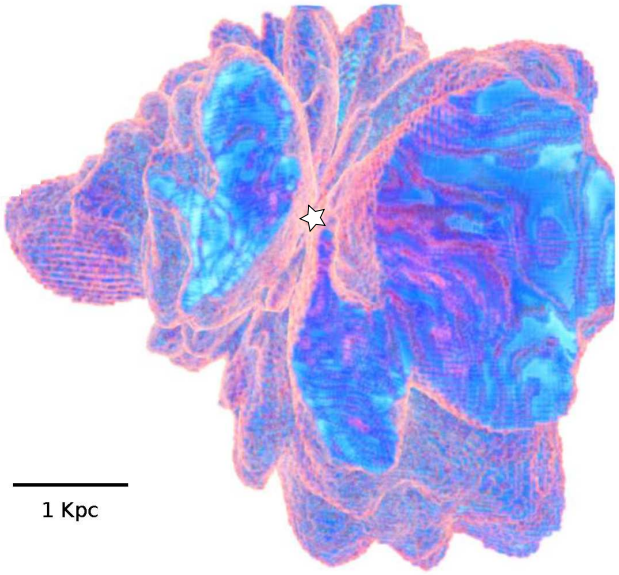

Figure 9.2: The He II region created by a $100\,\mathrm{M}_\odot$ Pop III star before it dies. The white star indicates the position of the star. The strong UV photons emitted from the star create an extensive He II region of a size about several kpc.

9.5 X-Ray Emission

A compact binary may be able to produce radiative feedback in the form of x-rays. In this section, we describe the treatment of the radiation from the x-ray binary. The algorithm of x-ray emission is based on Jeon et al. (2012). Instead of tracing the propagation of x-rays, we consider x-ray heating of the IGM. In the local Universe, the emission spectra from accreting back holes or neutron stars can be expressed as $F_\nu \propto \nu^\beta$, where ν is the frequency and β is the spectrum index. This spectra is from a combination of non-thermal synchrotron radiation and a multi-colored disk (MCD). By assuming that the BH emission physics in the early Universe is identical to that of the

local Universe, we apply the same spectra for the first black holes from the first stars.

The propagation of high-energy photons is assumed to form an isotropic radiation field, $\propto 1/r^2$, which only depends on the distance from the BH. The resulting photo-ionization and photo-heating rates can be written as (Jeon et al., 2012):

$$k_{\rm ion} = \frac{\dot{K}}{r_{\rm pc}^2}\left(\frac{\dot{M}_{\rm BH}}{10^{-6}{\rm M}_\odot\,{\rm yr}^{-1}}\right), \tag{9.32}$$

where

$$\dot{K} = [1.96, 2.48, 0.49]\times 10^{-11} \qquad {\rm sec}^{-1}, \tag{9.33}$$

and

$$\mathcal{H} = \frac{n_{\rm j}\dot{H}}{r_{\rm pc}^2}\left(\frac{\dot{M}_{\rm BH}}{10^{-6}{\rm M}_\odot\,{\rm yr}^{-1}}\right)\left(1-f_{\rm H/He}\right)\ , \tag{9.34}$$

where

$$\dot{H} = [7.81, 9.43, 1.63]\times 10^{-21} \qquad {\rm erg\,cm^{-3}\,sec^{-1}} \tag{9.35}$$

for H I, He I, He II, respectively. $n_{\rm j}$ is the number density of corresponding specie. $\dot{M}_{\rm BH}$ is the mass accretion rate and $f_{\rm H/He}$ are the fractions going to secondary ionizations.

Figure 9.3 shows the heating of the IGM from a x-ray binary. In this example, we assume the accretion rate dumping on the black hole is about $10^{-5}\,{\rm M}_\odot\,{\rm yr}^{-1}$. Unlike the ionizing photons, the x-rays can easily penetrate through the IGM because the cross section of the gas in IGM is relatively small to x-ray photons. The x-ray feedback can lead to the heating of the IGM in a broad and gentle way.

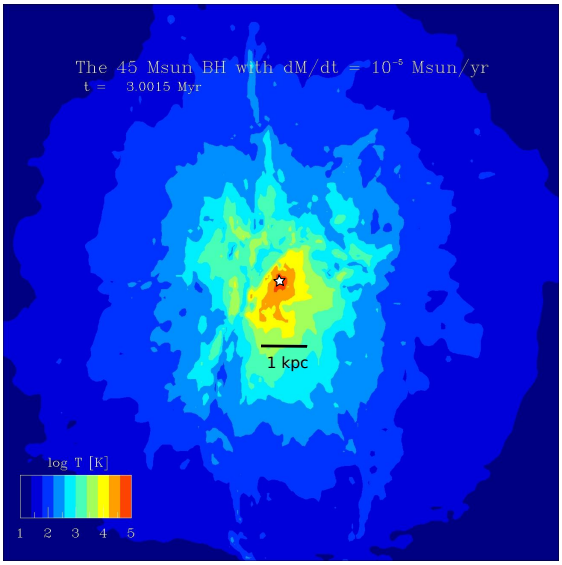

Figure 9.3: X-ray emission from the first compact binary: It shows the temperatures of the IGM heated by the first compact binary (the central white star) for 3 Myr.

9.6 Supernova Explosion and Metal Diffusion

After several million years, the massive Pop III stars eventually burn out their fuel, and most of them die as supernovae. As we discussed in Part I, the first supernovae are very powerful explosions accompanied by huge energetics and metals. In this section, we discuss how we model the SNe explosion in our cosmological simulation.

When the star reaches the end of its lifetime, we remove the star particles from the simulation and set up the explosions by injecting the explosion energy to desired particles surrounded by the previous sink. Because the resolution of the simulation is about 1 pc, we cannot resolve the individual SNe in both mass and space. Here we assume the SN ejecta is disturbed around a region of 10 pc, embedding the progenitor stars, in which most kinetic energy and thermal energy of ejecta are still conservative. We attach the metals to these particles based on the yield of our Pop III SN model. The explosion energy of hypernovae and pair-instability SNe can be up to $10^{52} - 10^{53}$ erg. For the iron-core collapse SN, it is about 1.2×10^{51} erg.

In our GADGET simulations, we are unable to resolve the stellar scale below 1 pc. However, the fluid instabilities of SN ejecta develop initially at a scale far below 1 pc. These fluid instabilities would lead to a mix of SN metals with the primordial IGM. Therefore, mixing plays a crucial role in transporting the metal, which could be the most important coolant for later star formation. To model the transport of metals, we apply a SPH diffusion scheme from Greif et al. (2009a) based on the idea of turbulent diffusion, linking the diffusion of a pollutant to the local physical conditions. This provides an alternative to spatially resolving mixing during the formation of supernova remnants.

A precise treatment of the mixing of metals in cosmological simulations is not available so far because the turbulent motions responsible for mixing can cascade down to very small scales, far beyond the resolutions we can achieve now. Because of the Lagrangian nature of SPH simulations, it is much more difficult than the direct modeling of mixing by resolving the fluid instabilities in SPH than in grid-based codes. However, we can assume the motion of a fluid element inside a homogeneously and isotropically turbulent velocity field, such as a diffusion process, which can be described by

$$\frac{\mathrm{d}c}{\mathrm{d}t} = \frac{1}{\rho}\nabla \cdot (D\nabla c), \tag{9.36}$$

where c is the concentration of a metal-enriched fluid-per-unit mass; D is the diffusion coefficient, which can vary with space and time; and $\frac{\mathrm{d}}{\mathrm{dt}}$ is the Lagrangian derivative. In SPH, the diffusion equation can be written as (Greif et al., 2009a)

$$\frac{\mathrm{d}c}{\mathrm{d}t} = \sum_j K_{ij}(c_i - c_j), \tag{9.37}$$

where the diffusion coefficient is

$$K_{ij} = \frac{m_j}{\rho_i \rho_j} \frac{4D_i D_j}{D_i + D_j} \frac{\boldsymbol{r}_{ij} \cdot \nabla_i W_{ij}}{r_{ij}^2}, \tag{9.38}$$

where i and j indicate the particle indices, m the mass, ρ the density, W_{ij} the kernel, and $\boldsymbol{r}_{ij}$,r_{ij} the vector and value of separations between two particles i and j. In GADGET simulations, the Courant condition limits the hydro time step and does not allow for large changes in the density between time steps, so Δt, Equation 9.37, can be integrated

$$c_i(t_0 + \Delta t) = c_i(t_0)e^{A\Delta t} + \frac{B}{A}(1 - e^{A\Delta t}), \tag{9.39}$$

with

$$A = \sum_j K_{ij}, \quad B = \sum_j K_{ij} c_j. \tag{9.40}$$

We can quickly examine Equation 9.39 by taking Δt to 0 and ∞. When Δt is close to 0, the concentration remains close to the original values. When Δt is close to ∞, concentration tends to average among neighboring particles.

After the SN explosion, metal cooling must be considered in the cooling network. We assume that C, O, and Si are produced with solar relative abundances, which are the dominant coolants for the first SNe. There are two distinct temperature regimes for these species. In low temperature regimes, $T < 2 \times 10^4\,\mathrm{K}$, we use a chemical network presented in Glover and Jappsen (2007), which follows the chemistry of C, C^+, O, O^+, Si, Si^+, and Si^{++}, supplemental to the primordial species discussed above. This network also considers effects of the fine structure cooling of C, C^+, O, Si, and Si^+. The effects of molecular cooling are not taken into account. In high temperatures, $T \geq 2 \times 10^4\,\mathrm{K}$, due to the increasing number of ionization states, a full non-equilibrium treatment of metal chemistry becomes very complicated and computationally expensive. Instead of directly solving the cooling network, we use the cooling rate table based on Sutherland and Dopita (1993), which gives effective cooling rates (hydrogen and helium line cooling, and *bremsstrahlung*) at different metallicities. Dust cooling is not included because the nature of the dust produced by Pop III SNe is still poorly understood.

Figure 9.4 shows a SN explosion at twenty million years after its onset. The metal of the SN has been dispersed to the IGM of a radius about 1 kpc. The SN ejecta has been cooled to temperatures below $10^5\,\mathrm{K}$ due to the metal cooling.

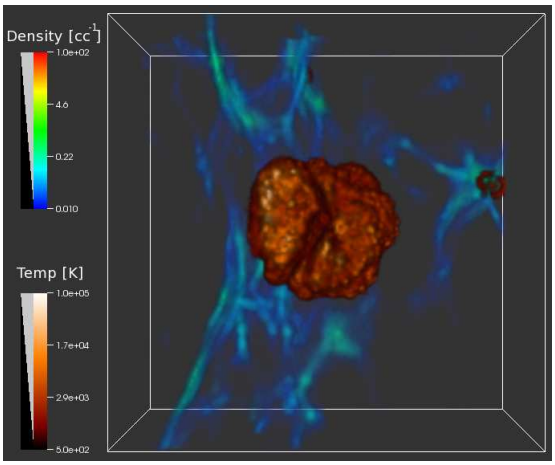

Figure 9.4: The first cosmic explosion. It shows the temperature (orange-hot color) and gas number density (hot color) distribution after one supernova exploded inside one of the minihalos. The physical size of the box is about 4 kpc at $z \sim 25$.

9.7 Code Performance

`GADGET` simulations that include several physical processes are very computationally expensive and must be run on supercomputers. It is good to know the scaling performance of the code so that we can better manage our jobs. To understand the parallel efficiency of `GADGET`, we perform a strong scaling study. The test problem is a ΛCDM problem including gas hydrodynamics of gas particles coupled with gravity of CDM, which started with the condition at $z = 100$ in a periodic box of linear size of 1 Mpc (comoving), using ΛCDM cosmological parameters with matter density $\Omega_m = 0.3$, baryon density $\Omega_b = 0.04$, Hubble constant $H_0 = 70\,\mathrm{kms}^{-1}\mathrm{Mpc}^{-1}$, spectral index $n_\mathrm{s} = 1.0$, and normalization $\sigma_8 = 0.9$, based on the CMB measurement from WMAP (Komatsu et al., 2009). The total number of particles for this problem is about 80 million (40 million for gas and 40 million for dark matter). This is the identical setup for our real problem, including the cooling and the chemistry of the primordial gas.

The purpose of the scaling test is to allow us to determine the optimal computational resources to perform our simulations and complete them within a reasonable time frame. We perform these tests on Itasca, a 10,000−CPU supercomputer located at the

Minnesota Supercomputing Institute. We increase the CPU number while running the same job and record the amount of time it takes to finish the run. For perfect scaling, the run time should be inversely proportional to the number of CPUs used. Figure 9.5 presents the results of our scaling tests. It shows a good strong scaling when the number of CPUs is $n_c \lesssim 300$. Once $n_c > 300$, the scaling curve becomes flat, which means the scaling is getting saturated, and $n_c = 256$ seems to be a turning point. Hence we use $n_c = 256 - 384$ for our production runs.

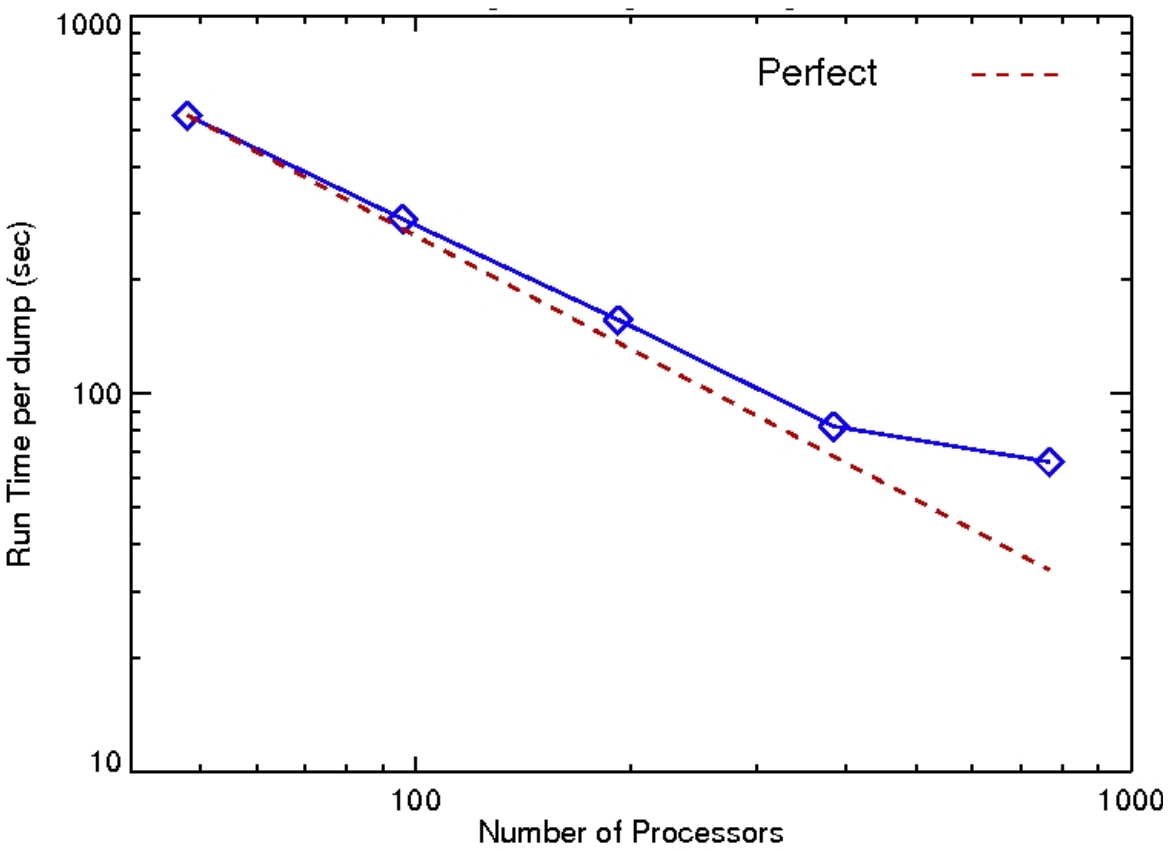

Figure 9.5: Strong scaling of `GADGET` on Itasca. The blue curve presents the scaling performance of `GADGET` on Itasca, and the red-dashed curve is the case of perfect scaling.

Chapter 10

Impact of the First Massive Stars

Recent studies of Pop III star formation suggest that the Pop III star-forming clouds can fragment to form binary or multiple stellar systems inside minihalos. In the chapter, we investigate the stellar feedback of Pop III stars of masses $60\,M_\odot$, $45\,M_\odot$, $30\,M_\odot$, and $15\,M_\odot$. We study the impact of single stars on their parent halos by considering radiation and chemical feedback from their supernovae.

10.1 New Mass Scale of the Primordial Stars

Modern cosmological simulations (Abel et al., 1997; Bromm et al., 1999) suggest that hierarchical assembly of dark matter (DM) halos provided the gravitational wells that allowed the primordial gas to form stars and galaxies inside them. As discussed in Chapters 1 & 8, the first generation of stars, Population III (Pop III) stars (Bond et al., 1984; Bromm and Larson, 2004; O'Shea et al., 2008), plays an important role in our understanding of the formation of the first galaxies. Pop III stars affected the early Universe in several different ways. Massive Pop III stars could emit strong UV radiation that built up extensive H II/He II regions. The metals forged in Pop III stars were later dispersed to the intergalactic medium (IGM) when stars died as supernovae (SNe), and quickly polluted the primordial gas that led to the formation of the second generation of stars (Population II stars) and the first galaxies (Barkana and Loeb, 2001; Bromm and Larson, 2004; Bromm et al., 2009). Different feedback mechanisms of the Pop III stars have been extensively studied by different groups, e.g., radiative feedback from

the Pop III stars (Abel et al., 2007; Yoshida et al., 2007; Greif et al., 2009a), chemical enrichment through the Pop III SNe (Wise and Abel, 2008; Greif et al., 2010a), and x-ray feedback from the Pop III remnant such as accreting black holes (Kuhlen and Madau, 2005; Alvarez et al., 2009; Jeon et al., 2012).

Results from stellar archaeology (Beers and Christlieb, 2005; Frebel, 2011), which studies the most metal-poor stars which kept the fossil imprints from the early Universe and possibly also from Pop III stars, in some cases do not support the chemical abundance pattern predicted from PSNe. In the yields predicted for PSN (Heger and Woosley, 2002), the elements of even atomic number are produced far more than those of odd atomic number due to the lack of neutron capture processes during the stellar evolution. There is no r-process or s-process. The Pop III CCSN models (Umeda and Nomoto, 2003; Heger and Woosley, 2010), however, can produce abundance patterns in good accord with the observation of metal-poor stars. Hosokawa et al. (2011) performed the simulations of Pop III star formation using the initial conditions from the cosmological simulations. Their results suggest that the radiation pressure from Pop III stars can halt the accretion and prevent the formation of stars more massive than $50\,M_\odot$. That implies that the fate of Pop III stars might largely fall in the regime of CCSNe instead of PSNe. Furthermore, recent cosmological simulations with higher resolutions have shown that the primordial gas cloud is able to fragment and produce stars of relatively lower mass of tens of solar masses (Turk et al., 2009; Stacy et al., 2010; Greif et al., 2011), organized in binaries or multiple stellar systems. Since these simulations only follow to the stage when the seed stars formed, it is still not clear whether these seed stars can merge again into single stars or become individual stars. However, these simulations suggest that fragmentation of the star-forming cloud may occur in the mini-halos, which suggests that the Pop III stars could have become less massive than we originally thought. Therefore, we study the impact of the first massive stars of masses $60\,M_\odot$, $45\,M_\odot$, $30\,M_\odot$, and $15\,M_\odot$ on their parent halos.

The structure of this chapter is as follows: in § 10.2 we describe the initial setup for single star models, and we detail our numerical approaches. The results of simulations are presented in § 10.3, and their impact is discussed in § 10.4.

10.2 Problem Setup

The primary code used for our simulations is the well-tested, massively-parallel cosmological code `GADGET` (Springel, 2005), which computes gravitational forces with a hierarchical tree algorithm and represents fluids by means of smoothed particle hydrodynamics (SPH). In order to simulate the stellar feedback of the stars, additional physical processes, such as chemical cooling, radiative transfer of ionizing photons from stars, and supernovae explosions, are required and have been implemented on `GADGET` (see Chapter 9).

Our simulations take the initial conditions from cosmological simulations from Greif et al. (2010a), which start with the condition at $z = 100$ in a periodic box of linear size of 1 Mpc (co-moving), using ΛCDM cosmological parameters with matter density $\Omega_m = 0.3$, baryon density $\Omega_b = 0.04$, Hubble constant $H_0 = 70\,\mathrm{kms^{-1}Mpc^{-1}}$, spectral index $n_\mathrm{s} = 1.0$, and normalization $\sigma_8 = 0.9$, based on the CMB measurement from WMAP (Komatsu et al., 2009). Greif et al. (2010a) used a standard zoom-in technique, a preliminary run with 64^3 particles; the study is hierarchically refined to generate the high-mass resolution inside the region resolving smaller structures such as the mini halos and the site for the first galaxy formations. It applied three consecutive levels of refinement; the mass of DM and gas particles in the highest resolution region is $m_\mathrm{DM} \sim 33\,\mathrm{M_\odot}$ and $m_\mathrm{sph} \sim 5\,\mathrm{M_\odot}$, respectively. Because the Jeans mass of primordial gas dominated by the molecular hydrogen cooling yields a characteristic density of $n_\mathrm{H} = 10^4\,\mathrm{cm^{-3}}$ and temperature of 200 K (Bromm et al., 2002), our current setup could marginally resolve the relevant scales.

Once the gas cloud is more massive than its Jeans mass, the gas quickly collapses and contracts toward its center, where the Pop III stars are born. In our current setup, we cannot follow the accretion of falling gas until the proto-star forms and the gas density can exceed $n_\mathrm{max} = 10^{22}\,\mathrm{cm^{-3}}$. Instead, we apply criteria for defining the Pop III star formation, the sink particle algorithm based on Johnson and Bromm (2007a). Once the hydrogen number density of a gas particle exceeds a threshold value of $n_\mathrm{max} = 10^4\,\mathrm{cm^{-3}}$, it is automatically converted into a collisionless sink particle that only interacts with other particles by gravity. This simple prescription for sink particles is sufficient to provide a marker for the position of a Pop III star and its remnants. In the simulations,

we cannot resolve the physical scale of stars. Hence, their stellar feedback is applied to the sink particles based on the sub-grid models that we describe in the following sections.

Stellar Models

We use stellar models of 15, 30, 45, and 60 $M_\odot$ from the library of Heger and Woosley (2010). These models do not include rotation, and there is also not mass loss due to stellar winds because of metallicity effect.

The stellar lifetimes are given in Table 10.1, and we separate out main-sequence (MS; central hydrogen burning) and post-MS (until supernova) evolution. In the case of the 15 $M_\odot$ star, we assume it explodes as a core-collapse supernova with 1.2×10^{51} erg = 1.2 B explosion energy. For our stars with initial masses of 30 $M_\odot$ and above, we assume that they do not explode as regular SNe by the core collapse mechanism for massive stars. Instead, we assume each will either collapse into a black hole (BH) and make no explosion, or explode as a hypernova (HN) with 10 B explosion energy (based on the collapsar model (Woosley, 1993)). The fates of the massive stars are summarized in Table 10.2. For simplicity and to limit the number of cases in this initial study, we focus only on these simplified, limiting cases. The metal yields from the explosions are taken from Heger and Woosley (2010) as well, where they were computed self-consistently for the respective explosion energies. Since our ray-tracing scheme cannot resolve a time scale less than a year, the radiation flash from the SN is not included here. In principle there could be flash of hard radiation from the shock breakout that may eventually be observable (Scannapieco et al., 2005), but the total energy in this flash is small, due largely to the predominantly small radii of the Pop III stars at the time of death. The radiation from the subsequent main part of the supernova light curve is largely at longer wavelengths and does not contribute much to the ionization. The amount of ionizing photons produced during SNe is less than 1 % of those produced in the main sequence. In a typical SN, only 1 % of the energy escapes in the form of radiation during the SN; 99 % goes into the kinetic energy of the ejecta. In the blue progenitors of SN stars, the light curve tends to be even fainter, so the ratio of radiation to kinetic energy is even more extreme.

Mass	MS	post-MS	total	fates	metals (SN/HN)
($M_\odot$)	(Myr)	(Myr)	(Myr)		($M_\odot$)
15	9.478	1.031	10.51	SN	1.388
30	5.208	0.509	5.77	BH, HN	6.876
45	3.995	0.394	4.39	BH, HN	13.26
60	3.426	0.345	3.77	BH, HN	20.66

Table 10.1: Stellar lifetimes and fates.

X[a]	Type	Masses	E^b	mass ejection	Notes
		($M_\odot$)	(B)		
S	SN	$\lesssim 25$	1.2	all but $\sim 1.5\,M_\odot$	leaves neutron star
B	BH	$\gtrsim 25$	0	None	complete collapse to BH
H	HN	$\lesssim 25$	10	$\sim 90\,\%$	big explosion, leaves black hole

Table 10.2: Summary of assumed stellar fate characteristics: [a] sentinel used in model names to indicate the fate of the star. [b] Explosion energy.

Mass	H I	He I	He II
($M_\odot$)	(10^{63})	(10^{63})	(10^{61})
15	0.64	0.16	0.10
30	1.82	0.72	1.37
45	2.98	1.45	4.34
60	4.18	2.21	8.31

Table 10.3: Number of ionizing photons emitted over the lifetime of a star.

Figure 10.1 shows the ionizing photon flux of the Pop III stars of $60\,M_\odot$ (S60), $45\,M_\odot$ (S45), $30\,M_\odot$ (S30), and $15\,M_\odot$ (S15). The flux increases with stellar mass. S60

produces about 10 times more H I photons than S15. For ionizing He II photons, the ratio of flux S60:S30:S15 is about 100:10:1. In Table 10.3, we list total ionizing photons emitted during the lifetime of stars. A $60\,M_\odot$ star produces about twice the amount of H I photons, six times more He II than a single $30\,M_\odot$ star. The ionizing power of a single $60\,M_\odot$ star seems to be stronger than that of two $30\,M_\odot$ combined. This implies that the overall radiation feedback of the first star can be weaker if a single mass fragments into multiple stars.

10.3 Results

Once the stars begin to shine, the gas inside the host DM minihalo is rapidly photo-heated up to temperatures of $T \sim 2 \times 10^4\,\mathrm{K}$ so that it can have sufficient kinetic energy and easily escape the gravitational well of the halo to form an outflow. The propagation of the I-front begins with a short supersonic phase (R-type), then switches to a subsonic phase (D-type) because the I-front is trapped behind a shock formed of photo-heated gas (Whalen et al., 2004). The I-front eventually is able to break out of the shock of gas and to propagate supersonically into the low-density IGM. Figure 10.2 shows the temperatures of the gas surrounded by the Pop III stars. A giant bubble of hot gas is created for each model, and the size of the bubble reflects its ionizing power, which depends on its mass. The shapes of the bubbles look very irregular and anisotropic, which is caused by the distribution of the IGM gas. As expected, the S60 creates the biggest and hottest bubble of a size about 5 kpc. S15 barely makes a bubble the size of 2 kpc, and its gas temperature is much cooler compared with the others.

To better evaluate the impact of the radiative feedback, we map the 3D structures onto 1D radial profiles in Figure 10.3. We first look into the density profile of photon-heated gas, which has escaped the host halo, and the gas density inside the halo has dropped below $0.2\,\mathrm{cm}^{-3}$. The outflow of gas extends to a radius of 100 pc, larger than the size of the host halo, so that radiative feedback can shut off the next star forming in the same halo by simply expelling its gas through radiation. Besides providing dynamic feedback, how do photons change the chemistry of the surrounding gas? Figure 10.3 also shows the H^+ fraction. The weaker UV source of S15 allows it to create a relatively smaller H^+ region. The H^+ region of S60, S45, and S30 has a radius about $1 - 2\,\mathrm{kpc}$,

which has an average gas temperature of about 10^4 K. This suggests that a single massive star of mass about $30\,M_\odot$ can create an extensive H II region in five million years. It is not clear whether the UV radiation can penetrate into nearby minihalos and affect their star formation. The ionization state of the gas lasts about $10 - 20$ Myr due to the cooling of the primordial gas.

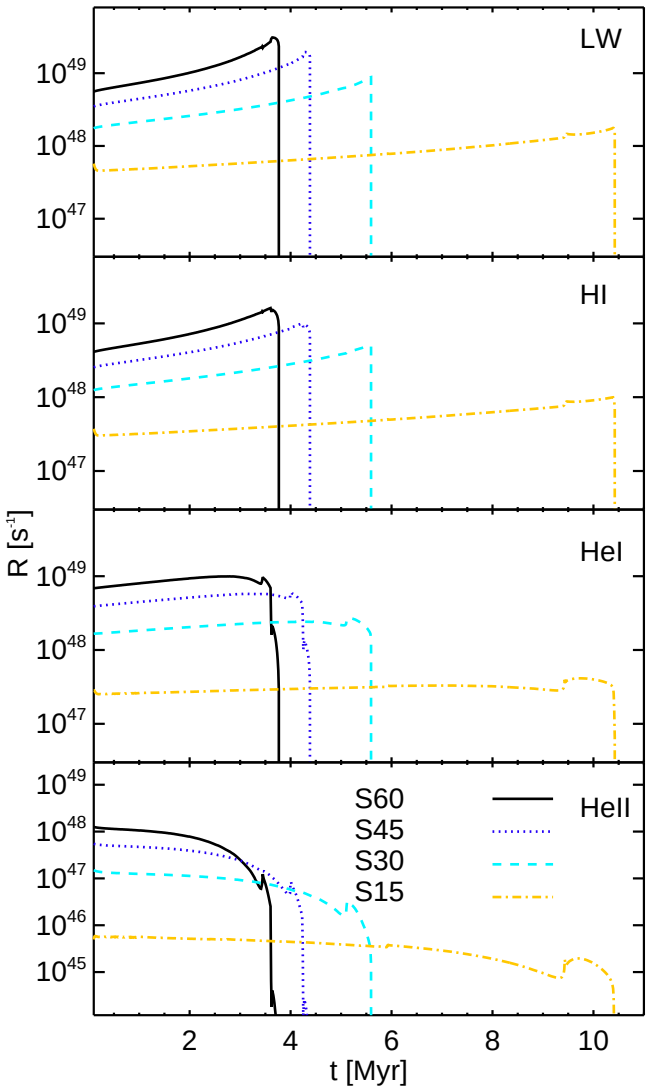

Figure 10.1: Evolution of the ionizing photon rate of 60 $M_\odot$, 45 $M_\odot$, 30 $M_\odot$, and 15 $M_\odot$ stars. When stars evolve onto the main sequence, the rates become uniform one million years before the stars die. After leaving the main sequence, the luminosity of the stars increases due to the expansion of the envelope leading a drop in temperature. It leads to an increase in the rates of H I ionizing photon (lower energy band) but a decrease in the rates of He I and He II ionizing photons (higher energy band).

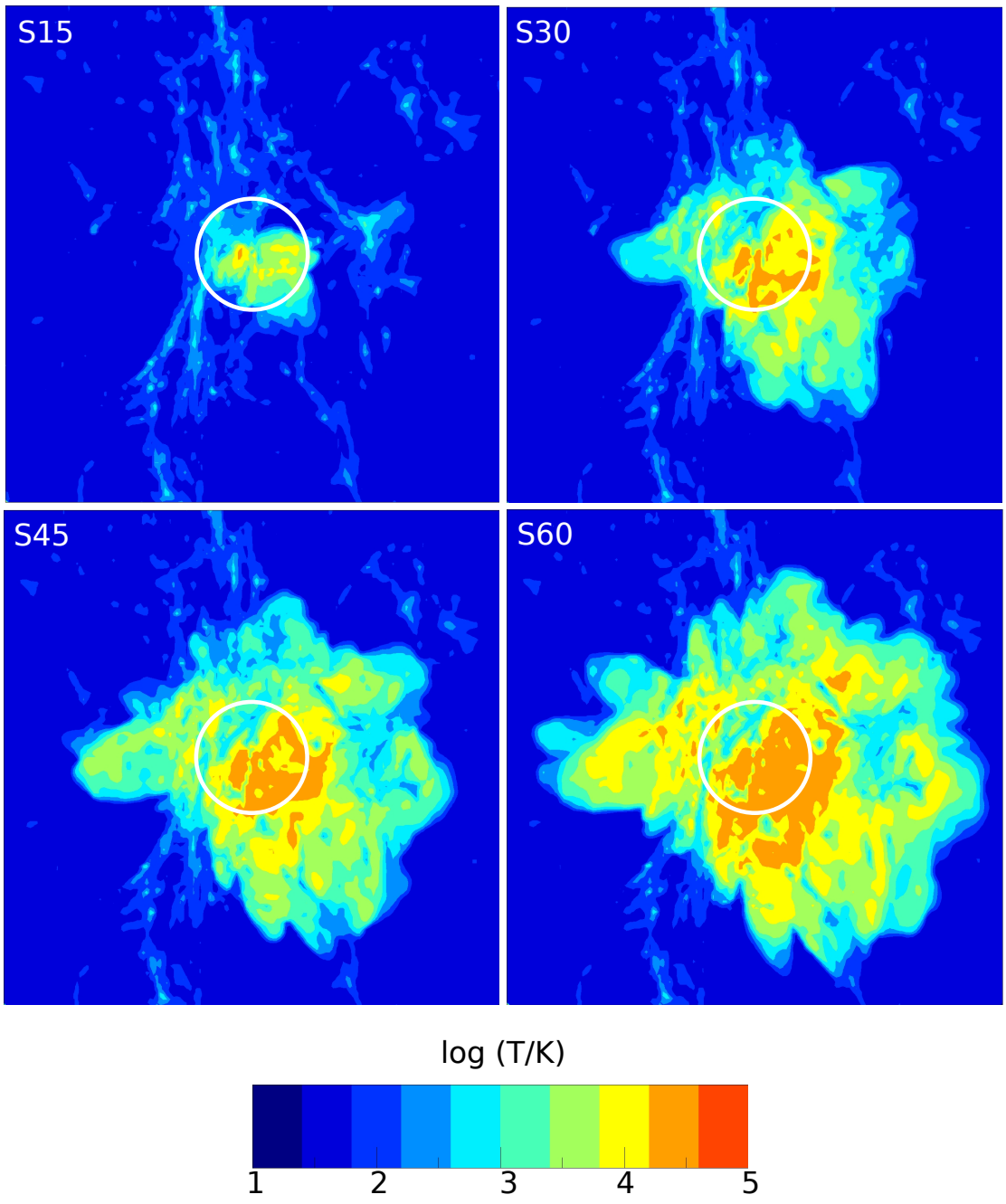

Figure 10.2: Radiative feedback of the first stars of S15, S30, S45, and S60. 2D colored maps show the gas temperatures around the first stars right after the death of the stars. The white circle has a radius of 1 kpc, and its center is located at the position of the star.

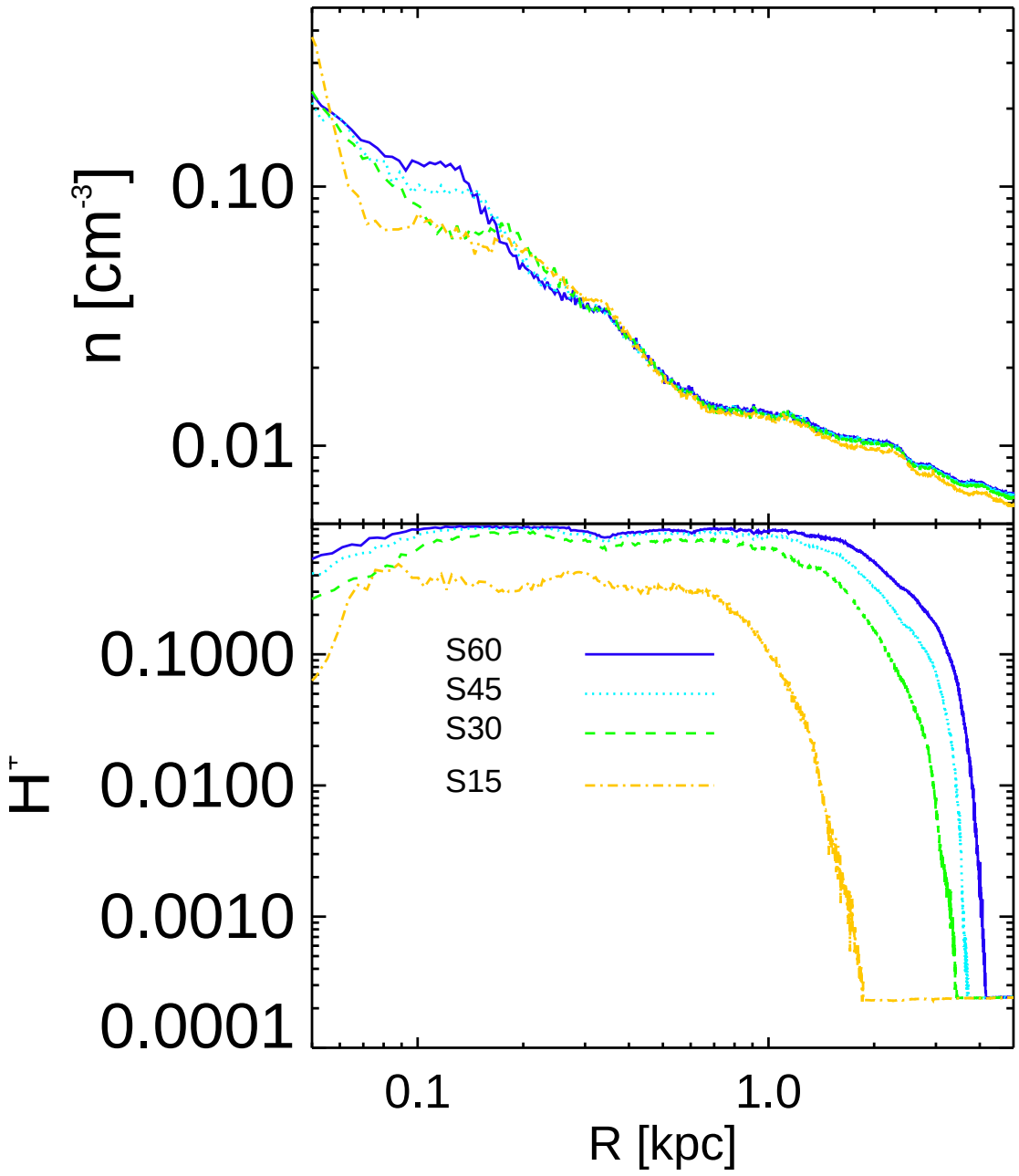

Figure 10.3: 1D profiles of density and H^+ fraction. The curves show the 1D projected profiles of density and H^+ fraction of the H II region created by the first stars.

10.3.1 Supernovae Explosions and Chemical Enrichment

When stars reach the end of their lives and die as SNe, we convert the star particle and surrounding collisionless particles into normal gas particles. The explosion energy and metals are injected into these converted gas particles. There are usually $100 - 200$ particles to carry the explosion energy and total metals. The hot ejecta first heat the surrounding gas; it creates a shock wave traveling at $10^9\,\mathrm{cm\,sec^{-1}}$ and reheats the relic H II region, which started to cool because of the death of the star. This shock works an alternative way of radiative feedback from SN and keeps warming the gas for an additional two million years. The shock can travel so fast because the density of the IGM is very low. The rewarming may keep the gas from collapse for some time. After the shock dissipates, the hot and metal-rich ejetca starts to propagate outward, forming a giant metal bubble. Because the resolution is insufficient to resolve the mixing caused by the fluid instabilities, we simulate mixing of metals with primordial gas by using a diffusion scheme based on Greif et al. (2009b).

The SNe inject both their energetics as well as the heavy elements freshly made out of its progenitor stars to the IGM of primordial gas. What does the overall feedback look like 15 Myr after the birth of a star? Figure 10.4 shows the resulting feedback of UV radiation and SNe/black holes 15 Myr after the birth of stars. At this moment, all stars have died as SNe or black holes, and the SNe ejecta has almost stalled for each case. We compare the cases of BHs and SNe. BHs here mean no additional feedback is taken into account in Figure 10.4. The simulations of BH feedback are followed with dynamics of gas and dark matter, cooling, and background cosmology. The cooling takes heat away from the relic photo-heated gas and decreases the temperature of H II from $10^4\,\mathrm{K}$ to about $10^3\,\mathrm{K}$. The H^+ starts to recombine with free e^+. In the case of S15, the star dies as a CCSN with an explosion energy about 1.2 B and a mass of $1.38\,\mathrm{M_\odot}$ of metals. Its metals are dispersed to a radius about 0.5 kpc with an average metallicity of $10^{-4} - 10^{-5}\,Z_\odot$. The S30, S45, and S60 are injected with an explosion energy of 10 B and carry out 6.87, 13.26, &20.66 $\mathrm{M_\odot}$ of metals, respectively. The size of the metal bubble has reached a radius of 1 kpc and chemically enriches the IGM to $10^{-2} - 10^{-4}\,Z_\odot$. One important question is whether the enrichment is homogeneous or very patchy. Overall results show a reasonable homogeneous mix. However, S60 shows some patchy sites of high-metallicity ($10^{-2}\,Z_\odot$) regions.

Figure 10.5 shows the projected profile of gas density and metallicity. The strong SNe blast now almost vacates the halo gas density, $n < 0.01$, which is about one magnitude lower than the IGM. The extent of void for CCSN and HN is about 200 pc and 500 pc, respectively. It is unlikely that consecutive star formation can occur at the same halo site at this time. The 1D profiles of metallicity suggest that for the same explosion energy to exist, the metallicity of S30 must be enriched slightly more rapidly than S45 and S60 because the ejecta of S30 have a higher velocity.

10.4 Discussion

We have presented the results from our cosmological simulations of the impact of the Pop III stars. We consider the realistic stellar feedback by using the updated Pop III star models. The single massive stars provide more abundant ionizing photons and quickly build up the H II in comparison with the lower-mass binaries. Instead of assuming the stars die as pair-instability supernovae, we apply the premise that the stars die as hypernovae with an explosion energy of $\sim 10^{52}$ erg, about ten times greater than the typical core collapse supernovae. Such explosions easily disperse the mass around the host halo and chemically enrich the IGM to an average metallicity of about $10^{-4}\,Z_{\odot}$ to an extent of 2 kpc. If the first galaxy was made of $10-100$ minihalos, we can expect that the average metallicity inside the first galaxies can be easily boosted to $10^{-3}\,Z_{\odot}$. Pop II star formation would then occur. Pop III stars impact their surroundings via different feedback mechanisms, as we discussed above. The feedback critically affects the baryonic contents of later structure formation. Using the forthcoming telescopes, such as the James Webb Space Telescope (JWST), we will have opportunities to examine our simulations to gain a better understanding of the stellar feedback of the first stars.

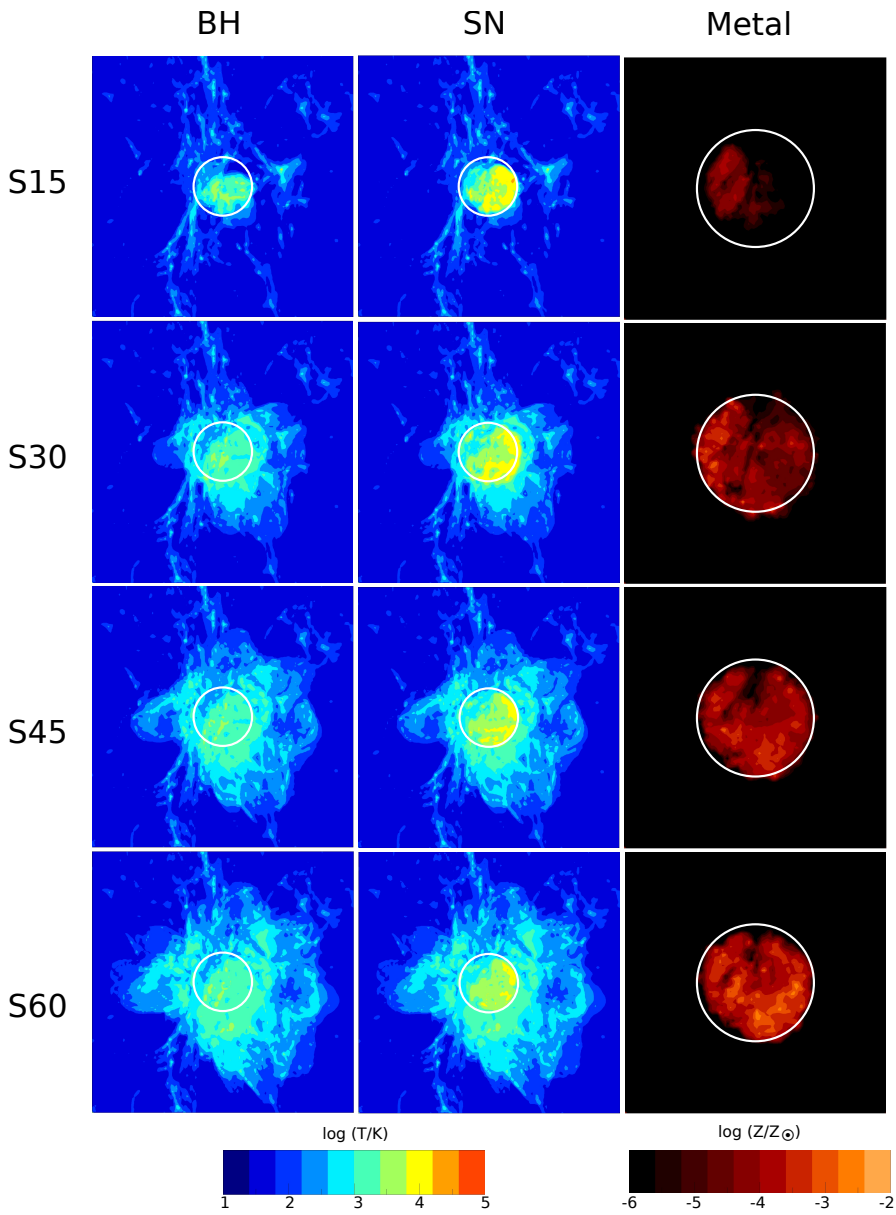

Figure 10.4: Comparison of the resulting feedback 15 Myr after the birth of the stars. The stars die as black holes or supernovae. For the scenario of black holes, their ray sources are simply shut down and no further feedback occur. If the star dies as a supernova, the third column panels show the metal distribution. The white circles have a radius of 1 kpc with the centers at the location of stars.

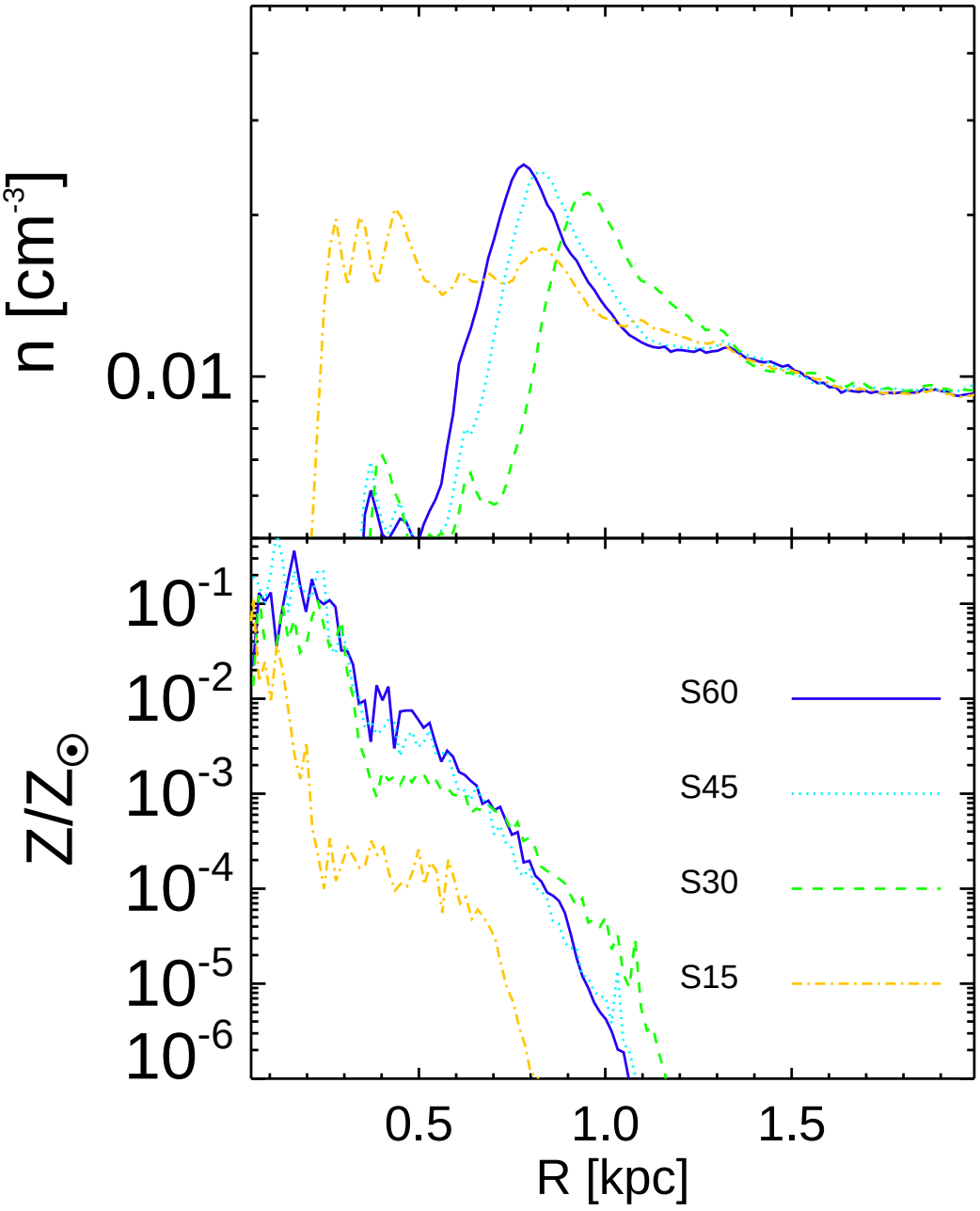

Figure 10.5: 1D profiles of density and metal distribution after the stars die as SNe. The gas density within the host halos has dropped to less than $0.005\,\mathrm{cm}^{-3}$. The ejected metal is mixed up to a radius of $\sim 1\,\mathrm{kpc}$ for S60, S45, and S30.

Chapter 11

Impact of the First Binaries

Recent studies of Pop III star formation suggest that the Pop III star-forming clouds can fragment to form binary or multiple stellar systems inside minihalos. We investigate the stellar feedback of Pop III binaries, comparing them with a single-star case. Specifically, we compare systems in which a mass of $60\,M_\odot$ goes into stars, varying from single stars to ones split up in binary stars of $30\,M_\odot + 30\,M_\odot$ stars or to an asymmetric binary of $45\,M_\odot + 15\,M_\odot$. We compare the impact of the binaries and the single star by considering radiation and chemical feedback from supernovae. We consider different scenarios for the first binary systems including the x-ray binary from the asymmetric case.

11.1 Formation of the First Binaries

Recent cosmological simulations with higher resolutions have shown that the primordial gas cloud is able to fragment and produce stars of a relatively low mass of tens of solar masses (Turk et al., 2009; Stacy et al., 2010; Greif et al., 2011) organized in binaries or multiple stellar systems. Since these simulations follow only to the stage when the seed stars form, it is still not clear whether these seed stars can merge again into a single star or remain individual stars. However, these simulations suggest that binary systems may be the promising channel for star formation in the minihalos. Since the evolution of the binary systems and their impacts to the IGM are different from those of a single star, it is worth investigating the feedback of the Pop III binary systems and studying how they affected the IGM and their host halos that later formed into

the first galaxies (e.g., Bromm and Yoshida, 2011). The evolving binaries might affect their host halos and the surrounding IGM through different feedback mechanisms, such as ionizing photons, supernova explosions, and x-rays. That it can be quite different from the feedback of the single stars which has been documented in the literature. In this chapter, we study the possible impacts of the first binary systems on the IGM and present the results of cosmological simulations by considering possible outcomes of the Pop III binary models with stars of $45\,M_\odot$+$15\,M_\odot$ (S45+S15) and $30\,M_\odot$+$30\,M_\odot$ (S30+S30). Our binary models consider the non-interacting binaries during their stellar evolution. However, more realistic binary models might have a much wider range of outcomes (Langer, 2012).

The structure of this chapter is as follows: in § 11.2, we describe the initial setup, including single and binary star models, and our numerical approaches. Our simulation results are presented in § 11.3, and their impact and comparison to previous results are discussed in § 11.4. Final summaries and conclusions are given in § 11.5.

11.2 Problem Setup

The primary code used for our simulations is `GADGET` (Springel, 2005), including chemical cooling, radiative transfer of ionizing photons from stars, x-ray emission, and supernovae explosion (see Chapter 9). The initial conditions for the first binary are identical to those in Chapter 10. In this section, we discuss the stellar models and stellar evolution assumptions we use in the simulations.

Binary Star Models

We study binary stars with a total mass of $60\,M_\odot$, specifically a system with two stars of equal mass (mass ratio 1:1) and another one with a mass ratio of 3:1, as suggested by star-formation simulations of the first stars. Binary stars with (close to) equal mass are common in the local Universe (Shu et al., 1987; Larson, 2003). To maintain the simplicity of the model, we assume there is no merger of binary stars, and we do not consider mass ejection as a crude approximation. We are aware of and advise the reader of the shortcomings of this crude simplification (Langer, 2012).

For our stars with initial masses of $30\,M_\odot$ and above, we assume that they do not

explode as regular SNe by the core collapse mechanism for massive stars. Instead, we assume each will either collapse into a black hole (BH) and make no explosion, or explode as a hypernova (HN) with 10 B explosion energy based on the collapsar model in Woosley (1993). For the asymmetric case ($45\,M_\odot + 15\,M_\odot$), we consider a case in which we assume the black hole accretes from the companion star and becomes an x-ray binary (XRB). We assume the system becomes an x-ray binary immediately after the primary star collapses into a black hole. For the hypernova case, we assume the majority of the mass is ejected from the system, and hence the system becomes unbound. In the black hole case, we approximate that all mass collapse into the black hole and that there is no kick, hence the system remains bound. We assume very weak winds for Pop III stars (Kudritzki, 2002), and hence there is no notable x-ray source from stellar winds. It seems somewhat artificial, but it might occur in some rare circumstances should the primary star have kick in just the right direction and with the right magnitude. We summarize the scenarios of our stellar evolution models:

1. 30+30 (HN)
   Both binaries first shine together for 5.7 Myr, then both stars die as HNe.

2. 30+30 (BH)
   Both binaries first shine together for 5.7 Myr, then both stars die as BHs.

3. 45+15 (BH) close binary
   Both stars first shine together for 4.39 Myr, then the $45\,M_\odot$ star dies as a black hole and forms an x-ray binary by transferring the mass onto the black hole remnant of the $45\,M_\odot$ star. Because of the significant mass loss due to mass transfer, the $15\,M_\odot$ dies as a white dwarf without a SN explosion.

4. 45+15 (HN) close binary
   Both stars first shine together for 4.39 Myr, then the $45\,M_\odot$ star dies as a HN. The $15\,M_\odot$ star evolves for another 6.01 Myr then dies as a CCSN.

Other possible cases are present: in a close binary case, the orbital velocity is high, and the $15\,M_\odot$ star will be ejected at several $100\,km\,s^{-1}$; for the wide binary case, the kick velocity is small, and the star will die essentially at the location of the original binary. But even in the close binary case we find that the ejection velocity likely is too

small for the star to travel a significant distance, about $0.1\,\mathrm{kpc\,Myr^{-1}}$, by assuming that the ejection speed of the companion star is about $100\,\mathrm{km\,s^{-1}}$ before it goes supernova. Thus, both cases are practically identical in terms of the dynamics of the ejecta, and we do not need to distinguish them.

Case	Masses	Separation	Fate	Fate	metals (SN/HN)
	($M_\odot$)	(distance)	1	2	($M_\odot$)
I	30+30	wide	HN	HN	13.74
II	30+30	wide	BH	BH	0.00
III	45+15	close	BH	..	0.00
III	45+15	close	HN	..	13.26
IV	60	..	HN	..	20.66

Table 11.1: Summary of binary model characteristics.

Figure 11.1 shows the ionizing photon flux of the Pop III binaries of $45\,M_\odot + 15\,M_\odot$, $30\,M_\odot + 15\,M_\odot$, and a single star $60\,M_\odot$. The ionizing photon rates are comparable within a factor of 2. However, the ionizing power of a single $60\,M_\odot$ star seems to be stronger than the other two binary cases. It implies that the overall radiation feedback of the first star can be weaker if a single massive entity fragments into multiple stars.

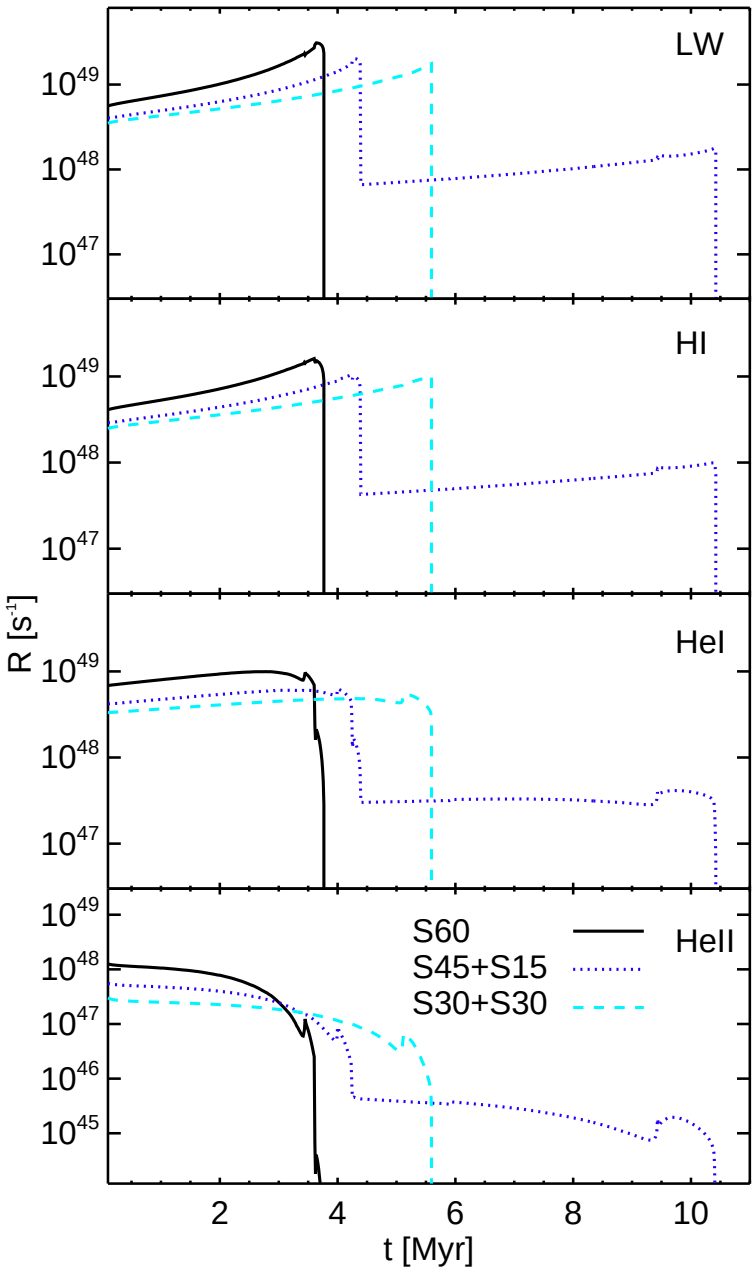

Figure 11.1: Evolution of the ionizing photon rate of the first binaries. The rate for each model is roughly uniform when the star enters the main sequence. At one million years before the stars die, the luminosity of the stars increases due to expansion, but the temperature drops. That leads to an increase in the rates of H I photons (lower energy band) but decreases the rates of He I and He II photons (higher energy band).

Table 11.2 lists the total of ionizing photons produced during the stellar evolution. The amount of ionzing photons for neutral hydrogen of S30+S30 and S45+S15 are very similar. For more energetic photons for ionizing He II, the table shows some difference among models. This is caused by the higher surface temperature for more massive stars.

Binary	H I (10^{63})	He I (10^{63})	He II (10^{61})	t_*^a (Myr)
S30+S30	3.64	1.44	2.74	5.77
S45+S15	3.62	1.61	4.43	10.51
S60	4.18	2.21	8.31	3.77

Table 11.2: Number of ionizing photons emitted over the lifetime of binary models, ^{a}: lifetime of a binary star (longest-lived component).

11.3 Results

11.3.1 Radiative Feedback

The first Pop III binary formed at a redshift of $z \sim 28$ inside a $5 \times 10^5 M_\odot$ DM minihalo in our simulations. Once these binaries evolve to the main sequence when the stable hydrogen burning at the core occurs, their surface temperature quickly rises to $\sim 10^5$ K and they begin to emit a large amount of ionizing photons for helium and hydrogen. Instead of using a constant surface temperature for the stars, we follow the evolution of the surface temperature based on the 1D Pop III stellar models from Heger and Woosley (2010) because the assumption of a constant surface temperature may be invalid at the late-time evolution of stars when the hydrogen shell burning occurs. Such burning expands the hydrogen envelope and decreases the surface temperature. This leads to an increase in the emission rate for H I, but it decreases rates for He I and He II. Once the stars begin to shine, the gas inside the host DM minihalo is shortly photo-heated to temperatures of $T \sim 2 \times 10^4$ K so that it can have sufficient kinetic energy and easily escape the gravitational well of the halo to form an outflow. The propagation of the I-front begins with a short supersonic phase (R-type), then switches to a subsonic phase (D-type) because the I-front is trapped behind a shock formed of photo-heated gas. The

I-front is able to break out of the shock of gas and propagate supersonically into the low-density IGM (Whalen et al., 2004).

Figure 11.2 shows the temperatures of gas surrounding the Pop III binaries and stars. A giant bubble of hot gas is created for each model, and the size of the bubble reflects its ionizing power. The shapes of the bubbles look very irregular and anisotropic; this is caused by the distribution of the IGM gas. This butterfly-like structure is related to the filaments of the structure in which photons tend to propagate further along voids among the filaments. The S60 creates the biggest and hottest bubble, of a size about 5 kpc. The size of the bubbles for both binaries looks very similar. The S30+S30 shows a slightly higher temperature than does the S45+S15 one.

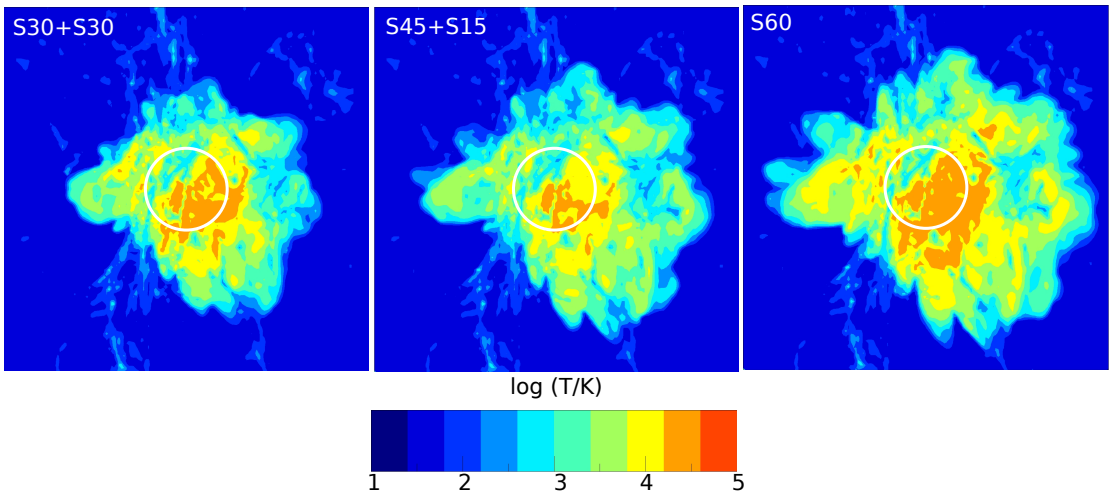

Figure 11.2: Radiative feedback of the first binaries of S30+S30, S45+S15, and a single massive star of S60. 2D colored maps show the temperatures around the first stars after the death of the stars. The white circle has a radius of 1 kpc, and its center is located at the position of the binaries or star.

To study the impact of the radiative feedback more closely, we map the 3D structures onto 1D radial profiles, as shown in Figure 11.3. We first look into the density profile of photon-heated gas. Photon heating by the first binaries has decreased the gas density of the host halo below $0.2\,\mathrm{cm}^{-3}$. The outflow of gas extends to a radius of 100 pc, which is larger than the size of the host halo. As in the single-star models, the radiative feedback

from binaries also shuts off the subsequent star formation in the same halo by expelling the gas. In addition to dynamic feedback, UV radiation also changes the chemistry of the IGM. Figure 11.3 show that that H^+ regions created by the first binaries are about $1-2$ kpc within five million years. This ionization state may last about ten or twenty of million years because of the cooling of the primordial gas. However, it is not clear if the UV radiation can penetrate nearby minihalos and affect their star formation.

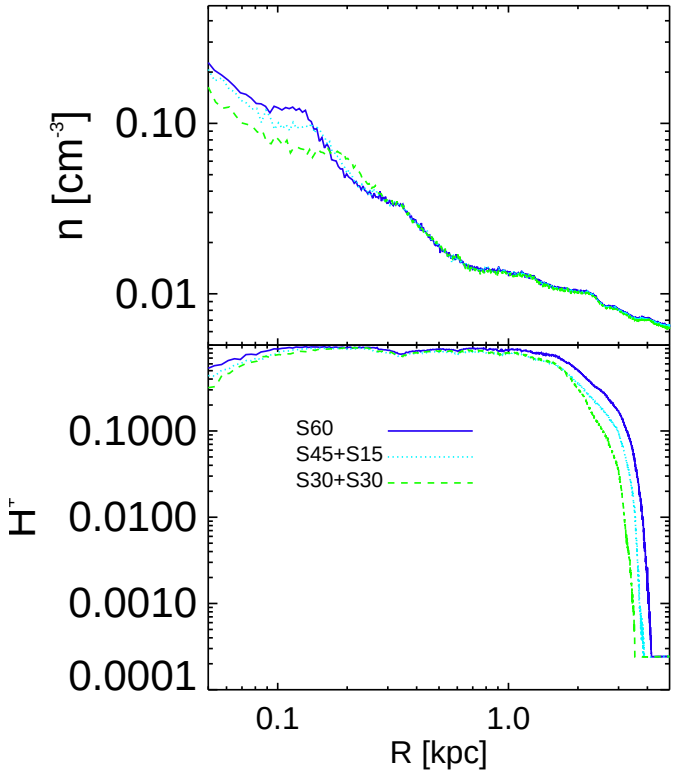

Figure 11.3: 1D profiles of density and H^+ fraction. The curves show the 1D-projected profiles of density and H^+ fraction of the HII region created by the first binaries.

11.3.2 Supernova Feedback

Massive stars and binaries tend to die in more much spectacular ways, as supernovae, in energetic explosions. Unlike previous popular pair-instability models for explosions,

we have core-collapse supernovae, including hypernovae for the $60\,M_\odot$ star. After the first star dies and injects the energetics and metals from SNe explosions, the hot SN ejecta with temperatures of $10^5 - 10^6\,K$ first creates a shock, which travels at a velocity of about $3 \times 10^4\,km\,s^{-1}$. This shock travels much faster than the ejecta and re-heats the relic H II. This shock works an alternative way of radiative feedback from the SN. But the cooling of primordial gas then starts to decrease the IGM temperature. The SN ejecta is now dispersed to the primordial IGM. The giant metal bubble is created and expands until its pressure is equal to the pressure of the IGM. The metallicity of the inner part of the SN ejecta fluctuates because of the highly clustered gas distribution around the host halo and the mixing process of the metals.

Now the first binaries reach the end of their lives and die as SNe or x-ray binaries. We first discuss the case of SNe explosions for S30+S30. The SNe inject both their energetics as well as the freshly made heavy elements produced by its progenitors to the pristine gas. The S30+S30 model assumes two $30\,M_\odot$ stars die as HNe at the same time. Figure 11.4 shows the metal enrichement of S30+S30 and S60 about 15 Myr after the birth of the stars. At this moment, the SNe ejecta is almost stalled in each case. The size of the metal bubbles looks similar. However, S30+S30 eject about $14\,M_\odot$ of metal. S60 ejects about $20\,M_\odot$ of metals and shows a relatively higher enrichment than S30+S30.

We compare the case of BHs and SNe. BHs here mean no additional feedback is taken into account, as is shown in Figure 11.4. BH feedback simulations are followed with dynamics of gas and dark matter, cooling, and background cosmology. The cooling takes heat away from the relic photo-heated gas and decreases the temperature of H II from $10^4\,K$ to about $10^3\,K$. H^+ then starts to recombine with free e^+.

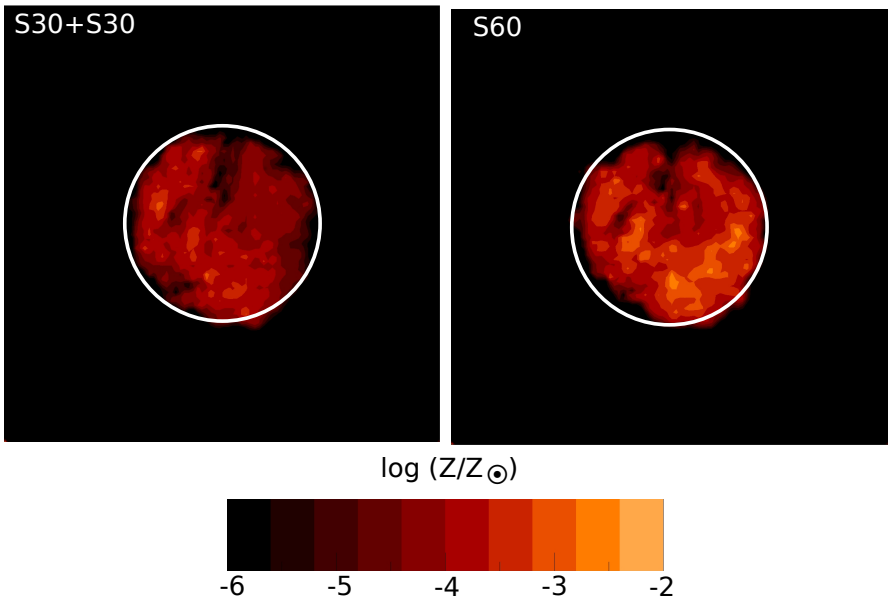

Figure 11.4: Metal distribution of the first star and binary. Two panels show the metals from S30+S30 and S60, respectively.

Figure 11.5 shows the projected profile of gas density and metallicity. The strong SNe blast now almost vacates $n < 0.01\,\mathrm{cm}^{-3}$ with a radius of 500 pc, which is about one magnitude lower than the IGM. SN explosions demonstrate a stronger kinetic feedback to the host halo than their radiative feedback of progenitor stars. Under such a low gas density, formation of another star in the same halo would be very unlikely at this moment. The only realistic possibility for the next star formation occurs after the mergers of the host and other halos later, which would provide a deeper gravitational well for star formation. The HN explosions of S30+S30 have polluted the pristine IGM with $10^{-3.5} - 10^{-5}\,Z_{\odot}$ with $r \sim 1\,\mathrm{kpc}$.

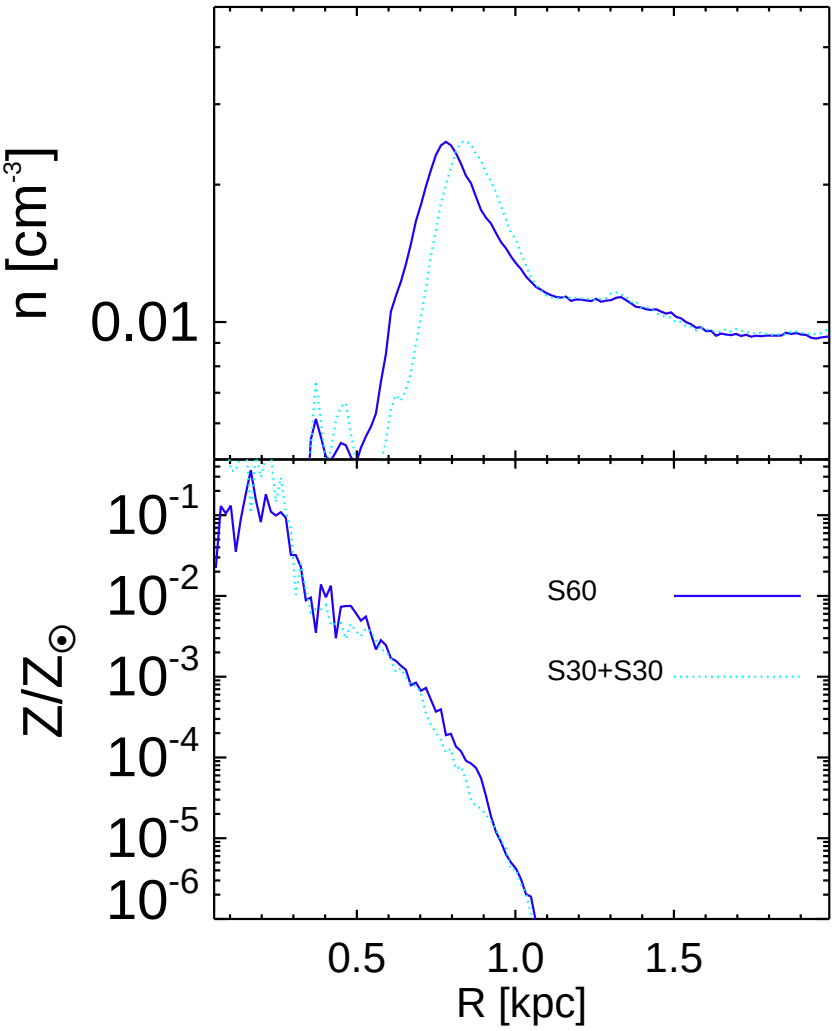

Figure 11.5: Density and metal distribution of the first star and binary.

11.3.3 X-Ray

One particularly interesting element of S45+S15 is its x-ray feedback. Because of the uncertainty of the stellar evolution model, $45\,M_{\odot}$ can possibly die into a black hole instead of blowing up as a SN. If both stars are closely separated, mass transfer from the

$15\,M_\odot$ star to the $45\,M_\odot$ black hole becomes possible. Mass accretion onto the compact object can efficiently extract the gravitational energy of the in-falling mass and turn it into the thermal energy of the accretion disk that can emit the strong x-rays. Unlike the ionizing photons from stars, the x-rays can more easily penetrate the IGM because there is lower metallicity in the primordial IGM. The energy of the x-ray can be deposited in the IGM through Compton scattering. Here we assume the constant accretion rate onto the central black hole is about $10^{-6}\,M_\odot\,yr^{-1}$, which allows the companion star to transfer its mass for several million years. Figure 11.6 shows a comparison of the fates of the first binaries, which become black holes or x-ray binaries. Without additional feedback, the temperatures of the relic H II quickly cool down so that the H^+ fraction decreases. Instead, the x-ray binary supplies an additional x-ray heating to maintain the temperatures of relic H^+. The magnitude of the x-rays depends on the accretion rate. The morphology of IGM temperatures due to the x-ray heating looks roughly spherical in symmetry. Because the IGM is optically thin for x-ray photons, its heating impacts a much more extensive region than does UV emission. We find the x-ray feedback may penetrate the gas of nearby halos and delay their star formation.

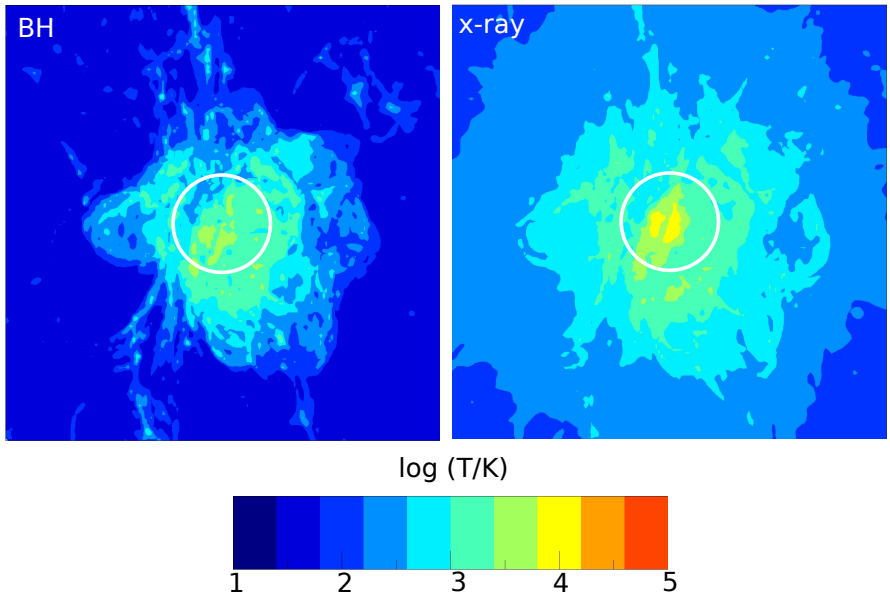

Figure 11.6: Radiative feedback of the x-ray binary; S45+S15. The 2D colored map shows the temperatures around the first x-ray binary. The accretion rate from the companion star S15 onto the central black hole is $10^{-6}\,M_{\odot}\,yr^{-1}$. The white circle has a radius of 1 kpc, and its center is located at the first binary.

11.4 Discussion

The first binary provides fewer ionizing photons than does a single massive star with a similar mass during its lifetime. A single massive star creates a more extensive photon-heated region when the star dies. However, it also leads to the larger flux but relatively shorter lifetime of the massive star, and the IGM cooling is somewhat faster, which means the temperature heated by the ionizing photons can drop in a time scale of ten million years. The lower-mass binary instead provides a relative stronger heating of the IGM because of their long life-span. The initial gas inside minihalos is driven out by the ionized photons. That happens in both the single and binary cases. In the photon-heated region, the gas temperatures rise to about $10^4\,K$, and the gas can easily escape the gravitational wells of the halos. The halo temperature is independent of the rate of ionizing photons of the stars; nevertheless, it would not exceed the surface temperature

of the star. For the density impact, the low-mass binary pushes gas farther than a single massive star because of the long time scale in pushing the gas out of the halo. This ejected gas from the host halo would prevent the second generation of stars from forming inside the previous halos hosting the Pop III stars for two reasons: there is not enough fuel for star formation, and it must wait until the collapse of later halos and subsequent gas infusions to foster the later star formation. Unlike the ionizing photons, the x-rays can easily penetrate the IGM because of the limited but not negligible cross section through the IGM for x-ray photons. The feature of x-ray feedback can impact the relic with a broad and gentle heating that even suppresses the region of relic H II and heats its surrounding temperature by a factor of two. More significant is that the duration of the x-ray binary can be at a time scale much longer than that of a single massive star. The uncertainty is in the mass transfer rate from the companion star to the central black hole; that sets the upper limit of the accretion time scale.

11.5 Conclusions

We have presented the results from our cosmological simulations of the impact of the Pop III binaries. We consider the most realistic stellar feedback by using the updated Pop III binary models. The single massive star provides more abundant ionizing photons and quickly builds up the H II in comparison with the lower-mass binaries. Instead of assuming the stars die as pair-instability supernovae, we postulate that the stars die as hypernovae with an explosion energy $\sim 10^{52}$ erg, about ten times that of the typical core collapse supernovae. Such explosions easily disperse the mass around the host halo and chemically enrich the IGM with a metallicity of about 10^{-4} $Z_{\odot}$. The Pop III binaries die as core collapse supernovae, hypernovae, or x-ray binaries. The supernovae from the binaries can drive strong metal bubbles similar to those of the single star. The difference in explosion energy results in a different size of the metal bubble. However, due to having comparable stellar masses, the size and level of enrichment for single stars and the binaries are very similar. But all SN metals cannot be retained inside the original host halo of the stars. We also investigate the x-ray scenario of the compact binaries. X-ray emission has a broad impact on the IGM because of the high degree of penetration of x-rays. If the x-ray binaries occur frequently for the Pop III stars, it

can have a significant impact on the mass scale of the collapse of the first galaxies by heating the IGM with x-rays.

In comparing the impacts for different models, we conclude that different types of the first stellar feedback play very important roles. The low-massive stars/binaries offer a lasting heating of the IGM and have an effective way to change the IGM. Another impact comes from the metals of SN. In the models presented here, the metal enrichment is created metal bubble of a physical size of 2 kpc with $Z \sim 10^{-4}\, Z_{\odot}$ in about 5 Myr. If one first galaxy contains $10 \sim 100$ minihalos, we can expect that the average metallicity inside the first galaxies can be easily boosted to $10^{-2} - 10^{-3}\, Z_{\odot}$, and the Pop II star formation would be able to occur. The collapse of mass-scale entities is still uncertain because the population of the Pop III stars is unknown. The Pop III binaries impact the IGM and their host halos in a manner similar to that of the single star during the stellar evolution and supernova phases. The interaction of binaries provides an alternative because it impacts their surroundings by emitting x-rays. With the forthcoming telescopes, such the James Webb Space Telescope (JWST), we have opportunities to spot the birth of the first stars, supernovae, and galaxies. The Pop III stars and binaries impact their surroundings via different feedback mechanisms, as we discussed earlier. These feedback differences critically affect the baryonic contents of later structure formation. Pop III binaries can impact the early Universe differently from the way that single stars can. By carefully examining the future data, we may discover that the fingerprints of their impacts shine a light on our understanding of the populations of the Pop III stars.

Part III

Summary & Outlook

Chapter 12

Summary

One of the frontiers in modern cosmology is understanding the end of the cosmic dark age, when the first luminous objects (e.g., stars, supernovae, and galaxies) transformed the simple early Universe into a state of ever-increasing complexity. In this thesis, we discussed several possible fates for the first stars as well as their impact on the early Universe. In Part I, we have discussed the supernovae from the first stars as well as very massive stars. In Part II, we have discussed the cosmological impact of the first stars, binaries, and supernovae.

For simulating the supernova explosion, we used a new hydro code, `CASTRO`, and built several associated physics modules. We have developed a new mapping technique for initializing multidimensional simulations of stellar explosions with 1D stellar evolution models, imprinting them with velocity perturbations that reproduce the Kolmogorov energy spectrum expected for highly turbulent convective regions in stars. We have built nuclear reaction networks that allow us to follow the entire evolution of thermonuclear supernovae by calculating the nucleosynthesis and the energetics during the explosion. In addition, we have developed codes for calculating the effects of rotation and the post-Newtonian correction due to general relativity.

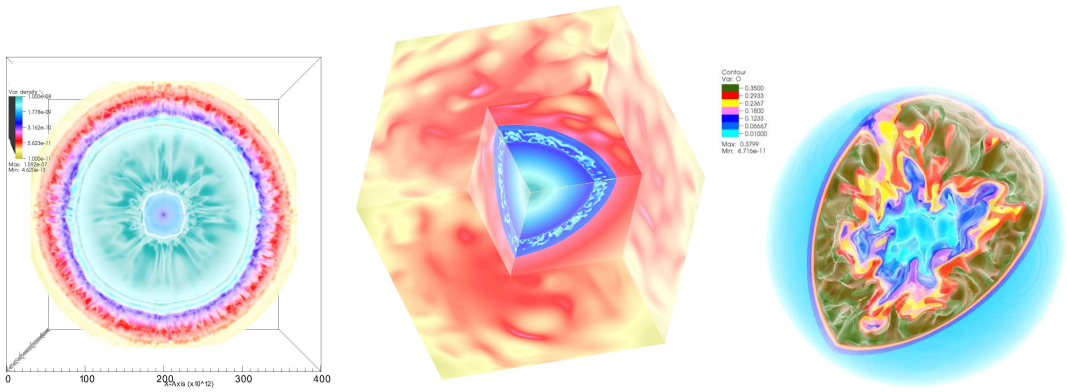

(a) PPSN (b) PSN (c) GSN

Figure 12.1: (a) 3D catastrophic collision of PPSN ejecta. (b) 3D pair-instability explosions. (c) An exploding supermassive star of $55,500\,\mathrm{M}_{\odot}$.

The thermonuclear supernovae of very massive stars include two types of pair-creation instability supernovae and one possible type of general relativity supernovae, as shown in Figure 12.1. The first stars with initial masses of $80-150\,\mathrm{M}_{\odot}$ might eject a few solar masses pulsationally; they are triggered by violent instabilities in stellar cores before they die. These ejected masses may lead to catastrophic collisions and power extremely luminous optical transients called pulsational pair-instability supernovae (PPSNe), which may account for the superluminous supernovae. In the simulation of a $110\,\mathrm{M}_{\odot}$ star, we find that the heavy elements ejected from the star are mainly ^{16}O and ^{12}C. There are no chemical elements heavier than ^{28}Si. When the ejecta from different eruptions collide, significant mixing is caused by the fluid instabilities. The mixed region is very close to the photo-sphere of PPSNe and potentially alters their observational signatures, such as light curves and spectra. The first stars with initial masses of $150-260\,\mathrm{M}_{\odot}$ eventually die as pair-instability supernovae (PSNe). The results of our simulations suggest that fluid instabilities driven by oxygen and helium burning arise at the lower and upper boundaries of the oxygen-burning shell at $\sim 20\,\mathrm{sec}$ to $100\,\mathrm{sec}$ after the onset of explosion. Figure 12.2 shows fluid instabilities driven by burning inside the PSNe. When the shock is slowed down by the extensive hydrogen envelope, a reverse shock forms and drives the development of Rayleigh–Taylor instabilities. These fluid

instabilities result in the mixing of the SN ejecta; the amount of mixing is dependent on the pre-supernova progenitors. For example, red supergiants demonstrate much more mixing than do blue supergiants. In addition to studying the non-rotating PSNe, we have performed 2D calculations to investigate the impact of rotation in the early stages of PSNe. The results show that rotation generates an asymmetric explosion caused by a non-isotropic core collapse. The angular momentum produces a resisting force for the runaway collapse, which dramatically affects the explosion energy and nucleosynthesis of PSNe. In the case of a 50% critical rotation rate of the oxygen core, ^{56}Ni production can be reduced by two orders of magnitude. An extreme case of a 100% rotation rate shows an interesting feature of overshooting along the equatorial direction. This is caused by non-synchronized ignitions of explosions, so that shocks run into the infalling gas and generate Richtmyer−Meshkov instabilities.

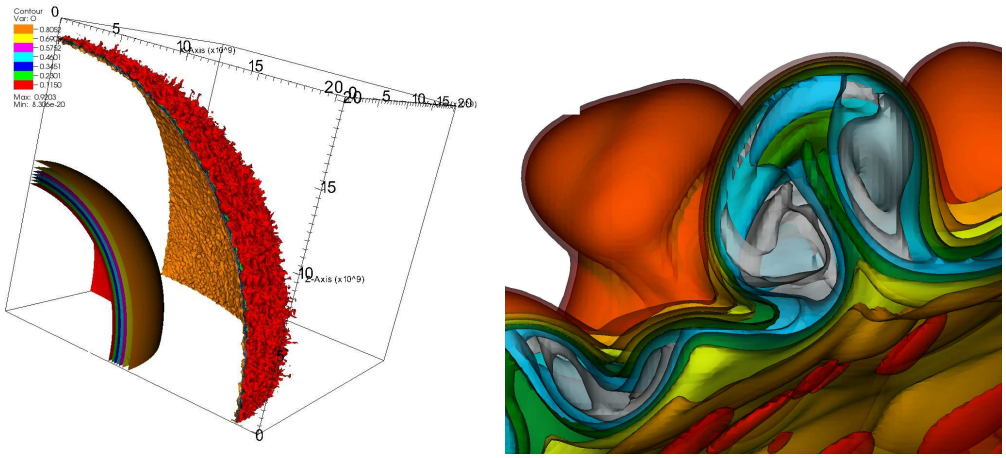

(a) (b)

Figure 12.2: Fluid instabilities during the onset of explosion. (a) Fluid instabilities driven by burning appear at the outer edge of the oxygen shell, shown in red.
(b) Close-up of the fluid.

The first stars seem to be promising progenitors for PSNe. However, observational evidence suggests that a few present-day stars are very massive, and they may be able

to die as PSNe too. With collaborators, we study PSNe from present-day stars by simulating a pre-supernova star of $0.1\,Z_{\odot}$. This star has an initial mass of $500\,\mathrm{M}_{\odot}$. Strong stellar wind triggers a strong mass-loss rate of the star; its mass becomes about $92.5\,\mathrm{M}_{\odot}$ before it dies as a PSN. Our results suggest very little mixing inside present-day PSNe because metals within the stellar envelope can strip the hydrogen envelope of the stars. This disfavors the formation of the reverse shock during the explosion and suppresses the development of fluid instabilities. Simulations show only a mild mixing caused by burning at the onset of explosion. Considering the PSNe, including rotation and metallicity, is there any possibility for supernovae to occur beyond $260\,\mathrm{M}_{\odot}$, which is an upper limit for SN explosions? In other words, what happens when extremely massive stars die? We report the discovery of an extraordinary supernova of a $55,500\,\mathrm{M}_{\odot}$ while investigating the properties of the first super massive stars. We infer that the possible driver of the explosion of a super massive star is triggered by general relativity, where the supporting pressure term becomes a source of gravity. This catalyzes the burning, leading to an explosion of energy up to $10^{55}\,\mathrm{erg}$, which is about 10,000 times more energetic than normal SNe. This also implies a narrow mass window in which the super massive stars may die as supernovae instead of collapsing into black holes. Violent mixing has been found inside the SNe ejecta.

These explosions produce a broad range of fluid instabilities and resulting mixing, as shown in Figure 12.3. Mixing of ejecta is reflected in the observational signatures. In observation, the supernovae with the most explosion energetics are the most promising targets for studying the early Universe.

Figure 12.3: Pseudo observational signatures of supernovae: Ia, PPSN, PSN, and GSN. Due to the enormous explosion energy or large out-shining radius, (P)PSN or GSN can be $10 - 100$ times brighter than a normal SN Ia. (Original image credit: NASA/HST/High-z SN Search Team)

In the second part of the thesis, we study the impact of the first stars and their SNe on the early Universe. The stellar feedback from the first stars could affect the later star formation and the assembly of the first galaxies. We use the modified `GADGET` to study the impact of the first stars and supernovae on their surroundings. Because the proper mass scale of the first stars and their population are very uncertain, we start by investigating the impact of a single first star on its host halo. The stellar impact depends on the mass of the stars; the more massive the stars are, the more UV photons can be produced, which leads to a more extensive region of ionized hydrogen and helium. The mass of a star also determines its fate. Depending on how massive they are, stars can die as several different kinds of supernovae, such as core-collapse supernovae and hypernovae, yielding different explosion energetics and amounts of metals. The metals dispersed by SNe can enrich the primordial gas and may lead to the formation of the second generation of stars forming inside the first galaxies. Several stellar scenarios are considered in our simulations. The results suggest that the first stars of masses $\sim 30 - 60\,\mathrm{M}_{\odot}$ can effectively create a H II region of a size about $3 - 4\,\mathrm{kpc}$ and enrich a

region of IGM gas of size $\sim 2\,\mathrm{kpc}$ to a metallicity of $\sim 10^{-3} - 10^{-5}\,Z_{\odot}$ by assuming they die as hypernovae of explosion energy of $10\,\mathrm{B}$. The chemical enrichment tends to be uniformly painted on the primordial gas instead of forming higher-metallicity clumps. Recent simulations of the first star formation suggest the formation of binaries inside the minihalos, so we investigate the impact of the first binaries. A unique feedback from the binaries is x-ray emission, from so-called x-ray binaries, that comes from the accretion of matter from the companion star onto the compact object. We select a series of binaries, combining two stars of different masses. The results show that the feedback is weaker from the binaries than from single stars with the same amount of mass as the binary in both radiative and chemical feedback. However, the emission from an x-ray binary may be able to heat up the gas inside the nearby minihalos and affect the subsequent star formation. Figure 12.4 shows a comparison of the large scale structure before and after stellar feedback, including UV radiation and the SN explosion. The gas density of the large scale structure remains intact, but the temperature has been heated up by radiation as well as the SN shock, resulting in a giant high-temperature bubble.

This dissertation is the first attempt to understand the evolution and explosions of massive stars and their cosmological consequences. Essentially, we try to fill a gap of understanding from the first stars to the consequent galactic environment. However, much effort is still required before the simulations are robust enough to offer meaningful predictions for the large telescopes of the future. The advancement of modern supercomputers will soon facilitate simulations that will be able to resolve the spatial scale and relevant physical processes to generate more realistic models. Combining the forthcoming data and promising simulations, we are about to reveal the mystery of the first stars, supernovae, and galaxies.

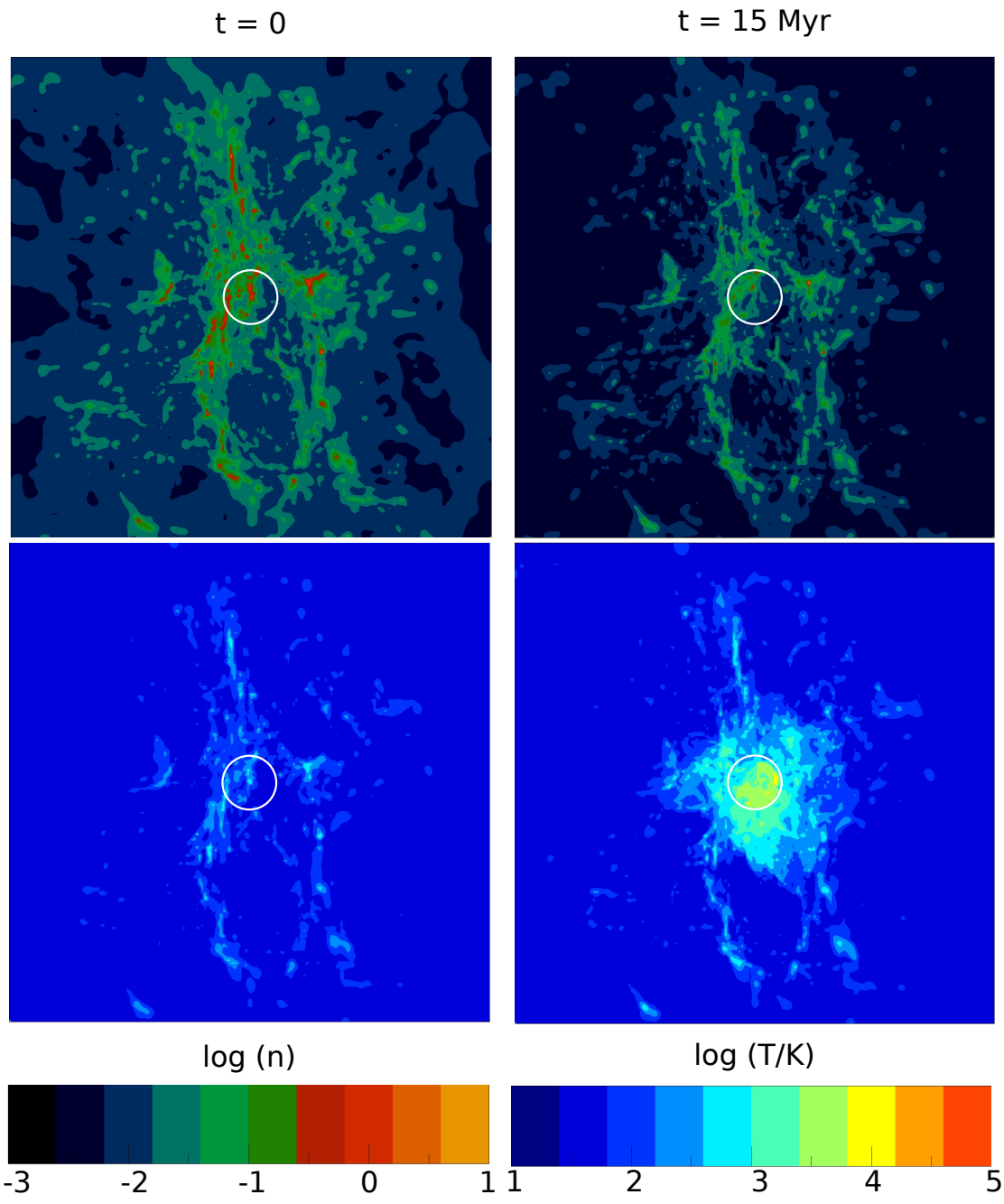

Figure 12.4: Cosmological impact of the first star and its supernova. Panels show temperatures and densities before/after the stellar feedback of the first star and its supernova. The white circles have a radius of 1 kpc centered at the star.

Chapter 13

Outlook

The results of my simulations shed a light of understanding on the underlying physical processes of the first supernovae and their impacts. However, astronomy is a science based on observational data. Models only offer a promising way of understanding the data. Strong theoretical models from simulations must offer useful predictions for observation, such as light curves or the spectra of targeted objects. The future telescopes will probe the early Universe and discover the information from the first supernovae. It is extremely urgent that simulations provide useful observational predictions before these telescopes start to collect data. For calculating predictions for these first SNe, a self-consistent radiation transport must be considered. Hydrodynamics simulations, including radiation calculations, can be very computationally expensive and technically difficult. One high-resolution 3D SN simulation may require several million CPU hours and can only be run on some of the most powerful supercomputers in the world. By collaborating with the research group at the Berkeley Laboratory, I will be using a new radiative hydro module of `CASTRO`, which will allow me to compute the light curves and spectra from my previous simulations.

I have performed a few test runs of `CASTRO` with a radiation module. Figure 13.1 shows the simulation of a radiative blast wave problem. In this simulation, the photons have been independently treated as a separated fluid. Decoupling of photons and gas usually occurs when the optical depth becomes small. In supernovae, it happens right before the shock breaks out the stellar surfaces. Hence we use radiative shock problems to test our radiation module.

In our cosmological simulations, we carry out very detailed studies of the impact of the first intermediate massive stars and binaries. The studies reveal different stellar feedback from their host halos. For the next step, we plan to continue evolving our feedback simulations until the minihalos merge into more massive halos of $10^8\,M_\odot$, which are promising candidates for the cores of the first galaxies, as shown in Figure 13.2. A technical challenge arises because such simulations also rely on radiation calculations that must consider radiation from multiple stars and trace their ray propagation. A new technology must be developed to facilitate this purpose for the first galaxy simulation. The first luminous objects, stars, supernovae, and galaxies hold the keys to understanding how the cosmic dark age was terminated. The detection of these objects will be the holy grail in modern cosmology. New ground and space telescopes with unprecedented apertures are planned for achieving this goal (see Table 13.1). These forthcoming ground-based facilities include the European Extremely Large Telescope (E-ELT), the Thirty Meter Telescope (TMT), and the Giant Magellan Telescope (GMT). In space, the James Webb Space Telescope (JWST) will take the lead.

Name	Type	Aperture (m)	Planned	References
E-ELT	Ground	40	2020+	Evans et al. (2013)
JWST	Space	6.5	2018+	Gardner et al. (2006)
TMT	Ground	30	2018+	Nelson and Sanders (2008)
GMT	Ground	24.5	2018+	Johns et al. (2012)

Table 13.1: Future telescopes planned for the science of the early Universe.

These telescopes will become the world's biggest eyes in the sky in human history and will allow us to probe the most distant Universe, showing when the first luminous objects such as stars, supernovae, and galaxies were about to form. Meaningful predictions of the first luminous objects through robust simulations are critical to the success of these observatories, which will be constructed by 2020. Before that date, significant efforts are needed to refine models to achieve the level of sophistication that will offer the most accurate scientific predictions for these forthcoming facilities. It is extremely urgent and important that we start to push the model frontiers along with the construction of

these telescopes. My future work will focus on connecting the models to observation.

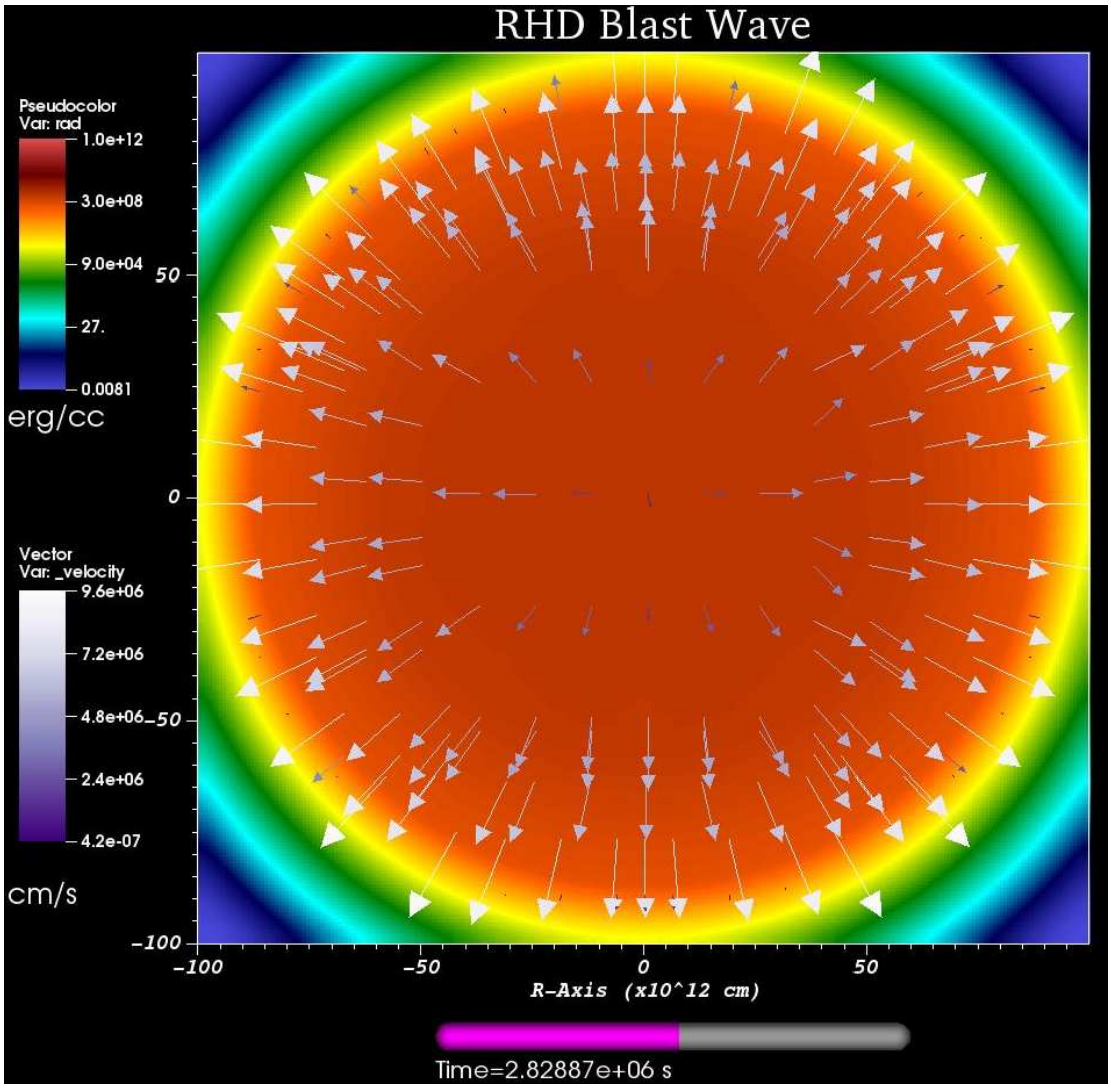

Figure 13.1: The radiative blast wave. The color codes show the radiation energy density, and vectors are velocities.

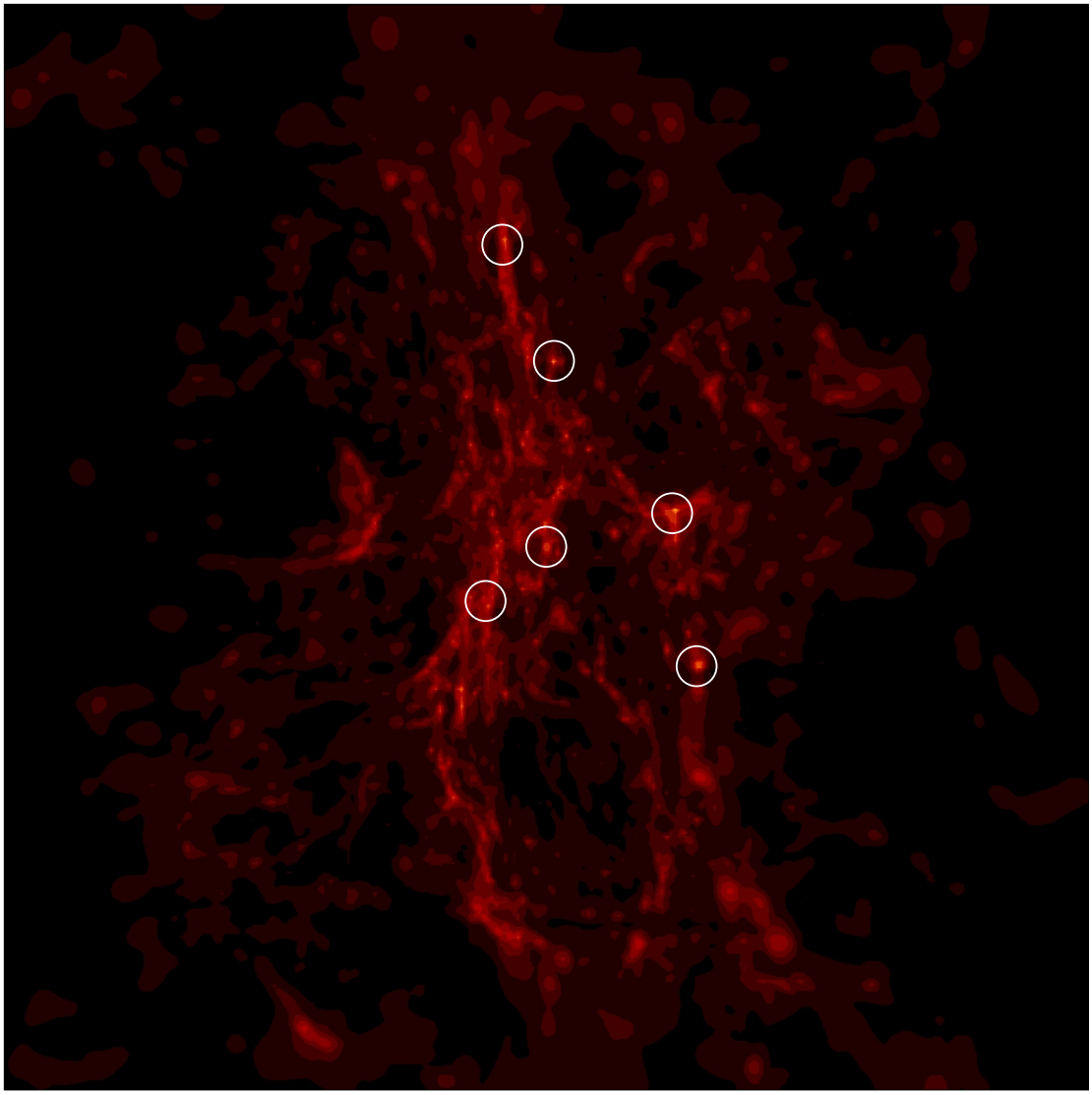

Figure 13.2: Distribution of minihalos at $z \sim 28$. Minihalos (circles) eventually merge through gravitational force and collapse to form a more massive halo of $\sim 10^8\,\mathrm{M}_\odot$, which is the progenitor of the first galaxy.

References

T. Abel, P. Anninos, Y. Zhang, and M. L. Norman. Modeling primordial gas in numerical cosmology. *Nature*, 2:181–207, August 1997.

T. Abel, G. L. Bryan, and M. L. Norman. The Formation and Fragmentation of Primordial Molecular Clouds. *ApJ*, 540:39–44, September 2000.

T. Abel, G. L. Bryan, and M. L. Norman. The Formation of the First Star in the Universe. *Science*, 295:93–98, January 2002.

T. Abel, J. H. Wise, and G. L. Bryan. The H II Region of a Primordial Star. *ApJ*, 659: L87–L90, April 2007.

G. Aldering, G. Adam, P. Antilogus, P. Astier, R. Bacon, S. Bongard, C. Bonnaud, Y. Copin, D. Hardin, F. Henault, D. A. Howell, J.-P. Lemonnier, J.-M. Levy, S. C. Loken, P. E. Nugent, R. Pain, A. Pecontal, E. Pecontal, S. Perlmutter, R. M. Quimby, K. Schahmaneche, G. Smadja, and W. M. Wood-Vasey. Overview of the Nearby Supernova Factory. In J. A. Tyson and S. Wolff, editors, *Society of Photo-Optical Instrumentation Engineers (SPIE) Conference Series*, volume 4836 of *Society of Photo-Optical Instrumentation Engineers (SPIE) Conference Series*, pages 61–72, December 2002.

A. S. Almgren, V. E. Beckner, J. B. Bell, M. S. Day, L. H. Howell, C. C. Joggerst, M. J. Lijewski, A. Nonaka, M. Singer, and M. Zingale. CASTRO: A New Compressible Astrophysical Solver. I. Hydrodynamics and Self-gravity. *ApJ*, 715:1221–1238, June 2010.

M. A. Alvarez and T. Abel. Quasar HII regions during cosmic reionization. *MNRAS*, 380:L30–L34, September 2007.

M. A. Alvarez, J. H. Wise, and T. Abel. Accretion onto the First Stellar-Mass Black Holes. *ApJ*, 701:L133–L137, August 2009.

D. Arnett. *Supernovae and nucleosynthesis. an investigation of the history of matter, from the Big Bang to the present.* Princeton University Press. 1996.

D. Arnett, C. Meakin, and P. A. Young. Turbulent Convection in Stellar Interiors. II. The Velocity Field. *ApJ*, 690:1715–1729, January 2009.

W. D. Arnett and C. Meakin. Toward Realistic Progenitors of Core-collapse Supernovae. *ApJ*, 733:78, June 2011.

G. Bader and P. Deuflhard. A semi-implicit mid-point rule for stiff systems of ordinary differential equations. *Numerische Mathematik*, 41:373–398, 1983. ISSN 0029-599X. URL `http://dx.doi.org/10.1007/BF01418331`. 10.1007/BF01418331.

R. Barkana and A. Loeb. In the beginning: the first sources of light and the reionization of the universe. *Phys. Rep.*, 349:125–238, July 2001.

R. Barkana and A. Loeb. The physics and early history of the intergalactic medium. *Reports on Progress in Physics*, 70:627–657, April 2007.

Z. Barkat, G. Rakavy, and N. Sack. Dynamics of Supernova Explosion Resulting from Pair Formation. *Physical Review Letters*, 18:379–381, March 1967.

J. Barnes and P. Hut. A hierarchical O(N log N) force-calculation algorithm. *Nature*, 324:446–449, December 1986.

T. C. Beers and N. Christlieb. The Discovery and Analysis of Very Metal-Poor Stars in the Galaxy. *ARA&A*, 43:531–580, September 2005.

M. C. Begelman, M. Volonteri, and M. J. Rees. Formation of supermassive black holes by direct collapse in pre-galactic haloes. *MNRAS*, 370:289–298, July 2006.

A. Beifiori, S. Courteau, E. M. Corsini, and Y. Zhu. On the correlations between galaxy properties and supermassive black hole mass. *MNRAS*, 419:2497–2528, January 2012.

H. A. Bethe. Supernova mechanisms. *Reviews of Modern Physics*, 62:801–866, October 1990.

J. R. Bond, W. D. Arnett, and B. J. Carr. The evolution and fate of Very Massive Objects. *ApJ*, 280:825–847, May 1984.

V. Bromm and R. B. Larson. The First Stars. *ARA&A*, 42:79–118, September 2004.

V. Bromm and A. Loeb. Formation of the First Supermassive Black Holes. *ApJ*, 596: 34–46, October 2003.

V. Bromm and A. Loeb. Accretion onto a primordial protostar. *New Astronomy*, 9: 353–364, June 2004.

V. Bromm and N. Yoshida. The First Galaxies. *ArXiv e-prints*, February 2011.

V. Bromm, P. S. Coppi, and R. B. Larson. Forming the First Stars in the Universe: The Fragmentation of Primordial Gas. *ApJ*, 527:L5–L8, December 1999.

V. Bromm, P. S. Coppi, and R. B. Larson. The Formation of the First Stars. I. The Primordial Star-forming Cloud. *ApJ*, 564:23–51, January 2002.

V. Bromm, N. Yoshida, L. Hernquist, and C. F. McKee. The formation of the first stars and galaxies. *Nature*, 459:49–54, May 2009.

M. Brouillette. The richtmyer-meshkov instability. *Annual Review of Fluid Mechanics*, 34:445–468, 2002.

A. Burrows, J. Hayes, and B. A. Fryxell. On the Nature of Core-Collapse Supernova Explosions. *ApJ*, 450:830, September 1995.

B. J. Carr, J. R. Bond, and W. D. Arnett. Cosmological consequences of Population III stars. *ApJ*, 277:445–469, February 1984.

S. Chandrasekhar. *Principles of stellar dynamics*. University of Chicago Press. 1942.

S. Chandrasekhar. *Hydrodynamic and hydromagnetic stability*. International Series of Monographs on Physics, Oxford. 1961.

E. Chatzopoulos and J. C. Wheeler. Hydrogen-poor Circumstellar Shells from Pulsational Pair-instability Supernovae with Rapidly Rotating Progenitors. *ApJ*, 760:154, December 2012.

E. Chatzopoulos, J. C. Wheeler, J. Vinko, R. Quimby, E. L. Robinson, A. A. Miller, R. J. Foley, D. A. Perley, F. Yuan, C. Akerlof, and J. S. Bloom. SN 2008am: A Super-luminous Type IIn Supernova. *ApJ*, 729:143, March 2011.

K.-J. Chen, A. Heger, and A. S. Almgren. Multidimensional simulations of pair-instability supernovae. *Computer Physics Communications*, 182:254–256, January 2011.

K.-J. Chen, A. Heger, and A. S. Almgren. to be submitted. *A&C submitted*, January 2012.

R. Chevalier and J. M. Blondin. Hydrodynamic instabilities in supernova remnants: Early radiative cooling. *ApJ*, 444:312–317, May 1995.

R. A. Chevalier. The hydrodynamics of Type II supernovae. *ApJ*, 207:872–887, August 1976.

R. A. Chevalier and C. M. Irwin. Shock Breakout in Dense Mass Loss: Luminous Supernovae. *ApJ*, 729:L6, March 2011.

Hank Childs, Eric S. Brugger, Kathleen S. Bonnell, Jeremy S. Meredith, Mark Miller, Brad J. Whitlock, and Nelson Max. A contract-based system for large data visualization. In *Proceedings of IEEE Visualization 2005*, page 190–198, 2005.

B. Ciardi and A. Ferrara. The First Cosmic Structures and Their Effects. *Space Sci. Rev.*, 116:625–705, February 2005.

J. P. Cox and R. T. Giuli. *Principles of stellar structure*. Gordon and Breach, 1968.

P. A. Crowther, O. Schnurr, R. Hirschi, N. Yusof, R. J. Parker, S. P. Goodwin, and H. A. Kassim. The R136 star cluster hosts several stars whose individual masses greatly exceed the accepted 150 $M_\odot$ stellar mass limit. *MNRAS*, 408:731–751, October 2010.

K. Davidson and R. M. Humphreys. Eta Carinae and Its Environment. *ARA&A*, 35: 1–32, 1997.

P. A. Davidson. *Turbulence : an introduction for scientists and engineers.* Oxford University Press, 2004.

T. Di Matteo, V. Springel, and L. Hernquist. Energy input from quasars regulates the growth and activity of black holes and their host galaxies. *Nature*, 433:604–607, February 2005.

S. Dodelson. *Modern cosmology.* Academic Press. 2003.

Iain S Duff, Albert M Erisman, and John K Reid. *Direct methods for sparse matrices.* Oxford University Press, Inc., New York, NY, USA, 1986. ISBN 0-198-53408-6.

S. Ekström, G. Meynet, C. Chiappini, R. Hirschi, and A. Maeder. Effects of rotation on the evolution of primordial stars. *A&A*, 489:685–698, October 2008.

C. Evans, M. Puech, B. Barbuy, N. Bastian, P. Bonifacio, E. Caffau, J.-G. Cuby, G. Dalton, B. Davies, J. Dunlop, H. Flores, F. Hammer, L. Kaper, B. Lemasle, S. Morris, L. Pentericci, P. Petitjean, D. Schaerer, E. Telles, N. Welikala, and B. Ziegler. ELT-MOS White Paper: Science Overview Requirements. *ArXiv e-prints*, February 2013.

X. Fan, V. K. Narayanan, M. A. Strauss, R. L. White, R. H. Becker, L. Pentericci, and H.-W. Rix. Evolution of the Ionizing Background and the Epoch of Reionization from the Spectra of z˜6 Quasars. *AJ*, 123:1247–1257, March 2002.

X. Fan, M. A. Strauss, R. H. Becker, R. L. White, J. E. Gunn, G. R. Knapp, G. T. Richards, D. P. Schneider, J. Brinkmann, and M. Fukugita. Constraining the Evolution of the Ionizing Background and the Epoch of Reionization with z˜6 Quasars. II. A Sample of 19 Quasars. *AJ*, 132:117–136, July 2006.

L. Ferrarese and H. Ford. Supermassive Black Holes in Galactic Nuclei: Past, Present and Future Research. *Space Sci. Rev.*, 116:523–624, February 2005.

L. Ferrarese and D. Merritt. A Fundamental Relation between Supermassive Black Holes and Their Host Galaxies. *ApJ*, 539:L9–L12, August 2000.

A. V. Filippenko. Optical Spectra of Supernovae. *ARA&A*, 35:309–355, 1997.

W. A. Fowler. The Stability of Supermassive Stars. *ApJ*, 144:180, April 1966.

A. Frebel. Exploring the Universe with Metal-Poor Stars. *ArXiv e-prints*, August 2011.

U. Frisch. *Turbulence. The legacy of A. N. Kolmogorov.* Cambridge University Press. 1995.

C. L. Fryer, S. E. Woosley, and A. Heger. Pair-Instability Supernovae, Gravity Waves, and Gamma-Ray Transients. *ApJ*, 550:372–382, March 2001.

B. Fryxell, D. Arnett, and E. Mueller. Instabilities and clumping in SN 1987A. I - Early evolution in two dimensions. *ApJ*, 367:619–634, February 1991.

B. Fryxell, K. Olson, P. Ricker, F. X. Timmes, M. Zingale, D. Q. Lamb, P. MacNeice, R. Rosner, J. W. Truran, and H. Tufo. FLASH: An Adaptive Mesh Hydrodynamics Code for Modeling Astrophysical Thermonuclear Flashes. *ApJS*, 131:273–334, November 2000.

G. M. Fuller, S. E. Woosley, and T. A. Weaver. The evolution of radiation-dominated stars. I - Nonrotating supermassive stars. *ApJ*, 307:675–686, August 1986.

A. Gal-Yam. Luminous Supernovae. *Science*, 337:927–, August 2012.

A. Gal-Yam, P. Mazzali, E. O. Ofek, P. E. Nugent, S. R. Kulkarni, M. M. Kasliwal, R. M. Quimby, A. V. Filippenko, S. B. Cenko, R. Chornock, R. Waldman, D. Kasen, M. Sullivan, E. C. Beshore, A. J. Drake, R. C. Thomas, J. S. Bloom, D. Poznanski, A. A. Miller, R. J. Foley, J. M. Silverman, I. Arcavi, R. S. Ellis, and J. Deng. Supernova 2007bi as a pair-instability explosion. *Nature*, 462:624–627, December 2009.

J. P. Gardner, J. C. Mather, M. Clampin, R. Doyon, M. A. Greenhouse, H. B. Hammel, J. B. Hutchings, P. Jakobsen, S. J. Lilly, K. S. Long, J. I. Lunine, M. J. McCaughrean, M. Mountain, J. Nella, G. H. Rieke, M. J. Rieke, H.-W. Rix, E. P. Smith, G. Sonneborn, M. Stiavelli, H. S. Stockman, R. A. Windhorst, and G. S. Wright. The James Webb Space Telescope. *Space Sci. Rev.*, 123:485–606, April 2006.

K. Gebhardt, R. Bender, G. Bower, A. Dressler, S. M. Faber, A. V. Filippenko, R. Green, C. Grillmair, L. C. Ho, J. Kormendy, T. R. Lauer, J. Magorrian, J. Pinkney, D. Richstone, and S. Tremaine. A Relationship between Nuclear Black Hole Mass and Galaxy Velocity Dispersion. *ApJ*, 539:L13–L16, August 2000.

W. Glatzel, K. J. Fricke, and M. F. El Eid. The fate of rotating pair-unstable carbon-oxygen cores. *A&A*, 149:413–422, August 1985.

S. C. O. Glover and A.-K. Jappsen. Star Formation at Very Low Metallicity. I. Chemistry and Cooling at Low Densities. *ApJ*, 666:1–19, September 2007.

D. Goodstein. *Adventures in cosmology*. World Scientific Pub. Co. 2011.

T. H. Greif, S. C. O. Glover, V. Bromm, and R. S. Klessen. Chemical mixing in smoothed particle hydrodynamics simulations. *MNRAS*, 392:1381–1387, February 2009a.

T. H. Greif, J. L. Johnson, R. S. Klessen, and V. Bromm. The observational signature of the first HII regions. *MNRAS*, 399:639–649, October 2009b.

T. H. Greif, S. C. O. Glover, V. Bromm, and R. S. Klessen. The First Galaxies: Chemical Enrichment, Mixing, and Star Formation. *ApJ*, 716:510–520, June 2010a.

T. H. Greif, S. C. O. Glover, V. Bromm, and R. S. Klessen. The First Galaxies: Chemical Enrichment, Mixing, and Star Formation. *ApJ*, 716:510–520, June 2010b.

T. H. Greif, V. Springel, S. D. M. White, S. C. O. Glover, P. C. Clark, R. J. Smith, R. S. Klessen, and V. Bromm. Simulations on a Moving Mesh: The Clustered Formation of Population III Protostars. *ApJ*, 737:75, August 2011.

A. H. Guth. Inflationary universe: A possible solution to the horizon and flatness problems. *Phys. Rev. D*, 23:347–356, January 1981.

A. Heger and S. E. Woosley. The Nucleosynthetic Signature of Population III. *ApJ*, 567:532–543, March 2002.

A. Heger and S. E. Woosley. Nucleosynthesis and Evolution of Massive Metal-free Stars. *ApJ*, 724:341–373, November 2010.

A. Heger, N. Langer, and S. E. Woosley. Presupernova Evolution of Rotating Massive Stars. I. Numerical Method and Evolution of the Internal Stellar Structure. *Apj*, 528: 368–396, January 2000.

A. Heger, S. E. Woosley, G. Martínez-Pinedo, and K. Langanke. Presupernova Evolution with Improved Rates for Weak Interactions. *ApJ*, 560:307–325, October 2001.

A. Heger, C. L. Fryer, S. E. Woosley, N. Langer, and D. H. Hartmann. How Massive Single Stars End Their Life. *ApJ*, 591:288–300, July 2003.

A. Heger, S. E. Woosley, and H. C. Spruit. Presupernova Evolution of Differentially Rotating Massive Stars Including Magnetic Fields. *ApJ*, 626:350–363, June 2005.

M. Herant and S. E. Woosley. Postexplosion hydrodynamics of supernovae in red supergiants. *ApJ*, 425:814–828, April 1994.

R. Hirschi. Very low-metallicity massive stars:. Pre-SN evolution models and primary nitrogen production. *A&A*, 461:571–583, January 2007.

R. Hirschi, G. Meynet, and A. Maeder. Stellar evolution with rotation. XII. Pre-supernova models. *A&A*, 425:649–670, October 2004.

T. Hosokawa, K. Omukai, N. Yoshida, and H. W. Yorke. Protostellar Feedback Halts the Growth of the First Stars in the Universe. *Science*, 334:1250–, December 2011.

R. M. Humphreys and K. Davidson. Studies of luminous stars in nearby galaxies. III - Comments on the evolution of the most massive stars in the Milky Way and the Large Magellanic Cloud. *ApJ*, 232:409–420, September 1979.

N. Itoh, H. Hayashi, A. Nishikawa, and Y. Kohyama. Neutrino Energy Loss in Stellar Interiors. VII. Pair, Photo-, Plasma, Bremsstrahlung, and Recombination Neutrino Processes. *ApJS*, 102:411, February 1996.

H.-T. Janka and E. Mueller. Neutrino heating, convection, and the mechanism of Type-II supernova explosions. *A&A*, 306:167, February 1996.

M. Jeon, A. H. Pawlik, T. H. Greif, S. C. O. Glover, V. Bromm, M. Milosavljević, and R. S. Klessen. The First Galaxies: Assembly with Black Hole Feedback. *ApJ*, 754: 34, July 2012.

C. C. Joggerst and D. J. Whalen. The Early Evolution of Primordial Pair-instability Supernovae. *ApJ*, 728:129–+, February 2011.

C. C. Joggerst, A. Almgren, J. Bell, A. Heger, D. Whalen, and S. E. Woosley. The Nucleosynthetic Imprint of 15-40 M $_{sun}$ Primordial Supernovae on Metal-Poor Stars. *ApJ*, 709:11–26, January 2010.

M. Johns, P. McCarthy, K. Raybould, A. Bouchez, A. Farahani, J. Filgueira, G. Jacoby, S. Shectman, and M. Sheehan. Giant Magellan Telescope: overview. In *Society of Photo-Optical Instrumentation Engineers (SPIE) Conference Series*, volume 8444 of *Society of Photo-Optical Instrumentation Engineers (SPIE) Conference Series*, September 2012.

J. L. Johnson and V. Bromm. The aftermath of the first stars: massive black holes. *MNRAS*, 374:1557–1568, February 2007a.

J. L. Johnson and V. Bromm. The aftermath of the first stars: massive black holes. *MNRAS*, 374:1557–1568, February 2007b.

J. L. Johnson, D. J. Whalen, C. L. Fryer, and H. Li. The Growth of the Stellar Seeds of Supermassive Black Holes. *ApJ*, 750:66, May 2012.

D. Kasen and L. Bildsten. Supernova Light Curves Powered by Young Magnetars. *ApJ*, 717:245–249, July 2010.

D. Kasen, S. E. Woosley, and A. Heger. Pair Instability Supernovae: Light Curves, Spectra, and Shock Breakout. *ApJ*, 734:102, June 2011.

R. Kippenhahn and A. Weigert. *Stellar Structure and Evolution.* Springer. 1990.

T. Kitayama, N. Yoshida, H. Susa, and M. Umemura. The Structure and Evolution of Early Cosmological H II Regions. *ApJ*, 613:631–645, October 2004.

E. W. Kolb and M. S. Turner. *The Early Universe.* Front. Phys., Vol. 69,. 1990.

E. Komatsu, J. Dunkley, M. R. Nolta, C. L. Bennett, B. Gold, G. Hinshaw, N. Jarosik, D. Larson, M. Limon, L. Page, D. N. Spergel, M. Halpern, R. S. Hill, A. Kogut, S. S. Meyer, G. S. Tucker, J. L. Weiland, E. Wollack, and E. L. Wright. Five-Year

Wilkinson Microwave Anisotropy Probe Observations: Cosmological Interpretation. *ApJS*, 180:330–376, February 2009.

J. Kormendy and D. Richstone. Inward Bound—The Search For Supermassive Black Holes In Galactic Nuclei. *ARA&A*, 33:581, 1995.

R. P. Kudritzki. Line-driven Winds, Ionizing Fluxes, and Ultraviolet Spectra of Hot Stars at Extremely Low Metallicity. I. Very Massive O Stars. *ApJ*, 577:389–408, September 2002.

M. Kuhlen and P. Madau. The first miniquasar. *MNRAS*, 363:1069–1082, November 2005.

N. Langer. Presupernova Evolution of Massive Single and Binary Stars. *ARA&A*, 50: 107–164, September 2012.

R. B. Larson. The physics of star formation. *Reports on Progress in Physics*, 66: 1651–1697, October 2003.

N. M. Law, S. R. Kulkarni, R. G. Dekany, E. O. Ofek, R. M. Quimby, P. E. Nugent, J. Surace, C. C. Grillmair, J. S. Bloom, M. M. Kasliwal, L. Bildsten, T. Brown, S. B. Cenko, D. Ciardi, E. Croner, S. G. Djorgovski, J. van Eyken, A. V. Filippenko, D. B. Fox, A. Gal-Yam, D. Hale, N. Hamam, G. Helou, J. Henning, D. A. Howell, J. Jacobsen, R. Laher, S. Mattingly, D. McKenna, A. Pickles, D. Poznanski, G. Rahmer, A. Rau, W. Rosing, M. Shara, R. Smith, D. Starr, M. Sullivan, V. Velur, R. Walters, and J. Zolkower. The Palomar Transient Factory: System Overview, Performance, and First Results. *PASP*, 121:1395–1408, December 2009.

A. Liddle. *An Introduction to Modern Cosmology, Second Edition*. Wiley-VCH. May 2003.

A. D. Linde. A new inflationary universe scenario: A possible solution of the horizon, flatness, homogeneity, isotropy and primordial monopole problems. *Physics Letters B*, 108:389–393, February 1982.

A. Loeb and F. A. Rasio. Collapse of primordial gas clouds and the formation of quasar black holes. *ApJ*, 432:52–61, September 1994.

P. Madau and M. J. Rees. Massive Black Holes as Population III Remnants. *ApJ*, 551: L27–L30, April 2001.

A. Maeder and G. Meynet. The Evolution of Rotating Stars. *ARA&A*, 38:143–190, 2000.

N. J. McConnell and C.-P. Ma. Revisiting the Scaling Relations of Black Hole Masses and Host Galaxy Properties. *ApJ*, 764:184, February 2013.

C. A. Meakin and D. Arnett. Turbulent Convection in Stellar Interiors. I. Hydrodynamic Simulation. *ApJ*, 667:448–475, September 2007.

A. Mezzacappa, A. C. Calder, S. W. Bruenn, J. M. Blondin, M. W. Guidry, M. R. Strayer, and A. S. Umar. An Investigation of Neutrino-driven Convection and the Core Collapse Supernova Mechanism Using Multigroup Neutrino Transport. *ApJ*, 495:911, March 1998.

J. J. Monaghan. Smoothed particle hydrodynamics. *ARA&A*, 30:543–574, 1992.

T. Moriya, N. Tominaga, M. Tanaka, K. Maeda, and K. Nomoto. A Core-collapse Supernova Model for the Extremely Luminous Type Ic Supernova 2007bi: An Alternative to the Pair-instability Supernova Model. *ApJ*, 717:L83–L86, July 2010.

T. J. Moriya, S. I. Blinnikov, N. Tominaga, N. Yoshida, M. Tanaka, K. Maeda, and K. Nomoto. Light-curve modelling of superluminous supernova 2006gy: collision between supernova ejecta and a dense circumstellar medium. *MNRAS*, 428:1020–1035, January 2013.

E. Müller. Simulation of Astrophysical Fluid Flow. In O. Steiner & A. Gautschy, editor, *Saas-Fee Advanced Course 27: Computational Methods for Astrophysical Fluid Flow.*, page 343, 1998.

J. W. Murphy and A. Burrows. Criteria for Core-Collapse Supernova Explosions by the Neutrino Mechanism. *ApJ*, 688:1159–1175, December 2008.

J. Nelson and G. H. Sanders. The status of the Thirty Meter Telescope project. In

Society of Photo-Optical Instrumentation Engineers (SPIE) Conference Series, volume 7012 of *Society of Photo-Optical Instrumentation Engineers (SPIE) Conference Series*, August 2008.

J. Nordhaus, A. Burrows, A. Almgren, and J. Bell. Dimension as a Key to the Neutrino Mechanism of Core-collapse Supernova Explosions. *ApJ*, 720:694–703, September 2010.

E. O. Ofek, P. B. Cameron, M. M. Kasliwal, A. Gal-Yam, A. Rau, S. R. Kulkarni, D. A. Frail, P. Chandra, S. B. Cenko, A. M. Soderberg, and S. Immler. SN 2006gy: An Extremely Luminous Supernova in the Galaxy NGC 1260. *ApJ*, 659:L13–L16, April 2007.

T. Ohkubo, H. Umeda, K. Maeda, K. Nomoto, T. Suzuki, S. Tsuruta, and M. J. Rees. Core-Collapse Very Massive Stars: Evolution, Explosion, and Nucleosynthesis of Population III 500-1000 M_{solar} Stars. *ApJ*, 645:1352–1372, July 2006.

B. W. O'Shea, C. F. McKee, A. Heger, and T. Abel. First Stars III Conference Summary. In B. W. O'Shea & A. Heger, editor, *First Stars III*, volume 990 of *American Institute of Physics Conference Series*, page D13, March 2008.

A. Pastorello, S. J. Smartt, M. T. Botticella, K. Maguire, M. Fraser, K. Smith, R. Kotak, L. Magill, S. Valenti, D. R. Young, S. Gezari, F. Bresolin, R. Kudritzki, D. A. Howell, A. Rest, N. Metcalfe, S. Mattila, E. Kankare, K. Y. Huang, Y. Urata, W. S. Burgett, K. C. Chambers, T. Dombeck, H. Flewelling, T. Grav, J. N. Heasley, K. W. Hodapp, N. Kaiser, G. A. Luppino, R. H. Lupton, E. A. Magnier, D. G. Monet, J. S. Morgan, P. M. Onaka, P. A. Price, P. H. Rhoads, W. A. Siegmund, C. W. Stubbs, W. E. Sweeney, J. L. Tonry, R. J. Wainscoat, M. F. Waterson, C. Waters, and C. G. Wynn-Williams. Ultra-bright Optical Transients are Linked with Type Ic Supernovae. *ApJ*, 724:L16–L21, November 2010.

B. Paxton, L. Bildsten, A. Dotter, F. Herwig, P. Lesaffre, and F. Timmes. Modules for Experiments in Stellar Astrophysics (MESA). *ApJS*, 192:3, January 2011.

J. A. Peacock. *Cosmological Physics*. Cambridge University Press. January 1999.

P. J. E. Peebles. *The large-scale structure of the universe*. Princeton University Press. 1980.

P. J. E. Peebles. *Principles of Physical Cosmology*. Princeton University Press. 1993.

A. A. Penzias and R. W. Wilson. A Measurement of Excess Antenna Temperature at 4080 Mc/s. *ApJ*, 142:419–421, July 1965.

D. H. Porter and P. R. Woodward. Three-dimensional Simulations of Turbulent Compressible Convection. *ApJS*, 127:159–187, March 2000.

William H. Press, Saul A. Teukolsky, William T. Vetterling, and Brian P. Flannery. *Numerical Recipes 3rd Edition: The Art of Scientific Computing*. Cambridge University Press, New York, NY, USA, 3 edition, 2007. ISBN 0521880688, 9780521880688.

D. Prialnik. *An Introduction to the Theory of Stellar Structure and Evolution*. Cambridge University Press. July 2000.

R. M. Quimby, G. Aldering, J. C. Wheeler, P. Höflich, C. W. Akerlof, and E. S. Rykoff. SN 2005ap: A Most Brilliant Explosion. *ApJ*, 668:L99–L102, October 2007.

R. M. Quimby, S. R. Kulkarni, M. M. Kasliwal, A. Gal-Yam, I. Arcavi, M. Sullivan, P. Nugent, R. Thomas, D. A. Howell, E. Nakar, L. Bildsten, C. Theissen, N. M. Law, R. Dekany, G. Rahmer, D. Hale, R. Smith, E. O. Ofek, J. Zolkower, V. Velur, R. Walters, J. Henning, K. Bui, D. McKenna, D. Poznanski, S. B. Cenko, and D. Levitan. Hydrogen-poor superluminous stellar explosions. *Nature*, 474:487–489, June 2011.

A. Rau, S. R. Kulkarni, N. M. Law, J. S. Bloom, D. Ciardi, G. S. Djorgovski, D. B. Fox, A. Gal-Yam, C. C. Grillmair, M. M. Kasliwal, P. E. Nugent, E. O. Ofek, R. M. Quimby, W. T. Reach, M. Shara, L. Bildsten, S. B. Cenko, A. J. Drake, A. V. Filippenko, D. J. Helfand, G. Helou, D. A. Howell, D. Poznanski, and M. Sullivan. Exploring the Optical Transient Sky with the Palomar Transient Factory. *PASP*, 121: 1334–1351, December 2009.

M. J. Rees. Black Hole Models for Active Galactic Nuclei. *ARA&A*, 22:471–506, 1984.

E. E. Salpeter. The Luminosity Function and Stellar Evolution. *ApJ*, 121:161, January 1955.

E. Scannapieco, P. Madau, S. Woosley, A. Heger, and A. Ferrara. The Detectability of Pair-Production Supernovae at z less 6. *ApJ*, 633:1031–1041, November 2005.

D. Schaerer. On the properties of massive Population III stars and metal-free stellar populations. *A&A*, 382:28–42, January 2002.

R. Schneider, K. Omukai, S. Bianchi, and R. Valiante. The first low-mass stars: critical metallicity or dust-to-gas ratio? *MNRAS*, 419:1566–1575, January 2012.

L. I. Sedov. *Similarity and Dimensional Methods in Mechanics*. Academic Press. 1959.

F. H. Shu, F. C. Adams, and S. Lizano. Star formation in molecular clouds - Observation and theory. *ARA&A*, 25:23–81, 1987.

S. J. Smartt. Progenitors of Core-Collapse Supernovae. *ARA&A*, 47:63–106, September 2009.

N. Smith and R. McCray. Shell-shocked Diffusion Model for the Light Curve of SN 2006gy. *ApJ*, 671:L17–L20, December 2007.

N. Smith, W. Li, R. J. Foley, J. C. Wheeler, D. Pooley, R. Chornock, A. V. Filippenko, J. M. Silverman, R. Quimby, J. S. Bloom, and C. Hansen. SN 2006gy: Discovery of the Most Luminous Supernova Ever Recorded, Powered by the Death of an Extremely Massive Star like η Carinae. *ApJ*, 666:1116–1128, September 2007.

V. Springel. The cosmological simulation code GADGET-2. *MNRAS*, 364:1105–1134, December 2005.

A. Stacy, T. H. Greif, and V. Bromm. The first stars: formation of binaries and small multiple systems. *MNRAS*, 403:45–60, March 2010.

A. Stacy, V. Bromm, and A. Loeb. Rotation speed of the first stars. *MNRAS*, 413: 543–553, May 2011.

A. Stacy, T. H. Greif, and V. Bromm. The first stars: mass growth under protostellar feedback. *MNRAS*, 422:290–309, May 2012.

R. S. Sutherland and M. A. Dopita. Cooling functions for low-density astrophysical plasmas. *ApJS*, 88:253–327, September 1993.

M. Tegmark, J. Silk, M. J. Rees, A. Blanchard, T. Abel, and F. Palla. How Small Were the First Cosmological Objects? *ApJ*, 474:1, January 1997.

F. X. Timmes. Integration of Nuclear Reaction Networks for Stellar Hydrodynamics. *ApJS*, 124:241–263, September 1999.

F. X. Timmes and F. D. Swesty. The Accuracy, Consistency, and Speed of an Electron-Positron Equation of State Based on Table Interpolation of the Helmholtz Free Energy. *ApJS*, 126:501–516, February 2000.

M. J. Turk, T. Abel, and B. O'Shea. The Formation of Population III Binaries from Cosmological Initial Conditions. *Science*, 325:601–, July 2009.

H. Umeda and K. Nomoto. First-generation black-hole-forming supernovae and the metal abundance pattern of a very iron-poor star. *Nature*, 422:871–873, April 2003.

T. A. Weaver, G. B. Zimmerman, and S. E. Woosley. Presupernova evolution of massive stars. *ApJ*, 225:1021–1029, November 1978.

D. Whalen, T. Abel, and M. L. Norman. Radiation Hydrodynamic Evolution of Primordial H II Regions. *ApJ*, 610:14–22, July 2004.

J. C. Wheeler. Final evolution of stars in the range 1,000 to 10,000 solar masses. *Ap&SS*, 50:125–131, August 1977.

J. H. Wise and T. Abel. Resolving the Formation of Protogalaxies. III. Feedback from the First Stars. *ApJ*, 685:40–56, September 2008.

W. M. Wood-Vasey, G. Aldering, B. C. Lee, S. Loken, P. Nugent, S. Perlmutter, J. Siegrist, L. Wang, P. Antilogus, P. Astier, D. Hardin, R. Pain, Y. Copin, G. Smadja, E. Gangler, A. Castera, G. Adam, R. Bacon, J.-P. Lemonnier, A. Pécontal, E. Pécontal, and R. Kessler. The Nearby Supernova Factory. *Nature*, 48:637–640, May 2004.

S. Woosley and T. Janka. The physics of core-collapse supernovae. *Nature Physics*, 1: 147–154, December 2005.

S. E. Woosley. Gamma-ray bursts from stellar mass accretion disks around black holes. *ApJ*, 405:273–277, March 1993.

S. E. Woosley. Bright Supernovae from Magnetar Birth. *ApJ*, 719:L204–L207, August 2010.

S. E. Woosley and T. A. Weaver. The physics of supernova explosions. *ARA&A*, 24: 205–253, 1986.

S. E. Woosley, A. Heger, and T. A. Weaver. The evolution and explosion of massive stars. *Reviews of Modern Physics*, 74:1015–1071, November 2002.

S. E. Woosley, S. Blinnikov, and A. Heger. Pulsational pair instability as an explanation for the most luminous supernovae. *Nature*, 450:390–392, November 2007.

S.-C. Yoon, A. Dierks, and N. Langer. Evolution of massive Population III stars with rotation and magnetic fields. *A&A*, 542:A113, June 2012.

N. Yoshida, S. P. Oh, T. Kitayama, and L. Hernquist. Early Cosmological H II/He III Regions and Their Impact on Second-Generation Star Formation. *ApJ*, 663:687–707, July 2007.

Y. B. Zeldovich and I. D. Novikov. *Relativistic astrophysics. Vol.1: Stars and relativity.* University of Chicago Press. 1971.

W. Zhang, L. Howell, A. Almgren, A. Burrows, and J. Bell. CASTRO: A New Compressible Astrophysical Solver. II. Gray Radiation Hydrodynamics. *ApJS*, 196:20, October 2011.

M. Zingale, L. J. Dursi, J. ZuHone, A. C. Calder, B. Fryxell, T. Plewa, J. W. Truran, A. Caceres, K. Olson, P. M. Ricker, K. Riley, R. Rosner, A. Siegel, F. X. Timmes, and N. Vladimirova. Mapping Initial Hydrostatic Models in Godunov Codes. *ApJS*, 143:539–565, December 2002.

Appendix A

Care has been taken in this thesis to minimize the use of technical terms and acronyms, but this cannot always be achieved. This appendix defines jargon terms in a glossary, and contains a table of acronyms and their meaning.

A.1 Physical and Astronomical Constants

Physical Constants		
Constant	Symbol	Approximate Value
Speed of light	c	3.00×10^{10} cm s^{-1}
Newton's constant	G	6.67×10^{-8} cm^3 g^{-1} s^{-1}
Planck's constant	$h_{\rm P}$	6.63×10^{-27} erg s
Electron charge	e	4.80×10^{-10} esu
Electron mass	m_e	9.11×10^{-28} g
Proton mass	$m_{\rm p}$	1.67×10^{-24} g
Boltzmann's constant	$k_{\rm B}$	1.38×10^{-16} erg K^{-1}
Radiation constant	$a_{\rm rad}$	7.56×10^{-15} erg cm^{-3} K^{-4}

Astrophysical Units

Unit	Symbol	Approximate Value
Solar mass	$M_\odot$	1.99×10^{33} g
Solar metallicity	$Z_\odot$	0.02
Solar radius	$R_\odot$	6.96×10^{10} cm
Solar luminousity	$L_\odot$	3.9×10^{33} erg^{-1} s^{-1}
Hubble constant	H_0	$100h$ km s^{-1} Mpc^{-1}
critical density	ρ_0	1.88×10^{-29} h^2 g^1 cm^{-3}
parsec	pc	3.08×10^{18} cm
kilo-parsec	kpc	3.08×10^{21} cm
astronomical unit	AU	1.50×10^{13} cm
light year	ly	9.46×10^{17} cm
Bethe	B	10^{51} erg

A.2 Acronyms

Table A.1: Acronyms

Acronym	Meaning
AAS	American Astronomical Society
AMR	Adaptive Mesh Refinement
BH	Black Hole
`CASTRO`	**C**ompressible **ASTRO**physics
CCD	Charge Coupled Device
CCSN	Core-Collapse SuperNova
CMB	Cosmic Microwave Background Radiation
CNO	Carbon-Nitrogen-Oxygen, a sequence of nuclear burning
COBE	Cosmic Background Explorer
DM	Dark Matter
DOE	Department of Energy
`GADGET`	**GA**laxies with **D**ark matter and **G**as int**E**rac**T**
E-ELT	European Extremely Large Telescope
EOS	Equation of State
GMT	Giant Magellan Telescope
GR	General Relativity
GRB	Gamma Ray Burst
GSN	GR-instability SuperNova
HR	Hertzsprung-Russell diagram
HST	Hubble Space Telescope
IAU	International Astronomical Union
IMF	Initial Mass Function
ISM	Inter-Stellar Medium
IGM	Inter-Galactic Medium
JWST	James Webb Space Telescope
LBNL	Lawrence Berkeley National Laboratory

Continued on next page

Table A.1 – continued from previous page

Acronym	Meaning
LBV	Luminous Blue Variable
ΛCDM	Lambda Cold Dark Matter
LISA	Laser Interferometer Space Antenna
LMXB	Low-Mass X-Ray Binary
LSST	Large Synoptic Survey Telescope
LTE	Local Thermodynamic Equilibrium
MHD	Magneto Hydro Dynamic
MXRB	Massive X-Ray Binary
NASA	National Aeronautics and Space Administration
NSE	Nuclear Statistical Equilibrium
NSF	National Science Foundation
QSO	Quasi-Stellar Object
Quasar	QUASi-stellAR radio source
PPSN	Pulsational Pair-instability SuperNova
PSN	Pair-instability SuperNova
SDSS	Sloan Digital Sky Survey
SFR	Star Formation Rate
SLSN	SuperLuminous SN
SMBH	Super Massive Black Hole
SMS	Super Massive Star
SN	SuperNova
SNR	SuperNova Remnant
SPH	Smoothed Particle Hydrodynamics
TMT	Thirty Meter Telescope
WMAP	Wilkinson Microwave Anisotropy Probe
XRB	X-Ray Binary
ZAMS	Zero Age Main Sequence